Aix*Marseille université

UNIVERSITÀ DI BOLOGNA

PHD THESIS

Université d'Aix-Marseille

Partner University: Università di Bologna

Doctoral School: *Sciences pour l'Ingénieur: Mécanique, Physique, Micro et Nanoélectronique*

Laboratory :
M2P2: Laboratoire de Mécanique, Modélisation & Procédés Propres

Thesis defended to obtain the title of Ph.D. of Science

Speciality : **Fluids Physics and Mechanics**

Numerical modelling of transport and turbulence in tokamak edge plasma with divertor configuration

---

Presented by:

Davide Galassi

Board of examiners for public Ph.D. defense on December 8, 2017:

Pr. Pascale Hennequin	Reviewer – École Polytechnique
Pr. Paolo Ricci	Reviewer – École Polytechnique Fédérale de Lausanne
Pr. Giovanni Lapenta	Examiner – University of Leuven
Dr. Eric Serre	Ph.D. Advisor – CNRS, M2P2 Laboratory
Pr. Domiziano Mostacci	Ph.D. Advisor – University of Bologna
Dr. Guido Ciraolo	Ph.D. Co-Supervisor - CEA IRFM, Centrale Marseille
Dr. Benjamin Dudson	Invited – University of York
Dr. Patrick Tamain	Invited – CEA IRFM

Aix*Marseille université

UNIVERSITÀ DI BOLOGNA

Thèse de doctorat

Université d'Aix-Marseille

Université Partenaire: Università di Bologna

École doctorale: *Sciences pour l'Ingénieur: Mécanique, Physique, Micro et Nanoélectronique*

Laboratoire d'accueil :
M2P2: Laboratoire de Mécanique, Modélisation & Procédés Propres

Thèse présentée pour obtenir le grade universitaire de docteur

Spécialité : **Mécanique et Physique des Fluides**

Modélisation numérique du transport et de la turbulence dans le plasma de bord des tokamaks avec configuration divertor

---

Presentée par:

Davide Galassi

Thèse soutenue publiquement le 8 Décembre 2017 devant le jury composé de:

Pr. Pascale Hennequin	Rapporteur – École Polytechnique
Pr. Paolo Ricci	Rapporteur – École Polytechnique Fédérale de Lausanne
Pr. Giovanni Lapenta	Examinateur – Université de Leuven
Dr. Eric Serre	Directeur de thèse – CNRS, Laboratoire M2P2
Pr. Domiziano Mostacci	Directeur de thèse – Université de Bologna
Dr. Guido Ciraolo	Co-Directeur de thèse – CEA IRFM, Centrale Marseille
Dr. Benjamin Dudson	Invité – Université de York
Dr. Patrick Tamain	Invité – CEA IRFM

Acknowledgements

First of all I would like to thank my PhD thesis director, Eric Serre, for having scientifically and personally accompanied me through these years. From the very first time that I spoke with him, he gave me advices that have always revealed successful. Moreover, he always encouraged me to participate in scientific events and in communicating my work, which are very important points in the life of a young researcher.
Then I owe a big thank to Guido Ciraolo. Guido believed in me from the first time that I arrived in France, and pushed me always beyond my limits, giving me strength and self-confidence. With him, not only I shared all my scientific career in fusion, but also many unforgettable moments in my personal life, such as the days spent in Vienna and the AC/DC concert in Marseille!
I want to thank then Domiziano Mostacci, for having allowed me to start my path in the fusion field, and for having followed me from Bologna until my PhD defence.
A very big thank goes to Patrick Tamain. Through these years he has taught me, with a lot of patience, all that I needed to know about plasma, turbulence and much more. At the beginning it was very difficult to follow, but I feel that I learnt much from our discussions, so that in the end we have been really able to have constructive dialogues. And the next time that we will meet as opponents on the football field at a PSI conference I will have no mercy!
The next on the thanking list is Philippe Ghendrih. In our discussion he provided an original point of view, and pushed me to question the common interpretation of the scientific problems that I was analysing, in order to get a personal and deep understanding. I am honoured to have worked with him, and I admire the humbleness and the sincere commitment with which he helps the students in their work.
I wish to thank Hugo Bufferand, for his constant help with the simulations, but also for the beers together in Oxford and Abingdon. I thank also Nicolas Fedorczak for the interesting discussions at the 508 building in Cadarache, and for his precious help in the study of my simulations.
A special thank goes to Thomas "the PoPe" Cartier-Michaud, for helping me in the last part of my thesis, with infinite generosity and patience. I admire in him these qualities even more than the scientific ones. I also thank Clothilde Colin, which introduced to me the TOKAM3X code and most importantly the daily traffic jam in Marseille! Many thanks also to Frederic Schwander, for the discussions and the coffees at the M2P2.
All these people that I mentioned, were ready to help me not only in the scientific life, but also from the personal point of view, every time that I needed, giving the priority to my future and to my personal and professional growth.

Moving to the PhD students with which I shared the last three years, it is difficult to categorize them and to put them in a list: I will do my best.
I would like to thank the PhD students of the 508 building at IRFM, and especially Alberto, Julien, Matteo, Serafina, and also the last arrived, Giacomino. The support that you gave me is priceless. In my mind will always echo the "Galaxy" song, which you put on all the times that I arrived. But we shared much more than this, as you know, and I would have to write another thesis for giving an idea of what we have lived together. From the 513 I must thank Nicolas, which was not only a close colleague, but also my first football trainer (even though maybe he regrets now to have put me in the role of striker)! I thank Claudia and Camille, which have shared the same destiny with TOKAM, Mirabeau...and much more. I would also like to thank Cristian: always remember our nights at SAF!
From the M2P2 I would like to thank Marianna, Eddy, Juan, William, Rachel, Eunok, Giorgio and Elisabetta. We passed great moments together, independently from the fact that we were in the office or in the city centre, drinking a pastis or watching weird tv series at Eddy's place. I also thank Federico and Raffaele with whom, even if they arrived in our group just a few time ago, I already get along very well.
I was really happy to see you every day that I came to work: the PhD was less painful with you on my side! We built very strong bonds, which I hope, and I think, will stay unchanged even after this experience. I wish to you all the best.
I thank the group of Italians working in Cadarache, which are too numerous to enumerate: they made me feel the italian warmth and joy, every time that I needed!
A special thank goes to my housemates: Adrien, Axel, Clément, Damien, Hugo, Katia, Mylène and also François (even if we were housemates for a short, intense time). All of you have simply made me feel at home. From the movies seen together, to the board games in the evening, to parties and apéros, and the jokes around the table at dinner: it was just an amazing time for me. I could not find better "colocs": thank you guys, Allée de Pomone is more than just a house, it is a true legend!
I deeply thank my family. Even if it was difficult at the beginning to live far away from each other, both for me and for them, they always supported me and encouraged me to pursue my professional objectives. I know that I can always count on them. Grazie mamma, papà e Lucia, I am very proud of you.
Finally I want to thank Silvia, my girlfriend. She has been on my side from the beginning of this adventure, until the end. She gave me the courage and the self-confidence that I needed to go on in the worst moments, and she was there when it was the time to celebrate. Grazie Silvia, this PhD work is also yours.

Summary

Nuclear fusion could provide a steady, non-CO_2-emitting, sustainable and abundant source of energy in the future. Nowadays, tokamaks offer the best performance, by confining a plasma at high temperature by means of a magnetic field. Two of the major technological challenges for the exploitation of tokamaks are the extraction of power and the confinement of plasma over long periods of time. These issues are associated with the plasma dynamics in the direction perpendicular to the magnetic field lines, in which turbulence plays a key role, determining the characteristic radial gradients. In this thesis we are interested in the modelling of the edge region of the plasma in the tokamak, which extends from the outside of the core to the Scrape-Off Layer (SOL) where the magnetic field lines intercept the wall. In particular we want to investigate the divertor configuration, adopted by most of the present tokamaks and by ITER, in which the central plasma is isolated from the walls by introducing a point, called X, where the magnetic field lines have a theoretically infinite length. With this magnetic configuration, it is possible to experimentally achieve the High confinement (H) mode. However, the plasma dynamics leading to this condition still lacks of a theoretically exhaustive explanation. Moreover, recent experiments have highlighted turbulence in the divertor region, and it is thus necessary to investigate its role on the equilibrium in edge plasma.
The numerical effort in the edge plasma simulation has been mainly focused, up to now, on simplified circular geometries. Exploiting the flexibility in the geometry definition of the fluid turbulence code TOKAM3X, developed through the collaboration of the IRFM at the CEA and the laboratory M2P2 at Aix-Marseille University, we study in this thesis the effects of the divertor geometry on turbulent transport and on the overall equilibrium in plasma edge.
A comparison with simulations in simplified circular geometry shows a similar intermittent nature of turbulence in the outermost region of the plasma. Nevertheless, the divertor geometry affects the shape and the amplitude of the fluctuations, especially in the vicinity of the X-point. In particular, the turbulent structures stretch radially with an inverse proportionality to the intensity of the poloidal field, ultimately affecting the transverse fluxes. The amplitude of the fluctuations, which has a maximum at the equatorial plane, is strongly reduced in the vicinity of the X point, due to the variation in the angle of incidence of the field lines, in agreement with recent experimental data. However, turbulence in the divertor seems to be effective in spreading the density profiles at the outer target.
Cross-field fluxes associated to turbulence and to average fields contribute in a comparable manner to the drive of flows in the parallel direction in the SOL. The resulting

flow pattern is strongly asymmetric, coherently with experimental observations. Equilibrium radial gradients are enhanced by the divertor geometry: more specifically, the low magnetic curvature and the magnetic shear are identified as two stabilising mechanisms for turbulent transport. In addition, a zone of increased stability, namely a transport barrier, systematically intervenes in the divertor configuration, partially inhibiting the radial transport at a given radial position. This mechanism is potentially very important for understanding the transition from low to high confinement mode, which will be the operational mode of ITER.
Globally, we highlight the importance of the local features of the magnetic field in determining the turbulent transport and, ultimately, the overall equilibrium in plasma edge. 3D turbulence global simulations in realistic geometry can thus give important guidelines both for the interpretation of experiments, and for a coherent description of edge transport with reduced models.

Résumé

La fusion nucléaire pourrait offrir dans l'avenir une nouvelle source d'énergie stable, non émettrice de CO_2, pérenne et disponible. Aujourd'hui, les tokamaks offrent les meilleures performances, en confinant un plasma à haute température au moyen d'un champ magnétique. Deux des enjeux technologiques majeurs pour l'exploitation des tokamaks sont l'extraction de puissance et le confinement du plasma sur des temps longs. Ces enjeux sont associés à l'équilibre complexe entre la dynamique du plasma dans la direction perpendiculaire aux lignes de champ magnétique, où la turbulence détermine les gradient caractéristiques, et la direction parallèle. Dans cette thèse, nous sommes intéressés par la modélisation de la région de bord du plasma dans le tokamak, qui s'étend de l'extérieur du plasma central à la Scrape-Off Layer (SOL), où les lignes de champ magnétique interceptent le mur. En particulier, nous voulons étudier la configuration divertor, adoptée par la plupart des tokamaks actuels et par ITER, dans laquelle le plasma central est isolé des parois en introduisant un point, appelé X, où les lignes de champs magnétiques ont une longueur théoriquement infinie. Avec cette configuration magnétique, il est possible d'atteindre expérimentalement le mode de confinement élevé (H) qui, pourtant, manque encore d'une explication théoriquement exhaustive. De plus, des expériences récentes ont mis en évidence la turbulence dans la région du divertor, et il est donc nécessaire d'étudier son rôle dans l'équilibre plasma. L'effort numérique dans la simulation du plasma de bord a été principalement axé, jusqu'à présent, sur des géométries circulaires simplifiées. En exploitant la flexibilité dans la définition de la géométrie du code de turbulence fluide TOKAM3X, né de la collaboration de l'IRFM au CEA et du laboratoire M2P2 de l'Université Aix-Marseille, nous étudions les effets de la configuration divertor sur le transport turbulent et sur l'équilibre global dans le plasma de bord.
Une comparaison avec des simulations en géométrie circulaire montre une nature intermittente similaire de la turbulence dans la région périphérique du plasma. Néanmoins, au voisinage du point X, les structures turbulentes s'étirent radialement avec une proportionnalité inverse à l'intensité du champ poloïdal, affectant finalement les flux transversaux. L'amplitude des fluctuations, maximale au plan équatorial, est fortement réduite près du point X, en raison de la variation de l'angle d'incidence des lignes de champ, en accord avec les données expérimentales récentes. Cependant, la turbulence dans le divertor semble être efficace pour étaler les profils de densité sur la cible externe.
Les flux transverses associés à la turbulence et à la moyenne des champs contribuent de manière comparable à l'établissement des flux dans la direction parallèle dans la SOL. L'écoulement qui en résulte est fortement asymétrique, de façon similaire aux observations expérimentales. Les gradients radiaux d'équilibre sont renforcés par la configuration di-

vertor: plus précisément, la faible courbure magnétique et le cisaillement magnétique sont identifiés comme deux mécanismes de stabilisation pour le transport turbulent. De plus, une barrière de transport intervient systématiquement dans la configuration divertor, inhibant partiellement le transport radial à une position radiale donnée. Ce mécanisme est potentiellement très important pour comprendre la transition du mode de confinement faible au confinement élevé, qui sera le mode opérationnel d'ITER.
Globalement, nous soulignons l'importance des caractéristiques locales du champ magnétique dans la détermination du transport turbulent et, finalement, de l'équilibre global dans le bord du plasma. Les simulations globales de turbulence 3D en géométrie réaliste peuvent ainsi donner des lignes directrices importantes à la fois pour l'interprétation des expériences, et pour une description cohérente du transport dans le plasma de bord avec des modèles réduits.

Riassunto

La fusione nucleare potrebbe fornire in futuro una fonte di energia sostenibile e abbondante, priva di emissioni di CO_2. Ad oggi, i tokamak offrono le migliori prestazioni, confinando un plasma ad alta temperatura per mezzo di un campo magnetico. Due delle principali sfide tecnologiche per lo sfruttamento dei tokamak sono l'estrazione della potenza termica ed il confinamento del plasma per lunghi periodi di tempo. Queste problematiche sono associate alla dinamica del plasma nella direzione perpendicolare alle linee di campo magnetico, in cui la turbolenza svolge un ruolo fondamentale, determinando i gradienti radiali caratteristici. In questa tesi siamo interessati alla modellizzazione del plasma di bordo del tokamak, che si estende dall'esterno del plasma centrale fino allo Scrape-Off Layer (SOL), dove le linee di campo magnetico intercettano la parete. In particolare vogliamo studiare la configurazione divertore, adottata dalla maggior parte dei tokamaks presenti e da ITER, in cui il plasma centrale viene isolato dalle pareti introducendo un punto chiamato X, dove le linee di campo magnetico hanno una lunghezza teoricamente infinita. Con questa configurazione magnetica è possibile sperimentare la modalità ad alto confinamento (H). Tuttavia, la dinamica che conduce a questa condizione manca ancora di una spiegazione teoricamente esaustiva. Inoltre, gli esperimenti recenti hanno messo in evidenza la turbolenza nella regione del divertore, e quindi è necessario esaminare il suo ruolo sull'equilibrio del plasma di bordo.
Lo sforzo numerico nella simulazione del plasma di bordo è stato focalizzato, finora, su geometrie circolari semplificate. Sfruttando la flessibilità nella definizione della geometria del codice di turbolenza fluida TOKAM3X, sviluppato attraverso la collaborazione dell'IRFM presso il CEA ed il laboratorio M2P2 presso l'Università di Aix-Marseille, si studiano in questa tesi gli effetti della geometria divertore sul trasporto turbolento e sull'equilibrio complessivo del plasma di bordo.
Un confronto con simulazioni in geometria circolare semplificata mostra una simile natura intermittente della turbolenza nella regione più esterna del plasma. Tuttavia, la geometria del divertore influenza la forma e l'ampiezza delle fluttuazioni, soprattutto nelle vicinanze del punto X. In particolare, le strutture turbolente si estendono radialmente con una proporzionalità inversa all'intensità del campo poloidale, influenzando in ultima analisi i flussi trasversali. L'ampiezza delle fluttuazioni, massima al piano equatoriale, è fortemente ridotta in prossimità del punto X, a causa della variazione dell'angolo di incidenza delle linee di campo, in accordo con i recenti dati sperimentali. Tuttavia, la turbolenza nel divertore sembra essere efficace nella diffusione dei profili di densità al target esterno.
I flussi perpendicolari al campo, associati alla turbolenza e ai campi medi, contribuiscono

in modo paragonabile alla determinazione dei flussi in direzione parallela nella SOL. Il pattern di flusso risultante è fortemente asimmetrico, coerentemente con le osservazioni sperimentali. I gradienti radiali di equilibrio sono rafforzati dalla configurazione divertore: più in particolare la bassa curvatura magnetica e lo shear magnetico sono identificati come due meccanismi di stabilizzazione per il trasporto turbolento. Inoltre, una zona di maggiore stabilità, vale a dire una barriera di trasporto, interviene sistematicamente nella configurazione divertore, inibendo parzialmente il trasporto in una data posizione radiale. Questo meccanismo è potenzialmente molto importante per comprendere la transizione dalla modalità di basso a quella di alto confinamento, che sarà la modalità operativa di ITER.
Globalmente, si evidenziano l'importanza delle caratteristiche locali del campo magnetico nel determinare il trasporto turbolento e, di conseguenza, l'equilibrio complessivo del bordo del plasma. Le simulazioni globali di turbolenza 3D in geometria realistica possono quindi dare importanti linee guida sia per l'interpretazione degli esperimenti, sia per una descrizione coerente del trasporto nel plasma di bordo con modelli ridotti.

List of Acronyms

- **AUG** : Asdex Upgrade (tokamak located in Garching, Germany)
- **DIII-D** : Doublet III-D (tokamak in San Diego, USA)
- **ELM** : Edge Localized Mode
- **HFS** : High Field Side
- **ITER** : International Thermonuclear Experimental Reactor (tokamak in construction in Cadarache, France)
- **JET** : Joint European Torus (European tokamak, located in Culham, UK)
- **JT-60U** : Japan Torus 60 (tokamak located in Naka, Japan)
- **LFS** : Low Field Side
- **LHD** : Large Helical Device (stellarator in Toki, Japan)
- **MAST** : Mega Ampère Spherical Tokamak (tokamak located in Culham, UK)
- **MHD** : MagnetoHydroDynamics
- **PFR** : Private Flux Region
- **SOL** : Scrape-Off Layer
- **TCV** : Tokamak à Configuration Variable (tokamak located in Lausanne, Switzerland)
- **Tore Supra** : Tokamak located in Cadarache, France, active until 2013
- **TORPEX** : Toroidal Plasma Experiment (tokamak located in Lausanne, Switzerland)
- **W7-X** : Wendelstein 7-X (stellarator in Greifswald, Germany)
- **WEST** : Tungsten (W) Environment in Steady-state Tokamak (tokamak located in Cadarache, France)

Contents

Chapter 1

Introduction

Contents

We present here some general concepts of plasma physics that will be used in the following chapters. Firstly, we describe the fusion and the main tokamak principles, with a focus on the different magnetic configurations. We introduce then the fluid approach for the modelling of transport in the edge plasma, including the interactions with solid components. Finally, we present the context and the objectives of this thesis.

1.1 Fusion as energy source

Thermonuclear fusion aims to be among the future contributors to the energy mix. The physical principle that can be exploited is the fusion reaction between two light nuclei, which leads to a more stable element, converting the mass defect into kinetic energy according to the famous Einstein's law. The two light nuclei must possess a thermal energy sufficient to overcome the strong electrostatic repulsion acting between two positively charged particles. Moreover, this energy must allow a sufficient collision probability between the two particles. Figure 1.1 shows the cross section of the fusion reaction as a function of the thermal energy.

One can see that the reaction

$$ {}^{2}_{1}D + {}^{3}_{1}T \rightarrow {}^{4}_{2}He(3.5\ MeV) + {}^{0}_{1}n(14.1\ MeV) \tag{1.1} $$

is the one occurring at lowest thermal energy. $D-D$ fusion reactions and $D-He_3$ can also be technically considered. Since the temperatures needed for the fusion reaction are extremely elevated, the matter is at the state of plasma, namely a gas formed by ionised

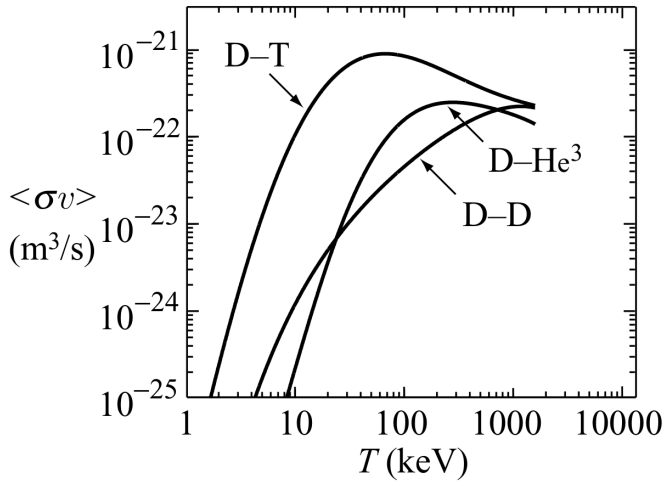

Figure 1.1: *Cross-section of fusion reactions for different couples of species, as a function of thermal energy, and averaged on the ions distribution functions. Figure reprinted from [1].*

atoms. In particular, at temperatures giving relevant fusion reaction rates, the plasma is completely ionised.
The kinetic energy of the products of the fusion reaction can be converted into thermal energy and, finally, to electric energy. One can see from equation (1.1) that fusion does not involve chain reactions, contrary to the nuclear fission. This makes an hypothetical fusion reactor intrinsically safe, although, on the other hand, a constant fuelling is needed to maintain the reaction. The fusion reaction does not directly produce heavy radioactive elements, thus limiting the necessary associated precautions. Moreover, the fuel, basically deuterium, can be found in large abundance in oceans water, so that its supply is practically infinite. While the physical principle and the advantages of fusion have been known from long time, its exploitation for civil applications is still not achieved, because of the complexity of the associated physical and technical challenges.
Different solutions are being explored for the design of nuclear fusion reactors. Each of them, in order to represent a viable energy source, must fulfil a positive power balance. In particular, one defines the amplification factor Q as

$$Q \equiv \frac{P_{fus}}{P_{inj}} \tag{1.2}$$

where P_{fus} is the total power produced by nuclear reactions and P_{inj} is the total power injected into the system. This global balance translates into a condition, called Lawson criterion [2]:

$$nT_i\tau_E > 3 \cdot 10^{21} \frac{keV\ s}{m^3} \tag{1.3}$$

where n is the density, T_i is the ion temperature, and τ_E is the confinement time. We

notice that temperature is expressed in eV, designating actually the thermal energy associated to the species. The confinement time is the typical decay time of the energy stored in the plasma, when all the energy sources are shut off.
There are two main concepts, explored to fulfil the Lawson criterion: the inertial and the magnetic confinement fusion. The inertial confinement fusion exploits the energy of multiple lasers to uniformly compress a fuel target, until high densities ($\sim 10^{31}\ m^{-3}$) and temperatures ($\sim 10\ keV$) are achieved, although for a very short confinement time ($\sim 10^{-11}\ s$). On the contrary, magnetic confinement fusion aims at achieving high-temperature plasmas ($\sim 10\ keV$) for a longer characteristic time ($\sim 1\ s$), but with a relatively low density ($\sim 10^{19} - 10^{20}\ m^{-3}$). The low power density produced per volume unit in magnetically confined plasmas is one of the main disadvantages with respect to other energy sources, such as nuclear fission, since it increases the necessary size of the devices and the associated costs.
Until now, the best performances in terms of amplification factor have been achieved in tokamaks, and the world record has been set by a JET (Joint European Torus) pulse in 1997, with a $Q \simeq 0.62$ [3]. The tokamak ITER, in construction at present in the Cadarache site (south of France), is expected to reach $Q \geq 10$ [4]. ITER corresponds therefore to a crucial step on the path towards the exploitation of fusion energy. The efforts of the international fusion community are joint in order to face the physical and technological challenges involved in the ITER project.

1.2 The tokamak principles

Let's see how the conditions necessary to achieve a good fusion reaction rate can be obtained in a tokamak. In order to do this, it is necessary to understand how the plasma, a conducting gas formed by electrically charged particles, behaves in presence of an electromagnetic field. The considerations here expressed are treated in detail in all the main plasma physics textbooks ([1], [5], [6] etc.).

1.2.1 Single particle motion

An electrically charged particle in an electro-magnetic field is subject to the Lorentz force. Its trajectory can be calculated by solving the equation of motion:

$$m\frac{d\vec{v}}{dt} = q\left[\vec{E}(\vec{x},t) + \vec{v}\times\vec{B}(\vec{x},t)\right] \tag{1.4}$$

This formulation is valid for non-relativistic velocities, which characterise plasmas that are studied in the framework of this thesis. Indeed the thermal velocity, defined as

$$v_{th} = \sqrt{\frac{k_B T}{m}} \tag{1.5}$$

can reach at most values of $\sim 10^6\ m/s$ for electrons, in the region of the plasma that we are interested in. In (1.5), k_B is the Boltzmann constant and T is expressed in K. We define the magnetic field unitary vector $\vec{b}$:

$$\vec{b} \equiv \frac{\vec{B}}{\|\vec{B}\|} = \frac{\vec{B}}{B} \tag{1.6}$$

Projecting equation (1.4) on the magnetic field, we obtain:

$$m\frac{dv_\parallel}{dt} = qE_\parallel \tag{1.7}$$

where the subscript $\parallel$ stands for the direction parallel to the magnetic field. The particle can thus stream freely along the magnetic field-line, and can only be accelerated by an electric field in the same direction.
If the electric field is null, and the magnetic field is uniform in space and time, the solution of (1.4) is a circular orbit called *cyclotron gyration*, on the plane perpendicular to the field-line. The characteristic frequency is the cyclotronic frequency

$$\omega \equiv \frac{|q|\,B}{m} \tag{1.8}$$

and the radius of the orbit, called *Larmor radius*, is

$$\rho_l \equiv \frac{v_\perp}{\omega} = \frac{mv_\perp}{|q|\,B} \tag{1.9}$$

where the subscript $\perp$ indicates the plane perpendicular to the magnetic field-line. The charged particle follows an helical trajectory around the magnetic field-lines, with a finite orbit radius. This is the fundamental principle of confinement exploited in magnetic fusion devices: the particle motion in the perpendicular direction is bounded to the field-line.
Different concepts of magnetic confinement devices have been historically tested. The tokamak exploits the feature of a toroidal geometry, which allows to bend a magnetic field-line and close it on itself. It is important indeed for hot ions to pass enough time on the magnetic field-lines, in order to obtain a sufficient confinement time.
However, this particle motion describes only an ideal situation. Considering now the trajectory in presence of homogeneous electric and magnetic fields, one finds that the guiding centre of the charged particles trajectory, which is the center of the cyclotron gyration, drifts with a velocity

$$\vec{v}_{E\times B} \equiv \frac{\vec{E}\times\vec{B}}{B^2} \tag{1.10}$$

This velocity is called $E \times B$ or *electric* drift velocity, and it is perpendicular to the

magnetic field-line. It is important to notice that this drift velocity does not depend on the particle charge, so it does not cause a net current.
In a toroidal device, a toroidal magnetic field, created in vacuum by means of a set of dedicated coils, has a shape given by the Ampère-Maxwell law in its integral form:

$$\vec{B} = \frac{\mu_0 I_{tor}}{2\pi R}\hat{e}_\varphi \tag{1.11}$$

where $\hat{e}_\varphi$ indicates the toroidal direction and I_{tor} is the total current flowing in the toroidal coils, which enclose the vacuum vessel, and lie on a transverse plane with respect to the toroidal direction. R is the radial distance from the main axis, and it is also the curvature radius for a toroidal field-line. Equation (1.11) describes a non-uniform magnetic field, with a variation scale length R much greater than the Larmor radius, which for hot deuterium ions can be of the order of the centimetre. Taking into account this scale separation, one can average the motion equation on the cyclotronic gyration, finding that the guiding centre moves with a drift velocity $\vec{v}_d$:

$$\vec{v}_d = \underbrace{\frac{1}{2}\frac{q}{|q|}\rho_l v_\perp \frac{\vec{B}\times\vec{\nabla}B}{B^2}}_{\vec{v}_{\nabla B}} + \underbrace{\frac{m}{qB^2}v_\parallel^2\frac{\vec{R}\times\vec{B}}{R^2}}_{\vec{v}_R} \tag{1.12}$$

where we identify the ∇B *drift* velocity $\vec{v}_{\nabla B}$, and the *curvature drift* $\vec{v}_R$. The drift velocity $\vec{v}_d$ is opposite for ions and electrons, and it is vertical in the case of a toroidal field with the described shape. If no further precaution was taken, the $\vec{v}_{\nabla B}$ and $\vec{v}_R$ drifts would generate a vertical electric field, and by consequence the plasma would drift horizontally because of the $E \times B$ drift. In a device with a radius of $\sim 2\ m$, in a purely toroidal field, particle would be lost in around 1 ms, which is well below the confinement time necessary to attain the Lawson criterion. It is necessary, therefore, to add a component to the magnetic field, able to limit these losses, called *poloidal* magnetic field.

1.2.2 The tokamak magnetic configuration

In tokamaks, the poloidal field is mainly produced by the electric current flowing in the plasma, called I_p, and can be adjusted by the insertion of several other coils enclosing toroidally the vacuum vessel. The plasma current flows in the toroidal direction, and it is induced in the plasma, which is a conductive mean, by a variable magnetic flux, produced by the central solenoidal coil. In other types of magnetic fusion devices, as *stellarators*, this poloidal magnetic field is principally produced by coils external to the plasma vessel.
The poloidal magnetic field is defined as the component of the magnetic field lying on a (R, Z) plane in a toroidal system, where Z is the vertical direction, also called *poloidal plane*. In order to compensate the losses by the ∇B and the curvature drifts, field-lines must have an helical shape, wrapped around a toroidal surface. Figure 1.2 shows an example of a magnetic field-line in a tokamak.

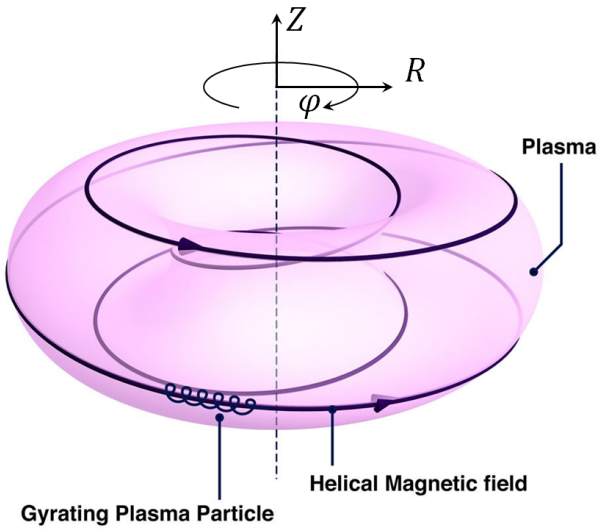

Figure 1.2: *Scheme of a magnetic field-line in a tokamak, lying on a magnetic surface, in pink. Figure adapted from EUROfusion website [7].*

The surfaces on which magnetic field-lines lie are called *magnetic surfaces*. During its motion on the field-line, particles undergo the vertical drift, which displaces them from the magnetic surfaces successively in the upward and in the downward directions, such that globally the effect of drifts is compensated.
The poloidal field has also a fundamental role in determining the plasma equilibrium. Indeed, the force due to the plasma pressure, directed radially outwards, must be compensated by and inward force due to the magnetic field. This equilibrium can be studied by means of the MHD (MagnetoHydroDynamics) branch of plasma physics, which considers the plasma as a single-fluid conductive mean, and takes into account the feedback of the plasma currents on the magnetic fields by means of the solution of the Ampère-Maxwell equation. The two basic equations determining the magnetic equilibrium are:

$$\begin{cases} \vec{\nabla} p &= \vec{j} \times \vec{B} \\ \vec{\nabla} \times \vec{B} &= \mu_0 \vec{j} \end{cases} \tag{1.13}$$

where $\vec{j}$ is the density current and p the plasma pressure. The poloidal magnetic field, along with the spatial variation of the toroidal field, contributes to the force opposing to the (essentially radial) plasma pressure force. We also notice from the first equation of system (1.13), that $\vec{B} \cdot \vec{\nabla} p = 0$. At the first order, so, magnetic surfaces are also isobars, with a high pressure at the centre decaying radially.
The magnetic equilibrium, in a toroidal axysimmetric system, as the one studied in this thesis, can be described as a series of nested toroidal magnetic surfaces, on which plasma pressure is basically constant. Figure 1.3 represents the magnetic surfaces in a tokamak.

As indicated in figure 1.3, we name r the radial distance from the magnetic axis, and θ the angular (or *poloidal*) coordinate on the (R, Z) plane (usually referred to the midplane). Usually, the poloidal magnetic field has a small amplitude if compared to the toroidal

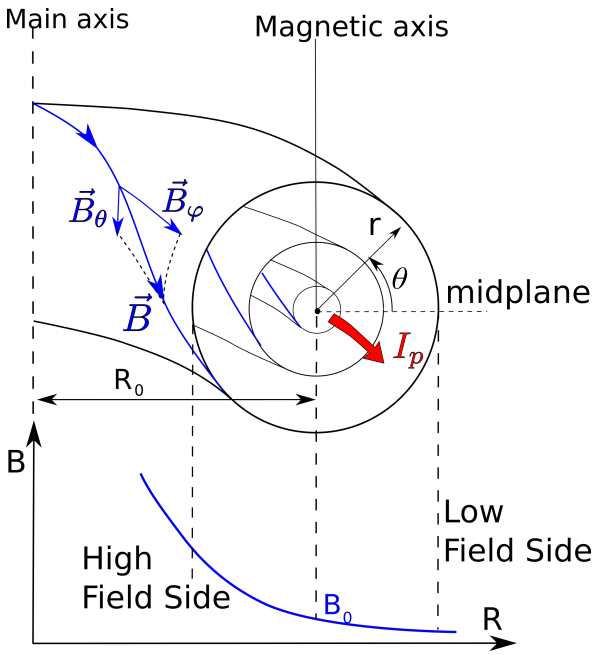

Figure 1.3: *Sketch of the nested magnetic surfaces in a tokamak. The basic geometric parameters are put in evidence. In the lower part of the figure the typical decay of the field amplitude with the major radius is represented.*

one ($\sim 1/10$), so the total magnitude of the magnetic field is roughly proportional to the inverse of the major radius. For this reason, we call Low Field Side (LFS), the region of the tokamak at larger distance R from the main axis, and HFS the region closer to it.

1.2.3 The field-line shape

The relative amplitude of the toroidal and poloidal components of the field determines the local inclination of the field-line. The angle formed by the field-line with the toroidal direction is referred to as *pitch angle*. Following the direction along the field-line, we can quantify the number of toroidal turns completed before to come back to the initial poloidal position. This quantity is called *safety factor*, and it is defined as (see [6], Chapter 3):

$$q \equiv \frac{\Delta\varphi}{2\pi} \tag{1.14}$$

where $\Delta\varphi$ is the variation in the toroidal angle. Considering a negligible component of the poloidal field with respect to the toroidal one, and straight field-lines, the total length of a field-line can be thus estimated as:

$$L_\parallel \sim 2\pi q R \tag{1.15}$$

However, as understandable from figure 1.3, the toroidal component varies along the field-line, as well as the poloidal one. A general expression for the calculation of the safety factor, is therefore the integral expression:

$$q = \frac{1}{2\pi} \oint \frac{B_\varphi}{R B_\theta} \, dl_\theta \tag{1.16}$$

where l_θ is the curvilinear poloidal coordinate. The shape of the magnetic field-lines, and by consequence also the safety factor, can be regulated acting on the currents intervening in the system.

1.3 Limiter and divertor configurations

Ideally, the confined plasma should be completely isolated from the walls of the vacuum chamber. However, it is technically impossible to build a magnetic field tangential at all the points to a certain surface. Magnetic field-lines intercept at some point a solid component: since particles are free to stream along the field-lines, this implies a particle flux, and by consequence also a heat flux, to the wall components, which must be limited in order to preserve the material. The simplest technical solution to control the fluxes to the wall components, is the insertion of a solid component with the function of target for the field-lines. Usually, we define *toroidal limiter* a component extending along the toroidal direction of the tokamak, on whose sides the magnetic field-lines impinge. Instead, a *poloidal limiter* is an obstacle for the field-lines extending in poloidal direction and placed at a precise toroidal position. A simple representation of the cross-section of a tokamak with toroidal limiter is given in figure 1.4.

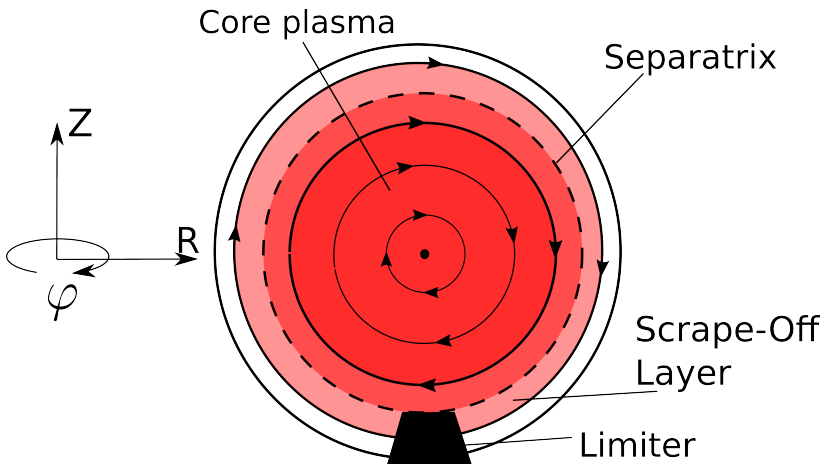

Figure 1.4: *Scheme of the limiter magnetic configuration. Arrows indicate the direction (arbitrary) of the poloidal magnetic field, which is the projection of the field-line on the poloidal plane.*

field-lines that intercept the solid components are commonly called (in a somehow mis-

leading way) *open field-lines*, and the plasma region with these lines is called *Scrape-Off Layer* (SOL), since the plasma is progressively lost to the wall. This region is separated from the *closed field-lines* by the magnetic surface named *separatrix*. Usually, we define the minor radius of the plasma, a, as the radial distance of the separatrix from the magnetic axis.
The limiter geometry was adopted by Tore Supra [8], and it is still used in other tokamaks (e.g. FTU [9] and ISTTOK [10]). Even if nowadays the limited configuration has been replaced in the majority of the tokamaks by the diverted one, it is still helpful in the operation and control of fusion devices. Indeed, in the early phases of a discharge, the plasma is usually created on the HFS of the tokamak. Therefore, the limiting action is given by the inner wall of the plasma chamber, before the passage to a divertor configuration. This evolution of the plasma magnetic equilibrium will be adopted also in ITER [11].
As one can see from figure 1.4, in limiter configuration the central plasma zone is very close to the point where field-lines intercept the solid component. This is an unfavourable situation, since the interactions between the plasma and the wall leads to an emission by the latter of neutral atoms. These atoms can be the result of a *recycling* process: indeed, ions impinging on solid wall components can be captured, then recombine, and, after a certain retention time, diffuse back to the plasma as neutral atoms. Moreover, the plasma flux can cause a chemical or a physical sputtering (see [12], Chapter 3 for a more detailed description of these phenomena), whose consequence consists in a release of atoms or molecules of the affected material towards the plasma region.
Neutral atoms have thus an elevated probability to ionise in the closed flux surfaces region, immediately close to the limiter, subtracting energy to the plasma electrons, and thus degrading performances. The *divertor* configuration is a solution to distance the core plasma from the solid components. Practically, a current with the same direction as the plasma current is induced in a coil, such that the respective generated poloidal fields sum up. As a consequence, a purely toroidal field-line is generated, whose projection on the poloidal plane is called *X-point*. At this point, the poloidal magnetic field is null and the magnetic field-line is theoretically infinite, as well as the safety factor q. A schematic representation of the divertor configuration is given in figure 1.5.

One can see that the divertor configuration introduces a topological zone called *Private Flux Region* (PFR). Moreover, the SOL is usually referred to as *Main SOL* in the poloidal region adjacent to the closed field-lines, and *divertor leg*, in the zone confining with the PFR. Figure 1.5 shows in particular a so-called *Single-Null* diverted plasma, which is the most common solution in tokamaks, including ITER. This means that the core plasma is separated by the open field-lines zone by only one X-point. In *Double-null* configurations, two X-points lie on the separatrix (approximately). Even more complicated configurations exist, such as the *Super-X*, where divertor legs are extremely extended, or the *Snowflake* where multiple X-points exist. These two latter configurations are being tested and represent possible solutions for the design of DEMO. Other divertor solutions have been tested in the past, such as the the *Ergodic divertor*, in which a perturbation is constantly applied to the magnetic field, such that the concept of magnetic surfaces vanishes, and the plasma flux is continuously re-distributed.

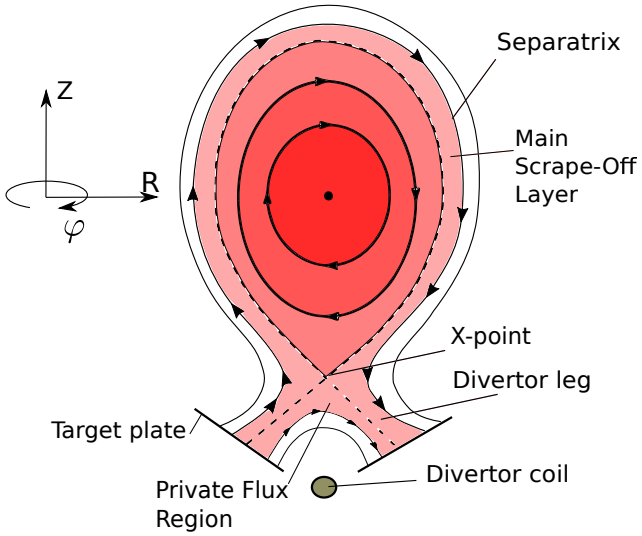

Figure 1.5: *Scheme of the diverted magnetic configuration.*

1.4 Transverse transport processes in tokamaks

In order to understand the global confinement in a tokamak, one has to evaluate the collective characteristics of the plasma, including the interactions among particles. In fact, we are interested in understanding how the tokamak global system can maintain high particles density and temperature at its centre, and at the same time reach reasonable characteristics at its peripheral region to deal with the presence of solid components. The physical phenomena that lead to the migration of particles or energy from the centre to the SOL region, across magnetic surfaces, are called *transverse transport processes*.

1.4.1 Classical, neoclassical and anomalous transport

Considering the collisions among particles trapped in their helical trajectory, one can calculate a typical collisional diffusion coefficient for the perpendicular direction, also said *classical*:

$$D_C \sim \nu_C \rho_l^2 \tag{1.17}$$

where ν_C is the typical collision frequency, and varies as $nT^{-3/2}$ [5], while the Larmor radius varies with $T^{1/2}$. This diffusion coefficient for deuterium ions can range from 10^{-4} to 10^{-2} $m^2 s^{-1}$.
A more advanced evaluation of the diffusion coefficient takes into account the real shape of magnetic field-lines, and especially the dependence on $1/R$ of the magnetic field amplitude in a toroidal geometry. The typical interaction length among particles in the perpendicular direction depends actually on the particle trajectory, which can be trapped in a banana orbit by a magnetic mirror effect [13], or on a circular orbit (passing particles) depending on the ratio of the parallel velocity of the perpendicular one. The transport

across magnetic surfaces induced by these particular particle orbits is called *neoclassical*. Depending on the collision frequency, different neoclassical transport regimes can exist, and the associated effective diffusive coefficient are typically a factor $10 - 100$ more elevated than the classical ones.
When measuring the actual value of effective diffusion coefficients in tokamaks, by evaluating the gradients of the transported quantities, the experimental values are of the order of 1 $m^2 s^{-1}$(see for example [14] for Tore Supra), both in the core and in the edge regions. This transverse transport was first called *anomalous*, and was then understood to be due to turbulence. Here we mean by turbulence a chaotic state of the plasma, characterised by oscillations in time and space on multiple scales. Excluding the electromagnetic instabilities, linked to the interactions between the plasma current and the magnetic field which constitute the main topic of the MHD models, several instability mechanisms are indeed at play in tokamak plasmas, which enhance the particles and heat transport from the magnetic axis in the outward radial direction. We will focus in this thesis on the so-called *electrostatic* turbulence.

1.4.2 H-mode and transport barriers

The plasma equilibrium is not simply determined by an effective radial diffusion of particles and energy. Indeed, under certain circumstances, transport can be reduced in specific regions, leading to a steepening of the local pressure radial gradient. These regions are the so-called *transport barriers*. In 1982, the tokamak ASDEX has shown for the first time the *H-mode*, meaning High confinement mode, in opposition to the usual Low confinement mode, in a divertor configuration [15]. The H-mode basically consists in an enhancement of the pressure radial gradient, associated to a transport barrier in a thin peripheral region of the plasma. Usually, we call *pedestal* the pressure jump associated to the H-mode. Moreover, we will name *edge plasma* the region extending from a radial position of $r \sim 0.8 - 0.9\ a$, where the pedestal can take place, up to the SOL region. An example of L-mode and H-mode profiles is shown in figure 1.6(left).

We can distinguish two types of transport barriers, basing on their radial location. The ETBs (External Transport Barriers) are located in the edge plasma, or in a region immediately close to the separatrix, while ITBs (Internal Transport Barriers) are by definition a feature of the core plasma. An example of profiles with visible internal transport barriers is reported in figure 1.6(right).
The formation of transport barriers at the plasma edge is of great importance in the determination of the global confinement, but the H-mode has also some characteristic side-effects. Indeed, another imprint of the achievement of the H-mode in a pulse is the appearance of ELMs (Edge Localized Modes). ELMs are sudden bursts due to the electromagnetic relaxation of the system, occurring with frequencies from 10 to 1000 Hz, and they transport significant quantities of energy stored in the core plasma towards the wall.
Nevertheless, the H-mode is a desirable operational condition in the perspective of a fusion reactor, and it will also be the basic operational mode for ITER. Despite this fact, a full theoretical understanding of the the passage from Low to High confinement,

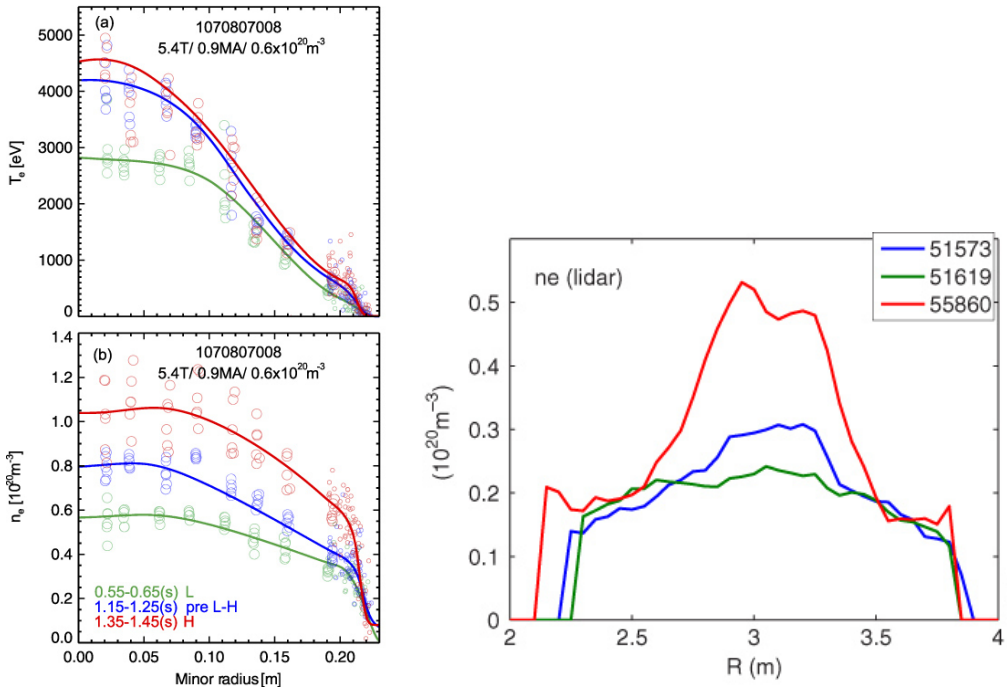

Figure 1.6: *Left: Electron density and temperature profiles comparison between L-mode and H-mode in Alcator C-mod, adapted from [16]. Right: Electron density profiles in the JET tokamak, with internal and external transport barriers. Different line colours correspond to different pulses. Figure adapted from [17].*

named *L-H transition*, is still lacking. The L-H transition seems to follow a threshold physics, with a bifurcating behaviour occurring once that a certain input power is exceeded. Nowadays, this power threshold is different for every device, and depends on several operational parameters: therefore, the prediction of the necessary input power for the ITER L-H transition is based on scaling laws [18] derived by experiments on multiple machines. Since it would be desirable to control the formation of transport barriers, a deeper understanding of this complex physical process is needed, and requires a joint effort in theoretical, numerical, and experimental analysis of the plasma edge.

1.5 The fluid approach in edge plasma modelling

1.5.1 From kinetic to fluid equations

When modelling a tokamak plasma, one can adopt different strategies. The latter can be chosen according to the specific problem that has to be simulated, and to the available computational resources. Ideally, one could simulate the plasma by solving the equation of motion for each particle. This approach would be extremely time consuming, and cannot be adopted for the description of the plasma in a tokamak, where the total number of particles is of the order $10^{20} - 10^{21}$, and interactions among particles must be taken

into account. It is recommendable then to adopt a statistical approach for the solution of the problem, and to seek for the probability density function, which expresses the average number of particles in an infinitesimal volume in the phase space $(\vec{r}, \vec{v})$. In order to get the probability density function f of the specie s, one has to solve the Boltzmann equation:

$$\partial_t f_s + \vec{v}_s \cdot \vec{\nabla}_{\vec{r}} f_s + \vec{a}_s \cdot \vec{\nabla}_{\vec{v}} f_s = \left(\frac{\partial f_s}{\partial t} \right)_C \tag{1.18}$$

where $\vec{r}$ represents the coordinates in space, $\vec{v}$ the particle velocity and $\vec{a}$ its acceleration. $\left(\frac{\partial f_s}{\partial t}\right)_C$ is the collisional term, and in a plasma basically represents the electrostatic collisions, which redistribute the velocity of the involved particles. The acceleration of particles is given, on average, by the collective electromagnetic fields, so that equation (1.18) takes the form:

$$\partial_t f_s + \vec{v}_s \cdot \vec{\nabla}_{\vec{r}} f_s + \frac{q_s}{m_s} \left[\vec{E}(\vec{x}, t) + \vec{v} \times \vec{B}(\vec{x}, t) \right] \cdot \vec{\nabla}_{\vec{v}} f_s = \left(\frac{\partial f_s}{\partial t} \right)_C \tag{1.19}$$

which is also known as Vlasov-Landau equation. In the kinetic approach, numerical codes solve this equation in six dimensions, plus the evolution in time of the system. This approach is particularly powerful for the description of a rarefied gas as the plasma, and it can describe the effects linked to modifications in the distribution function, such as the Landau damping [5]. In hot plasmas, but also at the interface between plasma and solid wall components (within some Debye lengths), the distribution function can be strongly perturbed, needing therefore the simulations with a kinetic code. The number of degree of freedom can be reduced in the gyro-kinetic approach, restricting the phase space to five dimensions. In gyro-kinetic modelling in fact, the perpendicular motion of particles is averaged, considering the Larmor gyration extremely fast with respect to the velocities in the other directions. The velocity phase space becomes then two-dimensional, where one dimension is represented by the velocity in the parallel direction, and one by the magnetic momentum μ. Kinetic and gyrokinetic codes are very demanding in terms of computational time.
The fluid approach allows a further reduction in the degrees of freedom of the problem, and, by consequence, on the necessary computational time. The fluid approach purpose is to determine the statistical moments of the distribution function. In order to derive the fluid equations, one must calculate the successive moments of the Boltzmann equation (1.19). The moment of order k for the distribution function of species s can be written as:

$$\mathcal{M}_s^{(k)} = \int_{-\infty}^{+\infty} \vec{v}_s^k f_s(\vec{r}, \vec{v}_s, t) d\vec{v}_s \tag{1.20}$$

A numerical model solving fluid equations, based on the averaging over the velocity space, is thus relatively less onerous from the computational point of view, since the unknowns are functions of the 3D space, with the evolution in time constituting the

fourth dimension. We present in the following, the equations obtained by the calculation of the moments of the Vlasov-Landau equation. We also define the k^{th} moment of the collisional term as:

$$\mathcal{C}_s^k = \int_{-\infty}^{+\infty} \left(\frac{\partial f_s}{\partial t}\right)_C \vec{v}_s^k d\vec{v}_s \tag{1.21}$$

A rigorous derivations of these equations can be found in the main plasma physics textbooks ([5],[6], etc.). We propose here a flavour of this derivation process, introducing the main fluid quantities, associated to the fluid approach, which will be used in the following chapters.

1.5.2 Continuity equation

The calculation of the moment of order 0 of the Vlasov-Landau equation allows to obtain the continuity equation, which represents the mass conservation:

$$\boxed{\partial_t n_s + \vec{\nabla}_{\vec{r}} \cdot (n_s \vec{u}_s) = S_s^n} \tag{1.22}$$

where the particle density is defined by the moment of order 0 of the distribution function:

$$n_s(\vec{r}, t) \equiv \mathcal{M}^0 = \int_{-\infty}^{+\infty} f_s\left(\vec{r}, \vec{v}_s, t\right) d\vec{v}_s \tag{1.23}$$

We notice that in the 0^{th} moment of the Boltzmann equation, a moment of order 1 of the distribution function appears. This quantity is the average fluid velocity, which is defined as:

$$\vec{u}_s(\vec{r}, t) \equiv \frac{\mathcal{M}^1}{n_s} = \frac{1}{n_s} \int_{-\infty}^{+\infty} \vec{v}_s f_s(\vec{r}, \vec{v}_s, t) d\vec{v}_s \tag{1.24}$$

The 0^{th} order moment of the collisional term, $\mathcal{C}_s^0$ represents the particles of a certain species which appear in the elementary volume. Typically, in plasmas, ionisation processes create ions and electrons, and must be taken into account into this term. We do not expand the expression of this term, and we rename it S_s^n.

1.5.3 Momentum equation

Calculating the moment of order 1 of the Boltzmann equation, one obtains the momentum conservation:

$$\boxed{m_s \left[\partial_t \left(n_s \vec{u}_s\right) + \vec{\nabla}_{\vec{r}} \cdot \left(n_s \vec{u}_s \otimes \vec{u}_s\right)\right] = n_s q_s \left(\vec{E} + \vec{u}_s \times \vec{B}\right) - \vec{\nabla}_{\vec{r}}\, p_s - \vec{\nabla}_{\vec{r}} \cdot \boldsymbol{\Xi}_s + \vec{\mathcal{R}}_s + \vec{S}_s^{\Gamma}} \tag{1.25}$$

One can notice in (1.25) the second order momentum of the distribution function. We can also define the velocity $\vec{v_s}' \equiv \vec{v}_s - \vec{u}_s$, whose statistical average is 0 by definition. One can develop the second order moment as:

$$\begin{aligned}\mathcal{M}^{(2)} &= \int_{-\infty}^{+\infty} \vec{v}_s \otimes \vec{v}_s f_s(\vec{v}_s)\, d\vec{v}_s = \int_{-\infty}^{+\infty} (\vec{u}_s + \vec{v_s}') \otimes (\vec{u}_s + \vec{v_s}') f_s(\vec{v}_s)\, d\vec{v}_s \\ &= \int_{-\infty}^{+\infty} \vec{u}_s \otimes \vec{u}_s f_s(\vec{v}_s)\, d\vec{v}_s \; + \vec{u}_s \otimes \cancel{\int_{-\infty}^{+\infty} \vec{v_s}' f_s(\vec{v}_s)\, d\vec{v}_s} + \cancel{\int_{-\infty}^{+\infty} \vec{v_s}' f_s(\vec{v}_s)\, d\vec{v}_s} \otimes \vec{u}_s \\ &\qquad + \int_{-\infty}^{+\infty} \vec{v_s}' \otimes \vec{v_s}' f_s(\vec{v}_s)\, d\vec{v}_s = n_s \vec{u}_s \otimes \vec{u}_s + \frac{\boldsymbol{\Pi}_s}{m_s}\end{aligned} \tag{1.26}$$

where we have defined the total pressure tensor as:

$$\boldsymbol{\Pi}_s \equiv m_s \int_{-\infty}^{+\infty} \vec{v_s}' \otimes \vec{v_s}' f_s(\vec{r}, \vec{v}_s, t)\, d\vec{v}_s \tag{1.27}$$

Here we can also introduce the isotropic pressure:

$$p_s \equiv \frac{Tr(\boldsymbol{\Pi}_s)}{3} \tag{1.28}$$

where Tr indicates the trace of a tensor. With this definition, $\boldsymbol{\Pi}_s = p_s \mathbb{I} + \boldsymbol{\Xi}_s$ where $\boldsymbol{\Xi}_s$ is the anisotropic part of the pressure tensor $Tr(\boldsymbol{\Xi}_s) = 0$.
The moment of order 1 of the collisional term is split in two parts. The first one, which we name $\vec{\mathcal{R}}_s$, represents the momentum exchanged among species by Coulombian collisions. The second one collects other momentum sources or sinks in the control volume, due for example to the interaction with neutral species. We name it $\vec{S}_s^{\Gamma}$. For the moment, we do not expand the expression of these terms.

1.5.4 Energy conservation equation

The conservation of the total energy is linked to the calculation of the second order moment of the Boltzmann equation. The total energy for a specie is defined as:

$$E_s^t = \frac{1}{2} m_s Tr(\mathcal{M}^{(2)}) \ = \frac{1}{2} m_s u_s^2 + \frac{3}{2} p_s \tag{1.29}$$

where the kinetic and the internal energies can be clearly identified. The fluid temperature is defined as:

$$T_s \equiv \frac{p_s}{n_s k_B} \tag{1.30}$$

with T_s expressed in K. The resulting equation is:

$$\boxed{\partial_t E_s^t + \vec{\nabla}_{\vec{r}} \cdot (E_s^t \vec{u}_s) = -\vec{\nabla}_{\vec{r}} \cdot (p_s \vec{u}_s) + n_s q_s \vec{u}_s \cdot \vec{E} - \vec{\nabla}_{\vec{r}} \cdot (\mathbf{\Xi}_s \vec{u}_s) - \vec{\nabla}_{\vec{r}} \cdot \vec{q}_s + \mathcal{Q}_s + S_s^E} \tag{1.31}$$

where $\mathcal{Q}_s$ represents the energy exchanged among different species. S_s^E represents the energy sources and sinks for the considered specie. The heat flux $\vec{q}_s$ is related to the third moment of of the distribution function:

$$\vec{q}_s = \frac{1}{2} m_s \int_{-\infty}^{+\infty} \|\vec{v}_s - \vec{u}_s\|^2 (\vec{v}_s - \vec{u}_s) f(\vec{v}_s) d\vec{v}_s \tag{1.32}$$

and thus needs to be expressed in function of lower order terms. From now on, every gradient denotes a spatial derivative, since we will not need derivatives in the velocity phase space.
We have shown that the k^{th+1}-moment of the distribution function appears in the calculation of the k^{th}-moment of the Boltzmann equation. Therefore, one needs to apply a closure to the system of equations presented.

1.5.5 Braginskii closures

In the set of fluid equations just presented ((1.22),(1.25),(1.31)), some quantities are left undetermined, and need to be calculated as functions of lower order moments of the distribution functions. In particular one needs to evaluate $\mathbf{\Xi}_s$, $\mathcal{R}_s$, $\vec{q}_s$ and $\mathcal{Q}_s$. These terms can be calculated starting from the Vlasov-Landau equation, and using a Fokker-Planck form for the collision term. We rely for this calculations on the Braginskii's work [19], as it is usual in the edge plasma community.
The hypothesis underlying the calculation, is that the distribution function can be ex-

panded around the Maxwellian, whose expression is:

$$f_M(\vec{r},\vec{v}) = n\left(\frac{m}{2\pi k_B T}\right)^{\frac{3}{2}} \exp\left(-\frac{m||\vec{v}-\vec{u}||^2}{2k_B T}\right) = \frac{n}{(2\pi)^{\frac{3}{2}}\, v_{th}^3} \exp\left(-\frac{||\vec{v}-\vec{u}||^2}{2v_{th}^2}\right) \quad (1.33)$$

In the edge plasma, this hypothesis is reasonable, since the number of collisions is sufficient to maintain the plasma close to the thermodynamic equilibrium. An important parameter that distinguishes the edge from the core plasma is the collisionality, commonly defined as:

$$\nu^* = \frac{L_\parallel}{\lambda_c} \quad (1.34)$$

where λ_c is the electrostatic collisions mean free path. Collisionality represents thus the average number of collisions that a charged particle undergoes while streaming on a field-line. In Tore Supra, for example, $\nu^* \sim 10^{-3}$ in the plasma core, while in the edge region ν^* is included in the range $5 - 100$.
As an example we show here the expression of the $\vec{\mathcal{R}}$ term, intervening in the momentum equation, calculated by Braginskii. This term is composed by two terms:

$$\vec{\mathcal{R}} = \vec{\mathcal{R}}_j + \vec{\mathcal{R}}_T \quad (1.35)$$

where $\vec{\mathcal{R}}_j$ is a friction force, due to the relative velocity of electron and ion velocity, and $\vec{\mathcal{R}}_t$ is a thermal force. Their expression is:

$$\vec{\mathcal{R}}_j = en_e\left(\frac{j_\parallel}{\sigma_\parallel}\vec{b} + \frac{\vec{j}_\perp}{\sigma_\perp}\right) \quad (1.36)$$

$$\vec{\mathcal{R}}_T = -0,71 n_e \nabla_\parallel T_e \vec{b} - \frac{3}{2}\frac{n_e}{\omega_{ce}\tau_e}\left(\vec{b}\times\vec{\nabla}T_e\right) \quad (1.37)$$

where $\sigma_\parallel$ et $\sigma_\perp$ are respectively the parallel and perpendicular electrical plasma conductivity, and τ_e is the electron-electron collision characteristic time:

$$\sigma_\perp = \sigma_0 T_e^{3/2} \qquad \sigma_\parallel = 1,96\ \sigma_\perp \quad (1.38)$$

with $\sigma_0 = e^2 n_e \tau_e / m_e$. We notice that $\vec{\mathcal{R}}$ has distinct parallel and perpendicular components.
The fluid equations including the Braginskii closure will be used in this thesis for the modelling of the edge plasma.

1.6 Plasma-wall interactions

The fluid equations just presented must be solved taking into account, through the boundary conditions, the interactions between the plasma and the solid surfaces, which is the most important difference between the transport processes in the closed flux surface region and in the SOL.
We are interested in particular in the dynamics along the magnetic field-line. At the interface between plasma and wall components, instead, in the early phase of a discharge, a negative charge accumulation occurs if the wall has a floating electric potential. This happens because of the much higher mobility of electrons with respect to ions. A positive electric field thus builds up, accelerating the ions towards the plasma wall, and repelling incoming electrons which do not have the necessary kinetic energy to overcome the electric potential barrier. The region over which the electric field develops is called *plasma sheath*, and it is represented schematically in figure 1.7.

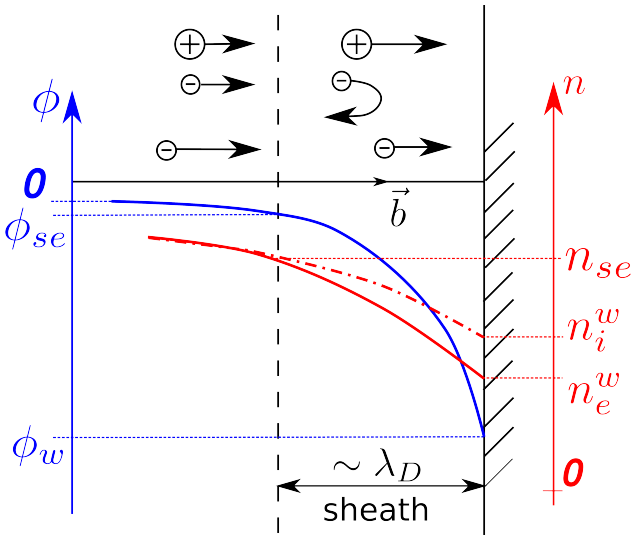

Figure 1.7: *Sketch of the plasma sheath, and of the density and potential fields in this region.*

The typical thickness of the plasma sheath is the Debye length, which is defined as:

$$\lambda_D = \sqrt{\frac{\varepsilon_0 T_e k_B}{n_e e^2}} \tag{1.39}$$

in edge plasma, where $n \sim 10^{19}$ and $T_e \sim 10\ eV$, is approximately $\lambda_D \approx 10^{-5}\ m$. Since this characteristic length is much shorter than the total length of a magnetic field-line, which is $L_\parallel \sim 10\ m$, we can reasonably assume the quasi-neutrality condition to be valid all over the domain. The electric field build-up process reaches the steady-state when the ion and the electron fluxes entering in the sheath become equal, so that the quasi-neutrality of the plasma outside this region is maintained.

1.6.1 The Bohm boundary condition

We need to study the dynamics at the sheath entrance, as it sets the boundary conditions in the parallel direction for the SOL plasma. This analysis can also be found in [12], Chapter 2. We take now as reference a null electric potential far from the sheath on the magnetic field-line, as shown in figure 1.7, so at an infinite distance if compared with the Debye length. The region where the potential starts to drop, and the ions to be accelerated, is sometimes called *pre-sheath*. Supposing that electrons follow the Boltzmann distribution, we get for the electron density at the sheath:

$$n_e = n_e^{se} \exp\left(\frac{e(\phi - \phi_{se})}{k_B T_e}\right) \tag{1.40}$$

where ϕ_{se} is the potential at the sheath entrance. In the bulk region of the Scrape-Off Layer the quasi-neutrality is valid and $n_i = n_e$. In the sheath this condition does not hold, and the Poisson's equation can be written as:

$$\frac{d^2\phi}{dx_\parallel^2} = -\frac{e}{\varepsilon_0}(n_i - n_e) \tag{1.41}$$

We have now to evaluate the ion density in the sheath. Using the energy conservation for the ions, and assuming $T_i \ll T_e$:

$$\frac{1}{2} m u_i^2 = -e\phi \tag{1.42}$$

where u_i is the ion velocity. Since the collision mean free-path λ_C is much bigger than the Debye length λ_D, the ionisation source is negligible in the sheath. The ion flux is therefore constant along the field-line, and using (1.42) we obtain

$$n_i = n_i^{se} \frac{u_i^{se}}{u_i} = n_i^{se} \sqrt{\frac{\phi_{se}}{\phi}} = n_{se} \sqrt{\frac{\phi_{se}}{\phi}} \tag{1.43}$$

where we have assumed that the sheath-entrance point is the last where the quasi-neutrality is valid. Substituting this last expression and the Boltzmann relation in the Poisson equation, we obtain:

$$\frac{d^2\phi}{dx_\parallel^2} = -\frac{e}{\varepsilon_0} n_{se} \left[\sqrt{\frac{\phi_{se}}{\phi}} - \exp\left(\frac{e(\phi - \phi_{se})}{k_B T_e}\right)\right] \tag{1.44}$$

Defining $\Delta \equiv \phi_{se} - \phi > 0$, we can expand

$$\sqrt{\frac{\phi_{se}}{\phi}} = \sqrt{1+\frac{\Delta}{\phi}} \approx 1 + \frac{1}{2}\frac{\Delta}{\phi_{se}} = 1 - \frac{1}{2}\frac{\Delta}{|\phi_{se}|}$$

and

$$\exp\left(\frac{e\left(\phi-\phi_{se}\right)}{k_B T_e}\right) \approx 1 - \frac{e\Delta}{k_B T_e}$$

obtaining:

$$\begin{aligned}\frac{d^2\Delta}{dx_{\parallel}^2} &\approx \frac{en_{se}\Delta}{\varepsilon_0}\left(\frac{e}{k_B T_e} - \frac{1}{2|\phi_{se}|}\right) \\ &= \frac{e^2 n_{se}\Delta}{\varepsilon_0 k_B T_e}\left(1 - \frac{k_B T_e}{2e|\phi_{se}|}\right)\end{aligned} \tag{1.45}$$

We notice that equation (1.45) admits an exponentially decaying solution, where the typical e-folding length is λ_D. The non-oscillatory solution exists only if:

$$|\phi_{se}|e \geq \frac{k_B T_e}{2}$$

Substituting equation (1.42), we obtain for ions velocity at sheath entrance:

$$v_{se} \geq c_s \qquad \text{with} \qquad c_s = \sqrt{\frac{k_B T_e}{m_i}} \tag{1.46}$$

which is the *Bohm criterion*, where c_s is the so-called *sound speed* in the plasma. This definition is given in analogy with the sound speed in neutral fluids, and it is the phase velocity of ion waves ([5], Chapter 2). Differently from the neutral fluids, where sound waves propagate through mechanical collisions, the ion waves propagate by means of electrostatic collisions. This result can be generalized for hot plasmas where $T_i \approx T_e$. The most general expression for the sound speed is:

$$c_s \equiv \sqrt{\frac{k_B(\gamma^e T_e + \gamma^i T_i)}{m_i}} \tag{1.47}$$

where γ^e and γ^i are the polytropic indexes referred respectively to electrons and ions, and they are equal to 1 if the plasma is isothermal and to 5/3 if the plasma is adiabatic with isotropic pressure. Since the sheath is narrow compared to collisional processes, with a first approximation can consider the plasma isothermal in this region. In the following and in general, $\gamma^i = \gamma^e = 1$ is assumed, so that the definition for the acoustic velocity

reduces to:

$$c_s \equiv \sqrt{\frac{k_B(T_e + T_i)}{m_i}} \tag{1.48}$$

We can define the parallel Mach number as the ratio of the parallel and the acoustic velocity:

$$M \equiv \frac{u_\parallel}{c_s} \tag{1.49}$$

By consequence, we can re-write the Bohm criterion as:

$$M_{se} \geq 1 \tag{1.50}$$

This condition takes into account the fact that the plasma can reach supersonic values even before reaching the sheath entrance. This can happen in the quasi-neutral plasma, if the source terms in the continuity or in the parallel momentum equation change sign along the parallel direction (see [20] for a detailed analysis of supersonic transitions).

1.6.2 Potential drop at the wall

Considering the Bohm condition (1.50) in its equality form, we can express the plasma flux at the sheath entrance in the following way:

$$\Gamma_{se} = n_{se} v_{se} = n_{se} c_s \approx n_{se} \sqrt{\frac{k_B(T_e + T_i)}{m_i}} \tag{1.51}$$

As already mentioned, the ion flux value can be considered constant across the sheath: we impose thus the equality of the fluxes at the wall and at the sheath entrance, $\Gamma_i^w = \Gamma_{se}$. We assume then that electrons maintain a Maxwellian distribution with a constant temperature through the sheath, therefore the average velocity in the parallel direction, here called z, will be given at the wall by the integration of the Maxwellian over the positive values of the velocities in z direction:

$$\bar{v}_e^w = \frac{n_e^w}{n_e^w \left(\sqrt{2\pi} v_{th_e}\right)^3} \int_{-\infty}^{+\infty} dv_e^x \int_{-\infty}^{+\infty} dv_e^y \int_0^{+\infty} n_e^w \exp\left(-\frac{v_e^{z\,2}}{2v_{th_e}^2}\right) v_e^z dv_e^z = \frac{v_{th_e}}{\sqrt{2\pi}} \tag{1.52}$$

For the determination of the electron density at the wall we need to use the Boltzmann's

distribution, giving:

$$n_e^w = n_{se} \exp\left(\frac{e(\phi^w - \phi_{se})}{k_B T_e}\right) \tag{1.53}$$

The electron flux at the wall then writes:

$$\Gamma_e^w = n_e^w \bar{v}_e^w = n_{se} \frac{v_{th_e}}{\sqrt{2\pi}} \exp\left(\frac{e(\phi^w - \phi_{se})}{k_B T_e}\right) \tag{1.54}$$

so we can write the current in parallel direction at the wall as:

$$\begin{aligned} j_\parallel^w &= e\left(\Gamma_i^w - \Gamma_e^w\right) \\ &= e\left(n_{se} c_s - n_{se} \frac{v_{th_e}}{\sqrt{2\pi}} \exp\left(\frac{e(\phi^w - \phi_{se})}{k_B T_e}\right)\right) \\ &= e n_{se} c_s \left(1 - \frac{v_{th_e}}{c_s \sqrt{2\pi}} \exp\left(\frac{e(\phi^w - \phi_{se})}{k_B T_e}\right)\right) \end{aligned} \tag{1.55}$$

Defining then a factor Λ, such that:

$$\frac{v_{th_e}}{c_s \sqrt{2\pi}} = \exp(\Lambda) \tag{1.56}$$

we have a general form of the current in parallel direction at the wall:

$$j_\parallel^w = e n_{se} c_s \left(1 - \exp\left(\Lambda + \frac{e(\phi^w - \phi_{se})}{k_B T_e}\right)\right) \tag{1.57}$$

In the case of a null current at the wall, $j_\parallel^w = 0$, we find:

$$\Lambda = \frac{e(\phi_{se} - \phi^w)}{k_B T_e} \tag{1.58}$$

which is the potential drop in the sheath in the case of a wall at floating potential. Substituting the expressions for the sound speed (1.48) and for the thermal velocity (1.5) in (1.57), the expression for the electric potential drop at the sheath for a floating surface becomes:

$$\Lambda = -\frac{1}{2} log\left[2\pi \frac{m_e}{m_i}\left(1 + \frac{T_i}{T_e}\right)\right] \tag{1.59}$$

For a deuterium plasma with $T_i \simeq T_e$, $\Lambda \sim 2.8$. In the pre-sheath the electric potential

undergoes a further $0.7k_BT_e$ drop due to ion acceleration. We thus notice also that the electric potential at the wall $\phi^w \simeq -k_BT_e(0.7+\Lambda)$ is proportional to the electron temperature. Therefore, the electric potential profile in the SOL approximately follow the electron temperature one at the target.
Equation (1.59) is the simplest expression for the potential drop. In fact the wall, undergoing the impact of electrons, ions, photons or excited neutrals, can emit secondary electrons, so that their outward flux sums up with the incoming plasma electron flux. This emission changes the charge balance, globally decreasing Λ value. A more detailed analysis of this problem can be found in [12], Chapter 25.

1.6.3 A sink mechanism

Ions and electrons, accelerated towards the wall, interact finally with the solid material. The electrons abundance leads to a sudden recombination of ions into neutral atoms, constituting effectively a sink mechanism for the SOL plasma. Therefore, in the simplest picture, the SOL is filled on one side from transverse transport, and these incoming fluxes are balanced by the losses towards the wall. In an approximate circular geometry, this particle balance can be expressed as:

$$\frac{\partial}{\partial r}\left(nv_r\right) = -\frac{\partial}{\partial x_\parallel}\left(nv_\parallel\right) \approx -\frac{nc_s}{L_\parallel} \tag{1.60}$$

In edge plasmas, transverse transport can be due to different mechanism. If we suppose the transport to be diffusive, with a diffusion coefficient constant in radial direction, we can write:

$$v_r = -\frac{D_n}{n}\frac{\partial}{\partial r}n \quad \Rightarrow \quad -D_n\frac{\partial^2}{\partial^2 r}n = -\frac{nc_s}{L_\parallel} \Rightarrow n = n(r_0)exp\left(-\frac{(r-r_0)}{\sqrt{\frac{D_nL_\parallel}{c_s}}}\right) \tag{1.61}$$

So, in this case, the density decay length is given by:

$$\lambda_n^{DIFF} = \sqrt{\frac{D_nL_\parallel}{c_s}} \tag{1.62}$$

In the case of a convective transport, with a constant radial velocity, instead,

$$v_r\frac{\partial}{\partial r}n = -\frac{nc_s}{L_\parallel} \Rightarrow n = n(r_0)exp\left(-\frac{(r-r_0)}{\frac{v_rL_\parallel}{c_s}}\right) \tag{1.63}$$

so that the associated density decay length is:

$$\lambda_n^{CONV} = \frac{v_r L_\parallel}{c_s} \tag{1.64}$$

We notice that in both cases, given the proportionality of the sink mechanism to the density itself, the density varies in the SOL with an approximately exponential decay. In realistic cases, transverse transport can be a combination of the two types described, or be complicated by additional factors, as the radial variation of radial velocity, so that radial profiles can significantly differ from exponential. However, in order to evaluate the typical decay length of a field in the SOL, an exponential fit is usually adopted.
The same evaluation can be extended to heat flux transport. The parallel heat flux decay length in the SOL is named λ_q: this quantity is extremely important in the framework of the power exhaust, since it sets the "wetted" surface, affected by the heat flux. This quantity is thus determined by the competing action of the perpendicular transport, in which turbulence plays a determinant role, and of the parallel transport. It is therefore necessary to address the problem of turbulence in the edge plasma, in order to understand the mechanisms regulating the heat flux decay length.

1.7 Context and objectives of the thesis

Turbulence developing in the edge plasma of tokamaks is nowadays accepted to play a major role in determining the transport of particles and energy from the hot centre towards the peripheral region. Ultimately, this transport affects the characteristic gradients appearing in the system. Hence, the consequences of turbulent transport are two-fold.
First of all, a reduction of turbulent transport would lead to steeper pressure gradients and a better global confinement of plasma, with beneficial consequences on fusion reaction rates. Turbulence is probably also involved in the formation of transport barriers in the closed flux surfaces region and in the transition from Low to High confinement mode [21]. The second key feature affected by turbulence in the edge plasma, is the exhaust of the excess power, in the region where magnetic field-lines impinge on solid components. In ITER, this will be an issue of major concern, and the power deposited on the divertor tungsten monoblocks will have to be maintained below a certain threshold, in order not to compromise the integrity of the material. Focusing on the inter-ELM period, in particular, the heat flux value must be kept below 10 MW/m^2 ([22], [23]). The power heat flux to the target depends ultimately on the heat flux decay length in the SOL λ_q, through the relation $q_{surf} = P_{sep}/(4\pi R_t \lambda_q f_g)$. Here P_{sep} is the power crossing the separatrix, carried by the plasma, R_t is the radius of the target plate and f_g is a factor linked to the field-line geometry, that can be shaped in order to minimise q_{surf}, although with some constraints. The principal factor determining the heat flux at the surface is therefore λ_q: this quantity is determined by the transport processes in edge plasma. However, also in this case, a complete understanding of the edge transport processes is still lacking from the theoretical point of view. Practically, the predictions for λ_q rely on multi-parameters scaling laws.

The divertor configuration seems to have a great impact both on the onset of transport barriers, and on the determination of the heat flux decay length. The H-mode has indeed then been achieved in most of the tokamaks operating with a divertor, whereas in limiter configuration the H-mode is more difficult to achieve, and can present different characteristics [24]. This element, along with the fact that the power threshold is sensible to geometric parameters of the plasma [18], suggests that the divertor configuration has a favourable impact on the formation of transport barriers. Regarding the power exhaust problem, the divertor geometry is characterised by unique features, as the presence of the PFR, which affects the heat flux profiles at the target plates. In the usual interpretation of the heat dynamics in the divertor, the PFR helps indeed in spreading the heat flux on a wider area ([25], [26]). Moreover, the divertor geometry seems to affect non-trivially the turbulent cross-field transport, so that the heat flux decay length is ultimately impacted. The scaling laws for the determination of λ_q differ indeed from limiter ([27],[28]) to divertor in L-mode [29] , and in H-mode [30]. These differences in the scaling laws highlight the complexity of the problem and the absence of a general theory able to capture the effects of different geometries.
Moreover, the presence of turbulence in the divertor region has been recently shown in different tokamaks (see [31] for MAST and [32] for Alcator C-Mod), by means of fast-imaging visible cameras. The X-point, and the particular associated magnetic geometry, could thus affect the turbulent transport and, by consequence, the above-mentioned features related to it.
It is important, therefore, to address the problem of turbulence in divertor configuration, which is the one adopted by the majority of the tokamaks including, in the future, ITER. In this thesis, we present the first results of 3D global turbulence simulations in X-point geometry, carried out with the TOKAM3X code [33], which has been developed in the last few years, in order to handle complex geometries. An example of 3D turbulence simulation in divertor geometry is represented in figure 1.8.

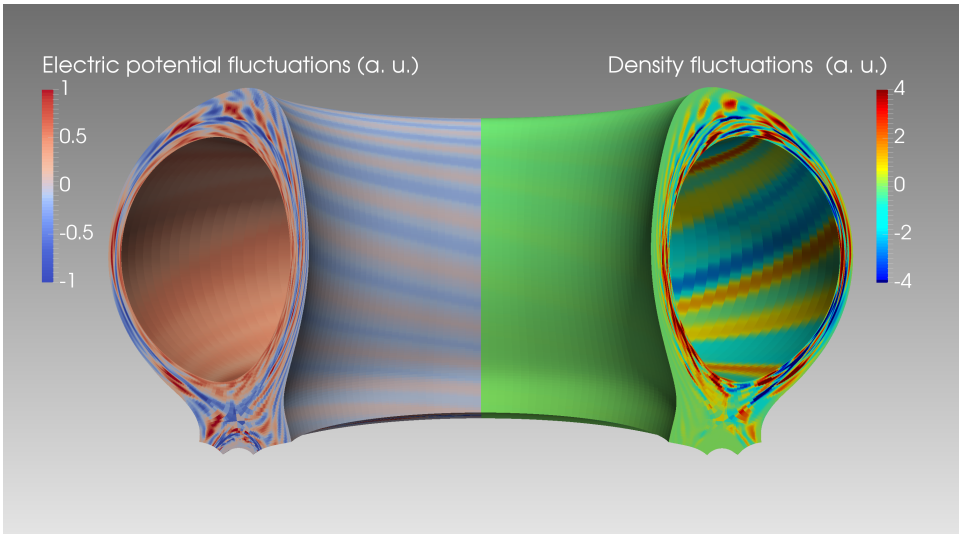

Figure 1.8: *3D view of a TOKAM3X simulation in a JET-like geometry. In the left quarter of the torus we represent the amplitude of electric potential fluctuations. In the right one, the density fluctuations.*

The objectives of this thesis are to identify and understand the peculiarities of edge turbulence in X-point geometry. The effects of the magnetic geometry must be evaluated both on local turbulence properties, and on the global edge plasma equilibrium. The flexibility in geometry definition of TOKAM3X is used to identify the effects due to the X-point and to other specific geometrical features of the divertor geometry. This numerical study takes advantage of the comparison with former simulations in limiter geometry, which have been widely investigated by TOKAM3X and other 3D turbulence codes.
Finally, we aim at verifying that TOKAM3X can coherently catch the basic features of the physical phenomena observed in tokamak edge plasma, in the perspective of the use of the code for the interpretation of experimental results.

Chapter 2

TOKAM3X: a 3D fluid turbulence code for edge plasma simulation

Contents

This chapter is devoted to the description of the TOKAM3X code, which will be used thereafter for the analysis of edge plasma turbulence. The derivation of the physical model is detailed, with the associated assumptions and the equations ordering. We introduce at this point the main instability mechanisms that can be observed with the TOKAM3X model. We show then how complex magnetic geometries are handled by the code. Finally we give a brief description of the numerical methods used for the model solution, and of the latest developments on boundary conditions implemented in the code in the framework of this thesis.
Part of the topics treated in this chapter is included in the publication [33] about TOKAM3X.

2.1 From 2D to 3D turbulence modelling

As discussed in Chapter 1, turbulence in the edge plasma intervenes in several key issues for the operation of a tokamak. Nevertheless, the understanding of turbulence and of the related transport is still incomplete. The aim of turbulence numerical modelling is to fill the gaps in the current understanding of turbulence, and to ultimately reach the ability to be predictive on edge plasma dynamics.
In this framework, the TOKAM3X 3D fluid turbulence code has been developed through a long-term collaboration between the IRFM institute of Cadarache (France), and the M2P2 laboratory of Marseille. This code, as well as the other codes of the same type

used in the fusion community, takes advantage of the knowledge acquired through the years of turbulence modelling, and it is continuously developed in order to increase its capability of describing edge plasma turbulence.

2.1.1 2D turbulence codes

2D fluid turbulence codes have been largely employed for the simulations of limited regions of the edge plasma. Examples of 2D turbulence codes are TOKAM2D [34] and HESEL [35]. These simulation tools have proven to describe well the turbulence properties in unstable zones of the edge plasma. In some cases, 2D turbulence codes have also been able to show dynamics similar to the L-H transition ([36], [35], [37]). Furthermore, these codes have the advantage to require a very limited computational time, and for this reason they are still used for investigations on fundamental turbulence properties (e.g. [38], [39]) and for comparison with experiments (e.g. [40]). A qualitative illustration of turbulence obtained in TOKAM2D simulations is shown in figure 2.1.

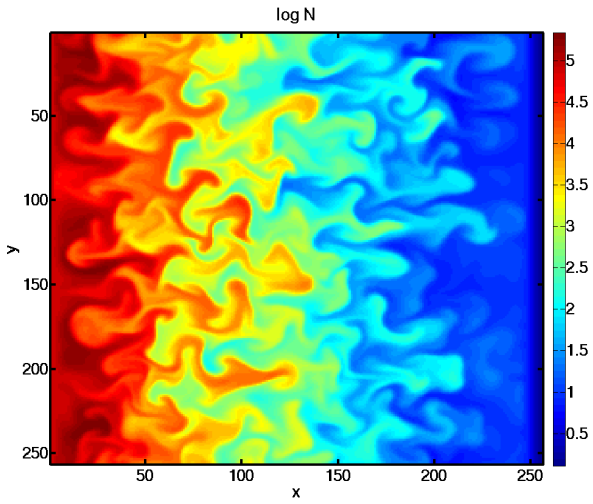

Figure 2.1: *Snapshot of the logarithm of plasma density obtained with TOKAM2D simulations (courtesy of N. Nace). x and y are measured in Larmor radii.*

However, 2D turbulence codes can only simulate a small region of the tokamak, where the plasma is unstable, as the region around the LFS midplane. A 3D description of turbulence in edge plasma have become necessary, following also the experimental evidences of an asymmetry in turbulent properties in the poloidal direction, with an enhancement of turbulent transport in the region around the LFS midplane (see [41] for Alcator C-mod, [42] for Tore Supra). These asymmetries ultimately affect the overall equilibrium in the SOL.

2.1.2 3D turbulence codes: objectives and state of the art

TOKAM3X, as others 3D fluid turbulence codes, has been conceived to overcome the limitations of 2D fluid turbulence codes for edge plasma. In particular, 3D turbulence codes can describe the 3D nature of turbulence, without averaging the parallel dynamics through the so-called *flute assumption*. As it will be clearer in the following, the improvement from 2D to 3D codes implies the simultaneous solution of the parallel and perpendicular dynamics, which are profoundly different, as understandable from the description of the single particle motion in section 1.2.1. However this complication is necessary, since the characteristic time scale of the motion in perpendicular direction is not negligible with respect to the parallel one. A qualitative comparison of these two quantities gives:

$$\tau_\perp \sim \frac{\lambda_N}{v_\perp} \sim \frac{10^{-2}\ m}{10^{2}\ m\ s^{-1}} \sim 10^{-4}\ s \qquad , \qquad \tau_\parallel \sim \frac{L_\parallel}{c_s} \sim \frac{10\ m}{10^{5}\ m\ s^{-1}} \sim 10^{-4}\ s \tag{2.1}$$

so that the parallel dynamics cannot be considered infinitely fast with respect to the perpendicular one. The evidence of these comparable characteristic times can be found in the poloidal asymmetries rising in tokamak edge plasma. It is widely known indeed that turbulence levels are stronger at the LFS midplane of tokamaks (see [43] for turbulent flux measurements on Alcator C-mod, [44] for fast imaging cameras on Tore Supra), with a certain poloidal spreading depending on specific plasma characteristics. The description of these large-scale effects are necessary in order to explain global flux patterns, and to describe coherently the plasma interaction with solid surfaces and, more in general, with the surrounding environment.
Multiple 3D fluid turbulence codes have thus been developed worldwide over the last years, in some of the major institutes of research on magnetic fusion. Along with TOKAM3X, other 3D fluid turbulence codes which share the main objectives are GBS [45] (developed at the École Polytechnique Fédérale de Lausanne, Switzerland), BOUT++ [46] (developed by University of York (UK) and international partners) and GRILLIX [47](Developed at the Institute of Plasma Physics in Garching, Germany).
In 3D codes, the edge plasma turbulence, characterised by small scales, which can be of the size of few millimetres, must be simulated in the global geometry of the tokamaks, which involves macroscopic length scales of the order of 1 meter. Moreover, the characteristic turbulence time scales, of the order of $10^{-5}s$, are small if compared to the typical confinement time (of the order of 1 s) and also with respect to the inter-ELM periods (around $10^{-3} - 10^{-1}s$), on which turbulence codes usually focus. Therefore, 3D turbulence codes solve multi-scale problems in time and space, and they demand significant computing resources. This type of code is usually executed on multiple processors in supercomputers.
3D turbulence codes have been able to reproduce some important physical results, as the asymmetric level of turbulence in the poloidal section and the global impact on the parallel flows in the SOL ([48], [49], [50]). The codes mentioned above have also undergone some validation exercises on seeded blobs propagation against experiments in TORPEX (Switzerland)[51] and MAST [52].

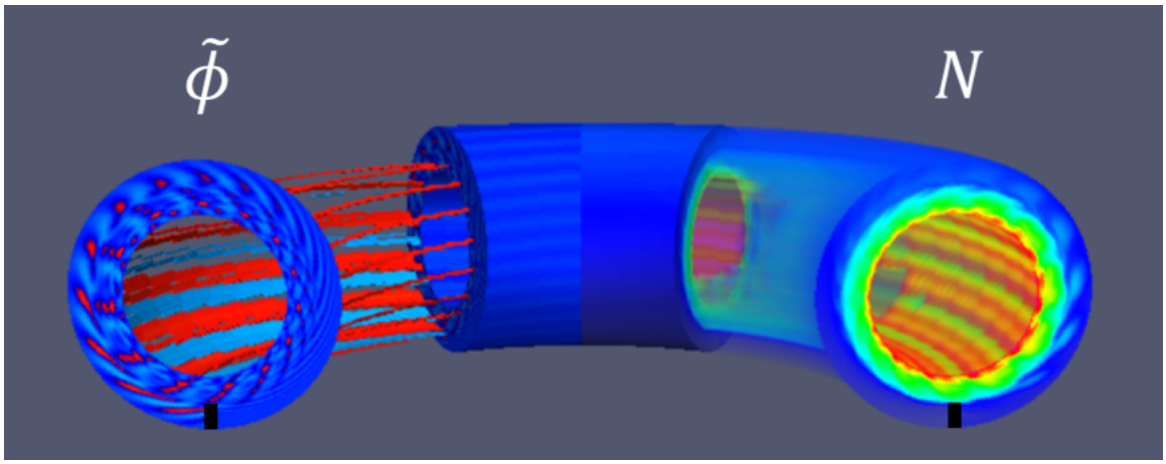

Figure 2.2: *Snapshot of a turbulent simulation with the TOKAM3X code in circular limiter geometry. On the left we represent the fluctuations of the electric potential field, on the right the total density (courtesy of P. Tamain).*

The effort in turbulence modelling has been mainly focused, up to now, on the study of plasmas with circular cross-section (an example is shown in figure 2.2). This geometry is particularly convenient, because it allows the use of a toroidal reference system, and it can be a good approximation for limiter configurations (excluding the Shafranov shift and the deformation of the magnetic surfaces occurring in a real plasma equilibrium). The divertor magnetic geometry is more difficult to model since, with the introduction of the X-point, it includes a topological discontinuity, and more in general a strong shaping of the magnetic surfaces cross-section, so that suitable numerical techniques must be developed.
TOKAM3X has been developed in the last few years to handle a divertor configuration [33]. Also the other mentioned codes have recently shown simulations in divertor geometry ([53], [54]).
It is worthy to remind that also some gyro-kinetic codes, as XGC1 [55], have recently demonstrated the capability to deal with a realistic magnetic geometry. Nevertheless, these codes are extremely computing-time consuming, and the actual physical time simulated is much lower than what can be achieved by the codes which adopt the fluid approach.

2.2 Derivation of the TOKAM3X drift-reduced equations

In tokamak plasmas the particle motion is strongly anisotropic, and this property reflects on fluid motion. Therefore, we will need to treat separately the direction parallel to the magnetic field $\vec{b}$, and the plane perpendicular to it. Starting from the fluid equations presented in the previous chapter, we need to adapt our model to the description of turbulence in strongly magnetised plasmas, as the ones characterizing tokamaks.
We separate in particular the velocities in parallel direction, $u_{s_\parallel}$, from the ones in perpen-

dicular direction $\vec{u}_{s_\perp}$. We aim at expressing the latter as functions of the other unknown fields. In this way, the only unknown velocity component for each solved species will be the parallel one. In order to do this, we need to make specific assumptions on the perpendicular velocity.

2.2.1 The drift velocity approximation

As discussed in Chapter 1, particles move with an helical trajectory around the magnetic field-lines. The centre of the cyclotronic movement displaces in the perpendicular direction with the so-called drift-velocities. The ordering of TOKAM3X equations is based on the hypothesis that turbulence develops on longer timescales than the ion gyration motion:

$$\frac{\omega}{\omega_C} \equiv \varepsilon_w \ll 1 \tag{2.2}$$

where we call ω_C the ion cyclotronic frequency. For deuterium plasmas, considering a magnetic field $1\,T$, $\omega_C \sim 5{\cdot}10^7 Hz$. The perpendicular velocity is thus expanded according to the small parameter ε_w, as:

$$\vec{u}_\perp = \varepsilon_\omega \vec{u}_\perp^{(1)} + \varepsilon_\omega^2 \vec{u}_\perp^{(2)} + ... \tag{2.3}$$

where the velocity is referred to the guiding centre, so it does not include the cyclotronic rotation (that would represent the order 0 of the velocity). We can now evaluate the order of different terms in the fluid equation of momentum conservation (1.25), projected on the perpendicular direction. For the ion species, we obtain:

$$\begin{aligned} m_i \partial_t \left(n_i \vec{u}_{i_\perp}\right) &\sim m_i n_i \varepsilon_w u_\perp \omega_C \\ m_i \vec{b} \times \vec{\nabla} \cdot \left(n_i \vec{u}_i \otimes \vec{u}_i\right) &\sim m_i n_i \varepsilon_w u_\perp \omega_C \\ n_i q_i \vec{u}_{i_\perp} \times \vec{B} &\sim m_i n_i u_\perp \omega_C \end{aligned}$$

The first two terms will be thus neglected at the first order. We notice that if we took as reference the electron cyclotron frequency, the parameter ε_w would have been even lower, so the same consideration can be applied for the two species. The remaining terms in the projection of the momentum conservation equation would need further hypothesis to be evaluated. Multiple ε coefficients can be defined, and every term of the equation would be proportional to one or more of them. The complete procedure of drift reducing is out of the scope of this thesis.

2.2.2 Fluid drifts

Following the procedure just described, we reach the following form for the perpendicular momentum conservation at the first order:

$$0 = n_s q_s \left(\vec{E}_\perp + \vec{u}^{(1)}_{s_\perp} \times \vec{B} \right) - \vec{\nabla}_\perp \, p_s \tag{2.4}$$

where the terms $\vec{\nabla} \cdot \mathbf{\Xi}_s$ and $\vec{\mathcal{R}}_s$ have been neglected. This hypothesis is based on the Braginskii closure, and will be briefly discussed in section 2.2.4. The cross product with the magnetic field $\vec{B}$ then gives, after a little algebra:

$$\vec{u}^{(1)}_{s_\perp} = \frac{\vec{E} \times \vec{B}}{B^2} + \frac{\vec{\nabla} p \times \vec{B}}{n_s q_s B^2} \tag{2.5}$$

We have derived in this way the expression for the two fluid drifts of first order. We identify in (2.5) the $E \times B$ drift:

$$\vec{u}_E \equiv \frac{\vec{E} \times \vec{B}}{B^2} \tag{2.6}$$

and the *diamagnetic drift* velocity:

$$\vec{u}_{\star,s} \equiv \frac{\vec{B} \times \vec{\nabla} p}{n_s q_s B^2} \tag{2.7}$$

We notice that the $E \times B$ fluid drift has the same expression as the one characterising the single particle motion. The diamagnetic drift, instead, is the expression of a collective effect, being related to the presence of a pressure gradient. The diamagnetic drift implies a very small transport of particles: the average diamagnetic velocity is given indeed by the average component of the particles gyration velocity in one direction, which is varying with the particle pressure gradient. Actually, the only net particle transport associated to the diamagnetic drift is given by the magnetic field curvature, so that the divergence of the of the diamagnetic flux reduces to the divergence of the ∇B drift, which is detailed in Appendix A. However, this drift velocity, as visible from (2.7), is dependent on the particle charge. Therefore, diamagnetic drift is responsible for a local electric charge separation.
We can now focus on the determination of the second order perpendicular velocity.

$$m_s \left[\partial_t (n_s \vec{u}^{(1)}_{s_\perp}) + \vec{\nabla} \cdot \left(n_s \vec{u}^{(1)}_{s_\perp} \otimes \vec{u}_s \right) \right] = n_s q_s \vec{u}^{(2)}_{s_\perp} \times \vec{B} + \vec{\nabla} \cdot \mathbf{\Xi}^{(1)}_\perp + \mathcal{R}_s \tag{2.8}$$

Taking the cross-field product with $\vec{B}$ as for the first order:

$$\vec{u}_p = \frac{m_i}{n_i q_i B^2}\vec{B} \times \left[\partial_t \left(n_i \vec{u}_{i_\perp}^{(1)}\right) + \vec{\nabla} \cdot \left(n_i \vec{u}_{i_\perp}^{(1)} \otimes \vec{u}_i\right)\right] + \frac{\vec{B} \times \left(\vec{\nabla} \cdot \mathbf{\Xi}_\perp^{(1)} + \mathcal{R}_i\right)}{n_i q_i B^2} \tag{2.9}$$

Since the polarisation velocity is proportional to the mass, and knowing that $m_e \ll m_i$, we can affirm that the polarisation current for electrons is negligible. Therefore, the polarisation current $\vec{j}_p = e n_i \vec{u}_p$ is associated to this velocity.
Even if the polarisation velocity is one order smaller than diamagnetic and $E \times B$ velocities, polarisation flux and current must be conserved in our system of equations, when they appear in a divergence form. Indeed while the polarisation current varies over short scales, comparable to the ones of turbulence, diamagnetic current varies on the device scale (since it is related to magnetic curvature). Therefore:

$$\left|\frac{\vec{\nabla} \cdot \vec{j}_p}{\vec{\nabla} \cdot j_\star}\right| \sim \left|\frac{j_p R}{j_\star \rho_L}\right| \sim \frac{\varepsilon_w}{\varepsilon_w} \tag{2.10}$$

So, when polarisation current appears under divergence form, it is kept in the equations (i.e. in the charge conservation equation), while when it appears as an advection velocity (for example in an operator as $u_p \cdot \vec{\nabla}$) it is neglected.

2.2.3 TOKAM3X hypotheses

In addition to the assumption on characteristic frequencies just presented, $\omega/\omega_C \ll 1$, necessary for the drift ordering, we will consider the ion Larmor radius ρ_L as the reference scale for the description of turbulence. Indeed, experimentally, the size of turbulent structures is of the order of 10^{-2} m, while the Larmor radius value in edge plasma is around $10^{-4} - 10^{-3} m$. Moreover, in the drift ordering we have averaged the cyclotronic motion, so it would not be coherent to describe turbulent structures smaller than the Larmor radius.
Several additional hypothesis are assumed in the derivation of the TOKAM3X model:

- **Quasi-neutrality** - Since in the edge plasma, $\lambda_D \ll \rho_L$, we can assume that the plasma is quasi-neutral:

  $$n_e \approx Z n_i \tag{2.11}$$

  where Z is the atomic number of the ion species. The quasi-neutrality implies also the conditions on sources:

  $$S_e^n \approx Z S_i^n \tag{2.12}$$

  In this thesis we consider $Z = 1$, identifying hydrogenic atoms. Only one ion species

is simulated.
As seen in Chapter 1, the quasi-neutrality does not hold in the plasma sheath. The latter is described in the code by means of the boundary conditions in the parallel direction at the interface with the wall components.

- **Negligible electron inertia** - The mass of electrons is much smaller than the one of the lightest ion (H^+):

$$m_e \ll m_i \tag{2.13}$$

- **Electrostatic assumption** - TOKAM3X is conceived to solve electrostatic turbulence. This means assuming that the vector potential is static $\partial_t \vec{A} = 0$. By consequence, also the magnetic field is constant in time, and the electric field depends only on the electric potential:

$$\vec{E} = -\vec{\nabla}\phi \tag{2.14}$$

Therefore, the simulations that we are going to show in this manuscript are suitable for the description of low β plasmas, where $\beta = 2\mu_0 p/B^2$ defines the ratio of the plasma pressure over the magnetic pressure. In fact, in this regime, the current produced in edge plasma is low if compared to the plasma current I_p. Thus, the feedback of the plasma current created by turbulence is not taken into account in the magnetic field, which is considered "frozen", and does not change in time. Typically, L-mode plasmas are characterized by low β, in contrast with H-mode plasmas, where the value of β can raise in the pedestal region.

2.2.4 TOKAM3X equations with ordering

In order to study the turbulence problem, it is necessary to solve the fluid equations regulating the dynamics of ions and electrons. Exploiting the quasi-neutrality hypothesis, we decide to solve electrons density conservation, since the polarisation velocity, which has a complicated expression, does not appear in it.

$$\partial_t n_e + \vec{\nabla} \cdot \left(n_e u_{e,\parallel} \vec{b} \right) + \vec{\nabla} \cdot (n_e \vec{u}_E) + \vec{\nabla} \cdot (n_e \vec{u}_{\star,e}) = S_e^n \tag{2.15}$$

Using the definition of parallel current, $j_\parallel = e n_i u_{i,\parallel} - e n_e u_{e,\parallel}$, we reformulate (2.15) as:

$$\partial_t n_e + \vec{\nabla} \cdot \left[\left(n_i u_{i,\parallel} - \frac{j_\parallel}{e} \right) \vec{b} \right] + \vec{\nabla} \cdot (n_e \vec{u}_E) + \vec{\nabla} \cdot (n_e \vec{u}_{\star,e}) = S_e^n \tag{2.16}$$

The diamagnetic drift is responsible for a small particle transport. In fact, the only part of the diamagnetic flux divergence which is not divergence-free is the one related to the

magnetic curvature. The calculation of this divergence is detailed in Appendix A, and results in:

$$\vec{\nabla}\cdot(n\vec{u}_{\star,s}) \approx \vec{\nabla}\cdot(n\vec{u}^{s}_{\nabla B}) \tag{2.17}$$

Substituting (2.17) in (2.16), we finally obtain the continuity equation solved by TOKAM3X:

$$\boxed{\partial_t n_e + \vec{\nabla}\cdot\left[\left(n_i u_{i,\parallel} - \frac{j_\parallel}{e}\right)\vec{b}\right] + \vec{\nabla}\cdot(n_e\vec{u}_E) + \vec{\nabla}\cdot(n_e\vec{u}^{e}_{\nabla B}) = S^n_e + \vec{\nabla}\cdot\left(D_N\vec{\nabla}_\perp n_e\right)} \tag{2.18}$$

In equation (2.18), we have added a diffusive operator in order to stabilise the smallest turbulence scales. The role of this operator will be clarified in section 2.7.1. We focus then on the momentum equation. The equation determining perpendicular velocity is already known, both for ions and electrons:

$$\vec{u}_{\perp,i} = \vec{u}_E + \vec{u}_{\star,i} + \vec{u}_p \qquad \vec{u}_{\perp,e} = \vec{u}_E + \vec{u}_{\star,e} \tag{2.19}$$

Therefore, we need an equation for the momentum in parallel direction. We project so the momentum conservation equation (1.25) on the parallel direction for each species. The details of this projection are given in Appendix A. We obtain:

$$0 = -n_e e E_\parallel - \nabla_\parallel p_e + \mathcal{R}_\parallel \tag{2.20}$$

$$m_i\left[\left(\partial_t n_i u_{\parallel,i}\right) + \vec{\nabla}\cdot\left(n_i u^2_{\parallel,i}\vec{b}\right) + \vec{\nabla}\cdot\left(n_i u_{\parallel,i}\vec{u}_{\perp,i}\right)\right] = n_i e E_\parallel - \nabla_\parallel p_i - \left(\vec{\nabla}\cdot\mathbf{\Xi}_i\right)\cdot\vec{b} - \mathcal{R}_\parallel + S^\Gamma_i \tag{2.21}$$

Where $m_e \ll m_i$ is applied: the inertial terms and the kinetic pressure are neglected for electrons. Here, $\mathcal{R}_\parallel = \mathcal{R}\cdot\vec{b}$ represents the parallel momentum exchanged between electrons and ions via collisions. In particular we will call $\mathcal{R}_{e,\parallel} = -\mathcal{R}_{i,\parallel} = \mathcal{R}_\parallel$ the momentum given from ions to electrons.
Making use of the quasi-neutrality assumption, we sum up equations (2.20) and (2.21), obtaining:

$$m_i\left[\partial_t\Gamma_{\parallel,i} + \vec{\nabla}\cdot\left(\Gamma_{\parallel,i}u_{\parallel,i}\vec{b}\right) + \vec{\nabla}\cdot\left(\Gamma_{\parallel,i}\vec{u}_{\perp,i}\right)\right] = -\nabla_\parallel\left(p_i + p_e\right) - \left(\vec{\nabla}\cdot\mathbf{\Xi}_i\right)\cdot\vec{b} + S^\Gamma_i \tag{2.22}$$

Where $\Gamma_{\parallel,i} = n_i u_{\parallel,i}$. One of the most difficult terms to develop is the divergence of the pressure tensor. This term reduces to the sum of two terms. The first one is a term

linked to collisions (see Braginskii's work [19] for the details), and we decide to treat it with a diffusive operator, introducing a diffusion coefficient on parallel momentum, D_Γ. The second term takes into account a finite Larmor radius effect. However, using a classical result of Braginskii's theory, this term exactly compensates the part of advection by diamagnetic drift which is not related to the curvature of the magnetic field (see Appendix A), in the so-called "diamagnetic cancellation" [56]. Indeed, only the curvature drift appears in the advection operator of parallel momentum.

$$\boxed{m_i \left[\partial_t \Gamma_{\parallel,i} + \vec{\nabla}\cdot\left(\Gamma_{\parallel,i} u_{\parallel,i}\vec{b}\right) + \vec{\nabla}\cdot\left(\Gamma_{\parallel,i}\vec{u}^i_{\nabla B}\right)\right] = -\nabla_\parallel\left(p_i + p_e\right) + S^\Gamma_i + \vec{\nabla}_\perp\cdot\left(D_\Gamma\vec{\nabla}_\perp\Gamma_{\parallel,i}\right)} \tag{2.23}$$

The parallel dynamics of electrons contributes to the determination of the parallel current. We can rewrite (2.20) as:

$$\boxed{e n_e J_\parallel\ \eta_\parallel - 0.71 n_e \nabla_\parallel T_e = -n_e e \nabla_\parallel \phi + \nabla_\parallel p_e} \tag{2.24}$$

Where the electrostatic assumption (2.14) has been applied and the parallel component of the momentum exchange $\mathcal{R}_\parallel$, obtained by Braginskii's calculations, has been explicitly written using (1.36) and (1.37). We refer to equation (2.24) as the *generalised Ohm's law*: this equation regulates the evolution of the parallel current. Supposing the plasma isothermal, and with negligible resistivity, we can write:

$$T_e k_B \nabla_\parallel n_e = n_e e \nabla_\parallel \phi \tag{2.25}$$

finding the well-known Boltzmann's distribution for electrons:

$$log\left(\frac{n_e}{n_{e,0}}\right) = \frac{e(\phi - \phi_0)}{k_B T_e} \tag{2.26}$$

In this particular case, electrons are sometimes referred to as "adiabatic" in the parallel direction.
Our system must conserve the electric charge, so we can write:

$$\vec{\nabla}\cdot\vec{j} = \vec{\nabla}_\perp\cdot\vec{j}_\perp + \vec{\nabla}\cdot\left(j_\parallel\vec{b}\right) = \vec{\nabla}_\perp\cdot\left(\vec{j}_p + \vec{j}_\star\right) + \vec{\nabla}\cdot\left(j_\parallel\vec{b}\right) = 0 \tag{2.27}$$

where the time-varying part is included in the polarisation current. The divergence of the diamagnetic current depends on the pressure gradient, so it couples this equation to the continuity equation (2.15). Substituting the divergence of the ∇B drift to the diamagnetic one, we can re-write the divergence of the diamagnetic current as:

$$\vec{\nabla}\cdot\vec{j}_\star = \vec{\nabla}\cdot\left(n_i\vec{u}^i_{\nabla B} - n_e\vec{u}^e_{\nabla B}\right) \tag{2.28}$$

This term is necessary for the triggering of turbulence, since it represents a local separation of the electric charge, which is necessary for the development of the electrostatic instability. The divergence of the parallel current can be seen as a reaction of the system to this charge separation: charge in excess can flow in parallel direction, and the parallel current, which must be inferred from (2.24), will be proportional to the plasma parallel conductivity. The divergence of the polarisation current is the most difficult term to be calculated, and gives the following result:

$$\vec{\nabla}_\perp \cdot \left(\vec{j}_p\right) = -m_i \partial_t \vec{\nabla} \cdot \left[\frac{n_i}{B^2}\left(\vec{\nabla}_\perp \phi + \frac{\vec{\nabla}_\perp p_i}{e n_i}\right)\right] - m_i \vec{\nabla} \cdot \left\{\vec{u}_i \vec{\nabla} \cdot \left[\frac{n_i}{B^2}\left(\vec{\nabla}_\perp \phi + \frac{\vec{\nabla}_\perp p_i}{e n_i}\right)\right]\right\} \tag{2.29}$$

The details of this calculation are exposed in Appendix A. Now we decompose temporarily the density and electric potential field, in an equilibrium component and a perturbation $x = \bar{x} + \tilde{x}$, such that $|\tilde{x}/\bar{x}| = \varepsilon_x \ll 1$. The decay lengths associated to the equilibrium and fluctuating components are respectively $L_\perp$ and $1/k_\perp$, such that $1/(k_\perp L_\perp) \simeq \varepsilon_x \ll 1$. In this framework, we can write:

$$\begin{aligned}
\frac{|n_i \nabla_\perp^2 \phi|}{\left|\vec{\nabla}_\perp \phi \cdot \vec{\nabla}_\perp n_i\right|} &= \frac{\left|\left(\bar{n}_i + \tilde{n}_i\right) \nabla_\perp^2 \left(\bar{\phi} + \tilde{\phi}\right)\right|}{\left|\vec{\nabla}_\perp \left(\bar{\phi} + \tilde{\phi}\right) \cdot \vec{\nabla}_\perp \left(\bar{n}_i + \tilde{n}_i\right)\right|} \\
&\approx \frac{\left|\bar{n}_i \left(L_\perp^{-2} \bar{\phi} + k_\perp^2 \tilde{\phi}\right)\right|}{\left|\left(L_\perp^{-1} \bar{\phi} + k_\perp \tilde{\phi}\right)\left(L_\perp^{-1} \bar{n}_i + k_\perp \tilde{n}_i\right)\right|} \cdot \left|\frac{L_\perp^2 \bar{\phi} \bar{n}_i}{L_\perp^2 \bar{\phi} \bar{n}_i}\right| = \frac{1 + L_\perp^2 k_\perp^2 \varepsilon_x}{\left(1 + L_\perp k_\perp \varepsilon_x\right)^2} \\
&\approx \frac{1 + \varepsilon_x^{-1}}{4} \gg 1
\end{aligned} \tag{2.30}$$

This approach translates into a Boussinesq-like approximation, which is commonly adopted in fluid mechanics and consists in neglecting the gradient of density in the calculation of the polarisation drift divergence. The validity of this hypothesis in edge turbulence plasma has been confirmed by a past work [57]. In order to write the equation in a conservative form, it is usual to introduce a quantity called *vorticity*, defined as:

$$\boxed{w = \vec{\nabla} \cdot \left(\frac{\vec{\nabla}_\perp \phi}{B^2} + \frac{\vec{\nabla}_\perp p_i}{n_i e B^2}\right)} \tag{2.31}$$

This field is named vorticity because of its role similar to the vorticity in fluid mechanics (in our case it is the projection on the magnetic field of the curl of a velocity field). We obtain for the divergence of the polarization current:

$$\vec{\nabla} \cdot \vec{j}_p = -m_i \partial_t (n_i \omega) - m_i \vec{\nabla} \cdot (\omega n_i \vec{u}) \tag{2.32}$$

We now apply the quasi-neutrality condition and we develop:

$$\vec{\nabla}\cdot\vec{j}_p = -m_i n\partial_t\omega - \cancel{m_i\omega\partial_t n} - m_i n\vec{u}\cdot\vec{\nabla}\omega - \cancel{m_i\vec{\nabla}\omega\cdot(n\vec{u})} \tag{2.33}$$

Where the continuity equation (2.15) has been substituted in (2.32). This assumption is reliable where the particle sources and the residual transport coefficient D_N are small compared to the other terms in the continuity equation. A further approximation is performed, admitting $\omega\vec{\nabla}\cdot\vec{u} \ll \vec{u}\cdot\vec{\nabla}\omega$: this allows to write the vorticity equation in conservative form, and corresponds to consider an incompressible flow. With these hypotheses, the charge conservation equation can be written as:

$$m_i\left[\partial_t w + \vec{\nabla}\cdot\left(\frac{w\Gamma_{\parallel,i}}{n}\vec{b}\right) + \vec{\nabla}\cdot\left(w(\vec{u}_E + \vec{u}^i_{\nabla B})\right)\right] = \frac{1}{n}\vec{\nabla}\cdot\left(J_\parallel\vec{b}\right) + \frac{1}{n}\vec{\nabla}\cdot\left(n\left(\vec{u}^i_{\nabla B} - \vec{u}^i_{\nabla B}\right)\right) \tag{2.34}$$

Also in the vorticity equation, a diffusive operator is added. The final equation reads:

$$\boxed{\begin{aligned} m_i\left[\partial_t w + \vec{\nabla}\cdot\left(\frac{w\Gamma_{\parallel,i}}{n}\vec{b}\right) + \vec{\nabla}\cdot\left(w(\vec{u}_E + \vec{u}^i_{\nabla B})\right)\right] = \\ \frac{1}{n}\vec{\nabla}\cdot\left(J_\parallel\vec{b}\right) + \frac{1}{n}\vec{\nabla}\cdot\left(n\left(\vec{u}^i_{\nabla B} - \vec{u}^i_{\nabla B}\right)\right) + \vec{\nabla}\cdot\left(D_W\vec{\nabla}_\perp w\right) \end{aligned}} \tag{2.35}$$

The equations describing the electron and the ion temperature evolution are not detailed here. Starting from (1.31), the derivation process can be carried out through similar approximations as the ones exploited for the other equations, along with collisional terms calculated through the Braginskii theory. The two equations for ions and electrons temperature will not be solved in the TOKAM3X simulations shown in this thesis, which are carried out in isothermal hypothesis. Nevertheless, the full model is now implemented in TOKAM3X [58].

2.2.5 TOKAM3X dimensionless equations

Every quantity in TOKAM3X is normalised according to characteristic scales allowing to describe the edge turbulence. In particular length scales are normalised to the ionic Larmor radius ρ_L, and the time scales to the inverse of the cyclotronic frequency ω_C, which, according to the ordering used to derive the equations, is much bigger than the characteristic electrostatic turbulence frequencies. We have thus:

$$\hat{\vec{\nabla}} \equiv \rho_L\ \vec{\nabla} \qquad , \qquad \hat{t} \equiv \omega_C\ t$$

Where the symbol $\hat{}$ is used here to indicate dimensionless quantities. The most important fields appearing in TOKAM3X equations are normalised with respect to reference quantities as follows:

$$\hat{N} \equiv \frac{n}{n_0} \quad , \quad \hat{T} \equiv \frac{T}{T_0} \quad , \quad \hat{\Phi} \equiv \frac{e\phi}{T_0} \quad , \quad \hat{u} \equiv \frac{u}{v_{th}}$$

where the electric potential energy is normalised to the thermal energy, and the velocity according to thermal velocity. Here the reference temperature must be expressed in J, so that the electric potential energy is normalised on the reference thermal one.
Reminding the definitions of Larmor radius (1.9) and cyclotronic frequency (1.8), one can see that the normalisation of equations depends entirely on 4 reference quantities:

$$n_0 \quad , \quad T_0 \quad , \quad B_0 \quad , \quad m_i$$

Which are indeed indicative of the plasma conditions (density and temperature), the magnetic field applied in the tokamak at the magnetic axis (B_0) and the mass of the ion species m_i. Only once these reference parameters are determined, one can infer the outputs of the TOKAM3X code with dimensions, which can be compared, in principle, with experimental results.
Additional fields appearing in TOKAM3X equations are normalised according to the aforementioned quantities:

$$\hat{\Gamma} \equiv \frac{\Gamma_\parallel}{n_0 v_{th}} \quad , \quad \hat{J}_\parallel \equiv \frac{J_\parallel}{e n_0 v_{th}} \quad , \quad \hat{P} \equiv \frac{p}{n_0 T_0} \quad , \quad \hat{W} \equiv \frac{w \rho_L^2 e}{T_0} \quad , \quad \hat{S}_N \equiv \frac{S^n}{n_0 \omega_C}$$

Four physical parameters appear explicitly in TOKAM3X equations, and must be set by the user: these are D_N, D_Γ, D_W and $\eta_\parallel$ (D_N and D_W appear in diffusion operators similarly to D_Γ and their role is discussed in section 2.7.1). From the normalisation of the density, parallel momentum and vorticity conservation equations, one obtains:

$$\hat{D}_N \equiv \frac{D_N}{\rho_L^2 \omega_C} \quad , \quad \hat{D}_\Gamma \equiv \frac{D_\Gamma}{\rho_L^2 \omega_C} \quad , \quad \hat{D}_W \equiv \frac{D_W}{\rho_L^2 \omega_C}$$

From the normalisation of the generalised Ohm's law:

$$\hat{\eta}_\parallel \equiv \frac{\eta_\parallel e^2 n_0}{m_i \omega_C} = \frac{e n_0}{B_0}$$

In the following, the symbol $\hat{}$ will be dropped, and all the quantities will be referred to (if it is not otherwise mentioned) as dimensionless.
The resulting system of equations describes the conservation equation for the electron density N, the ion parallel momentum Γ, and the vorticity W. The parallel current $J_\parallel$ and the electrostatic potential Φ intervenes through the electric charge balance (vorticity

conservation (2.38)) and through the Ohm's law (2.39).

$$\partial_t N + \vec{\nabla}\cdot\left(\left(\Gamma - J_\parallel\right)\vec{b} + N\vec{u}_E + N\vec{u}^e_{\nabla B}\right) = S_N + \vec{\nabla}\cdot\left(D_N\vec{\nabla}_\perp N\right) \tag{2.36}$$

$$\partial_t \Gamma + \vec{\nabla}\cdot\left(\Gamma^2/N\vec{b} + \Gamma\vec{u}_E + \Gamma\vec{u}^i_{\nabla B}\right) = -\nabla_\parallel\left[N(T_e + T_i)\right] + \vec{\nabla}\cdot\left(D_\Gamma\vec{\nabla}_\perp\Gamma\right) \tag{2.37}$$

$$\partial_t W + \vec{\nabla}\cdot\left(W\Gamma/N\vec{b} + W\vec{u}_E + W\vec{u}^i_{\nabla B}\right) = \vec{\nabla}\cdot\left(N\left(\vec{u}^i_{\nabla B} - \vec{u}^e_{\nabla B}\right)\right) + \vec{\nabla}\cdot\left(J_\parallel\vec{b}\right) + \vec{\nabla}\cdot\left(D_W\vec{\nabla}_\perp W\right) \tag{2.38}$$

$$N\nabla_\parallel\Phi - \nabla_\parallel NT_e - 0.71N\nabla_\parallel T_e + \eta_\parallel N J_\parallel = 0 \tag{2.39}$$

In order to simplify the numerical approach, density at the denominator of the RHS of (2.34) is approximated the reference value n_0, i.e. to 1 in dimensionless units. This technique is adopted in order to simplify the numerical approach, described in section 2.5, in the hypothesis that the density value does not move significantly from the reference one. Furthermore, in (2.36) and (2.38), a diffusive operator has been introduced. This operator helps the numerical solution by dissipating the energy on the smallest turbulence scales.
We use for vorticity the generalised definition:

$$W = \vec{\nabla}\cdot\left(\frac{\vec{\nabla}_\perp\Phi}{B^2} + \frac{\vec{\nabla}_\perp\left(NT_i\right)}{NB^2}\right) \tag{2.40}$$

therefore taking into account the ion pressure. The drifts in perpendicular direction are expressed as:

$$\vec{u}_E = (\vec{B}\times\vec{\nabla}\Phi)/B^2 \qquad , \qquad \vec{u}^{i/e}_{\nabla B} = \pm 2T_{i/e}(\vec{B}\times\vec{\nabla}B)/B^3, \tag{2.41}$$

with the sign + for the ions i and − for the electrons e.
In equations (2.36)-(2.40), normalising temperatures to the reference value T_0 we choose to impose constant temperatures in space and time:

$$T_e = T_i = 1 \tag{2.42}$$

Notice that this choice is not mandatory: temperature fields can be prescribed as spatial functions not evolving in time. In the isothermal hypothesis, so, the particles pressure

coincides with their density:

$$P_e = NT_e = N \qquad , \qquad P_i = NT_i = N \tag{2.43}$$

We also notice that the term describing the thermal currents in (2.39) vanishes.

2.3 Main instability mechanisms

The physical model solved by TOKAM3X allows the description of several instability mechanisms in the edge plasma. We illustrate here the main ones, always considering an isothermal framework.

2.3.1 Interchange instability

One of the main instabilities in edge plasma is called *interchange instability*, and it appears at the LFS of the tokamak. In this region, the background pressure gradient is directed towards the magnetic axis, as well as the magnetic field gradient. Figure 2.3 represents schematically the mechanism which causes the onset of the interchange instability in the edge plasma.

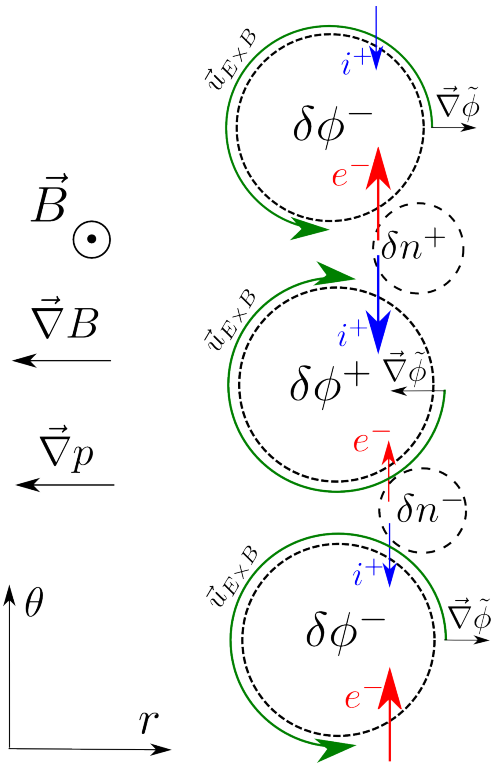

Figure 2.3: *Sketch of the interchange instability mechanism in the LFS of a tokamak.*

Let's suppose that a perturbation of the electric potential, with a sinusoidal shape in the poloidal direction, superposes to the background plasma: alternative regions of increased and lowered electric potential will appear, which we represent as cells tracing an isopotential contour. The local potential gradient will thus be directed radially towards the centre (towards the exterior) of a positive (negative) electric potential cell. This electric potential gradient causes an $E \times B$ velocity to develop along the contours of the cells. This velocity is the same for electrons and ions and, with the orientation of the magnetic field that we have chosen, it is directed clockwise (counterclockwise) for a positive (negative) potential cell. This $E \times B$ circulation causes a zone of increased density, denoted by δn^+, when particles are advected from the inner to the outer side, because of the background pressure gradient. On the contrary, a zone with lowered density, identified by δn^-, appears between two potential cells which advect particles from a low density to a high density region. The opposite situation would occur in the HFS since the density gradient would be reversed. Particles in zones where density is perturbed experience the diamagnetic drift: the ions drift downwards, while the electrons drift upwards. The diamagnetic flux departing from the zone of increased density is higher than the one from the lowered density: therefore, as visible in figure 2.3, a positive electric potential cell would receive a higher ion flux than an electron one, and vice-versa for a negative potential cell. This divergence of diamagnetic current is compensated by the divergence of the polarisation current. This balance is actually a Poisson equation with an effective permittivity of nm_i/B^2, as one can infer from the divergence of the polarisation current (2.33). An accumulation of charge leads thus to an increase of the potential perturbation of the same sign $\delta\phi$. Therefore, potential perturbations amplitude increase in an unstable way, and the density perturbation with them. This simple picture also shows that in interchange turbulence, the phase in poloidal direction between density and potential fluctuations is around $\pi/2$. On the HFS, the position of increased/lowered density would switch, leading to a net current of opposite charge with respect to the electric potential cell, having thus a stabilizing effect.
Another feature immediately understandable from figure 2.3 is the presence of convective cells, corresponding to isopotential contours. Zones of high density are expelled from the high density region in outward direction, giving rise to a turbulent structure with a characteristic mushroom shape (in other words, a zone of locally increased density is always associated with an electric dipole, which advects it radially outwards by $E \times B$ drift).

2.3.2 The simplest interchange model

In the simplest picture, plasma can be considered isothermal without varying qualitatively the description of interchange dynamics. In this framework, a simple model has been proposed by Hasegawa-Wakatani [59], which has been largely studied in literature. In this model, a scale separation is performed between the equilibrium components of the fields and the fluctuating ones, which will be indicated here by the symbol " ˜ ". The fields are normalised to the equilibrium quantities, $\tilde{N} = \tilde{n}/n_{eq}$, $\tilde{T} = \tilde{T}/T_{eq}$, $\tilde{\Phi} = \tilde{\phi}\ e/T_{eq}$. We consider here the simple variant given by the following two equations (see also [60], Chapter 3), which express the electric charge and the pressure conservations, in the plane

(r, θ) perpendicular to magnetic field lines. Considering only the dominant terms:

$$\begin{cases} \partial_t \rho_L^2 \nabla_\perp^2 \tilde{\Phi} = -2\vec{u}^e_{\nabla B} \cdot \vec{\nabla} \tilde{P} \\ \partial_t \tilde{P} = -\vec{u}_{\star,e} \cdot \vec{\nabla} \tilde{\Phi} \end{cases} \tag{2.44}$$

Assuming perturbations of the form $\tilde{X} = X_0 \exp(ik_r r + ik_\theta \theta + i\omega t)$, the two equations write:

$$\begin{cases} i\omega \rho_L^2 k_\perp^2 \tilde{\Phi} = -2\vec{u}_{\nabla B,e} \cdot \vec{\nabla} \tilde{P} \\ i\omega \tilde{P} = -\vec{u}_{\star,e} \cdot \vec{\nabla} \tilde{\Phi} \end{cases} \tag{2.45}$$

where $k_\perp^2 = k_r^2 + k_\theta^2$. From the system (2.45) we can calculate the expression of the linear growth rate:

$$\gamma = \frac{k_\theta^2}{k_\perp^2} \frac{\sqrt{\vec{u}^e_{\nabla B} \cdot \vec{u}_{\star,e}}}{\rho_L} \tag{2.46}$$

where the diamagnetic velocity has been considered incompressible. This simple model shows already the basic features of the interchange turbulence. Indeed, one can see that this instability can develop only in presence of a magnetic curvature, so that $\|\vec{u}^e_{\nabla B}\| \neq 0$. Moreover, substituting the expressions for the drift velocities one finds:

$$\gamma \propto \sqrt{\vec{\nabla} B \cdot \vec{\nabla} p} \tag{2.47}$$

Therefore, the interchange-type instabilities can exist only in the region of "bad curvature" of the tokamak, that is to say at the Low Field Side. Since the pressure gradient points towards the magnetic axis of the tokamak, in this region $\vec{\nabla} B \cdot \vec{\nabla} p > 0$, and in particular this product is maximum at the LFS midplane.
The system of equations (2.44) is similar to the one describing the Rayleigh-Bénard turbulence, where the electric potential corresponds to the velocity potential, for an incompressible velocity, and the pressure corresponds to the temperature. The curvature term $\vec{u}^e_{\nabla B} \cdot \vec{\nabla} \tilde{P}$ appearing in the electric potential equation, so, corresponds to the gravity field acting on the fluid. In the same way, the Rayleigh-Bénard instability is destabilised when the gravity force is aligned to the temperature gradient.
In the system (2.44) we have considered a simple geometry in the plane perpendicular to a field line. If we add the loss terms in the parallel directions, which are non-zero if the parallel resistivity is non-null, the developing turbulent structures are called *Resistive Ballooning Modes*. This is commonly done in 2D turbulence codes such as TOKAM2D [34], which solve a model similar to (2.44), but taking into account the advection terms in perpendicular and parallel directions. In particular, the physical model of TOKAM2D, in its isothermal version, is:

$$\begin{cases} \partial_t N + [\Phi, N] &= -\sigma_\parallel N e^{\Lambda-\Phi} + S_N + D\nabla_\perp^2 N \\ \partial_t \nabla_\perp^2 \Phi + [\Phi, \nabla_\perp^2 \Phi] &= g\frac{\partial_\theta \ln N}{r} + \sigma_\parallel (1 - e^{\Lambda-\Phi}) + \nu\nabla_\perp^4 \Phi \end{cases} \tag{2.48}$$

Where the normalization of each quantity is the same as the one explained before. Moreover, length scales are normalised to the Larmor radius ρ_L and time scales to the inverse of the cyclotronic frequency ω_C. Here the Poisson's brackets are defined as $[\Phi, X] = \vec{B}/B^2 \cdot \left(\vec{\nabla}\Phi \times \vec{\nabla}X\right)$, and they represent thus the advection by the $E \times B$ drift. The parallel dynamics terms on the RHS, linking the potential gradient to the sheath potential, are thought to be applied only to open flux surfaces. However, by regulating the $\sigma_\parallel$ parameter as a mask function, one can artificially introduce closed flux surfaces [37]. The systems is forced by a source of particles S_N, in a so-called *flux-driven* approach, opposed to the *gradient-driven* one, where background equilibrium gradients are prescribed.
Since 2D codes lack of a 3D description of the magnetic field, the driving curvature term must be reduced to a parameter of the code, g (reminding the analogy with the Rayleigh-Bénard system), which represents the local curvature of the magnetic field. The parallel losses terms on the right-hand side are averaged over the field line. 2D turbulence codes take indeed advantage of the so-called flute assumption: the parallel transport is considered extremely fast with respect to the perpendicular one, so that fluctuations can be considered homogeneous on the parallel direction at characteristic time scales of turbulence. We recognise here the Bohm boundary condition (1.57): the losses in the parallel direction, simulating the plasma sheath action, are controlled through the parallel conductivity parameter $\sigma_\parallel$. In 3D turbulence codes instead, the curvature and the parallel losses are not parameters of the model, and they result from the full 3D description of the magnetic field.

2.3.3 Resistive drift waves

Resistive Drift Waves (RDW) can be destabilised whenever a parallel resistivity and a density gradient are at play [5]. Figure 2.4 shows a schematic view of an electric potential perturbation in poloidal direction.

The vertical electric field causes a radial $E \times B$ drift of the plasma. However, if the electrons show an adiabatic behaviour, following the Boltzmann distribution, the electron density δn_e immediately follows the electric potential one, $\delta n_e/n_e = e\delta\phi/(k_B T_e)$. Therefore, there will be a drift wave propagating with the electron diamagnetic velocity in poloidal direction. However, no transport is at play since $E \times B$ velocities and density are out of phase of $\pi/2$. If a parallel resistivity, or, in other terms, a friction force in parallel direction, is at play, electrons do not match instantaneously the potential perturbation, so that a phase shift exist between the two wave-forms. By consequence, the $E \times B$ drift transports particles from a denser zone to a more rarefied one, amplifying therefore the instability. The collisionality is particularly strong in edge plasmas, so these instabilities must be taken into account in our analysis.

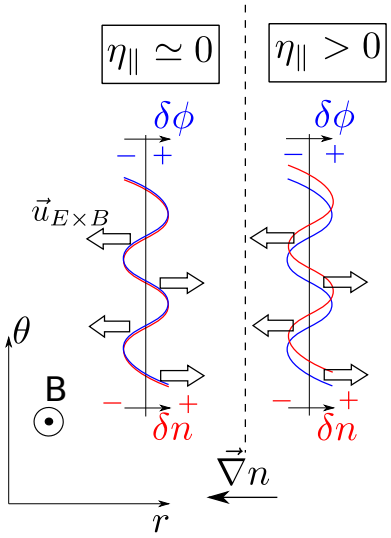

Figure 2.4: *Schematic representation of the RDW instability. The average density gradient is negative in radial direction. The left (right) panel represents a situation without (with) parallel resisitivity. δn and $\delta\phi$ indicate respectively density and potential perturbations.*

2.3.4 Kelvin-Helmoltz

Another turbulent mechanism, well-known in neutral fluid dynamics, is the Kelvin-Helmoltz instability. In plasmas, see [61], this instability can rise because of the radial gradient of the parallel flows. As explained in section 1.6, in the SOL the plasma is accelerated in the pre-sheath region up to the sound speed in the parallel direction. The criterion for the development of this kind of instability reads ([61], [62]):

$$\left(\frac{\partial \langle M \rangle_{t,\varphi}}{\partial r}\right)^2 - \left(\frac{\partial log(\langle N \rangle_{t,\varphi})}{\partial r}\right)^2 > 0 \tag{2.49}$$

In the vicinity of a limiter, at the interface between the open and the closed field lines region, where normally the parallel flows are much lower in absence of momentum injection, the Mach number increases sharply, possibly triggering the Kelvin-Helmoltz instability.

2.4 Magnetic geometry: a versatile approach

TOKAM3X is based on a flux-surface aligned coordinate system. Along with a suitable domain decomposition, described in section 2.5.2, this coordinate system allows the description of complex magnetic configurations.

2.4.1 Curvilinear coordinates

First of all, it is useful to derive a suitable mathematical description for the magnetic field in a tokamak. Usually, we know the magnetic field from experiments (for example by means of magnetic field reconstruction codes as EFIT [63]) as a function of the cylindrical coordinates, $\vec{B} = \vec{B}(R, Z, \varphi')$, where R is the major radius, Z is the vertical distance from the magnetic axis, and φ' is the curvilinear coordinate along the toroidal direction. Because of the anisotropy of the transport processes in a tokamak plasma, it is useful to adopt a coordinate system based on the magnetic topology of the magnetic field. In particular, we adopt a coordinate system which is aligned with the flux surfaces. These coordinates have a three dimensional, non-orthogonal local basis (see [64], Chapter 2). For any arbitrary set of three scalars $\left(u^i, u^j, u^k\right)$, which represent our generalised coordinates, we can pass from the cylindrical coordinates system to the set of generalised coordinates, by means of the following transformation that we can define as:

$$(R, Z, \varphi') = \vec{R}\left(u^i, u^j, u^k\right) \tag{2.50}$$

For every point in the 3D space, we can identify a curve over which two of the three parameters are constants and the last is free to vary. We can call these curves *coordinate curves*. We can thus identify, for every point, a set of vectors which are tangent to the three coordinate curves:

$$\vec{e}_i = \frac{\partial \vec{R}}{\partial u^i} \quad \vec{e}_j = \frac{\partial \vec{R}}{\partial u^j} \quad \vec{e}_k = \frac{\partial \vec{R}}{\partial u^k} \tag{2.51}$$

These vectors are called *tangent-basis* vectors, and they represent the *covariant basis*. In a similar way, we can identify three *coordinate surfaces*, where one of the three parameters is constant and the other two can vary. The system of three vectors perpendicular to these surfaces, named *reciprocal-basis* vectors is then:

$$\vec{e}^i = \vec{\nabla} u^i \quad \vec{e}^j = \vec{\nabla} u^j \quad \vec{e}^k = \vec{\nabla} u^k \tag{2.52}$$

Which constitute the so-called *contravariant basis*. Here the gradients are calculated in the cylindrical coordinate system. Figure 2.5 shows a schematic view of the coordinate curves and of the vectors of the local covariant or contravariant bases, in a 2D coordinates system.

It can be shown ([64], Chapter 2) that the two basis fulfil the important relationship:

$$\vec{e}^i \cdot \vec{e}_j = \delta^i_j \tag{2.53}$$

Moreover, the triple products of the vectors of the two basis are reciprocal:

$$\vec{e}_i \times \vec{e}_j \cdot \vec{e}_k = J = \mathcal{J}^{-1} \equiv \left(\vec{e}^i \times \vec{e}^j \cdot \vec{e}^k\right)^{-1} \tag{2.54}$$

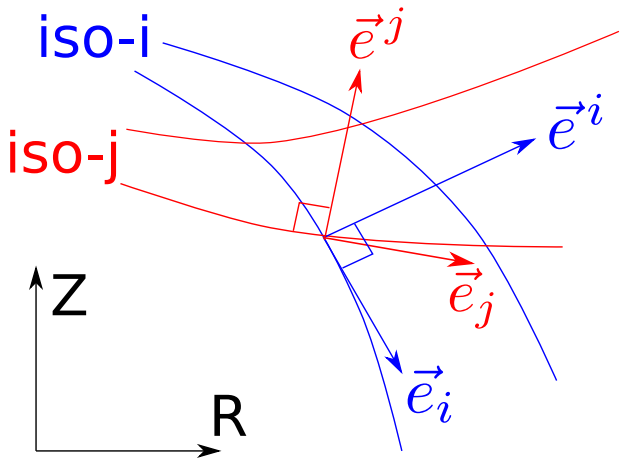

Figure 2.5: *Coordinate curves in a 2D space and associated local bases.*

where J is the Jacobian of the transformation $\vec{R}$, and it represents geometrically the elementary volume element. One can obtain the vectors of the contravariant basis from the ones of the covariant basis with the relation:

$$\vec{e}_i = J\vec{e}^{\,j} \times \vec{e}^{\,k} \quad , \quad \vec{e}^{\,i} = \frac{1}{J}\vec{e}_j \times \vec{e}_k \tag{2.55}$$

Where (i, j, k) must form a cyclic permutation of (1,2,3). Every vector can thus be written equivalently in covariant or contravariant basis, in the following way:

$$\begin{aligned} \vec{X} &= X^i\vec{e}_i + X^j\vec{e}_j + X^k\vec{e}_k \\ &= X_i\vec{e}^{\,i} + X_j\vec{e}^{\,j} + X_k\vec{e}^{\,k} \end{aligned} \tag{2.56}$$

We will use the relations just presented in order to develop a proper description of the magnetic field in TOKAM3X.

2.4.2 A physics-based choice of the coordinate system

We must now choose a proper triplet of independent parameters which is suitable for the description of the magnetic field. We assume the existence of flux surfaces, which are tangent in every point to the magnetic field lines. These surfaces are labelled by the coordinate ψ. The second parameter is the curvilinear coordinate θ, which varies along a flux surface in the poloidal plane. Finally, we take the toroidal angle as third parameter, calling it φ. Since the magnetic field is divergence-free, one can re-write it in terms of a vector potential $\vec{A}$, such that:

$$\vec{B} = \vec{\nabla} \times \vec{A} \tag{2.57}$$

If we choose, similarly to what is proposed in [13]:

$$\vec{A} = \psi_p \vec{\nabla}\varphi + \psi_t \vec{\nabla}\theta \tag{2.58}$$

then we can re-write the magnetic field as:

$$\vec{B} = \vec{\nabla}\psi_p \times \vec{\nabla}\varphi + \vec{\nabla}\psi_t \times \vec{\nabla}\theta \tag{2.59}$$

If we take ψ_p as functions of the only variable ψ, and $\psi_t = \psi_t(\psi, \theta)$, then our definition of the magnetic field will satisfy the property $\vec{B} \cdot \vec{\nabla}\psi = 0$, meaning that the magnetic field has no ψ component in the covariant basis, so it is more convenient to express it in this basis rather than in the contravariant one. This relation also tells us that the magnetic field lines lie on the flux surfaces. Taking into account the dependency of the arbitrary functions on ψ, we re-write 2.59 as:

$$\vec{B} = \frac{d\psi_p}{d\psi}\vec{\nabla}\psi \times \vec{\nabla}\varphi + \frac{\partial\psi_t}{\partial\psi}\vec{\nabla}\psi \times \vec{\nabla}\theta \tag{2.60}$$

At this point, we can notice that our particular choice of the two functions ψ_p and ψ_t implies a precise physical meaning: they represent the flux of magnetic field respectively in poloidal and toroidal directions. Calculating the magnetic field flux over a surface, we obtain, using the property 2.53:

$$\begin{aligned} \int \vec{B} \cdot \mathrm{d}\vec{S} &= \oint \vec{A} \cdot \mathrm{d}\vec{l} \\ &= \oint_\psi \left(\psi_p \vec{\nabla}\varphi + \psi_t \vec{\nabla}\theta\right) \cdot (\vec{e}_\psi \, \mathrm{d}\psi + \vec{e}_\theta \, \mathrm{d}\theta + \vec{e}_\varphi \, \mathrm{d}\varphi) \\ &= \oint_\psi (\psi_p \, \mathrm{d}\varphi + \psi_t \, d\theta) \end{aligned} \tag{2.61}$$

For a closed line on a flux surface enclosing the main axis, but not the magnetic axis, we obtain the poloidal flux $\Psi_p(\psi) = 2\pi\psi_p$. A closed line enclosing instead the magnetic axis, but not the main one gives the toroidal flux $\Psi_t(\psi) = \oint \psi_t(\theta, \psi) d\theta$. Ψ_t and Ψ_p are measured in Wb.
Considering an axisymmetric field, which is a reasonable approximation for a tokamak, one has the following properties:

$$\vec{e}_\varphi \cdot \vec{e}_\psi = \vec{e}_\varphi \cdot \vec{e}_\theta = \vec{e}^{\,\varphi} \cdot \vec{e}^{\,\psi} = \vec{e}^{\,\varphi} \cdot \vec{e}^{\,\theta} = 0 \qquad , \qquad \vec{e}^{\,\varphi} \times \vec{e}_\varphi = 0 \tag{2.62}$$

Considering (2.55), we understand that $\vec{e}^{\,\varphi}$ is parallel to $\vec{\nabla}\psi \times \vec{\nabla}\theta$, so we can re-write

(2.60) as:

$$\vec{B} = \frac{d\psi_p}{d\psi}\vec{\nabla}\psi \times \vec{\nabla}\varphi + B_\varphi \vec{\nabla}\varphi \tag{2.63}$$

where B_φ is the toroidal field component in the contravariant basis. Moreover, passing from the curvilinear length φ' to the angle φ, we obtain:

$$\|\vec{e}_\varphi\| = \|\vec{e}^\varphi\|^{-1} = R \tag{2.64}$$

We choose then ψ_t such that:

$$\frac{\partial \psi_t}{\partial \psi} = \frac{FJ}{R^2} \tag{2.65}$$

We check, then, that the Ampère's law is verified. Using (2.54) and (2.64) we get:

$$\begin{aligned} \oint \vec{B} \cdot d\vec{l} &= \oint \left(\frac{d\psi_p}{d\psi}\vec{\nabla}\psi \times \vec{\nabla}\varphi + \frac{FJ}{R^2}\vec{\nabla}\psi \times \vec{\nabla}\theta \right) \cdot \mathrm{d}\varphi \; \vec{e}_\varphi \\ &= 2\pi F = \mu_0 I_{tor} \end{aligned} \tag{2.66}$$

Hence:

$$F = \mu_0 I_{tor}/(2\pi) \tag{2.67}$$

This quantity is proportional to the toroidal current I_{tor}, and it is left as a parameter in the code. Thus for the magnetic field:

$$\begin{aligned} \vec{B} &= \frac{d\psi_p}{d\psi}\vec{\nabla}\psi \times \vec{\nabla}\varphi + \frac{FJ}{R^2}\vec{\nabla}\psi \times \vec{\nabla}\theta \\ &= \frac{d\psi_p}{d\psi}\vec{\nabla}\psi \times \vec{\nabla}\varphi + \frac{FJ}{R^2}\frac{\vec{e}_\varphi}{J} \\ &= \frac{d\psi_p}{d\psi}\vec{\nabla}\psi \times \vec{\nabla}\varphi + \frac{F}{R^2}R^2\vec{e}^\varphi \end{aligned} \tag{2.68}$$

Finally obtaining that $B_\varphi = F$. The second component of the magnetic field can be expanded as:

$$\frac{d\psi_p}{d\psi}\vec{\nabla}\psi \times \vec{\nabla}\varphi = -\frac{1}{J}\frac{d\psi_p}{d\psi}\vec{e}_\theta \tag{2.69}$$

So the resulting magnetic field component in the poloidal direction, in covariant basis, is:

$$B^\theta = -\frac{1}{J}\frac{d\psi_p}{d\psi} \tag{2.70}$$

Combining the two components of the field we obtain:

$$\begin{aligned} \vec{B} &= -\frac{1}{J}\frac{d\psi_p}{d\psi}\vec{e}_\theta + \frac{B_\varphi}{R^2}\vec{e}_\varphi \\ &= B^\theta \vec{e}_\theta + B^\varphi \vec{e}_\varphi \end{aligned} \tag{2.71}$$

It is useful to express magnetic field components with respect to unitary vectors, as they correspond to the physically measurable values.

$$\vec{B} = \hat{B}^\theta \frac{\vec{e}_\theta}{|\vec{e}_\theta|} + \hat{B}^\varphi \frac{\vec{e}_\varphi}{|\vec{e}_\varphi|} \tag{2.72}$$

One can notice that $\hat{B}^\varphi = B^\varphi \; R = \frac{F}{R}$. The toroidal field is thus inversely proportional to R; this important characteristics of tokamaks is thus taken into account.

2.4.3 Safety factor in TOKAM3X simulations

It is useful to give a local definition of the safety factor, that allows us to calculate the integrated safety factor for an arbitrary field line shape:

$$q_{loc}(\psi,\theta) = -\frac{\mathcal{J}\frac{\partial\psi_t}{\partial\psi}}{\mathcal{J}\frac{d\psi_p}{d\psi}} = -\frac{FJ}{R^2\frac{d\psi_p}{d\psi}} \tag{2.73}$$

This quantity is an expression of the local pitch angle. Using (2.73) for an arbitrary field line shape, we have so:

$$\begin{aligned} q(\psi) &= \frac{1}{2\pi}\oint q_{loc}(\psi,\theta)\; d\theta \\ &= -\frac{1}{2\pi}\oint \frac{FJ}{R^2\frac{d\psi_p}{d\psi}}\; d\theta \\ &= \frac{1}{2\pi}\oint \frac{\hat{B}^\varphi\,|\vec{e}_\theta|}{R\hat{B}^\theta}\; d\theta \end{aligned} \tag{2.74}$$

finding the well-known integral formula of [6]. This expression is well defined for closed field lines. In open field lines, we perform the integration on the main SOL only. One

can notice that, in circular geometry, the local safety factor reduces to:

$$q_{loc}(r,\theta) = \frac{\hat{B}^{\varphi} r}{R\hat{B}^{\theta}} \tag{2.75}$$

where r is the minor radius. This expression is the same as the one for the global safety factor in a large aspect ratio tokamak with circular flux surfaces: in that ideal case indeed, the pitch angle would be constant on the flux surfaces. In the following, when referring to the poloidal and the toroidal field, we will refer to $\hat{B}^{\theta}$ and $\hat{B}^{\varphi}$, respectively, dropping the " ˆ " symbol.

2.4.4 Mesh grid construction and magnetic field calculation

Since TOKAM3X describes electrostatic turbulence, the poloidal flux function does not change during the simulation. Therefore, it is sufficient to fix the magnetic field components in order to run a simulation. As specified in section 2.4.2, the toroidal field has a known shape ($\propto 1/R$), and only the value on the magnetic axis, F, must be chosen. The poloidal magnetic field, instead, depends on the plasma current distribution in the machine, and must be derived from the poloidal flux function using equation (2.70).
We can adopt two different approaches in determining the poloidal magnetic field of a simulation, which are described in the following. In particular we distinguish a case where the magnetic geometry is analytical, and a case where the magnetic equilibrium is obtained from experimental data.

- **Analytical geometries** - When we use analytical geometries, we can choose the $q(\psi)$ profile, paying attention to make a physically wise choice. In particular, a parabolic profile in radial direction, similar to the one found in experiments, is usually set. Equation (2.74) allows then to calculate the poloidal flux function, starting from the mean safety factor.

$$\boxed{\text{Analytical grid} - J(R,Z)} \rightarrow \boxed{q(\psi) \text{ imposed}} \rightarrow \boxed{\Psi_p(\psi) \text{ calculated}} \rightarrow \boxed{B^{\theta}}$$

  TOKAM3X allows to choose several analytical geometries, and in particular:

  - Circular geometry with only closed flux surfaces
  - Circular geometry with only open flux surfaces, with an infinitely thin limiter
  - Circular geometry with open and closed flux surfaces, and infinitely thin limiter
  - Circular geometry with open and closed flux surfaces, with a thick limiter
  - Slab geometry

In the case of circular geometry, through the input parameters of the code, the user can choose a set of geometrical parameters, including:

- The plasma elongation κ
- The plasma triangularity δ
- The position of the limiter

- **Realistic magnetic equilibria** - In this approach we derive the magnetic equilibrium from a real map $\Psi_p(R, Z)$, obtaining the poloidal field in every point. In practice, in every tokamak, the Ψ_p function of a plasma discharge is reconstructed with a certain frequency (usually of the order of the kHz), using some magnetic diagnostics and dedicated softwares as *EFIT* [63].
  The function $\Psi_p(R, Z)$ is thus imported into a mesh generator. The mesh generator builds the 2D grid on the poloidal section, according to the chosen number of grid points, and to the total chosen extension of the grid in radial and poloidal directions. In particular, the knots of the mesh will be all aligned on iso-ψ_p contours. This condition is fundamental in order to have a flux-surface aligned mesh grid. The grid in poloidal direction can be chosen, in principle, according to the needs of the user. The only constraint is to get, in the end, a structured mesh. However, let's notice that non-orthogonal meshes imply the calculation of "crossed terms" in ψ and θ directions in the operators used in TOKAM3X, and a strong non-orthogonality could cause numerical instabilities. Therefore, iso-θ lines are usually set orthogonal to iso-ψ_p. Nevertheless, the grid can be refined in θ and in ψ direction according to the specific cases and to physical considerations.
  Once the grid set, the transformation from the (R, Z, φ') basis to the (ψ, θ, φ) one is fixed, and so also its Jacobian. We have then all the necessary elements to calculate the local B^θ value. We can schematise this approach as follows:

$$\boxed{\Psi_p(R, Z) \text{ from experiments}} \rightarrow \boxed{\text{Mesh grid built} - J(R, Z)} \rightarrow \boxed{B^\theta}$$

  Here $q(\psi)$ is not fixed, but can be calculated a posteriori, using (2.74). Figure 2.6 shows an example of poloidal flux function and the associated mesh grid.

Once the poloidal field is calculated, the flux function can be multiplied by a parameter called *psiscale* in order to change the ratio between toroidal and poloidal magnetic field. Moreover, the user can fix the angular sector in toroidal direction with the parameter L_φ. The code thus generates the 3D mesh by replicating the grid built in the poloidal plane on each point in the toroidal direction N_φ times. The toroidal angular width of each cell is then $\delta_\varphi = L_\varphi / N_\varphi$.
The coordinates system presented in this chapter must be discretised. Indeed, TOKAM3X makes use of a 3D structured mesh, where the three directions are identified by the triplet $(i_\psi, i_\theta, i_\varphi)$: this basis is the numerical discretisation of the (ψ, θ, φ) one described previously. While ψ is already an index of flux surface coordinate, and corresponds thus to i_ψ, the mesh construction determines the discretised coordinates i_θ and i_φ. The calculation of the metric coefficients in generalised geometry, required in the expression of the

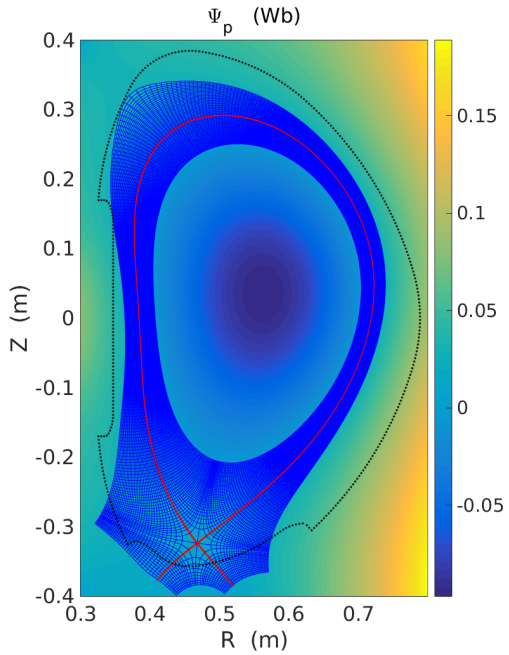

Figure 2.6: *Poloidal flux function of a COMPASS discharge (shotnumber 5249, t = 1100 ms). Superposed to it, in blue, the mesh built by the mesh generator of TOKAM3X. The red line represents the separatrix, corresponding theoretically to the 0 value of the Ψ_p function. In black dotted line, the projection on the poloidal plane of COMPASS vessel wall contour.*

operators, is detailed in Appendix B.

2.5 Numerical method

2.5.1 Numerical schemes

TOKAM3X is based on a conservative finite-differences discretization method for the solution of the partial differential equations presented in section 2.2.5. The evolution in time is calculated with a Runge-Kutta scheme of arbitrary order (in practice, orders from 1 to 4 are implemented in the code).
Advection terms are advanced with an explicit scheme. In particular, TOKAM3X uses a shock-capturing Roe-Marquina scheme (see [65] and [66]), based on a WENO (Weighted Essentially Non Oscillatory) interpolation [67] for the reconstruction of the advection terms.
The vorticity equation (2.38) is treated differently from the others, since the evolution of the parallel current has a much faster dynamics of the perpendicular advection terms. In a first step, the advection terms are advanced explicitely, as in the other equations. Then, substituting the expression of the parallel current (2.39) and of the vorticity (2.40)

in the remaining terms, the equation is solved with an implicit method, with the electric potential function as unknown. At this intermediate step, the following linear system has to be solved:

$$\left(\mathcal{L}^{\perp} + \mathcal{L}^{\parallel}\delta t\right)\Phi^{t+1} = W^{\star} - \left(\mathcal{L}^{\perp} + \mathcal{L}^{\parallel}\delta t\right) log\left(N^{\star}\right) \tag{2.76}$$

Where the quantities with the $\star$ superscript are result from the explicit advancement of the equations. The operators appearing on the LHS are $\mathcal{L}^{\perp} = \vec{\nabla} \cdot \left(\frac{1}{B^2}\vec{\nabla}_{\perp}\right)$ and $\mathcal{L}^{\parallel} = \vec{\nabla} \cdot \left(\frac{1}{\eta_{\parallel}}\vec{b}\nabla_{\parallel}\right)$. The operator $\mathcal{L}^{\perp} + \mathcal{L}^{\parallel}\delta t$ is thus a 3D operator which has to be inverted. This matrix is sparse, and, because of the big coefficient $\delta t/\eta_{\parallel}$ appearing in it, usually ill-conditioned, thus difficult to invert with an iterative method. Instead, a direct method, based on the L-U decomposition, is usually adopted, with the help of dedicated libraries as PASTIX [68].
The diffusive terms are also solved with an implicit advancement, in order to avoid CFL problems when using large diffusion coefficients. This is not the case in the majority of the domain, where the diffusive terms are of the same order or lower than the others. However the implicit treatment is necessary in zones where diffusion coefficients are raised on purpose, called "buffer" regions, described in section 2.6.1.
For further details on the numerical solution we address the reader to the paper [33].

2.5.2 Multi-domain decomposition

In order to solve a complex geometry, as the diverted one, with a structured mesh, the geometrical domain is decomposed in several sub-domains, named *zones*, according to the magnetic topology. Zones are rectangular in the (ψ, θ) space, and they are retailed such that all the cells on one of the boundaries are adjacent to another zone or to a physical boundary of the domain. Each side of a zone is surrounded by a certain number of layers of ghost cells. These ghost cells allow the communication between adjacent zones, as well as the imposition of boundary conditions. Figure 2.7 shows two examples of multi-domain splitting.

This domain-splitting method is a common practice in 2D transport codes, such as, for example, SolEdge2D [69] or SOLPS [70]. The 2D transport codes for the simulation of the edge plasma are focused on the plasma-wall interactions, and must thus deal with the complexity of the real geometry of magnetic field and plasma-facing components. Therefore, numerical methods and techniques, as the domain decomposition, necessary to solve complex geometries, have been implemented and tested for long time. This expertise is being embedded at present in 3D turbulence codes, where the complexity of the physical model and the 3D geometry set additional challanges in the implementation of the same numerical techniques.

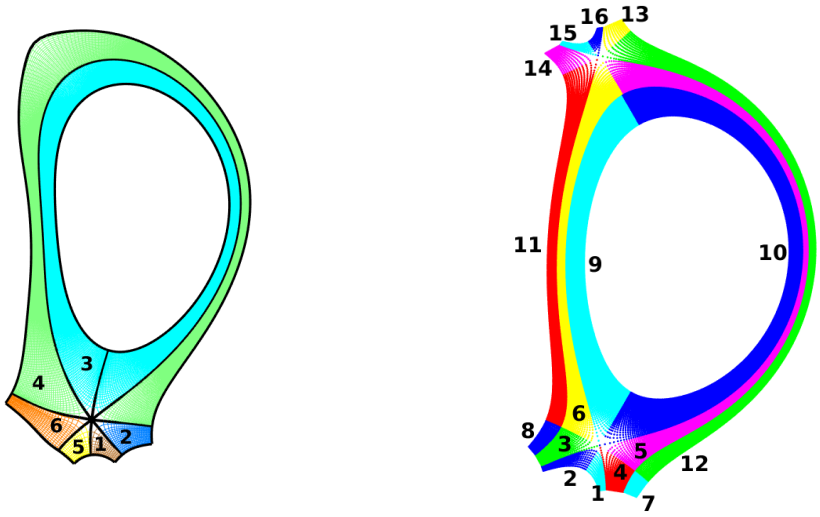

Figure 2.7: *Example of multi-domain decomposition in a COMPASS-like geometry (left) and on a WEST-like geometry (right, courtesy of F. Nespoli).*

2.6 Boundary conditions

Periodic conditions are applied in toroidal direction over the whole domain, relying on the axysimmetry of the tokamak configuration. Periodicity is applied also in the poloidal direction, in the closed flux surfaces zone. The reference coordinate system in TOKAM3X is aligned on flux surfaces, and usually an orthogonal mesh is adopted, in order to limit the numerical issues linked to non-orthogonal mesh. Therefore, the coordinate system is not aligned, in general, with plasma-facing components. With a simple approach, the geometrical domain is cut both in ψ and θ directions at convenient locations, in order to approximate the position of plasma-facing components. At the outer radial boundary, therefore, field lines are parallel to the outermost surface. A Neumann condition $\partial_\psi \cdot = 0$ is applied to all the variables (N, Γ, Φ, W). This condition nullifies the diffusive flux at the outer boundary, but not necessarily the component of the convective one perpendicular to the wall, that is to say Nu^ψ. In particular, one must pay attention to the ∇B flux to the walls, which enters into the overall electric charge balance. In divertor configuration, the same Neumann conditions are applied to the radial inner boundary of the PFR.
In poloidal direction, field lines lie on a (θ, φ) plane, and in the SOL they intercept the solid component (the limiter, or a divertor target) with a specific incidence angle, generally variable along the ψ direction. These are the most difficult boundary conditions to deal with: indeed, the plasma dynamics at the interface with solid walls is regulated by the presence of the plasma sheath. The sheath region has a characteristic width of the order of the Debye length. As already mentioned, this length is much shorter than the field line length, and, moreover, of the characteristic ionisation mean free path. This translates into the fact that this region is almost non-collisional, and the Braginskii closure is no longer valid. In this region indeed the species distribution functions differ significantly from the Maxwellian: a kinetic code should be used for a rigorous description. TOKAM3X, as the majority of fluid codes, considers therefore an infinitely thin sheath

layer, and imposes the Bohm's boundary conditions at the sheath entrance(1.50). Let's see how these conditions are applied to the fields calculated by the code. The plasma density at the sheath is not directly affected by the Bohm's boundary conditions. The parallel momentum is imposed such that:

$$\left|\Gamma_i^{\parallel}\right|_{|_b} \geq nc_s \rightarrow |\Gamma| \geq N\sqrt{T_e+T_i} \Rightarrow \begin{cases} \Gamma_{|_{b1}} \geq N\sqrt{T_e+T_i} \\ \Gamma_{|_{b2}} \leq -N\sqrt{T_e+T_i} \end{cases} \tag{2.77}$$

Where the unnormalized and the normalized conditions are shown. Here $b1$ is the boundary where the parallel direction points towards the wall, and $b2$ is the boundary at the opposite side of the field line. In TOKAM3X, this condition is combined with a logic one. If the flux is already super-sonic ($|\Gamma| > N\sqrt{T_e+T_i}$) in the last cell, then its value is replicated in boundary ghost cells. In the opposite case, the sonic condition, $|\Gamma| = N\sqrt{T_e+T_i}$ is imposed.
The plasma sheath affects also electrons dynamics, and therefore the parallel current at the wall, as derived in Chapter 1. In TOKAM3X, we decide to set the electric potential value at the wall $\phi^w = 0$, so that the Bohm condition on parallel current (1.57) writes:

$$j^{\parallel}_{|_b} = \pm nec_s\left(1-\exp\left(\Lambda-\frac{\phi}{k_BT_e}\right)\right) \rightarrow J_{\parallel_{|_b}} = \pm N\sqrt{T_e+T_i}\left(1-\exp\left(\Lambda-\frac{\Phi}{T_e}\right)\right) \tag{2.78}$$

Where the sign $+$ is referred to the boundary $b1$, and $-$ to $b2$. $J_{\parallel}$ is not calculated explicitly in the code. The Ohm's law is instead substituted in its expression in order to obtain a condition on the electric potential.

$$\frac{1}{\eta_{\parallel}}\left[\frac{\nabla_{\parallel}\left(NT_e\right)}{N}-\nabla_{\parallel}\Phi-0.71\nabla_{\parallel}T_e\right] = \pm N\sqrt{T_e+T_i}\left(1-\exp\left(\Lambda-\frac{\Phi}{T_e}\right)\right) \tag{2.79}$$

Since at the sheath, the electric potential Φ is close to ΛT_e, this boundary condition is linearised into:

$$\nabla_{\parallel}\Phi = \frac{\nabla_{\parallel}\left(NT_e\right)}{N}-0.71\nabla_{\parallel}T_e \mp \eta_{\parallel}N\sqrt{T_e+T_i}\left(\frac{\Phi}{T_e}-\Lambda\right) \tag{2.80}$$

Equation (2.80) represents a Robin condition, where the weight of the Dirichlet part is proportional to the parallel resistivity. This value is usually very low, around 10^{-5}. Depending on the specific simulations, so, the Neumann part can be dominant with respect to the Dirichlet one. In this case, the 3D vorticity operator suffers of ill-conditioning, and it is more difficult to invert.

2.6.1 Fluxes control at the inner radial boundary

In order to guarantee the conservation properties of the code, in addition to a conservative numerical scheme, it is necessary to control the physical sources and sinks.
In the case of the particle density, TOKAM3X imposes a volumetric source. The sink mechanisms are given by the fluxes at the geometrical boundaries. In particular, at the interface with solid targets, Bohm's boundary conditions impose a net particle outflow. At the radial boundaries where a Neumann condition is imposed, the turbulent fluxes directed outwards are not perfectly controlled, and they can vary with the characteristic periodicity of turbulence. However, Neumann conditions in radial direction tend naturally to suppress turbulence. Indeed turbulent fluxes at the outer boundary in ψ direction in simulations with all the geometry types (limiter and divertor), are verified to be around the 1% of the value at the separatrix (and even lower at the inner radial boundary of the PFR).
The radial inner boundary is the most complex to numerically deal with. This boundary does not represent a physical border, but just a limitation in the geometrical domain. This limitation is due both to the fact that computational costs must be limited, and to the scarce applicability of fluid theory to the core plasma.
One must thus control the incoming and outgoing fluxes from the inner radial boundary. Since our system is flux-driven, a simple Dirichlet condition could force the gradient on large-scale, affecting the overall equilibrium of the system. A Neumann condition with a null flux was imposed in previous releases of TOKAM3X. However, in the region close to the boundary, strong gradients build up, and a particularly strong turbulence can be found. If turbulence is not inhibited, radial convective inward and outward fluxes can freely cross the inner boundary. In order to be sure to control the radial fluxes, at the inner boundary, a null flux condition is hard-coded:

$$\Gamma^{\psi} = 0 \tag{2.81}$$

This condition zeroes all the convective fluxes at the boundaries. In this way, without losing the conservation of the different fields, we do not have undesired losses or sources. Since the boundary condition (2.81) is imposed also on diamagnetic fluxes, currents through the inner boundary are also null.
However, dealing with a "closed box" on the inner side does not necessarily represent a perfect physical solution of the inner boundary problem. We notice that the poloidal direction is not constrained, with this solution, in any way. Poloidal, and parallel fluxes are thus allowed. When radial fluxes are artificially stopped, the system tends to react with flows in parallel, or poloidal direction.
We found, in particular, that the downward ion ∇B flux (or upward ∇B flux for electrons), being stopped at the inner radial boundary, leads to a positive charge accumulation at the top of the inner boundary, and of a negative charge at the bottom. This accumulation thus generates a radial electric potential gradient directed downwards, both at the top and at the bottom of the machine. As a consequence, a steady $E \times B$ poloidal flux is directed towards the LFS midplane, carrying most of the particles (which enter in the system through the volumetric source). Figure 2.8 illustrates qualitatively this effect.

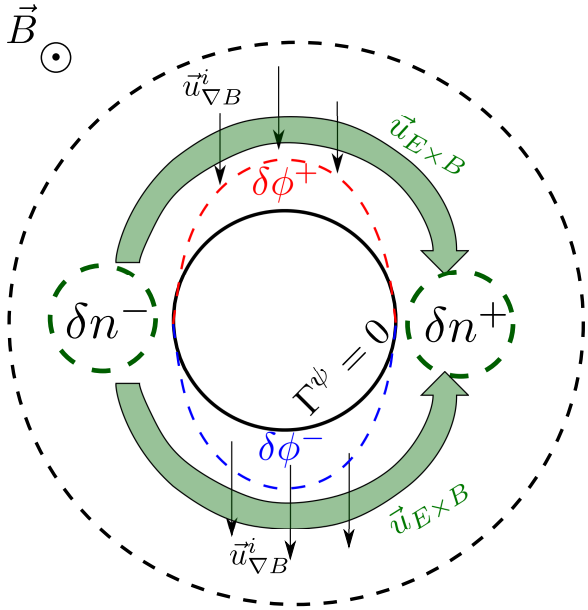

Figure 2.8: *Schematic view of the poloidal asymmmetry generated by the boundary condition $\Gamma^\psi = 0$ at the inner boundary of the geometrical domain. The zones of electric potential build-up are indicated with $\delta\phi^\pm$ and the ones of density variation with $\delta n^\pm$.*

We end up, so, with a system where charge cumulates at the top and bottom of the machine, while particles are brought from the inner to the outer midplane. One could wonder why, if there is a pressure imbalance between the inner and the outer midplane, the parallel transport does not compensate perfectly this situation, restoring an homogeneous total pressure. This can be understood by the analysis presented in Appendix C.
This configuration leads thus to strong poloidal asymmetries in the edge region, which are not physically justified, because entirely due to the arbitrary choice of boundary conditions. Experimentally, usually the average density on a line of sight is measured in the closed flux surfaces region. In order to have an information on poloidal asymmetry, one should instead rely on local measurements at different poloidal positions. Some basic information, for example, can be inferred from measurements carried out on Alcator C-Mod at the inner and outer midplane, by means of reciprocating Langmuir probes [41]. These experimental results, regarding L-mode discharges, show that plasma static pressure is almost equal at the inner and at the outer midplane. A further precaution must thus be taken in order to maintain a poloidal symmetry in the closed flux surface region.
In order to prevent the density and charge cumulation at the inner radial boundary, a strong variation of the diffusive operator is imposed near this position, trough a mask function:

$$\partial_t X = \cdots + \vec{\nabla} \cdot \left(\Upsilon D_X^0 \vec{\nabla}_\perp X \right) \tag{2.82}$$

Where X is a generic conserved quantity and D_X^0 is the associated diffusion coefficient. In

our numerical solution, Υ is a mask function with an Heaviside shape in radial direction, such as

$$\Upsilon = \Upsilon_0 H(\psi - \psi_0) \tag{2.83}$$

where we call Υ_0 "buffer coefficient". When the value of this parameter is elevated enough (usually 10^8) it can guarantee the dominance of the diffusion operator in the region where the mask function is active. In particular, it is necessary to increase locally the diffusion in poloidal direction, in order to homogenise plasma over a flux surface, while one can limit the diffusion in ψ and φ directions. Alternatively, one can numerically homogenise plasma quantities over the first flux surfaces with an averaging operation. This "buffer region" must be limited in radial direction to few points (usually from 1 to 4) in order to lose the smallest possible portion of geometrical domain.
The use of a buffer region at the inner radial boundary in the closed flux surfaces region is common in codes for turbulence simulations, both fluid (e.g. GBS [45]), and kinetic or gyro-kinetic (e.g. GYSELA [71]), and it was used also in TOKAM3X with $\Upsilon = 10^2$, as shown in figure 2.9a. This technique is usually adopted in order to control turbulence and the associated fluxes. We underline here that the use of elevated values of the diffusion coefficient, combined with the boundary condition $\Gamma^\psi = 0$, allows to stop fluxes across the inner boundary and to mitigate the large-scale fluxes caused by this condition. In figure 2.9 we see a comparison between two identical simulations in presence of weak (a) and strong (b) diffusive buffer zones.

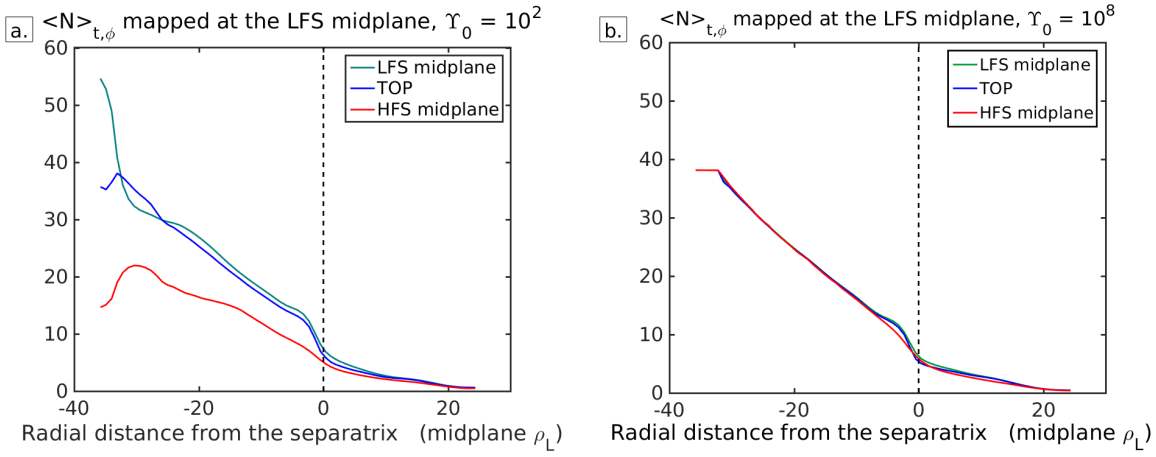

Figure 2.9: *a) Radial profile of the average density at different poloidal positions, remapped at the LFS midplane, for a COMPASS-like diverted simulation, where a buffer zone with $\Upsilon_0 = 10^2$ is used. b) Density profiles referred to a simulation with $\Upsilon_0 = 10^8$.*

One can notice the density accumulation at the LFS midplane in the case of low Υ. In figure 2.9b, a flat density region indicates the buffer zone. The turbulence properties are not perturbed at radial locations not adjacent to the buffer zone, and a more physical situation, with the in-out equilibrium of the plasma pressure, is restored. Even if the poloidal asymmetries in closed flux surfaces are strongly reduced by the buffer zone, they can still exist, as one can notice in proximity of the separatrix. A more detailed study

on the poloidal asymmetries in the closed flux surfaces region is presented in Appendix C.

2.6.2 Verification and validation of TOKAM3X

TOKAM3X has been verified with the Method of Manufactured Solutions [33]. A further, more stringent verification process is being carried out, by means of the PoPe (Projection On Proper Elements) method [72]. The first results are presented in Appendix D.
Along with GBS, BOUT++ and HESEL, TOKAM3X has undergone several multi-code validation tests, especially on seeded blobs propagation. The first of these experiments has been performed on the TORPEX tokamak [51]. This work consisted in a comparison in blob propagation velocity between experiments and the involved numerical tools. In [51], one can also find a more detailed comparison among the different presented codes. More recently, an experiment of the same type has been carried out on MAST [52].

2.7 Simulations set-up

2.7.1 Physical parameters of the simulations

The isothermal version of the TOKAM3X model is characterized by few parameters. Three of them are the diffusion coefficients for the conserved quantities, appearing on the right-hand side of the respective equations D_N, D_Γ and D_W. These coefficients determine the relative weight of the diffusive operator with respect to the other terms appearing in the equation. From a physical point of view, the diffusion operator can be seen as the representation of some transport mechanisms which are is included in the model (classical, neoclassical, etc.). The diffusion coefficients values are generally kept as low as possible, so that electrostatic turbulence can be the main transport mechanism. Usually in the simulations presented in this work, their value is set to $0.5 \cdot 10^{-2} \rho_L^2 \omega_C$. For a tokamak of the size of COMPASS, for example, with a 0.9 T toroidal field and a temperature in the edge region $\simeq 20\ eV$, the Larmor radius value would be around $7 \cdot 10^{-4}\ m$, and the cyclotronic frequency about $4 \cdot 10^7\ s^{-1}$. This values result in a diffusion of $\sim 0.1\ m^2/s$, which is a value slightly higher than the characteristic neoclassical values. In some simulations, this coefficient is reduced by a factor 5, being thus more compatible with neoclassical transport coefficients. However, numerical diffusion can intervene, and preliminary estimations seem to indicate that it can be comparable to the imposed physical diffusion coefficient, when the value of the latter is low (see Appendix D).
The fourth parameter is the parallel resistivity. This quantity is related to the plasma collisionality, and its expression according to Braginskii's theory [19], considering a hydrogenic and quasi-neutral plasma, is:

$$\eta_\parallel = 0.51 \nu_*' \frac{m_e}{m_i} \frac{log\Lambda_C}{log\Lambda_C^*} T_e^{-3/2} \tag{2.84}$$

where $\frac{log\Lambda_C}{log\Lambda_C^\star}$ is the normalised Coulomb logarithm. We notice in particular the typical dependence of resistivity on $T_0^{-3/2}$. An edge plasma characterized by the parameters mentioned before, and by a density of around $4 \cdot 10^{18}\ m^{-3}$, would lead to a dimensionless resistivity of about $0.5 \cdot 10^{-5}$, slightly lower then the one usually imposed in simulations. Finally, the TOKAM3X user can choose the amplitude of the particle source forcing the system. The particle source S_N is located at the inner boundary of the domain, in the closed flux surfaces region. It is poloidally and toroidally constant, and it has a Gaussian shape in the radial direction:

$$S_N(\psi) = S_N^0 \exp\left(-\frac{(\psi - \psi_0)^2}{\Delta\psi}\right) \tag{2.85}$$

where ψ_0 is the innermost flux surface in the domain, and $\Delta\psi$ is a parameter chosen such that the half width of the Gaussian corresponds to 2 grid points. The source function falls thus very rapidly in the radial direction, so that in the rest of the domain the density profiles are not affected by the source shape.

2.7.2 Set-up of the reference simulations

In this thesis, we will present the results of several different TOKAM3X simulations, carried out with different magnetic geometries. We choose three cases which will be referred to as reference simulations, since they have been subject of the most extensive analyses. One of the reference simulations is carried in limiter geometry, with an infinitely thin toroidal limiter. In divertor simulations, we build the mesh grids starting from a COMPASS magnetic equilibrium, and from a JET magnetic equilibrium: in this way we can verify that the observations on simulation results in one divertor geometry are not restricted only to that particular case. Figure 2.10 shows the mesh grids used in these simulations.

In all the reference simulations the minor radius a is set to 256 ρ_L. This is an important quantity, as it sets the ratio between the size of the simulated domain and ρ_L, the reference length scale for the description of turbulence. Another free geometrical parameter is the aspect ratio $A \equiv R_0/a$, which can vary from one case to another.
In the three reference cases, the toroidal magnetic field is imposed to be equal to B_0 at the magnetic axis. However, the poloidal field changes among the different configurations, and therefore also the safety factor profile, which is calculated with (2.74) and represented in figure 2.11.

One can notice in figure 2.11 the singularity of the safety factor at the separatrix in divertor geometry. In the open field lines region, the safety factor is not well-defined, since magnetic field lines close into the wall outside the simulated domain. Hence, only the main SOL region is retained in the calculation of q.
Table 2.1 resumes the geometrical, physical and numerical parameters of the reference simulations:

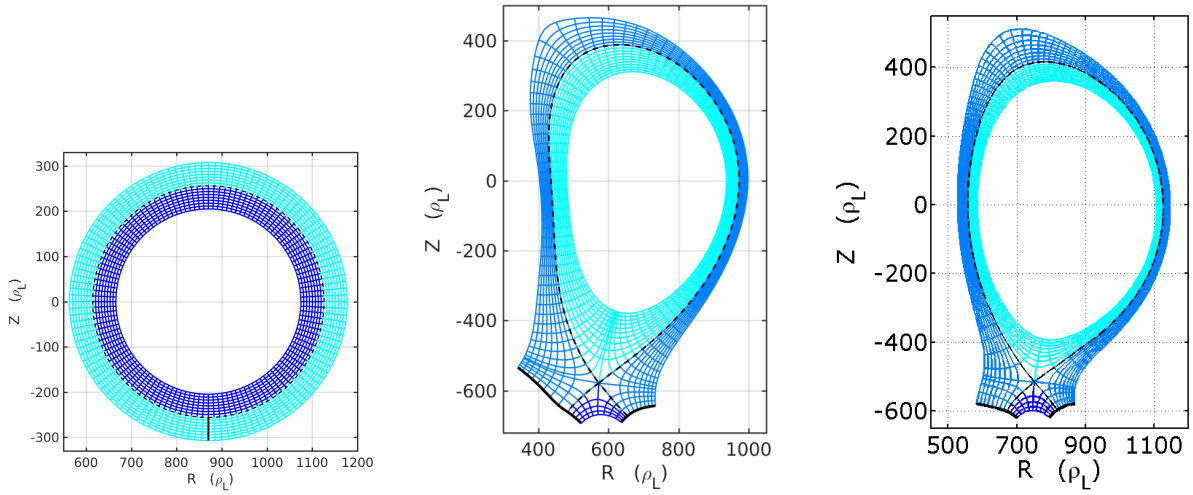

Figure 2.10: *Poloidal section of the mesh grid used for limiter (left), diverted COMPASS-like (centre) and diverted JET-like (right) simulations. The represented mesh grid is coarser by a factor 4 with respect to the actual one, in order to increase the visibility.*

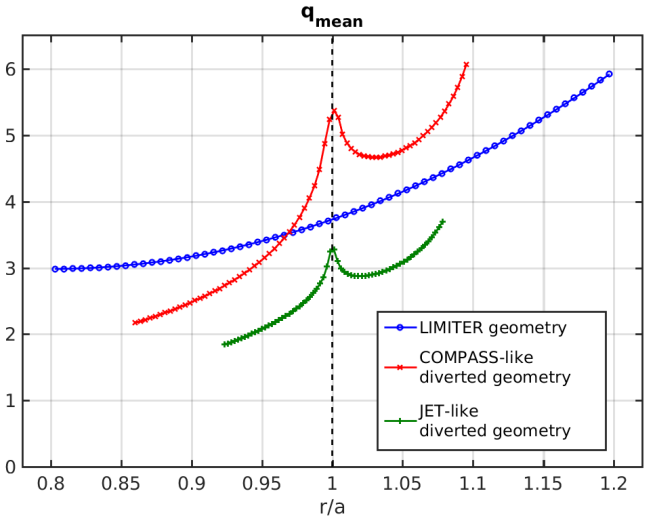

Figure 2.11: *Radial profile of the safety factor in the reference simulations, remapped at the LFS midplane. The dashed line represents the separatrix position.*

Geometry	Limiter	Diverted COMPASS-like	Diverted JET-like
A	3.4	2.8	3.4
$\rho^\star = \rho_L/a$	$1/256$	$1/256$	$1/256$
L_φ	$\pi/2$	$\pi/2$	$\pi/2$
$\eta_\parallel(B_0/en_0)$	10^{-5}	10^{-5}	10^{-5}
D_N , D_Γ , $D_W(\rho_L^2\omega_C)$	$5\cdot10^{-3}$	$5\cdot10^{-3}$	$5\cdot10^{-3}$
$S_N^0(\rho_L^{-3}\omega_C)$	$4\cdot10^{-3}$	$4\cdot10^{-3}$	$4\cdot10^{-3}$
N_ψ (edge)	32	40	32
N_θ (edge)	512	350	512
N_ψ (SOL)	32	40	32
N_θ (SOL)	512	350	512
N_ψ (divertor leg)		32	32
N_θ (divertor leg)		16	16
N_ψ (PFR)		9	16
N_θ (PFR)		16	16
N_φ	32	32	32

Table 2.1: *Table of the reference simulations with associated parameters.*

2.8 TOKAM3X model and boundary conditions recap

The TOKAM3X model used in this thesis:

Particle balance equation :

$$\partial_t N + \vec{\nabla}\cdot\left((\Gamma - J_\parallel)\vec{b}\right) + \vec{\nabla}\cdot(N\vec{u}_E) + \vec{\nabla}\cdot(N\vec{u}^e_{\nabla B}) = \vec{\nabla}\cdot\left(D_N\vec{\nabla}_\perp N\right) + S_N$$

Parallel momentum balance equation :

$$\partial_t \Gamma + \vec{\nabla}\cdot\left(\frac{\Gamma^2}{N}\vec{b}\right) + \vec{\nabla}\cdot(\Gamma\vec{u}_E) + \vec{\nabla}\cdot\left(\Gamma\vec{u}^i_{\nabla B}\right) = -2\nabla_\parallel N + \vec{\nabla}\cdot\left(D_\Gamma\vec{\nabla}_\perp\Gamma\right)$$

Charge balance equation :

$$\begin{aligned}\partial_t W + \vec{\nabla}\cdot\left(\frac{W\Gamma}{N}\vec{b}\right) &+ \vec{\nabla}\cdot(W\vec{u}_E) + \vec{\nabla}\cdot\left(W\vec{u}^i_{\nabla B}\right)\\ &= \vec{\nabla}\cdot\left(J_\parallel\vec{b}\right) + \vec{\nabla}\cdot\left(N(\vec{u}^i_{\nabla B} - \vec{u}^i_{\nabla B})\right) + \vec{\nabla}\cdot\left(D_W\vec{\nabla}_\perp W\right)\end{aligned}$$

Parallel Ohm's law :

$$\eta_\parallel N J_\parallel = -N\nabla_\parallel\phi + \nabla_\parallel N$$

Vorticity definition :

$$W = \vec{\nabla}\cdot\left(\frac{1}{B^2}\vec{\nabla}_\perp\phi + \frac{\vec{\nabla}_\perp N}{NB^2}\right)$$

Drift velocities :

$$\vec{u}_E = \frac{\vec{B}\times\vec{\nabla}\Phi}{B^2} \quad , \quad \vec{u}^i_{\nabla B} = 2\frac{\vec{B}\times\vec{\nabla}B}{B^3} \quad , \quad \vec{u}^e_{\nabla B} = -2\frac{\vec{B}\times\vec{\nabla}B}{B^3}$$

Boundary Conditions:

	Density	Parallel Momentum	Electric Potential	Vorticity
Radial inner boundary (edge)	$\partial_\psi N = 0$ $N u^\psi = 0$	$\partial_\psi \Gamma = 0$ $\Gamma u^\psi = 0$	$\partial_\psi \Phi = 0$	$\partial_\psi W = 0$ $W u^\psi = 0$
Radial outer boundary (SOL)	$\partial_\psi N = 0$	$\partial_\psi \Gamma = 0$	$\partial_\psi \Phi = 0$	$\partial_\psi W = 0$
Radial inner boundary (PFR)	$\partial_\psi N = 0$	$\partial_\psi \Gamma = 0$	$\partial_\psi \Phi = 0$	$\partial_\psi W = 0$
Target plates	$\partial_\theta^2 N = 0$	$\lvert\Gamma\rvert \geq \sqrt{2} N$	$\nabla_\parallel \Phi = \nabla_\parallel log(N)$ $\pm \eta_\parallel N \sqrt{2} \left(\Phi - \Lambda\right)$	$\partial_\theta^2 W = 0$

Chapter 3

Turbulence local properties in TOKAM3X simulations with divertor configuration

Contents

Turbulence local properties are investigated in simulations with X-point geometry, and compared with the ones in limiter configuration. The 3D shape of turbulent structures is discussed, underlining the role of the flux expansion and its impact on transverse fluxes. We evaluate the spatial distribution of the fluctuations amplitude, with particular focus on the divertor region, and we highlight the effect of the X-point on turbulent structures.
Part of the topics treated in this chapter are included in the publication [73].

Turbulent transport in the edge plasma is governed by the competing actions of perpendicular and parallel transport. Local properties of edge turbulence can thus be affected by the shape of the magnetic field lines. The divertor geometry has several peculiarities with respect to the limiter one, which could influence the turbulent structures properties, shape and propagation. In particular, the X-point introduces a zone of low poloidal field, and theoretically infinite field line length, possibly altering turbulence.
The flute assumption, widely adopted in the 2D transport codes such as, for example, TOKAM2D [34] and HESEL [35], reduces the problem by one dimension, averaging the parallel dynamics over the field line. The TOKAM3X code allows to study the problem of the filament dynamics in a generalised geometry, including the divertor configuration [33], simulating both open and closed flux surfaces in a global approach. We aim here at understanding the effect of complex geometry on turbulence local properties.
Since TOKAM3X adopts a flux-driven approach, it does not assume any scale separation assumption in theory. In practice, the smallest resolved space and time scales are set by

the grid and by the time step, respectively. Here and in the following, we will often separate a posteriori the *average* and the *fluctuating* components of a field. For the generic field X, we define the fluctuating component as:

$$\tilde{X}(t,\psi,\theta,\varphi) = X(t,\psi,\theta,\varphi) - \langle X(t,\psi,\theta,\varphi)\rangle_{t,\varphi} \tag{3.1}$$

Since our system is axisymmetric, it is invariant in the toroidal direction. Moreover, we usually analyse the turbulence properties when a pseudo-steady state is reached, so when the system oscillates around an equilibrium state. Therefore, the average component $\langle X\rangle_{t,\varphi}$ can be seen as the behaviour of the background plasma, which is roughly constant in time and in the toroidal direction. In this section, we will focus on the fluctuating part of the fields. The background equilibrium, its origin and characteristics, will be treated in Chapter 5, and they are strictly related to turbulence itself.

3.1 Driving instability and statistical properties

3.1.1 Dominant instability mechanism

As described in section 2.3, different types of instabilities can develop in our simulations, so it is useful to understand which is the dominant instability mechanism. We show in figure 3.1 an example of a map of density fluctuations in limiter and divertor geometries.

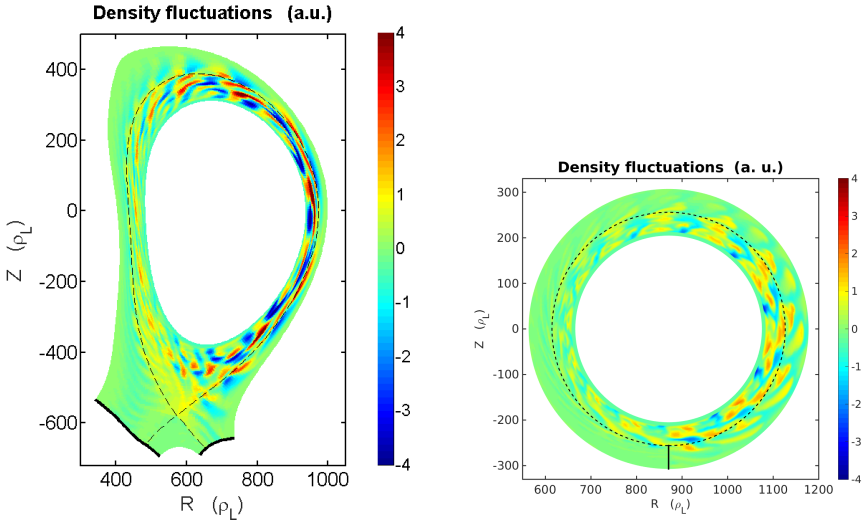

Figure 3.1: *Snapshot of density fluctuations amplitude in divertor (left) and limiter (right) at fixed timestep and totoidal position. Simulations were run with similar parameters, listed in table 2.1, except for the safety factor profile.*

In both divertor and limiter configurations, turbulence is found to develop at the LFS midplane, in the closed flux surface region. Turbulent structures spread then almost instantaneously along the parallel direction, and propagate then in poloidal and radial

directions, reaching ultimately the SOL. As visible in figure 3.1, in COMPASS-like simulations, with the set of parameters that we used, the extension of turbulent structures in the poloidal direction usually ranges between $10 - 100\ \rho_L$ at the LFS midplane, and it is poloidally variable. Turbulent modes must be compatible with the fact that we are simulating a toroidal sector of the tokamak of $\pi/2$, so the toroidal mode number n must be a multiple of 4. We find in our simulations that mode numbers $m(\psi) \simeq 8\ q(\psi)$ and $m(\psi) \simeq 12\ q(\psi)$ are usually dominant.
The size of the turbulent structures in the poloidal plane is typical of RBM turbulence. Resistive Drift Waves (RDW) linear growth rates, instead, could be dominant in case of perpendicular wavenumbers close to $1\ \rho_L^{-1}$. This has been reported by the linear analysis of physical systems similar to the one solved by TOKAM3X [74], and by non-linear simulations [75], where both RBM and RDW may appear. RDW fluctuations, whose size in perpendicular direction should be small if compared to RBM, are not observed in our simulations.
Since we usually study turbulence properties when the turbulent regime is quasi-static and fully developed, a criterion based on the linear growth rate could be insufficient to evaluate the difference between RBM and RDW [76]. An alternative way to distinguish RBMs from RDW is to calculate the phase among density and potential structures. In fact, interchange turbulence has a typical phase shift of around $\pi/2$, while the resistive drift waves are characterized by shifts close to 0. We calculate the cosine of the phase shift as:

$$cos(\delta)(\psi, \varphi, t) = \frac{\left\langle \tilde{N}\tilde{\Phi} \right\rangle_\theta}{\sqrt{\left\langle \tilde{N}^2 \right\rangle_\theta \left\langle \tilde{\Phi}^2 \right\rangle_\theta}} \tag{3.2}$$

which is a global estimation of the phase, which takes into account all the possible modes. Figure 3.2 shows the cosine of the phase shift, in function of time and toroidal direction.

As one can notice from figure 3.2, the phase is almost constant in the toroidal direction, indicating quasi-field aligned turbulent structures, and evolves in time. The phase shift is roughly included in the range $0.3\pi < \delta < 0.7\pi$, and the average phase $\langle\delta\rangle_{t,\varphi} \simeq 1.54$, which is actually almost coincident with $\pi/2$. These elements are a signature of the interchange turbulence, and they are in line with the theoretical expectations detailed in the work by B. Scott [76].
The Kelvin-Helmoltz instability can also possibly develop. However, in reference divertor simulations, the radial gradient of the parallel Mach number is usually low if compared to the density radial gradient in almost all the simulated domain. Even if turbulence could change locally this property, on average the criterion for the development of this kind of instability (2.49) is not fulfilled in divertor configuration, so we do not expect the Kelvin-Helmoltz instability to intervene.
Although the main transport mechanism at play in limiter simulations is the interchange turbulence, the Kelvin-Helmholtz (KH) instability cannot be excluded. As one can see from figure 3.1 indeed, there is an up-down asymmetry in the turbulence intensity, which is higher at the bottom. In this region, both on the HFS and on the LFS of the lim-

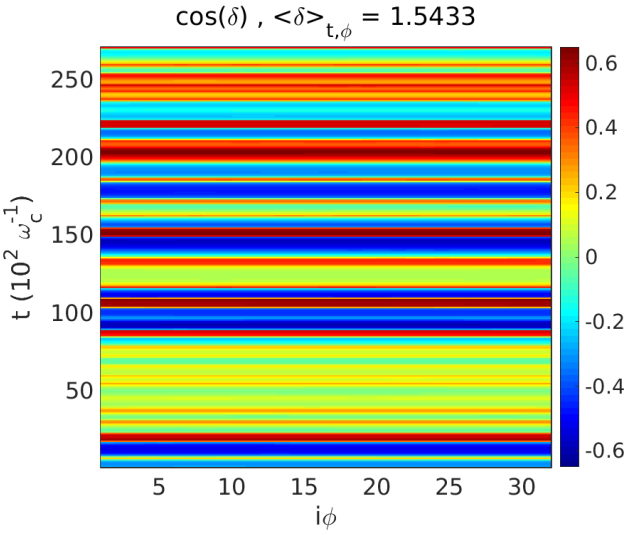

Figure 3.2: *Cosine of the phase between density and potential fluctuations in poloidal direction, averaged on k_θ spectrum and referred to a flux surface at $r/a \sim 0.95$, in a COMPASS-like configuration. On the abscissa, the toroidal coordinate, on the ordinate, the time.*

iter, the linear growth rate for the interchange instability γ is proportional to $\sqrt{\vec{\nabla}B \cdot \vec{\nabla}p}$ and so $\gamma \simeq 0$. The criterion for the development of the KH instability (2.49) is instead respected. Indeed, in the closed field lines region, the parallel Mach number is close to 0 and the density is almost uniform on the flux surface. Instead, in the vicinity of the limiter, the parallel Mach number approaches the unity value because of the Bohm condition, while density drops only by a factor two with respect to the LFS midplane. The KH instability thus develops across the separatrix, in the vicinity of the limiter position, in the case of infinitely thin limiter.

3.1.2 Radial variation in statistical distribution of fluctuations

Edge turbulence is further characterised by evaluating its statistical moments, which provide important information on turbulence nature. This analysis is useful since there is a widespread knowledge on the statistical properties for turbulence in the edge region, that makes possible a comparison with experimental data, usually inferred from Langmuir Probes in the SOL [77].
We focus now on density fluctuations, and we sample their amplitude in time and toroidal direction, for a given point in the poloidal section. Figure 3.3 shows the Probability Distribution Functions (PDFs) of the density fluctuations at different radial positions in the divertor and limiter reference cases, at the LFS midplane.

We can notice from figure 3.3 that, naming σ the standard deviation, fluctuation levels are essentially included within a range of $-2\,\sigma$ to $3\,\sigma$ for the considered positions, in both divertor and limiter cases, with isolated events which can exceed these values. In both

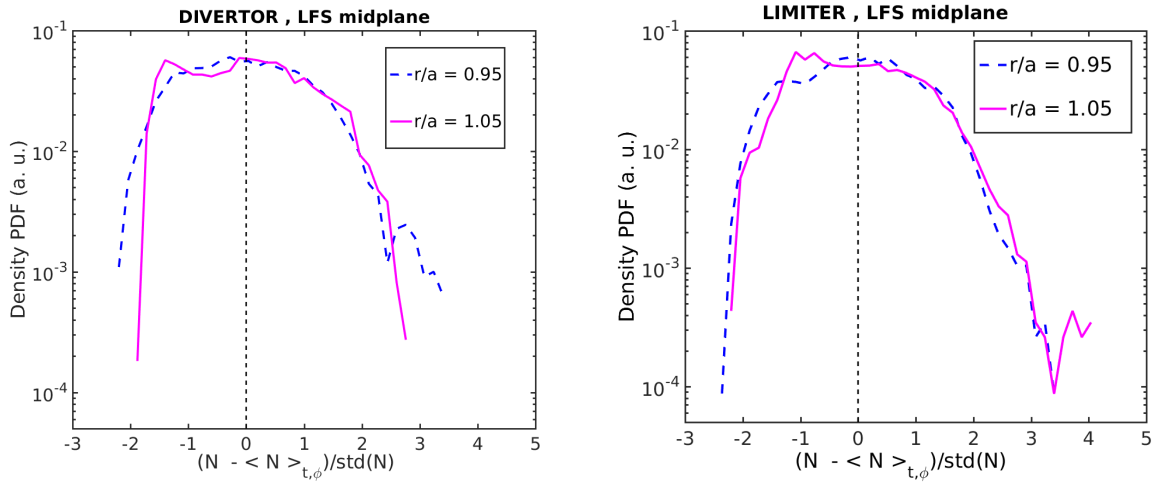

Figure 3.3: *PDF of density fluctuations in divertor (left) and limiter (right) geometries, calculated at different radial locations on the LFS midplane. PDFs are normalised on the number of points in toroidal and time directions.*

cases, PDFs present a shape close to Gaussian in the closed flux surfaces region, meaning a symmetry in negative and positive amplitude events probability. Instead, in the SOL, PDFs present an asymmetric character, with the presence of isolated, large amplitude positive fluctuations and more frequent low-amplitude negative fluctuations. The intermittent character of edge turbulence is a universal feature in tokamaks. These elements were already highlighted in TOKAM3X limiter simulations in [78]. Here we show, by the comparing two simulations with similar parameters, that the divertor geometry does not affect significantly the turbulence statistical properties, at least for radial positions far from the separatrix. The major difference between limiter and divertor cases occurs in the vicinity of the separatrix, and in particular up to $r/a \sim 1.03$ outside the separatrix. Here the PDF in the divertor case seems to be strongly affected by the presence of a transport barrier, whose effect will be better characterised in Chapter 5. The asymmetry in the PDFs of the density fluctuations can be quantified by the skewness, defined as:

$$\mathcal{S} \equiv \left\langle \left(N - \langle N \rangle_{t,\varphi}\right)^3 \right\rangle_{t,\varphi} \Big/ \left\langle \left(N - \langle N \rangle_{t,\varphi}\right)^2 \right\rangle_{t,\varphi}^{3/2} \tag{3.3}$$

Figure 3.4 shows a comparison of the radial profile of $\mathcal{S}$ at the LFS midplane in the divertor COMPASS-like and in limiter geometries.

The two skewness profiles show a similar trend in limiter and in divertor geometry. We find in particular that the skewness $\mathcal{S}$ is negative in the flux surfaces further from the separatrix in the closed field lines region and it increases radially crossing the 0 value before the separatrix. In limiter configuration, skewness remains positive, and generally increases also in the SOL. This corresponds well with what has been observed previously in TOKAM3X limiter simulations [78], but also in TOKAM2D simulations [34]. In divertor simulations, the turbulence properties seem to be perturbed in the vicinity of the separatrix, where skewness drops even to negative values, before to start again to

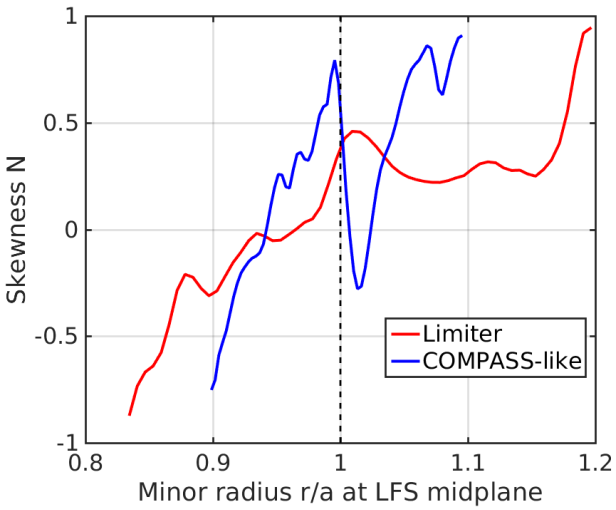

Figure 3.4: *Density fluctuations skewness radial profile at the LFS midplane, comparison between the limiter and COMPASS-like divertor geometry. The leftmost points, located in the buffer region, have been excluded from the plot.*

increase at $r/a \simeq 1.05$. However, at the LFS midplane, skewness increases in radial direction in the SOL. This trend corresponds well to experiments on AUG [77].

3.1.3 Poloidal variation in statistical distribution of fluctuations

It is worth to study the change of the PDFs with the poloidal position. Figure 3.5 shows the PDFs for density fluctuations at different poloidal positions.

Simulations show little variability in the density fluctuations PDF along the poloidal direction, both in limiter and in divertor geometry, as shown in figure 3.5 (top and bottom). Nevertheless, as shown in the centre panel of figure 3.5, in the region next to the X-point, PDFs appear to be perturbed, showing in particular a low skewness both in closed and open flux surfaces.
In the work by P. Tamain et al. [78], a study on turbulence in limiter TOKAM3X simulations had shown a positive skewness in a poloidal sector of 120° centred on the LFS midplane, in the closed flux surface region, showing a significant poloidal asymmetry in the PDFs. The discrepancy between the new simulations and the results shown in [78] are not straightforwardly explainable. However, in the new release of the code, differently from the one used in [78], the ion pressure is included in the vorticity definition (2.40). This change has provoked the build-up of steeper potential gradients in the closed flux surface region. The $E \times B$ poloidal velocity is thus stronger in new simulations, and tends to advect turbulent structures all around the poloidal length, leading probably to similar turbulence characteristics.
Globally, fluctuations statistical properties in divertor configuration are similar to what was previously found in limiter simulations. However, peculiar features of the divertor, such as the presence of the X-point locally modifies turbulence properties, generally

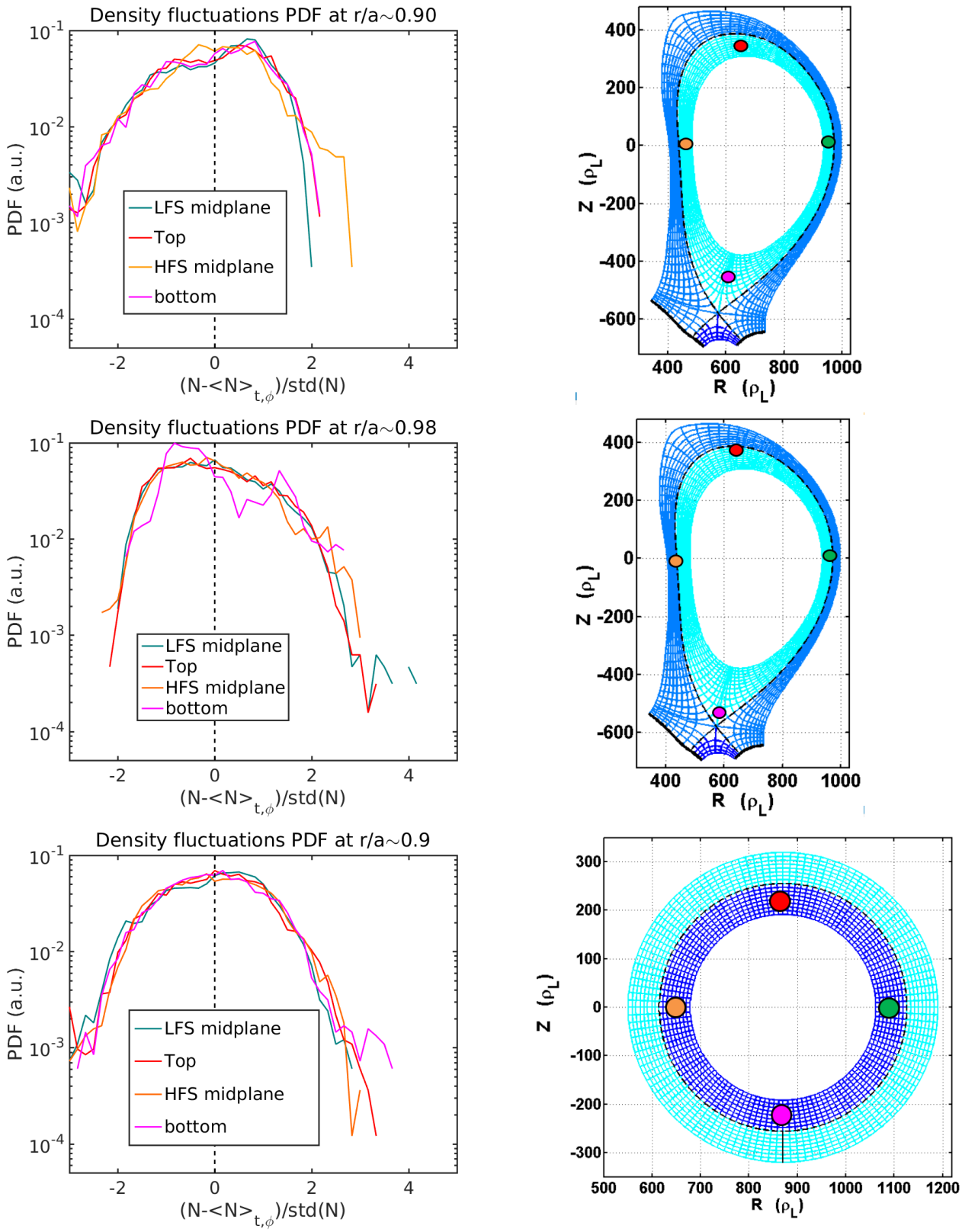

Figure 3.5: *Top: Density fluctuations PDF calculated at 4 different poloidal positions in COMPASS-like diverted geometry, on the flux surface corresponding to $r \simeq 0.9\ a$. Centre: Density fluctuations PDF calculated at 4 different poloidal positions, on the flux surface corresponding to $r \simeq 0.98\ a$. Bottom: PDF calculated at 5 different poloidal positions in a limiter geometry, on the flux surface corresponding to $r \simeq 0.9\ a$.*

lowering the probability of low-amplitude events.

3.2 3D shape of turbulent structures

3.2.1 Parallel extension

Turbulent structures are continuously evolving, both in amplitude, position and velocity, and in local shape. Let's focus now on the shape of turbulent structures.
Three-dimensional turbulence codes as TOKAM3X are built in order to drop the flute assumption, so that the described turbulence structures actually have a 3-D shape. We can evaluate the efficiency of the parallel transport with respect to the perpendicular one by calculating the auto-correlation parallel length for a typical turbulent structure at a certain time. We plot in figure 3.6 the parallel auto-correlation length for the density fluctuations in a COMPASS-like diverted geometry.

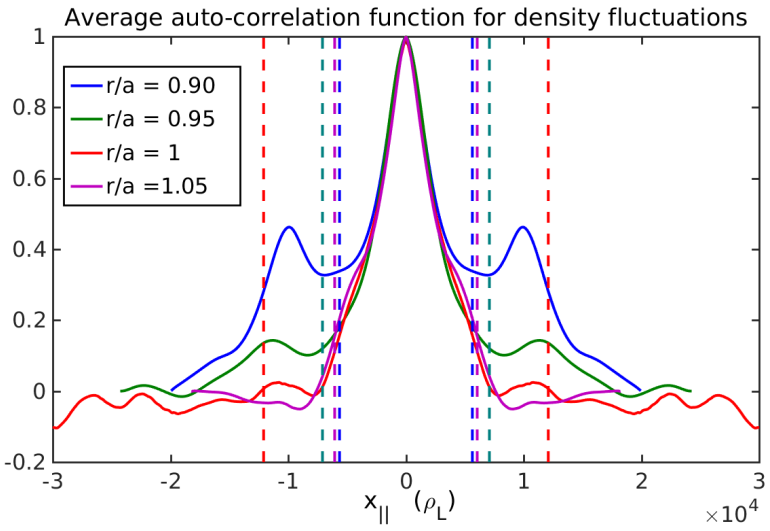

Figure 3.6: *Auto-correlation length in parallel direction of density fluctuations, calculated at different radial positions, and averaged on time, in the COMPASS-like divertor simulation. Dotted vertical lines are plotted at the parallel length corresponding roughly to half of a poloidal turn, namely to* $L_{\parallel} = \pi q(r) R_0$*, at the radial position identified by the same colour.*

In this particular case, one can see that the auto-correlation length in the parallel direction is of the order of $10^4 \rho_L$. The actual value that can be retained for the parallel correlation length is the one corresponding to the first local minimum in the auto-correlation function. As expected, this value largely exceeds the size in the poloidal direction at the LFS midplane of the same structure, which is of the order of $10 - 100$ ρ_L, confirming the efficiency of parallel transport with respect to the perpendicular one. As highlighted in figure 3.6, the typical parallel correlation length corresponds roughly to the distance spanned in a poloidal half-turn. This can be readily explained considering the ballooning

nature of interchange turbulence, since the instability linear growth rate ($\propto \sqrt{\vec{\nabla}B \cdot \vec{\nabla}p}$) is maximum at the LFS midplane, and varies with an approximately cosine shape in the poloidal direction. The autocorrelation length increases progressively going radially outwards, following the increasing of the safety factor q, i.e. the parallel length associated to a poloidal turn. This fact is coherent with previous TOKAM3X limiter simulations, which where analysed in [79]. The parallel auto-correlation function shows a constant broadness, and the position of the first local minimum varies slightly, following the elongation of the magnetic field length. Only in the first open flux surfaces, the X-point seems to limit the coherence of fluctuations, leading to a lower auto-correlation length than expected. Further out in the SOL, elevated fluctuation levels can be registered in the vicinity of the target, so the extension of the correlation length is similar to the total connection length.
Electric potential fluctuations are found to behave qualitatively in the same way. However, a longer auto-correlation length is typically observed, with a lower asymmetry between LFS and HFS. This analysis confirms the 3D shape of the fluctuations, which are slightly misaligned with respect to magnetic field lines, and determine thus the poloidal asymmetry of turbulent transport.

3.2.2 Shape in the poloidal plane

We focus now on the deformation of the turbulent structures in the poloidal plane. One of the first noticeable features of turbulent structures in divertor configuration is their deformation along a flux surface. Figure 3.7 shows an example of the poloidal profile of the fluctuation in the density logarithm.

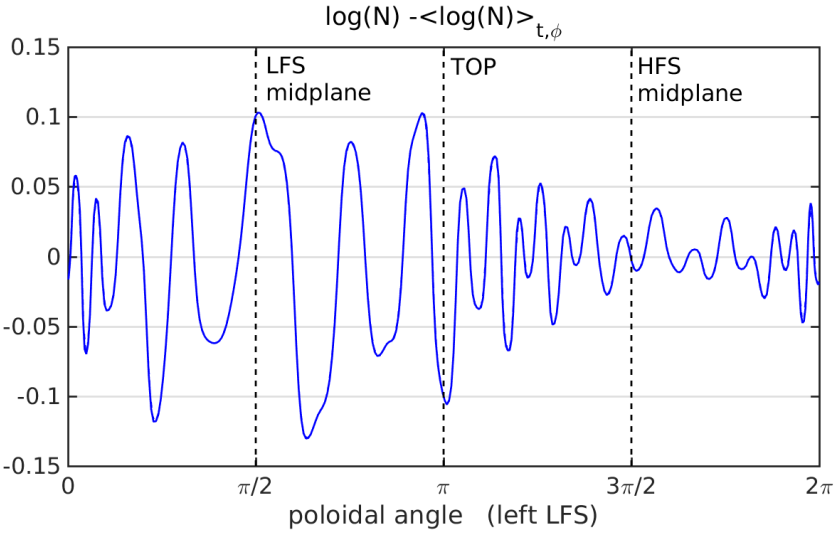

Figure 3.7: *Poloidal profile of the fluctuating part of the density logarithm, for a flux surface radially located at the middle of the edge region ($r/a \simeq 0.95$) at a specific time step and toroidal position, in the reference COMPASS-like diverted simulation. The origin of the abscissa corresponds to the bottom, so in this case the poloidally closest position to the X-point.*

One can notice that the size of the structures in poloidal direction is generally bigger at the LFS midplane, while filaments shrink in poloidal direction when approaching the X-point.
In order to explain this behaviour of the structures, we have to consider that turbulence, as shown in section 3.2.1, is strongly aligned on the magnetic field, with $k_{\parallel} \ll k_{\theta}$. As a first order approximation, we can consider the local fluctuation amplitude as constant over a flux tube. The admissible solution for a field-aligned fluctuation in a toroidal geometry, with an helical shape of magnetic field lines, can be derived analytically (see for example [60]) and reproduced numerically [80]. This problem has extensively been studied principally in the framework of gyrokinetic simulations: the shape of field-aligned turbulent structures in the poloidal section does not depend on the specific type of instability among the interchange mechanisms, so that these analyses can be extended to the edge turbulence. Here we will focus on two elements that appear considering the shape of a flux tube in a generalized axisymmetric geometry, and in particular the flux expansion and the finite aspect ratio effects, which are usually not taken into account in analytical calculations. We do not adopt an analytical approach, but instead we investigate the shape of filaments analysing simulation results. We must recall here the definition of a flux tube:

$$\frac{\partial}{\partial x_{\parallel}}(\vec{B} \cdot d\vec{S}) = 0 \tag{3.4}$$

Where $x_{\parallel}$ is the parallel coordinate along the field line. Our coordinate system is flux surface aligned, as explained in Chapter 2. This means that the actual value of the poloidal flux function is constant along our ψ coordinate, designating a flux surface. By consequence, the distance between flux surfaces represents the radial extension in the physical space of a flux tube. Taking the LFS midplane as reference position, we can define the flux expansion as:

$$f_x(\psi, \theta) = \frac{\|\vec{\nabla}\psi_{mp}(\psi)\|}{\|\vec{\nabla}\psi(\psi, \theta)\|} \tag{3.5}$$

where the subscript mp indicates that the quantity is calculated at the LFS midplane. Because of the null divergence of the magnetic field $\vec{B}$, the cross-section S of the flux tube is conserved along the parallel direction. In order for the total volume of a turbulent structure to be conserved, so, the extension of the fluctuation in the so-called binormal direction must be inversely proportional to the flux expansion. It is therefore logical to expect the wave number in the binormal direction to change according to the poloidal location, and in particular to be proportional to the local flux expansion (the poloidal direction will be here and in the following analysis used instead of the binormal direction, relying on the small amplitude of the poloidal field with respect to the toroidal one). Moreover, from the flux tube definition, we know that its cross-section is inversely proportional to the magnitude of the magnetic field. We must apply so a further correction to the expected value of the wave number in the binormal direction, which will be also proportional to the magnetic field amplitude. Considering the inverse proportionality of

the total magnetic field on the major radius, we expect:

$$k_\theta(\psi,\theta) = k_\theta^{mp}(\psi)\frac{f_x(\psi,\theta)R^{mp}(\psi,\theta)}{R(\psi,\theta)} \tag{3.6}$$

This variation in the poloidal wave number has already been analysed theoretically ([81]), basing on an analytical description of the magnetic field in the vicinity of the X-point, and reproduced numerically (see Walkden et al. [82]) using seeded blobs in realistic flux-tube geometries. The magnetic shear represents a further mechanism which can locally deform a turbulent structure, as well described in [83] and [84]. Also in the case where the magnetic shear is considered, the total cross-section of a turbulent structure is conserved, in absence of dissipative mechanisms. Figure 3.8 shows a sketch of the blobs deformation caused by the flux expansion.

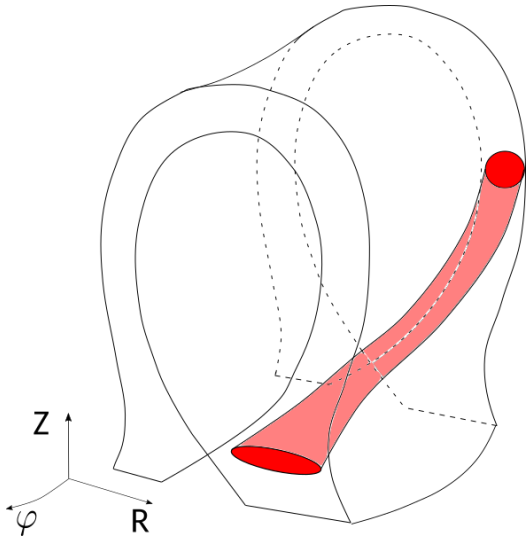

Figure 3.8: *Sketch of the deformation of a turbulent structure aligned to the magnetic field.*

We analyse now the shape of a turbulent structure in a COMPASS-like simulation on a single flux surface, excluding the effect of magnetic shear. In particular, on the poloidal profile of the density fluctuation shown in figure 3.2.1, referred to a flux surface located at $r/a \simeq 0.95$, we locate the maxima and the minima, and from their distance in the poloidal direction we infer the poloidal wave number, using the expression:

$$k_\theta^{TK3X} = \frac{2\pi}{2\left(\theta^{max} - \theta^{min}\right)} \tag{3.7}$$

where θ here is the curvilinear coordinate in the poloidal direction, and the superscripts max and min indicate two consecutive local maximum and minimum values. The specific time step and toroidal position have been chosen such that one single mode is dominant over the others: this prevents the superposing of different modes, which could appear as a single mode of lower k_θ, or as multiple modes with higher k_θ. In figure 3.9 we show the

comparison between the local value of the poloidal wavenumber calculated according to 3.7, and the theoretical prediction 3.6 based on geometrical considerations.

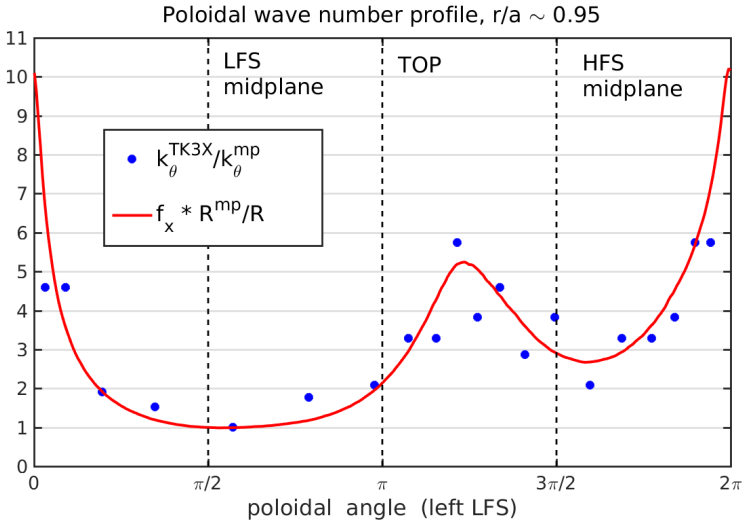

Figure 3.9: *Poloidal profile of the calculated local poloidal wave number, normalised to the LFS midplane value (localised at $\pi/2$), in the reference COMPASS-like diverted simulation. This profile is compared with the one theoretically predicted.*

One can notice that the prediction coincides very well with the code results. This has been verified for various radial positions and for different magnetic configurations used in the simulations, always showing a very good agreement among prediction and values calculated by the code. The peak values for the poloidal wave number can be found in the positions where the flux expansion is stronger. In this particular case, the peak placed between π and $3\pi/2$ represents the top of the machine, where the flux surfaces get significantly expanded. The peaks at the bottom correspond to the point poloidally closer to the X-point. We can see that here the effect of the flux expansion is extreme, and structures get very elongated, and thin in the poloidal direction. Here we see an amplification of more than a factor 5 at the X-point with respect to the LFS midplane. In our case, in the vicinity of the X-point, structures get extremely thin in the poloidal direction, almost reaching the typical size of the mesh. Therefore, it is critical in 3-D turbulence codes to have a sufficiently refined mesh resolution in poloidal direction around the X-point. Ideally the poloidal grid resolution should follow the k_θ dependence shown in (3.6).
This analysis shows also that, once that the value of the local wave number of a specific mode is determined at one poloidal position, then it is possible to approximately calculate it on the whole poloidal direction with a simple transformation.
In the case of a limiter configuration, with circular flux surfaces, no flux expansion is at play, so the variation of the poloidal local wave number on a flux surface is only determined by the magnetic field strength. Therefore, k_θ is approximately proportional to the inverse of the major radius, as shown in figure 3.10: this is a “finite aspect ratio" effect.

As visible in figure 3.10, it is not easy to observe the finite aspect ratio effect in this

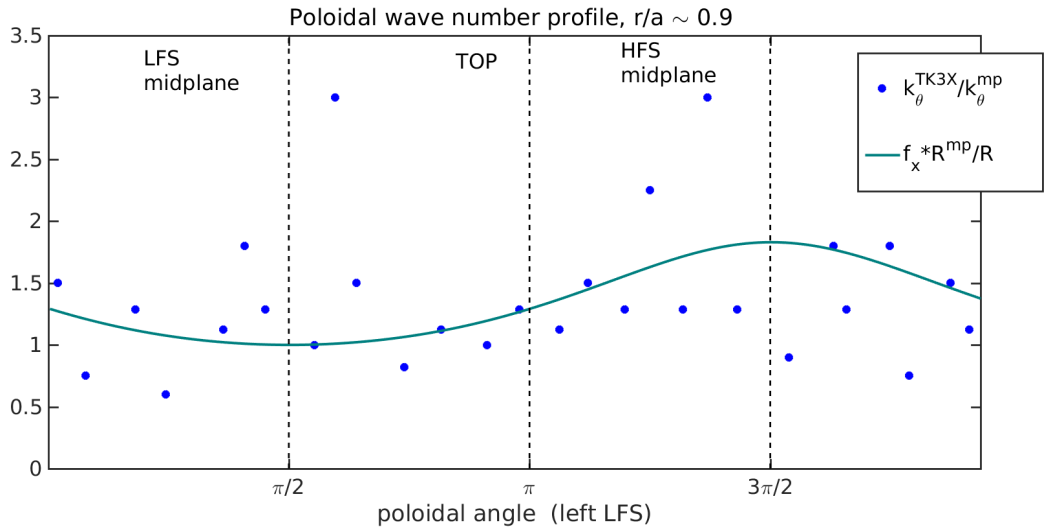

Figure 3.10: *Poloidal profile of the calculated local poloidal wave number, normalized to the LFS midplane value (localized at $\pi/2$), for a flux surface at $r/a \simeq 0.95$ in the reference limiter simulation, compared with the theoretical prediction.*

case, even if one can have a glimpse of it from the proposed analysis. Indeed, especially at the HFS, when structures are characterised by long parallel connection length, they superimpose in the poloidal plane, forming a complex pattern with constructive and destructive interference [80].
An important consequence of this geometrical feature related to the flux expansion is the poloidal wave number spectra analysis. This is a usual practice in order to study the turbulence properties. When performing a Fourier analysis on the modes on a certain flux surface, we understand now that the poloidal curvilinear coordinate must be scaled according to the factor appearing in (3.6). The shape of the spectra are found to be very sensitive to this feature. If the Fourier analysis of the modes was done in the curvilinear poloidal coordinate, artificial modes would appear, which in turn are only a local deformation of the same turbulent structures.

3.2.3 Flux expansion effect on transverse fluxes

An immediate consequence of the variable shape of the structures along the poloidal direction, is the spatial variation of the $E \times B$ fluxes in the radial direction. Indeed, we can write the $E \times B$ velocity in the ψ direction, associated to a particular mode k_θ as:

$$u_E^\psi \simeq -\frac{k_\theta \Phi}{B} \tag{3.8}$$

Recalling (3.6) and focusing on the magnitude of radial velocities, this gives:

$$\left| u_E^\psi \right| \simeq f_x k_\theta^{mp} \Phi \tag{3.9}$$

Equation (3.9) tells us that the velocity in the ψ direction varies locally according to the flux expansion. This result could seem trivial, but it leads to a couple of important reflections. First of all, for a flux-driven system as the one described by our model, the particle flux in the radial direction is not necessarily proportional to the density gradient, as it could be thought considering a diffusive transport. Rather, the radial flux evaluated in the real space (so in $m^{-2}s^{-1}$) depends on the flux expansion, beyond the fact that it has a poloidal dependence given by ballooning. Figure 3.11a represents the flux amplitude in the physical space (the quantities being expressed in $\rho_L^{-2}\omega_C$).

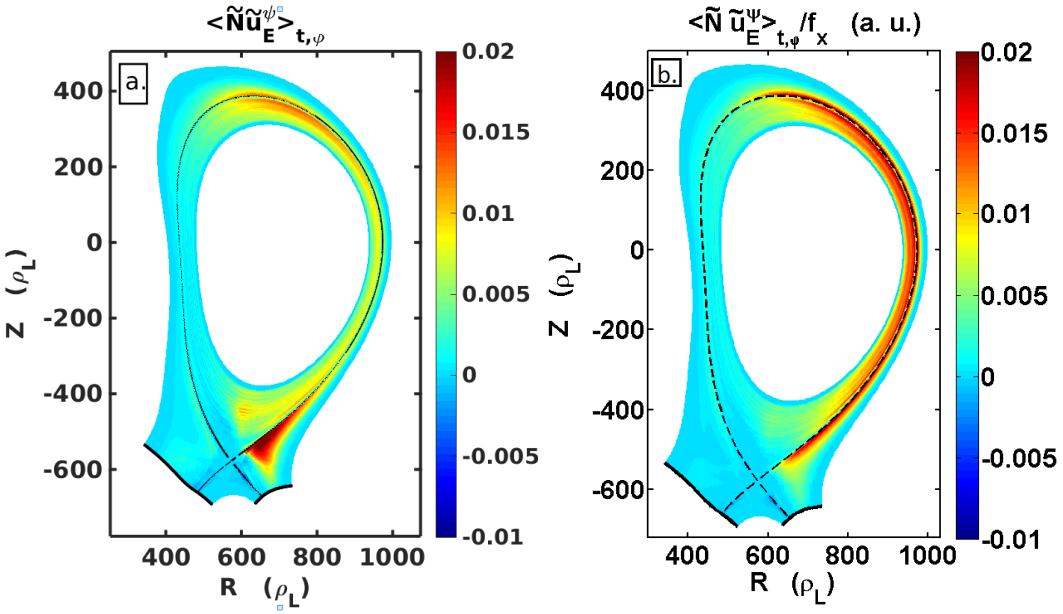

Figure 3.11: *a) 2D map of the $E \times B$ turbulent flux in ψ direction, for a COMPASS-like simulation. b) Turbulent flux normalised by the flux expansion.*

The $E \times B$ turbulent flux in the SOL is peaked in the vicinity of the X-point, where the flux expansion is larger. Also, it is stronger at the top of the machine than at the LFS midplane. When measuring a radial flux so, the latter must always be scaled according to the flux expansion, in order to have a coherent picture of the transport properties. In this case, instead of using definition (3.5) and using the outer midplane as reference position, we normalize the $\vec{\nabla}\psi$ gradient on its average value on the flux surface, in order to conserve the integral value of the flux over the flux surface. We can write so:

$$f_x(\psi,\theta) = \frac{\left\langle \| \vec{\nabla}\psi(\psi,\theta) \| \right\rangle_\theta}{\| \vec{\nabla}\psi(\psi,\theta) \|} \tag{3.10}$$

Therefore, scaling fluxes in the ψ direction by the flux expansion, one can study the transverse fluxes across the flux surfaces, independently from the spacing among each other. In order to evaluate the effectiveness of turbulent transport it is thus interesting to move to a framework independent from simple geometric effects, since, as we have seen, turbulence tends to adapt to the flux tube geometry.

Figure 3.11b shows the turbulent fluxes scaled by the flux expansion. The flux pattern represented in this figure is clearly more similar to the usual picture of the interchange turbulence, showing the classic ballooning at the LFS midplane (see, for example, TOKAM3X simulations in limiter configuration presented in [78]). In this framework indeed, we are independent from the structures transformation described in section 3.2.2, so turbulent fluxes distribution depend only on the amplitude of fluctuations and not on their shape. The distribution of the fluctuation amplitude in the poloidal cross-section, useful to evaluate where the main de-confinement occurs, is detailed in section 3.3.

3.2.4 Discussion on the flux expansion geometrical effect on fluxes

The turbulent particle flux enhancement by the flux expansion detailed in section 3.2.3, consequence of the auto-organization of edge turbulence, could be a useful indication for the improvement of the transverse transport description in 2D transport codes. These codes are nowadays the most widely used tools for the interpretation of the experimental results, and they are also used for the design of specific components of the tokamak, as the divertor and the first wall, of new fusion devices. In this kind of codes, a similar set of fluid equations as in 3D turbulence codes is solved, but a closure is made on transverse transport, adopting a diffusive description. Focusing on the ψ direction, the closure can be expressed as follows:

$$\left\langle \tilde{N}\tilde{u}^{\psi} \right\rangle_t = -D^{\psi}\vec{\nabla}\left\langle N \right\rangle_t \cdot \frac{\vec{e}^{\psi}}{\|\vec{e}^{\psi}\|} \approx -D^{\psi}\partial_{\psi}\left\langle N \right\rangle_t \|\vec{\nabla}\psi\| \tag{3.11}$$

where D^{ψ} is a diffusion coefficient which is usually derived from experimental data, and in particular by an exponential fit of the radial profiles at the LFS midplane. A similar closure is used also for the momentum and energy conservation equations. Here we see that the turbulent flux is described through a diffusive operator. Perpendicular fluxes associated to mean-field drifts can instead be described self-consistently in 2D transport codes (see for example [85], [86], [87], [88]). A spatial dependency can be imposed for the diffusion coefficient, in order to take into account the ballooned nature of turbulent transport, even if in most cases this coefficient is chosen constant in space. Alternatively, or in addition, a pinch velocity can be prescribed ([89]). In an axysimmetric equilibrium, this closure allows a 2D description of the problem, with a simplified description of the transverse transport.
The results detailed in section 3.2.3 show that a correction taking into account the flux expansion effect could improve the diffusive closure approach. Considering the $E \times B$ as the main component of the cross-field flux, the turbulent flux appearing at the Left-Hand side of (3.11) could be expressed as:

$$\left\langle \tilde{N}\tilde{u}^{\psi} \right\rangle_t (\theta,\psi) = \left\langle \tilde{N}\tilde{u}^{\psi} \right\rangle_{t_{|\psi,mp}} f_x(\theta,\psi) f_{ball}(\theta,\psi) \tag{3.12}$$

where f_{ball} is a function which represents the transverse transport ballooning, and whose

integral on a flux surface should be equal to 1 in order to conserve the total flux value. From (3.11) so, an effective diffusion coefficient could be calculated as:

$$\begin{aligned} D_{eff}^{\psi} &= -\frac{\left\langle \tilde{N}\tilde{u}^{\psi} \right\rangle}{\partial_{\psi} \langle N \rangle \, \|\vec{\nabla}\psi\|} \\ &= -\frac{\left\langle \tilde{N}\tilde{u}^{\psi} \right\rangle_{|\psi,mp} f_x f_{ball}}{\partial_{\psi} \langle N \rangle \, \|\vec{\nabla}\psi\|} \\ &= D_{mp}^{\psi} \frac{\partial_{\psi} \langle N \rangle_{|\psi,mp}}{\partial_{\psi} \langle N \rangle} f_x^2 f_{ball} \end{aligned} \tag{3.13}$$

where the t subscript has been dropped. We have to consider that the average density gradient in ψ direction can vary poloidally, especially in the SOL, depending on the parallel equilibrium, so it cannot be determined a priori. However, we remark that, in the case of constant densities over a flux surface, and so also constant $\partial_{\psi} \langle N \rangle$, one would find a diffusion coefficient $D_{eff}^{\psi} \propto f_x^2$. We also notice that the function f_{ball} decays poloidally from the LFS midplane, so in the regions where f_x is elevated, as the X-point and the top of the machine, the two corrections due to the ballooning and to the flux expansion partially compensate.
The correction of the diffusion coefficient given by (3.13) could strongly perturb the equilibrium in 2D transport codes, and its impact will be evaluated in a future work, using the 2D transport code SolEdge2D. One of the ongoing efforts at the IRFM institute is the implementation of reduced turbulent models in 2D plasma edge transport codes [90]. With this technique, one could exploit the relatively low computational cost of a 2D code, while keeping a simplified description of interchange turbulence, which regulates the transverse transport. In this framework, the evaluation of turbulent properties, and their effect on global equilibrium in TOKAM3X simulations with realistic geometries, can give important guidelines for the description of interchange turbulence in a reduced model.

3.3 Distribution of fluctuations amplitude in the poloidal section

After having discussed the shape of turbulent structures, we would like now to evaluate the amplitude of fluctuations. If we represent fluctuations in a Fourier space, considering only the spatial variation in θ and dropping temporarily the subscript in k_{θ}, we obtain the following form:

$$\tilde{N} = \int_{k^N \neq 0} \left| \tilde{N}_{k^N} \right| e^{i\left(k^N \theta + \delta_k^N + \omega t\right)} dk^N \quad , \quad \tilde{\Phi} = \int_{k^{\Phi} \neq 0} \left| \tilde{\Phi}_{k^{\Phi}} \right| e^{i\left(k^{\Phi} \theta + \delta_k^{\Phi} + \omega t\right)} dk^{\Phi} \tag{3.14}$$

The flux in ψ direction, can be expressed as:

$$\tilde{\Gamma}^{\psi} = \tilde{N}\tilde{u}_E^{\psi} \simeq -\frac{1}{B}\tilde{N}\frac{\partial}{\partial\theta}\tilde{\Phi} = \frac{1}{B}\int_{k^N\neq 0}\int_{k^\Phi\neq 0} k_\theta^\Phi \left|\tilde{N}_{k^N}\right| \left|\tilde{\Phi}_{k^\Phi}\right| e^{i\left(\delta-\frac{\pi}{2}\right)} dk^\Phi dk^N \tag{3.15}$$

where δ is the phase shift in θ direction, between density and potential fluctuations, and, as mentioned before, its value in our simulations is around $\pi/2$ for every $k_\theta^\Phi = k_\theta^N$. The wave number k_θ^Φ, contains the information about the dependence of the turbulent flux on the flux expansion discussed in section 3.2.3. Studying the amplitude of density and potential fluctuations, independently from k_θ^Φ, allows us to understand the origin of the turbulent fluxes, independently from the flux expansion.
We calculate so the average standard deviation of fluctuations, sampling data in time and toroidal directions. In section 3.1 we have seen that turbulent events can have a magnitude that exceeds largely the standard deviation. However, the standard deviation itself is indicative of an average amplitude of the fluctuations. With this procedure, we get a description of turbulence integrated over the k_θ spectrum. Figure 3.12 shows the distribution of density and potential fluctuations over the poloidal section in the reference COMPASS-like simulation.

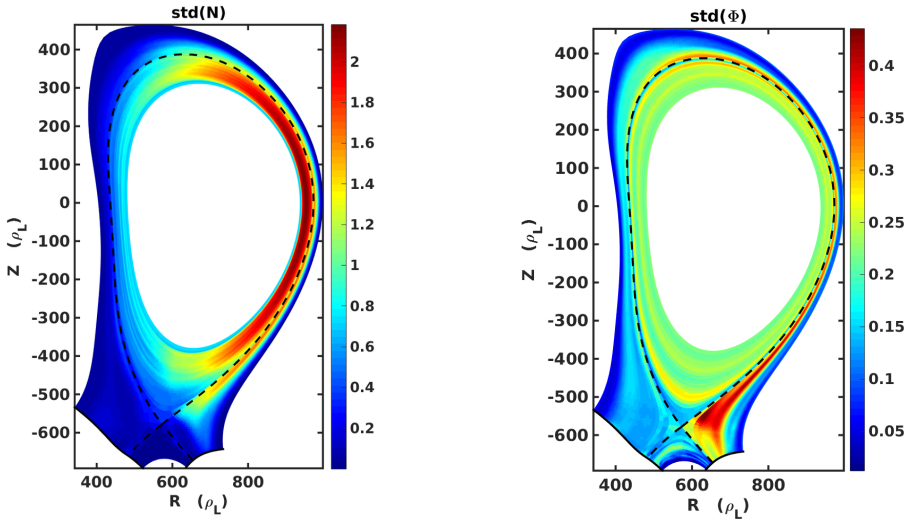

Figure 3.12: *Left: Poloidal distribution of density fluctuation standard deviation in the COMPASS-like reference simulation. Right: Same chart for potential fluctuations.*

A first look at figure 3.12 shows the ballooning nature of turbulence in COMPASS-like geometry simulations. Interestingly, this ballooning character is significantly more evident in density fluctuations than in potential ones in the closed flux surface region. In the SOL, instead, both density and potential fluctuations have a maximum between the LFS midplane and the outer divertor leg region. This distribution is consistent with the parallel correlation length calculated in section 3.2.1, and considering equation (3.15), allows to understand the radial flux distribution shown in figure 3.11. In particular, we find that the amplitude of density fluctuations is slowly decreasing going radially outwards in the closed flux surface region.

Electric potential fluctuations resulting from simulations are instead distributed quite homogeneously in the closed flux surfaces. In the SOL, both density and potential fluctuations are drained quite rapidly and they decay up to a level close to 0 at the outer radial boundary.
At the outboard midplane, radially close to the separatrix, the level of density fluctuations in the SOL reaches values of $\sim 50\%$ of the average density. This high level of fluctuations has been observed in the SOL of multiple tokamaks [91], and indicates the propagation of coherent structures into a region of low background density level. In limiter configuration we obtain, instead, a density fluctuation level of $\delta N/N \sim 20\%$. This is due, at least partly, to the background density gradient, which is much steeper in divertor configuration, as it will be better explained in a later section.
Also in the SOL, the density fluctuation amplitude has a maximum at the LFS midplane, showing a ballooning character. Nevertheless, on the LFS, fluctuations seem to maintain a large amplitude up to the divertor region. Turbulence characteristics in the divertor are described in the next section.

3.3.1 Turbulence in the divertor region

Turbulence in the divertor region is a relatively unexplored domain in numerical global simulations of plasma edge. Some BOUT++ simulations of DIII-D discharges in realistic geometry were presented in Cohen et al. [92], but no dedicated study was carried out on turbulence in the divertor. Moreover, those simulations were carried out fixing background steady-state values for the different fields, in a so-called "gradient-driven" approach. This method has been proven (see [34]) not to be suitable for the description of turbulence in the edge plasma, since it is not able to catch some of its fundamental features, as the shape of the PDF functions. We are performing here, instead, a "flux-driven" turbulence study, where also large-scale gradients are free to evolve basing on sources and sink mechanisms. Figure 3.13 shows the shape and the amplitude of density fluctuations in divertor region.

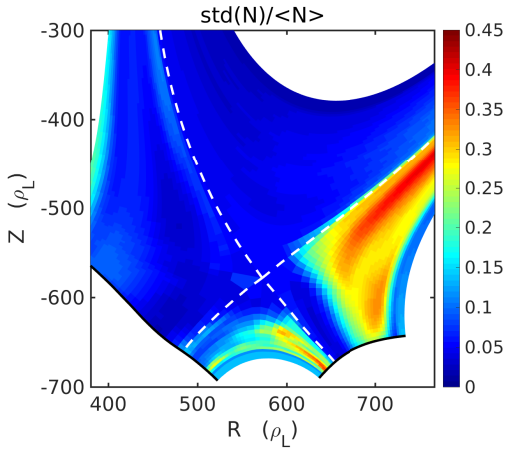

Figure 3.13: *Ratio between standard deviation of the density fluctuations, and density average value $\langle N \rangle_{t,\varphi}$, zoom on the divertor region.*

Plasma fluctuations are found in the PFR, as one can notice from figure 3.13. The amplitude of density fluctuations is very weak, and can be observed only if compared to the average value, as done in figure 3.13, which falls rapidly in this region of a factor $10^3 - 10^4$ with respect to the separatrix value. Although the phase between density and potential fluctuations in the poloidal direction is, also at this location, around $\pi/2$, the low amplitude of the fluctuations causes an almost null level of turbulent transport. The fluctuations registered in this region appear to be a consequence of the spreading of turbulent structures from the outer divertor SOL to the PFR. At the separatrix, there is a region where fluctuations are partially, but not totally damped (see section 3.3.2), so, even if weakened, they manage to reach the PFR and spread in it.
The outer divertor leg plasma is unstable with respect to the interchange instability, since $\vec{\nabla}B\cdot\vec{\nabla}p > 0$. Potential and density fluctuations (whose amplitude is shown in figure 3.12) lead in this region to a non-negligible turbulent transport, with a value up to the 20% of the outboard midplane, as visible in figure 3.11. Turbulence structures are strongly connected to the LFS midplane, which is the location where filaments are expelled preferentially from the edge region. Both on the low and high field sides, filaments get strongly elongated in the radial direction as a consequenc of the flux expansion introduced by the X-point, as understandable from the analysis carried in section 3.2.2. The fast visible camera images of MAST divertor (see [31], [93]) clearly confirm this feature, as visible in figure 3.14.

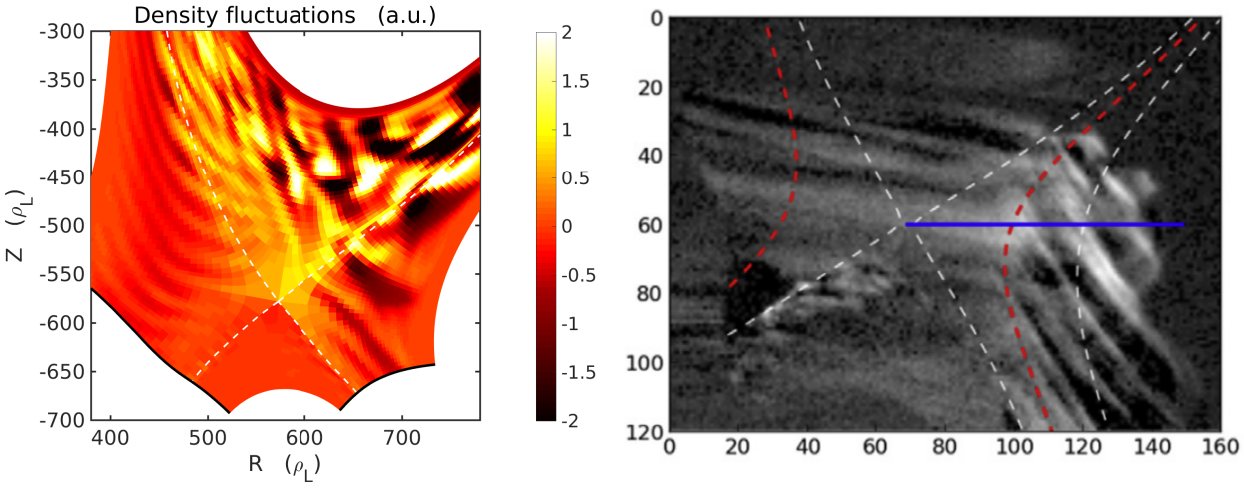

Figure 3.14: *Left: snapshot of density fluctuations at a specific timestep in a COMPASS-like simulation, zoom on the divertor. Right: Fast visible camera image of turbulent structures in MAST divertor, reprinted from [93]: the red dashed line on the outer divertor leg delimits the quiescent zone.*

3.3.2 A quiescent zone in the outer divertor leg

Interestingly, as one can notice in figure 3.13, density fluctuations seem to be strongly damped in the first few flux surfaces outside the separatrix in the outer divertor leg.

Electric potential structures undergo the same kind of damping, even if in a less marked way with respect to density fluctuations. This feature has been also found in divertor simulations with JET-like geometry. The damping of turbulent structures near the separatrix in the outer divertor leg seems to be a universal characteristic of our divertor simulations, even if the extension of this quiescent region varies with the particular magnetic and physical parameters. Experimentally, MAST divertor images acquired by the fast-imaging cameras clearly show a comparable result, shown in figure 3.14. In [93] it is reported that filaments are strongly damped from the separatrix to the first opened flux surfaces in the divertor region on MAST.
With the TOKAM3X simulations in divertor geometry, we can investigate the cause of this damping. The average plasma pressure in the outer divertor leg shows a profile that can be described by an exponential function convoluted with a Gaussian (similarly to what is widely done for the parallel heat flux profile [30]). Since the maximum of the pressure profile is radially located outwards with respect to the separatrix, the pressure gradient reverses in the vicinity of the PFR, leading to an interchange-stable zone, as illustrated by figure 3.15.

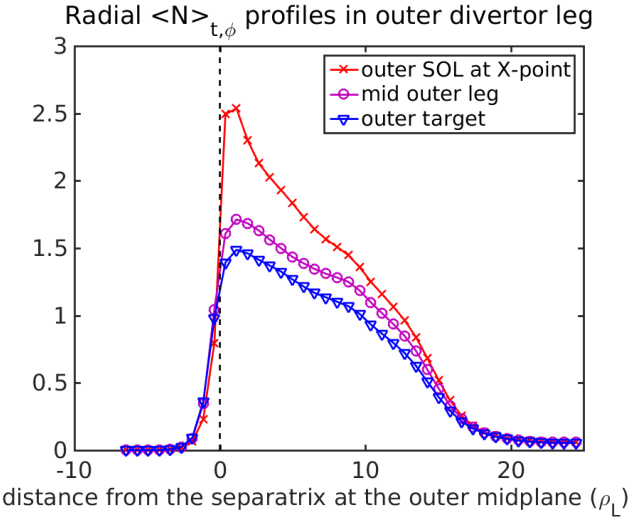

Figure 3.15: *Average density radial profiles at different poloidal positions in the outer divertor leg in COMPASS geometry. Profiles are remapped at the LFS midplane.*

However, the quiescent zone is radially more extended than the position of the density peak, as one can notice from the comparison between figure 3.15 and figure 3.14 (left). By consequence, the damping of density and potential fluctuations seems not to be due only to the lack of turbulence driving. Instead, we can focus on the damping mechanisms acting in this region. The X-point introduces indeed a region of long parallel connection length, that in COMPASS-like SOL goes up to more than $3 \cdot 10^4$ ρ_L (a factor ~ 3 greater than the far SOL), and might affect turbulence properties. We have shown in section 3.2.2 that poloidal wave numbers can be extremely large in regions where the flux expansion value is elevated. Thus, a diffusive mechanism could more easily damp the fluctuations in the vicinity of the X-point, since it is more effective on smaller wave numbers. However, calculating the weight of the diffusive term with respect to the others appearing in the mass conservation equation, it does not seem to have a significant role in the region close

to the X-point.
In [93], it is argued that the strong magnetic shear in the X-point vicinity could be correlated to the fluctuation damping. This damping would be due so to the shearing effect of the magnetic field on turbulent structures. For a simplified circular geometry of the flux surfaces, the global magnetic shear is defined as:

$$s = \frac{r}{q}\frac{\partial q}{\partial r} \tag{3.16}$$

where r is the minor radius and q is the safety factor. In simple circular geometry the growth rate associated to the ITG turbulence has been proven to be maximum for a shear of $s = 0.5$, both analytically [60] and numerically with linear (see for example [74]) and non-linear gyrokinetic simulations [94]. The growth rate decays rapidly depending on other parameters, in a quite asymmetric way between higher and lower values of magnetic shear. Considering that both ITG and RBM are driven by an interchange mechanism, one can expect the magnetic shear to be stabilising also for the turbulence observed in TOKAM3X simulations. The precise value of the optimum shear for the developing of the interchange instability could be slightly different in a generalised flux-surface geometry. There is actually no agreement on the local magnetic shear calculation in a generalised geometry: different expressions can be found in [95], [96], [97]. These expressions do not recover, in general, the global shear definition in a circular geometry. We propose therefore an intuitive definition, which expresses simply the local magnetic shear as the variation of the average pitch angle in the ψ direction. Considering the global definition of the safety factor for circular flux surfaces (2.75), we can re-write (3.16) as:

$$s = \frac{B^\theta R}{B^\varphi}\frac{d}{dr}\frac{rB^\varphi}{B^\theta R} \tag{3.17}$$

Now, in order to avoid the calculation of r, which is ill-defined in divertor geometry, we develop (3.17) as:

$$s = 1 + \frac{B^\theta R}{B^\varphi}\frac{d}{dr}\frac{B^\varphi}{B^\theta R} \rightarrow s_{loc} = 1 + \frac{B^\theta R\|\vec{\nabla}\psi\|}{B^\varphi}\frac{d}{d\psi}\frac{B^\varphi}{B^\theta R} \tag{3.18}$$

This definition of the magnetic shear takes into account the spacing among flux surfaces, and coincides with (3.16) when applied to a circular geometry. This generalization of the magnetic shear has been applied also in the works by Hahm et al. ([98], [99]) for the calculation of the $E \times B$ shear in a generalised magnetic geometry. The local magnetic shear calculated for the reference simulations is shown in figure 3.16:

Since magnetic field lines get more and more tilted starting from the X-point and getting radially outwards, the resulting magnetic shear is negative in the outer divertor leg. Moreover, as one can infer from figure 3.16, the shear value in this zone can be dramatically strong, and would diverge to infinite if calculated exactly at the X-point. This negative shear explains the orientation of turbulent structures in the outer divertor leg, which are directed towards the target, as shown in figure 3.14 (left). A strong shear is

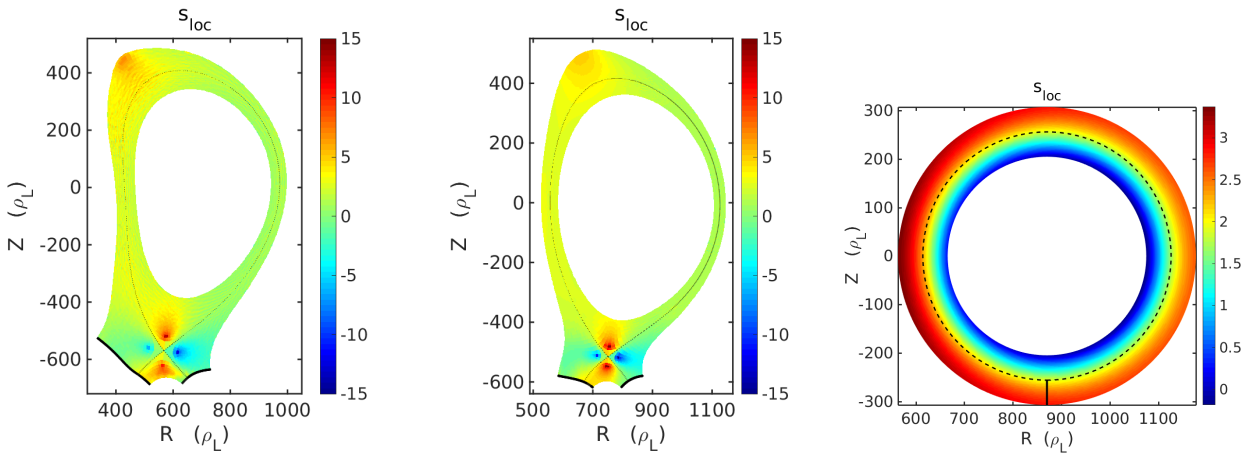

Figure 3.16: *2D map of the local magnetic shear in a COMPASS-like (left), a JET-like (centre) and a limiter simulation (right).*

found also at the top of the divertor simulations, because of the proximity of the second X-point. Instead, at the LFS, the magnetic shear is not particularly strong at the separatrix. In a limiter simulation with parabolic safety factor profile, the local shear is instead limited to much lower values and has a relatively small variation throughout the domain.
Focusing on the divertor region, we find a correlation between the low amplitude of density fluctuations and the local magnetic shear, calculated with (3.18). As visible in figure 3.17, density turbulent structures get strongly damped when they attain a zone with $|s_{loc}| \sim 5$. This damping occurs also at the top of the machine, where these values of magnetic shear can be reached, especially with a strong elongation. Figure 3.17 shows the low amplitude of density fluctuations in the vicinity of the X-point in a COMPASS-like divertor simulation, and the strong amplitude of the local magnetic shear in the same region.

A negative shear is widely known to have a strong stabilising effect for interchange turbulence. This has been proven both numerically [100] and experimentally [101]. These elements suggest a role of the magnetic shear induced by the X-point in damping turbulence in the divertor region.
Although with positive values, a strong magnetic shear appears also in the closed flux surface region, in the vicinity of the X-point. As visible from figure 3.17, fluctuation levels are strongly reduced also in the closed flux surface region in proximity of the X-point, suggesting a correlation with the magnetic shear damping mechanism. It is worth to mention that a strong damping effect has been underlined recently in TOKAM3X simulations of a seeded blob, in a slab geometry with an imposed magnetic shear [102]. Although simulations in [102] are carried in an open-field line region, and the blobs dynamics could be slightly different, they highlighted that the propagation of the turbulent structure is strongly obstructed by a varying field line pitch angle, leading ultimately to its suppression. In our global simulations in divertor geometry, magnetic shear effect is limited to a portion of the turbulent structure, which is strongly connected to the LFS midplane, where the shear is lower. The effectiveness of the shear damping could thus

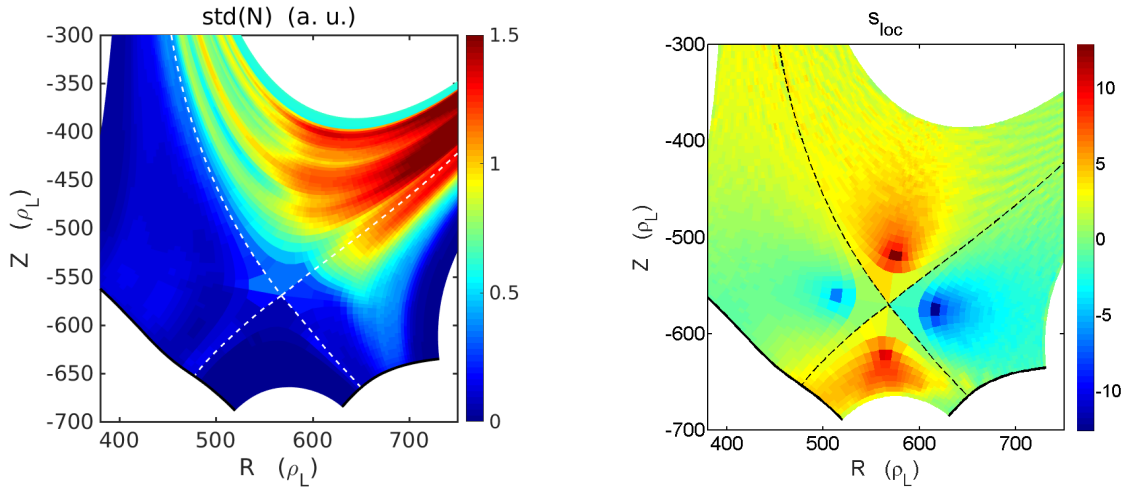

Figure 3.17: *Left: Density fluctuations standard deviation in divertor geometry, zoom on the divertor region. Right: Local magnetic shear, zoom on the divertor region.*

be weaker because of the restricted spatial extension of this magnetic feature.
This damping mechanism could have important implications in the formation of transport barriers, as explained in Chapter 5.

Chapter 4

Global effects of turbulent transport on SOL equilibrium

Contents

In this chapter we analyse the macroscopic effects of turbulent and mean field fluxes on the equilibrium in the Scrape-Off Layer. The parallel flow pattern is explained, with attention to the topological and geometrical features introduced by the X-point. Then we discuss the influence of the divertor shape on the density decay length in the SOL. These large-scale properties of the SOL, observed in TOKAM3X simulations, are compared with experimental results.
Part of the topics in this chapter is included in publications [73] and [103].

4.1 Drive of parallel flows in the Scrape-Off Layer

We focus in this section on the macroscopic effects of turbulence on the global equilibrium in the parallel direction. Understanding the parallel flow pattern in the Scrape-Off Layer of tokamaks is important for several reasons. First of all the divertor imbalance in heat exhaust depends on the poloidal asymmetry in heat transport [104], and determines the plasma conditions at the target plates. Secondly, the parallel flow in the SOL affects neutral recycling and the interaction with the plasma. Moreover, plasma rotation could possibly affect the particle and heat transport from the edge region to the SOL, and consequently on the overall confinement [41].
The SOL equilibrium analysis has been the subject of multiple investigations, both experimental and numerical. From the numerical point of view, 2D transport codes have been so far the most used tools to interpret the parallel flow equilibrium. We intend

here to assess the role of turbulent transport in the determination of the equilibrium in the SOL. TOKAM3X simulations allow us to evaluate the turbulent contribution in the driving of parallel flows, taking into account a realistic diverted magnetic geometry.

4.1.1 State of the art of experimental observations and simulations

Among the other measurable quantities in the SOL plasma, the parallel Mach number, defined by (1.49), is one of the easiest to compare with simulations. Indeed, the Mach number is a dimensionless quantity, which does not depend directly on the source of particles and, moreover, it is constrained between ± 1 by the Bohm boundary conditions (excluding supersonic transitions). This quantity is measured by Langmuir probes, which are common diagnostics installed in all the main tokamaks (see [105] for a review). A large database of Mach measurements is thus available (see, for example, [106] and the included references). Despite the abundance of information about the parallel flow in the SOL (and in the last closed flux surfaces, where reciprocating Langmuir probes can plunge), some important features are not yet well understood, because of the large number of physical mechanisms that come into play in the driving of parallel flows. A universal and well-known characteristic of the parallel flows in the SOL is their poloidal asymmetry. Indeed, measurements on different machines (JET [107], C-Mod [41], Tore Supra [42], etc.), obtained under a great variety of conditions, show a global flow directed on average to the inner target for the majority of the poloidal section in the Scrape-Off Layer. This is translated to a Mach number towards the inner target close to ~ 0.5 at the top of the plasma, if $\vec{u}^{i}_{\nabla B}$ points downwards. This value reveals, as will be clarified later, the presence of an asymmetrical transport process which moves the stagnation point towards the outer midplane.
A big numerical simulation effort has been dedicated, and is still ongoing, in order to explain and reproduce the poloidal asymmetry feature. 2D transport codes as SOLPS and EDGE2D are able to describe carefully the effects of the wall geometry and the impact of the neutral physics on the parallel flow equilibrium. Despite this fact, a common problem found in simulations done with this kind of codes, is an underestimation of the Mach number value at the top of the plasma. The Mach number value is constrained between $\pm$ 1 by Bohm boundary conditions, if we exclude supersonic transitions happening far from the target [20], and in the ideal case of field lines perpendicular to the wall. If no asymmetry is taken into account in transport processes, 2D transport codes predict at intermediate positions, as the top of the machine, Mach numbers that can be one order of magnitude lower than the measured ones. If the ballooned turbulent transport is modelled by a spatially variable diffusion coefficient, characterised by an ad-hoc Gaussian shape profile centred at the LFS midplane, the reproduced Mach number is enhanced up to values with a correct order of magnitude (typically 0.2 [107]), but still lower than what expected from experiments. Only with the simulation of a supplementary outward pinch velocity, which advects particles on the LFS, 2D transport codes can effectively recover realistic values of the parallel Mach number (see [89]). This fact suggests that this kind of code is not able, at the moment, to catch the whole physics behind the driving of the

parallel SOL flows.
On the other hand, 3D turbulence codes such as GBS, BOUT++ and TOKAM3X have tackled this problem, highlighting the role of turbulence in the build-up of asymmetries in the SOL. Simulations were mainly run in limiter configuration ([48], [49]), finding a position of the stagnation point close to the LFS midplane in the case of limiter placed at the bottom of the machine, and recovering realistic values of the Mach number at the top and at the HFS midplane. In [50], the Mistral experimental case on Tore-Supra is reproduced numerically: the parallel flow pattern is studied assuming different positions of the toroidal limiter (bottom, LFS midplane, top, HFS midplane), and highlighting a good qualitative agreement with experiments.
We intend here to study the problem of the driving of parallel flows in the SOL, running simulations in divertor configuration, where the topological and geometrical peculiarities could lead to different features with respect to the limiter case. With respect to the state of the art of numerical simulations, so, we introduce a more accurate description of the magnetic geometry effect, and we aim at decoupling the effects of turbulent transport from the the contribution of the mean-field drifts.

4.1.2 Turbulent and mean-field fluxes distribution in the poloidal section

As a first step in the understanding of the role of large scale drifts and small-scale turbulence in the driving of parallel flows, we can evaluate separately mean-field and turbulent fluxes. In Chapter 3 we have studied the distribution of density and potential fluctuations in the poloidal section, and we have related it to the distribution of turbulent fluxes. However, since TOKAM3X does not assume scale separations, and the total flux is given by the coupling of all the possible modes, the global fluxes can be decomposed only a posteriori in a *mean-field* component and a *fluctuating* component. For the $E \times B$ flux in the ψ direction, which is one of the main actors in transverse transport, averaging on time and toroidal direction, we obtain:

$$\left\langle N u_E^{\psi} \right\rangle_{t,\varphi} = \langle N \rangle_{t,\varphi} \left\langle u_E^{\psi} \right\rangle_{t,\varphi} + \left\langle \tilde{N} \tilde{u}_E^{\psi} \right\rangle_{t,\varphi} \tag{4.1}$$

The first, mean-field component of the flux in equation (4.1) can be self-consistently included in 2D transport codes (see [85], [86], [87], [88]). This is valid for all the types of drifts ($E \times B$, $\vec{\nabla} B$ and centrifugal). On the other hand, these codes cannot reproduce self-consistently the coupling terms leading to the turbulent part of the flux.
We calculate so mean-field and fluctuating components of the $E \times B$ transverse flux in the reference COMPASS-like simulation. Since the source of particles is localised, in our simulations, in the closed flux surfaces region, it is interesting to understand how these particles are transported towards the SOL across the separatrix.

Figure 4.1a shows the poloidal distribution of the total particle flux at the separatrix as if it was measured in the physical space, that is to say, in $m^{-2}s^{-1}$ units. This flow appears extremely peaked at the X-point location, and with a local maximum at the top.

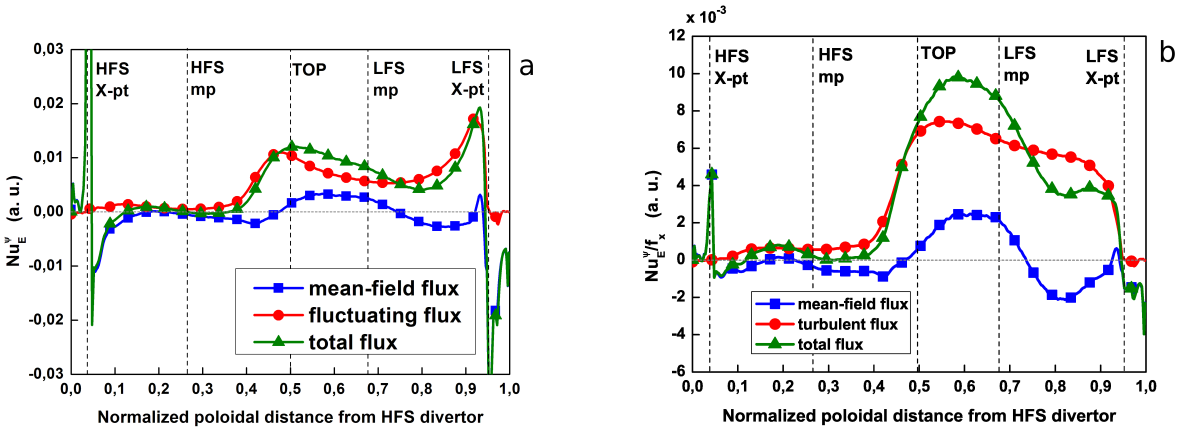

Figure 4.1: *a) Poloidal profile of the turbulent, mean-field and total $E \times B$ particle flux in the ψ direction at the first open flux surface. b) Profiles of the fluxes normalised by the flux expansion.*

Actually, this reflects the geometric effect of the flux expansion that has been discussed in section 3. In particular, the wavelength in the poloidal direction, and consequently the $E \times B$ flux in the ψ direction are modified as described by equation (3.8). We want to study, instead, how effective these fluxes are in transporting particles and momentum across flux surfaces, since this is the relevant information for confinement. In order to do this, we can simply scale our flux by the local flux expansion value. The resulting profile is plotted in figure 4.1b.
Turbulent flux is distributed in the LFS, with a peak located slightly over the outboard midplane. Looking instead at the mean-field component of the flux, a "sinus" shape can be observed at a location around the LFS midplane. This particular shape can be easily explained considering the Ohm's law (2.39). In the case of a small parallel resistivity and in absence of temperature gradients, the electric potential parallel gradient follows the one of the density logarithm (quasi-adiabatic behaviour). In a sheath limited regime plasma density has a maximum at the stagnation point and its value goes down to the half at the target (admitting the total pressure conservation on a field line). A density parallel gradient thus builds up in the SOL, and it is followed in this case by a parallel gradient in electric potential. This gradient changes its sign, so, in the vicinity of the stagnation point, which in this case is placed slightly under the LFS midplane, leading to an inversion of the direction of the perpendicular $E \times B$ drift. The mean-field $E \times B$ fluxes can thus be directed inwards, towards the plasma core, on one side of the stagnation point, and outwards on the other side.

Figure 4.2 shows the 2D complete map of the mean-field and turbulent fluxes. In the edge region the $\vec{u}^i_{\nabla B}$ velocity, which is directed downwards, causes the build-up of an up-down electric potential dipole. This causes an $E \times B$ mean-field velocity directed horizontally outwards. This "pinch" velocity must be taken into account on the HFS, where almost no turbulence is at play, but is almost negligible on the LFS when compared to the turbulent

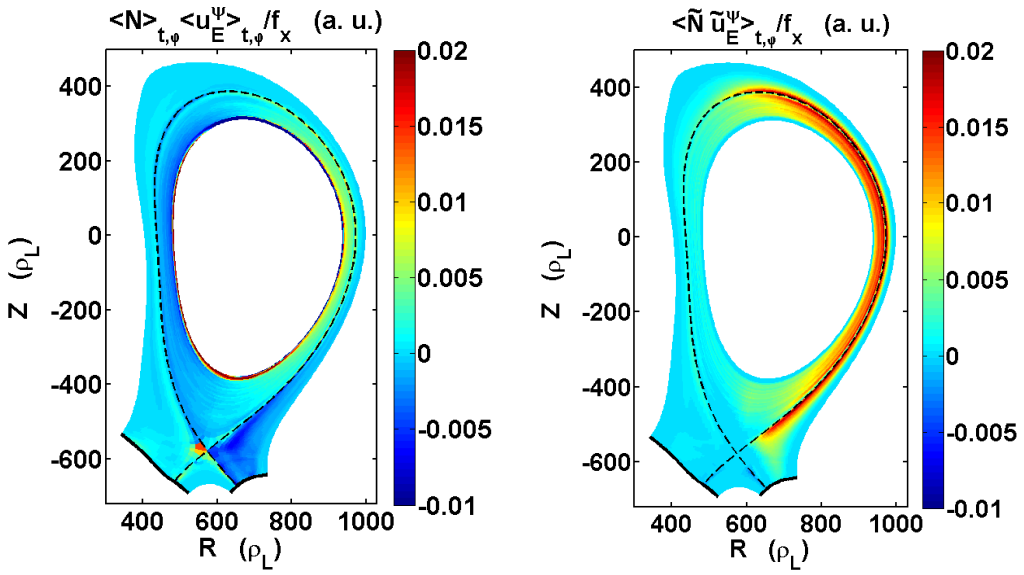

Figure 4.2: *Comparison of mean-field and turbulent $E \times B$ fluxes in ψ direction in a COMPASS-like simulation.*

flux. Moreover, as one can deduce from its cosine shape in the poloidal coordinate, its integral on the flux surface is close to 0, and so it does not affect much the average particle transport across the flux surfaces. In the SOL, the fluctuating component is dominant on the LFS, while on the HFS both the components are weak.
We observe, more in general, that at some positions in the poloidal section, as in the vicinity of the X-point, the amplitude of the mean-field $E \times B$ flux can be comparable to (or even exceed) the turbulent flux. This is a peculiarity of the strongly shaped flux surfaces introduced with the X-point geometry. In simple circular geometry (or Cartesian in even more simplified cases) in fact, the effects of the mean $E \times B$ drifts are small if compared to the turbulent fluxes, if we exclude the region immediately close to the solid walls where big poloidal gradients of electric potential can build-up (this characteristic of the limiter configuration was already highlighted by GBS simulations [49]). In the outer SOL instead, mean-field and turbulent fluxes have comparable magnitude, and they both decay to 0 approaching the external radial boundary.

4.1.3 $E \times B$ circulation at the X-point

It is interesting, in COMPASS-like simulations, to highlight more carefully the characteristics of transverse fluxes in the divertor region. Figure 4.3 illustrate the $E \times B$ flux crossing the separatrix in the divertor legs.

In the divertor, turbulent transport across the separatrix seems to be negligible if compared to the mean-field $E \times B$ drift. This can be stated, though, only for few flux surfaces outside the separatrix, where turbulence is strongly damped as described in Chapter 3. In the outer divertor leg a turbulent transport pointing towards the far SOL is found in simulations, with a value around 20% of the one at the LFS midplane, as shown in

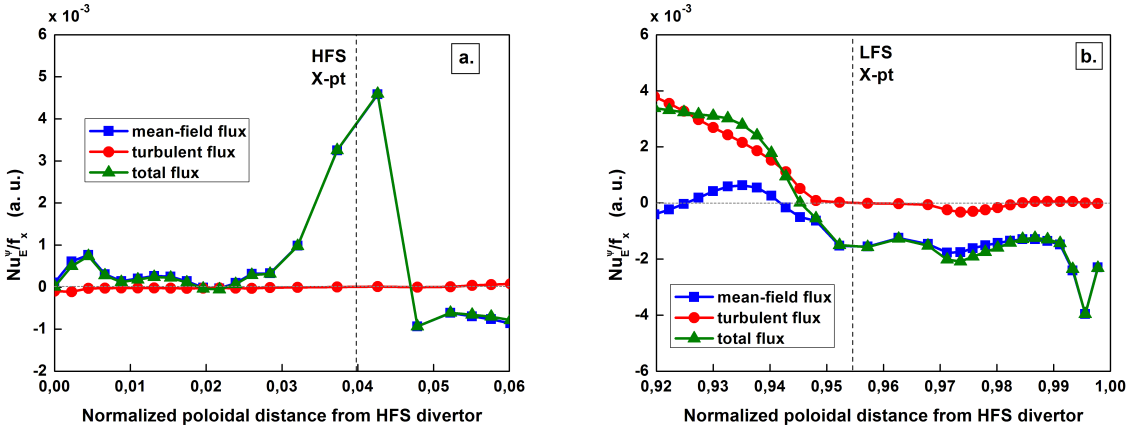

Figure 4.3: *a) Mean-field and fluctuating components of $E \times B$ fluxes in ψ direction scaled with f_x, calculated at the separatrix. Zoom on the HFS divertor leg region. b) Zoom on the LFS divertor leg region.*

figure 4.2. This peculiarity is very interesting, since a significant turbulent transport in the divertor leg could lead to a broadening of the SOL width [108]. In COMPASS-like simulations, we register indeed a broad radial density profile at the outer target. This feature will be discussed later in this chapter.
The process regulating the mean-field fluxes in the divertor is the build-up of parallel gradients described before. The mean-field $E \times B$ drift, so, drives a complex flux pattern around the X-point, which is represented in figure 4.4.

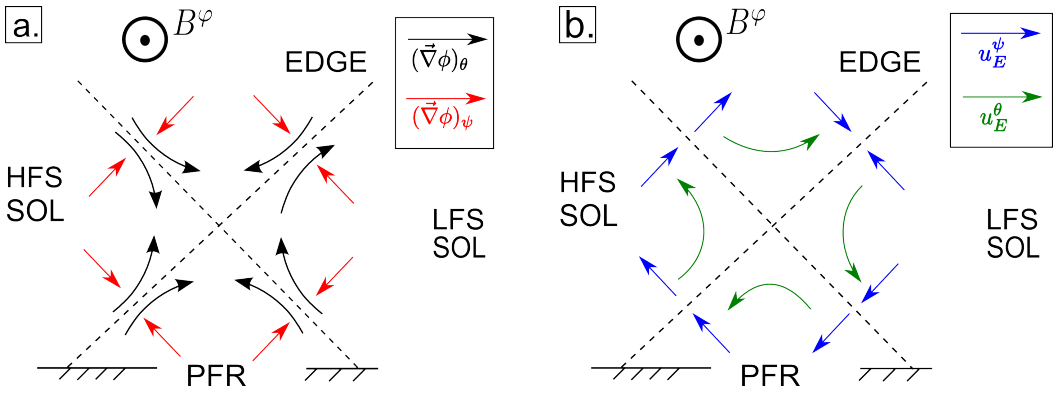

Figure 4.4: *a) Electric potential gradient, averaged on time and toroidal direction, decomposed in ψ and θ directions, in the divertor region. b) $E \times B$ flux pattern around the X-point.*

In order to understand the $E \times B$ flux pattern around the X-point it is necessary to study the gradient of the electric potential, shown schematically in figure 4.4a. In ψ direction, the electric potential has a maximum at (or very close to) the separatrix. This is commonly observed in tokamaks. In our simulations indeed, electric potential decays radially in the SOL. In closed field lines, the electric potential is determined by a complex

charge balance (2.38), and its gradient is directed, as it is usually observed in L-mode plasmas, towards the separatrix (see for example [109]). In the SOL, electric potential roughly follows the poloidal profile of the density logarithm, as understandable by the Ohm's law (2.24).
In the closed field lines, a dipole structure builds up, with a poloidal maximum at the X-point. In the SOL, as explained before, electric potential peaks at the LFS midplane. However, on the HFS, we find in our simulations a second peak in the vicinity of the X-point. This happens since in the first $\sim 5\ \rho_L$ of the main SOL, the electric potential keeps the same poloidal shape as in the LCFS, with a peak at the X-point.
The described electric potential distribution gives rise to the $E \times B$ flux pattern illustrated in figure 4.4b, as one can verify from the drift expression (2.6). We can see that u_E^{ψ} is directed in the LFS SOL towards the PFR. The PFR behaves thus as a sink of particles on the LFS, even if, as shown in figure 4.1, the magnitude of the losses is small if compared to the midplane outward fluxes. On the inner leg (figure 4.3b), the $E \times B$ flux across the separatrix is directed instead towards the outer SOL. However, since density is relatively low in the PFR, this outward radial flux is negligible. The potential peaking at the X-point, causes an inward $E \times B$ velocity just above the X-point on the HFS. We can thus see from figure 4.4b how a particle, through the θ and ψ components of the $E \times B$ velocity could travel from the LFS to the HFS, through the PFR. This is a coupling mechanism between the two SOL branches, active in a region close to the X-point.
This same circulation pattern has been observed numerically in 2D transport codes as UEDGE [86], but also experimentally on DIII-D [110], in which case a similar potential peak at the X-point is highlighted. It must be reminded, however, that, as stated by the generalised Ohm's law (2.24), the potential distribution in parallel (and so, also poloidal) direction is strongly dependent also on temperature parallel gradients, which are not at play in the presented simulations. Temperature parallel gradients can gain a great importance in a high-recycling divertor regime, in which electric potential parallel gradient can reverse, and the direction of the mean-field $E \times B$ drift with them. A consistent inclusion of the related physics will be needed to evaluate the importance of these effects.

4.1.4 Evaluation of the relative effects of the driving mechanisms

We wish now to evaluate the weight of the different transverse transport mechanisms in the driving of parallel flows. In order to do this, we can exploit the model proposed by J. Gunn et al. in [42], which allows to analyse the parallel Mach number as a function of the distribution of the particle source on the flux surface. The model, isothermal, is based on a simplified version of the mass and parallel momentum conservation equations at the steady state:

$$\begin{cases} \frac{\mathrm{d}}{\mathrm{d}x_\parallel}\left(NMc_s\right) = S \\ \frac{\mathrm{d}}{\mathrm{d}x_\parallel}\left(Nc_s^2\left(1+M^2\right)\right) = 0 \end{cases} \tag{4.2}$$

where $x_\parallel$ is the parallel length and S is a generalised particle source for the parallel flow. Comparing this equation with the particle conservation (2.36) solved in TOKAM3X we can notice that the term S includes not only a volumetric source (as the ionization one), but also the advection terms in the perpendicular direction related to the $E \times B$ and ∇B drifts (curvature terms are neglected in the model). Indeed, in TOKAM3X simulations, the ionization term is non-zero only where the particle source is imposed, namely in the edge region. In the rest of the geometrical domain, the perpendicular transport is the only source for the parallel flow. In the parallel momentum conservation, the conservation of the total pressure along the field line is assumed, coherently with the fact that neutral physics is not taken into account, and momentum loss processes as the charge exchange are absent. This hypothesis is well fulfilled in TOKAM3X simulations, at least for flux surfaces sufficiently far from the separatrix (where fluid drifts can be a cause of loss of momentum towards the PFR, as explained later in this chapter). The Mach derivative in the parallel direction, that can be derived from the system (4.2), can be expressed as:

$$\frac{dM}{dx_\parallel} = \frac{1+M^2}{1-M^2}\frac{S}{Nc_s} \tag{4.3}$$

We can see that the Mach number derivative in parallel direction is positive when the particle source is positive. In our case, poloidal profiles are almost always monotonic, indicating a positive source everywhere on the field line. Exceptions are the zones in the vicinity of the PFR, that represent a particle sink. Moreover these zones represent a sink also for the parallel momentum, which is transported across the flux surfaces by the same mechanisms as particles: the total pressure so is no more conserved on the field line and the model (4.2) is hardly applicable.
We now perform a variable change, and we define $s_\parallel$ as:

$$s_\parallel = \frac{1}{\langle S \rangle L}\int_{-L/2}^{s} S \quad \mathrm{d}x_\parallel \quad , \quad \langle S \rangle = \frac{1}{L}\int_{-L/2}^{L/2} S \quad \mathrm{d}x_\parallel \tag{4.4}$$

Where L is the total connection length measured from one target to the other. With some simple algebra, and imposing the Bohm boundary conditions in the equality form, $M(s_\parallel = 0) = -1$ and $M(s_\parallel = 1) = 1$, one can find:

$$\frac{M}{M^2+1} = s_\parallel - \frac{1}{2} \tag{4.5}$$

This equation tells us that the stagnation point, namely where $M = 0$, is located where the center of mass of the total source is, that is to say where $s_\parallel = 0.5$. We can now try to express explicitly the terms that compose the source:

$$S = -\vec{\nabla} \cdot (N\vec{u}_E) - \vec{\nabla} \cdot \left(N\vec{u}^{i}_{\nabla B}\right) \tag{4.6}$$

Where we have referred to the conservation of the ion density. Therefore, for the introduced variable $s_\parallel$:

$$s_\parallel = \frac{\int_{-L/2}^{s} S \quad \mathrm{d}x_\parallel}{\int_{-L/2}^{L/2} S \quad \mathrm{d}x_\parallel} = \frac{\int_{-L/2}^{s} -\vec{\nabla}\cdot(N\vec{u}_E) - \vec{\nabla}\cdot(N\vec{u}_{\nabla B}) \quad \mathrm{d}x_\parallel}{\int_{-L/2}^{L/2} -\vec{\nabla}\cdot(N\vec{u}_E) - \vec{\nabla}\cdot(N\vec{u}_{\nabla B}) \quad \mathrm{d}x_\parallel} \sim \frac{\int_{-L/2}^{s} \vec{\nabla}\cdot(N\vec{u}_E) + \vec{\nabla}\cdot(N\vec{u}_{\nabla B}) \quad \mathrm{d}x_\parallel}{\int_{-L/2}^{L/2} \vec{\nabla}\cdot(N\vec{u}_E) \quad \mathrm{d}x_\parallel} \tag{4.7}$$

where we have underlined the fact that globally, on a flux surface, the divergence of the ∇B flux is negligible if compared to the $E \times B$ one (in particular in our simulation the ratio of the two is usually lower than the 5%). It is interesting to notice that, despite this fact, the ∇B drift contributes to determine the stagnation point position as shown by equation (4.7), as it sums with other terms.
Both the turbulent and the large-scale drifts contribute in determining the source for the parallel flux. The contribution of turbulence flux is given mainly by the radial component of its divergence, depicted in red in figure 4.5. On the other hand, the poloidal component of the divergence of the poloidal $E \times B$ flux is not negligible in the SOL, and it has a similar amplitude than the radial one. Therefore, it is represented in figure 4.5 in green. Sources and sinks located in the divertor legs are not represented since, as stated before, they are almost negligible with respect to the upstream plasma.

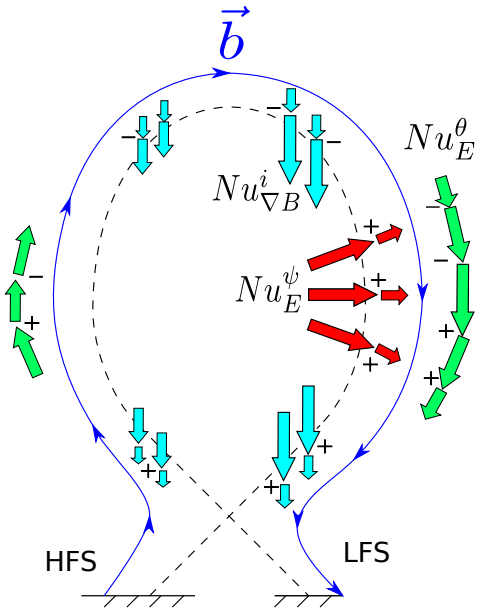

Figure 4.5: *Distribution on the poloidal plane of particle sources for the parallel flow given by the transport processes acting between closed and open field lines. Plus and minus signs represent respectively positive and negative particle sources for the parallel direction.*

One can notice in figure 4.5 that the global distribution of particle sources due to transport mechanisms is strongly asymmetric. The nature of the interchange turbulence, ballooned at the LFS midplane is the main cause for this characteristic, as it was already highlighted, for example, in [48], [49] and [50] for the limiter case. Positive sources for the parallel flow are located mainly between the midplane and the X-point on the LFS. We can notice that the ∇B drift shifts the position of the stagnation point towards the X-point. A more quantitative picture of the different terms intervening in the driving of the parallel flows is shown in figure 4.6.

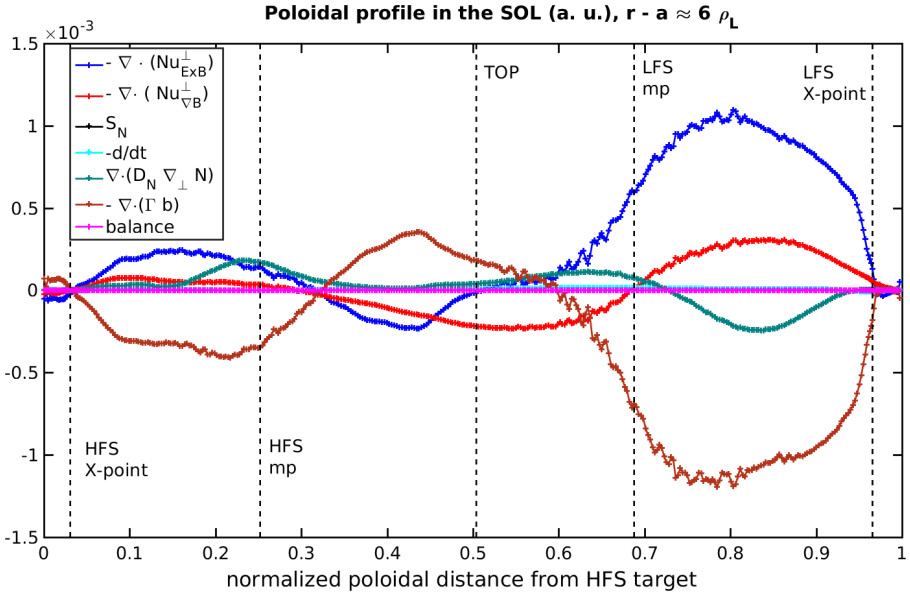

Figure 4.6: *Poloidal profile of the different terms intervening in the mass balance at the separatrix, averaged on time and toroidal direction. Every term is calculated as if it was on the RHS of the density conservation equation, and "balance" is the sum of all the other terms.*

From figure 4.6, we can see that the parallel term $\vec{\nabla} \cdot (\Gamma \vec{b})$ responds to the different perpendicular source terms. As affirmed before, these terms peak between the LFS midplane and the LFS X-point, and the dominant one are the ones related to the $E \times B$ and the ∇B drifts. The parallel flux which develops as a reaction of the parallel flow to the curvature drift is also known as Pfirsch-Schlüter flow, and it has been extensively studied in the framework of the neoclassical theory, especially for the core plasma region (see [6], Chapter 4).

It is now more clear that, even in order to identify the principal terms which drive parallel flows, it is necessary to evaluate particle fluxes in a framework independent from the flux expansion. Indeed, looking at the fluxes in the spacial coordinates as represented in figure 4.2a, could lead to the misleading conclusion that the main sources of particles for the SOL are located at the X-point. Instead, the distribution of the parallel Mach number confirms that we are interested in the effectiveness of the transport across the flux surfaces, which is principally concentrated around the LFS midplane.

The source distribution of the analysed case leads to a distribution in the parallel Mach

number which is represented in figure 4.7a.

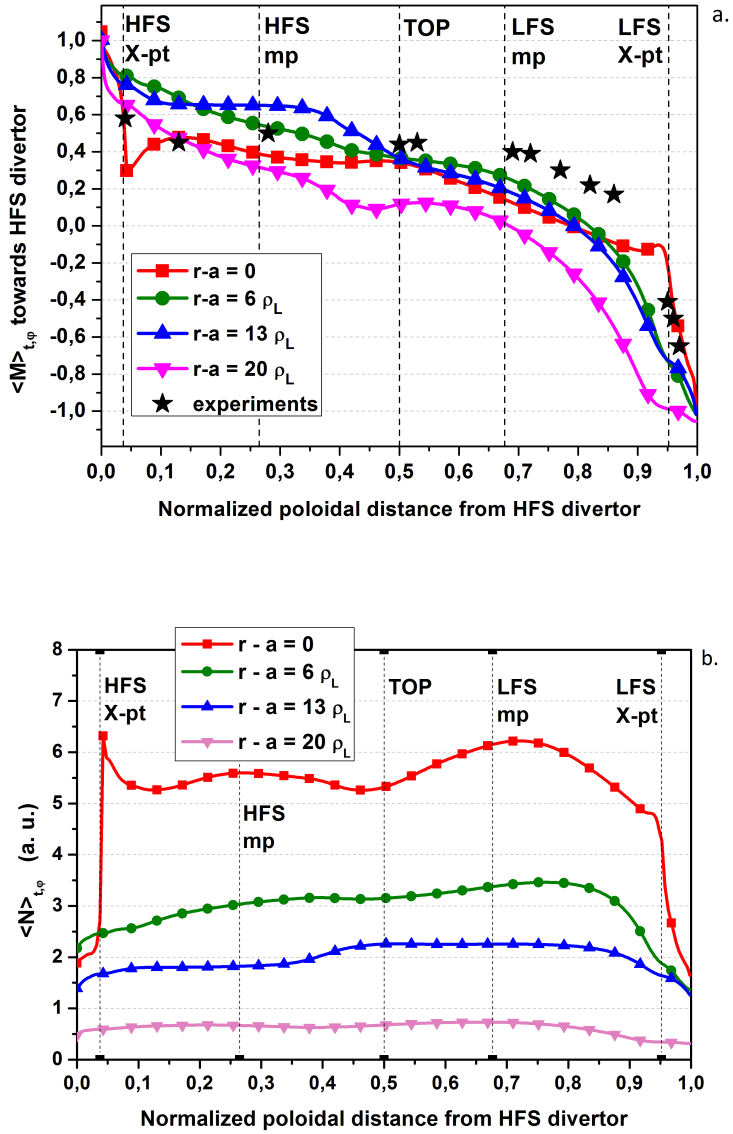

Figure 4.7: *a) Poloidal profile of the parallel Mach number in the SOL, for a COMPASS-like simulation, at different radial positions. Simulations are here compared to results from the multi-machine experiment presented in [106], represented by stars. b) Correspondent poloidal profiles of the average density in the SOL.*

We can notice that, as expected from the qualitative analysis shown above, the stagnation point is located between LFS midplane and the X-point, where the maximum of the particle source is concentrated. In this region, the Mach number towards the HFS divertor rises rapidly from a value close to -1 to about 0.25 at the outer midplane and ~ 0.4 at the top of the plasma. At the separatrix, the Mach number increase around the LFS of the X-point is more sharp. In the HFS, just above the X-point, a decrease in

the Mach number is found: according to (4.3), this corresponds to a negative source of particles. In this region indeed, as shown in figure 4.4, the electric potential peaks poloidally at the X-point, causing an $E \times B$ flux directed towards the centre (and it is not followed by a similar flux from the far SOL, where the electric potential changes its poloidal shape). This negative source for the SOL causes a decrease in the Mach number, and so, for the pressure conservation on the field line, a proportional increase in density, noticeable in figure 4.7b. Since this accumulation affects several points in the main HFS SOL near the X-point, and the code does not lose its conservation properties, we can exclude a numerical effect. Going radially outwards in the SOL, the source becomes more homogeneous over the parallel length (and also, the field line length itself shrinks going further from the X-point).
A good agreement is found with the multi-experiment data from L-mode discharges reported in [106], both for the position of the stagnation point and for the value of the Mach number at the top position. These characteristics of the parallel flows seems to be quite universal in the SOL of the tokamaks. Nevertheless, experiments seem to show a position of the stagnation point even closer to X-point. Beyond the neutral physics and the energy transport, another element can affect the Mach number distribution: the Bohm-Chodura boundary conditions at the target plates, which extend the boundary conditions at the entrance of the sheath to cases where field lines are not perpendicular to the walls and in presence of drifts [111]. In unnormalised terms:

$$M_{\parallel} + \frac{u_E}{c_s \tan(\alpha)} \geq 1 \tag{4.8}$$

Where α is the incidence angle. Since the main component of the $E \times B$ drift is the poloidal one, and it points towards the outer target in the SOL, the absolute value of the Mach number could be decreased at the outer target, and increased at the inner one, thus shifting further the stagnation point towards the LFS X-point.

4.1.5 Pressure conservation in the parallel direction

A similar analysis of the poloidal distribution of the sources can be carried out on parallel momentum conservation (2.37). It is important, in particular, to verify if the total pressure Π is conserved along the field lines, and if not, which are the main mechanisms leading to pressure losses. In dimensionless terms, Π is defined as:

$$\Pi = N(T_e + T_i)(1 + M^2) \tag{4.9}$$

and in the isothermal assumption with $T_e = T_1 = 1$, $\Pi = 2N(1 + M^2)$. Figure 4.8a represents the total pressure profile at several radial positions in the SOL.

From figure 4.8a we can observe that total pressure is almost conserved along the field lines, with the exception of the first few Larmor radii outside the separatrix. At the separatrix, the main pressure losses are localised in the divertor region, and they are due mainly to perpendicular advection of the parallel momentum by $E \times B$ drift. A slight

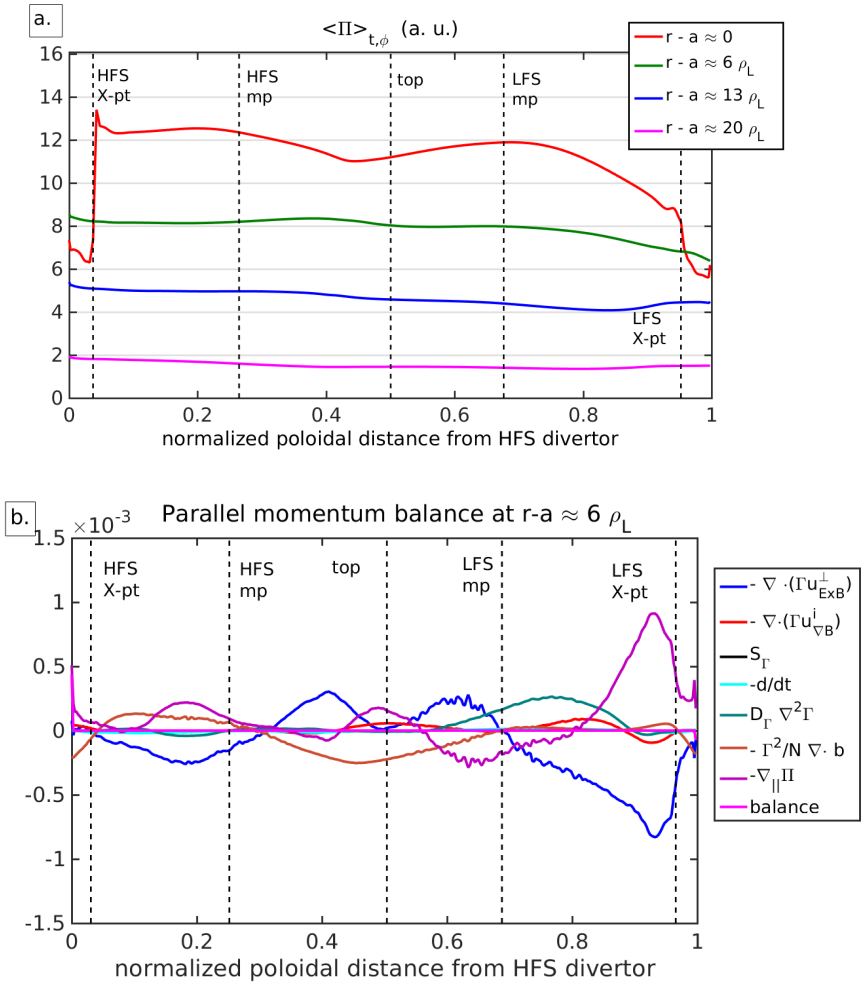

Figure 4.8: *a) Poloidal profiles of the total pressure at different radial positions in the SOL, in the reference COMPASS-like simulation. b) Poloidal profile of the parallel momentum balance at $r-a \approx 6\ \rho_L$. Terms are calculated in the RHS of equation (2.37), and the term "balance" is the sum of the others.*

increase in total pressure can be noticed groing from the LFS towards the HFS, even if the relative diffeence of total pressure between the two targets does not exceed the 20%. In order to understand this behaviour, we isolate the total pressure parallel gradient term in the parallel momentum balance, expressing it as:

$$\nabla_{\parallel}\Pi = \vec{\nabla}\cdot\left(\frac{\Gamma^2}{N}\vec{b} + 2N\vec{b}\right) - 2N\vec{\nabla}\cdot\vec{b} - \frac{\Gamma^2}{N}\vec{\nabla}\cdot\vec{b} \tag{4.10}$$

Substituting (4.10) in (2.37), we find the terms plotted in figure 4.8b, with $\nabla_{\parallel}\Pi$ expressed explicitely. We can state that the increase in total pressure is due to parallel momentum advection by the $E \times B$ drift, and so also by turbulence. Practically, the parallel momentum in the edge region is transported to the SOL by transverse transport. Even if parallel Mach number is low in the closed flux surfaces region, the density is higher than in the SOL, so in the two regions the plasma carries a comparable parallel momentum.

In particular, parallel flux in the edge region is directed in the opposite direction with respect to the magnetic field, determining then a positive parallel gradient towards the HFS divertor.

4.2 Reverse toroidal field simulations

In section 4.1.2 we separated a posteriori a mean-field and a fluctuating component. However, turbulent transport affects the equilibrium in the poloidal direction, thus impacting also the mean-field fluxes. A widely used strategy in experiments, in order to decouple self-consistently the effects of turbulence from the ones of large scale drifts, is to repeat the plasma discharge with the same characteristic parameters, but with a reversed toroidal field. The inversion of the toroidal field, indeed, should reverse the direction of the drift velocities, as it is clear by their definition (2.41), neglecting the component proportional to the poloidal field ($B^\theta \ll B^\varphi$). Turbulence instead, which is driven by the curvature of the field, regardless of its direction, should develop as in the case with normal field orientation. Therefore, admitting that the global equilibrium would not be perturbed significantly (this is questionable, since in many experimental cases the reversed toroidal field configuration degrades the confinement), one can easily disentangle the effects produced by drifts and the ones by turbulence. This exercise has been carried out on several tokamaks (see [107] for JET, [41] for Alcator C-mod, [112] for JT60-U, etc.) where two options can be equivalently adopted: the inversion of the toroidal field, or the symmetric up-down flip of the plasma configuration (that has the same effect). This exercise is reproduced here numerically, by simply reversing the direction of the toroidal field, and running a new simulation with the same parameters as the reference one.

4.2.1 The relative importance of drifts and turbulence

We evaluate the parallel Mach number in a COMPASS-like simulation with a reversed toroidal field, that is to say, with ions ∇B drift pointing towards the top of the device. We calculate both poloidal and radial profiles of the parallel Mach number, and we plot them in figure 4.9.

The first noticeable feature in figure 4.9a is the displacement of the stagnation point from below the LFS midplane to a location close to the top, which leads to a more poloidally symmetric parallel flow pattern. In the case of reversed toroidal field, the parallel flow at the LFS midplane is reversed, and directed towards the outer target. This feature has been observed in experiments on multiple tokamaks, and in particular the profiles measured on Alcator C-Mod [41] look qualitatively very similar to the one obtained in this simulations, with a positive, radial maximum in the Mach number profile in the case of normal toroidal field. The position and the amplitude of this peak depends on how far the LFS midplane is from the stagnation point at that specific flux surface. In our case, for the normal B^φ, the peak occurs at around 7 ρ_L distance from the separatrix. Going radially outwards, the particle source becomes more homogeneous on the flux surface and

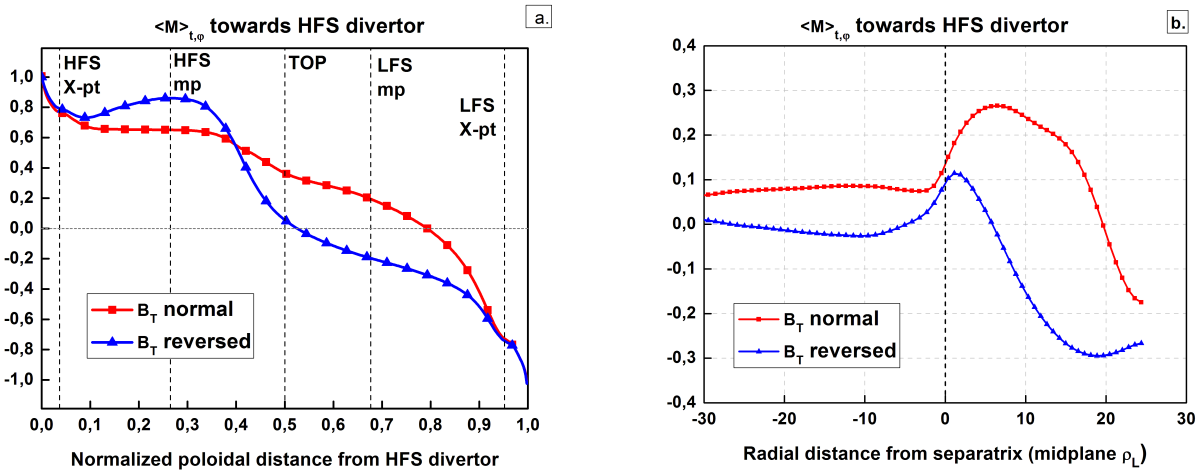

Figure 4.9: *a) Comparison of the profile of the average parallel Mach number with normal and reversed toroidal fields, at a flux surface in the SOL located ar* $r-a \sim 13\ \rho_L$. *b) Radial profile of the average parallel Mach number at the LFS midplane in case of normal and reversed* B^{φ}.

the stagnation point moves upwards to the LFS midplane (after $r-a \sim 20\ \rho_L$ there is a non-negligible influence of the wall). In the reversed toroidal field case, instead, the stagnation point moves progressively towards the top, generating stronger parallel flows towards the outer target at the LFS midplane. The coherence of the simulation results both in poloidal and in radial direction suggests that TOKAM3X can catch the main transport processes at play in the SOL, and the consequent equilibrium.
Qualitatively, we can explain the displacement of the stagnation point by representing the different sources in the SOL.

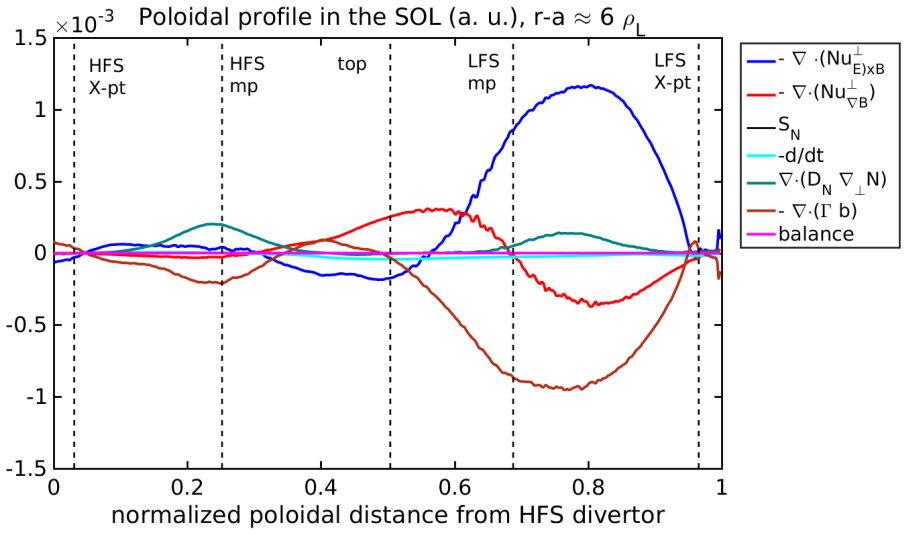

Figure 4.10: *Poloidal profile of the terms intervening in the density conservation in the reversed field case, calculated at the RHS. The term "balance" is the sum of the others.*

Comparing figure 4.10 with 4.6, we notice that while the $E \times B$ source of particle is almost unchanged, the ∇B drift, changing sign, gives a positive contribution at the top and a negative at the bottom, causing the shift of the stagnation point.
If we evaluate the Mach number at the top, we find a difference $|\Delta M| = M^{norm}_{TOP} - M^{rev}_{TOP} \simeq 0.40$ between the cases with normal and reversed toroidal field, for most of the radial extension of the SOL. If we look at the effects on the Mach number of drifts and turbulence as simply the sum of two contributions, for the normal B^{φ} case we can write:

$$M^{norm}_{TOP} = \Delta M^{dr} + \Delta M^{turb} \simeq 0.4 \tag{4.11}$$

Where the superscripts dr and $turb$ are referred respectively to the contribution assigned to drifts and to turbulence. For the reversed B^{φ} case:

$$M^{rev}_{TOP} = -\Delta M^{dr} + \Delta M^{turb} \simeq 0 \tag{4.12}$$

Substituting (4.12) in (4.11), we obtain $\Delta M^{dr} \simeq \Delta M^{turb} \simeq 0.2$. This is clearly a simplified evaluation, and relative to a specific location in space. However, this qualitative analysis tells us that the weight of turbulence and large-scale drifts in determining the parallel SOL flow is comparable. Numerical tools so, in order to reproduce the right values of parallel flows, must account both for the large-scale drifts and the micro-scale turbulent transport.

4.2.2 Equilibrium with reversed toroidal field

Even if the poloidal equilibrium changes with the inversion of toroidal field, we must verify the plausibility of the assumption of similar radial equilibrium. In figure 4.11 we plot a comparison of the radial profiles of the average density for normal and reversed toroidal field configurations.

One can notice that the global radial equilibrium is very similar in the two cases. For the purpose of the analysis of the driving of the SOL parallel flow, the assumption of unchanged turbulent properties is justified. However, a slightly enhanced confinement is found in the normal toroidal field case, with a $\sim 10\%$ difference in average density near the LCFS, and a smaller density decay length in the SOL. The radial equilibrium is dependent on turbulent transport, which regulates the difference between the two cases, and would need a further dedicated analysis.

4.3 Discussion on the ionisation source distribution

In TOKAM3X simulations, parallel flows in the SOL are driven by particle sources, which are transported out of the closed flux surfaces by large-scale drifts and micro-scale turbulence. However, plasma interaction with neutral species represents a further source, basically through the mechanism of ionisation. In high-recycling regimes, where

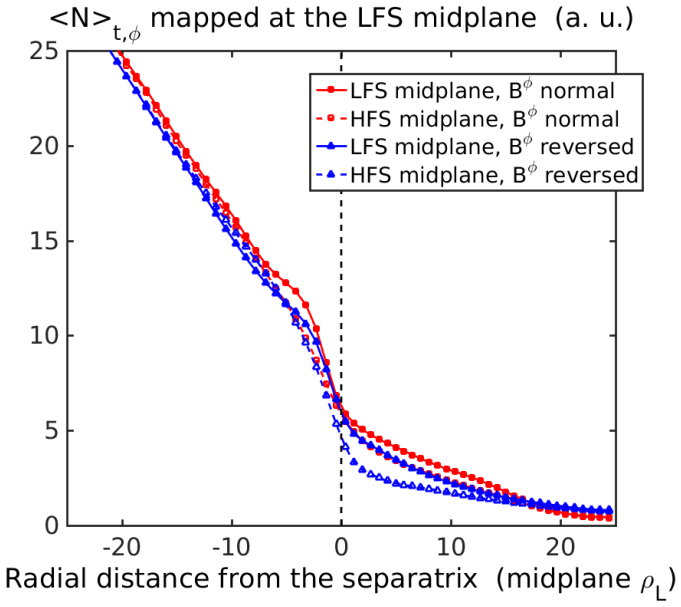

Figure 4.11: *Radial profile of the average density at LFS and HFS midplane for normal and reversed toroidal field in the COMPASS-like reference simulation. Profiles are remapped at the LFS midplane.*

the temperature at the target drops considerably, the ionisation plasma source, located in the vicinity of the target, largely exceeds the particle source coming from the core, by a factor up to 100. Following the model presented in this chapter, this would mean a strong increase of the parallel Mach number in front of the targets, and a substantially flat profile elsewhere. Nevertheless, the global poloidal asymmetry of parallel flux seems to be a universal feature in L-mode discharges. In [106], in fact, it is shown that different tokamaks in different operating conditions show a similar trend of the parallel Mach number in the SOL. Accurate measurements of parallel flows on Alcator C-mod ([41], [43]), find the same pattern of SOL parallel flows independently from divertor regimes. A possible explanation is advanced in the work by B. LaBombard et al. [41]: the ionisation source coming from walls could follow a different and independent flow loop, being suddenly transported to the main chamber by cross-field transport, and not contributing to the parallel flow in proximity of the separatrix. However, in order to consistently verify this hypothesis, and evaluate the weight of different sources for the parallel flow, a turbulence code should be coupled with a neutral model. TOKAM3X is being developed in this sense, being recently coupled to the Montecarlo kinetic code EIRENE [113]. Other codes, such as GBS, already implement a kinetic model for neutrals. In the work by Wersal et al. [114], turbulent simulations are run with the neutral model activated, showing cases characterised by different average densities. The effect of the change in average density on the parallel Mach number profile seems to be small: simulations did not explore, though, a full high-recycling regime, so further investigations on this problem are needed.

4.4 Effect of divertor transport on SOL width

We have seen in Chapter 3, that turbulence is observed in the outer leg of the divertor, both in experiments ([115], [32]) and in simulations. In TOKAM3X, this turbulence is also associated with a non-negligible particle flux. We aim at understanding, so, if the turbulent transport in the divertor region can affect the density profile at the outer divertor target. In order to do this, we take advantage both of recent experimental results, and of TOKAM3X simulations.

4.4.1 Experimental evidence of density spreading in a long outer divertor leg

Recent experiments have been carried out on the TCV tokamak, with the objective to inspect the influence of the divertor leg length on the SOL width [108]. TCV is a tokamak which allows a flexible magnetic geometry, through the action of 16 independent poloidal coils, so it is suitable for this kind of experiments. Moreover, it is equipped a large set of diagnostics. For the above-mentioned experiment, conditions at the LFS midplane are monitored through the HTRS (High Resolution Thomson Scattering), and, in the SOL, by a reciprocating Langmuir probe. At the outer strike point position, both Langmuir probes and infrared cameras are used to measure the plasma heat flux.
Three different plasma geometries have been investigated, maintaining the same set of parameters (plasma current, plasma major and minor radii, toroidal field and input power). The only geometric feature varying from one configuration to the other is the outer divertor leg length: the magnetic geometries explored in the experiment are shown in figure 4.12.

One can notice from figure 4.12 that, along with the change in the poloidal length of the outer divertor leg, also the parallel connection length between the outer strike point and the outer midplane is affected. One of the requirements of the experiment, was to maintain in the three cases the same plasma conditions, in order to inspect independently the effects of the divertor leg length. This condition has been verified for the closed flux surfaces region by means of the Thomson Scattering, which has revealed similar profiles up to the separatrix in the three cases. However, as it is clear from figure 4.12, the reciprocating probe was able to acquire data only in the intermediate leg length configuration: it is assumed that, by continuity with edge conditions, also the radial profiles at the LFS midplane in the SOL plasma are similar in the three configurations.
We are interested here in the density radial profile at the outer target. Similarly to the technique usually adopted in the study of the heat flux profiles ([26], [30]), one can fit the radial density profile through a convolution of an exponential and a Gaussian function:

$$n(x) = \frac{n_0}{2} exp\left(\left(\frac{\mathcal{S}_n}{2\lambda_n}\right)^2 - \frac{x}{\lambda_n f_x}\right) \cdot \mathrm{erfc}\left(\frac{\mathcal{S}_n}{2\lambda_n} - \frac{x}{\mathcal{S}_n f_x}\right) + n_{bg} \tag{4.13}$$

where x represents the linear coordinate along the target, with origin at the separatrix,

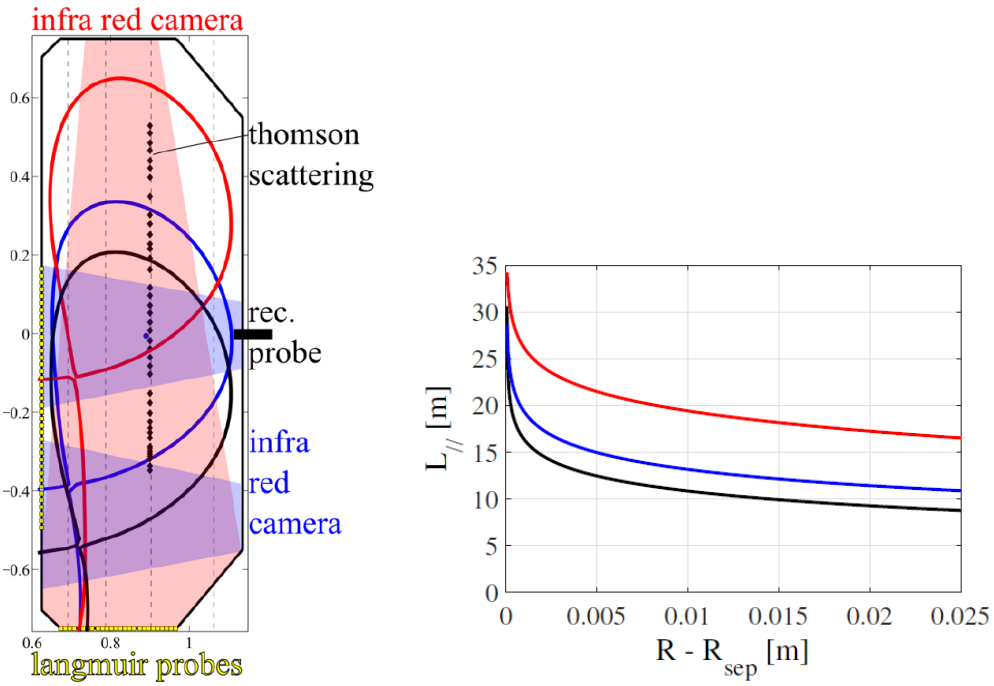

Figure 4.12: *Left: Sheme of a section of the TCV vessel, with the diagnostics involved in the experiment, and the three plasma shapes investigated. Right: Connection length from outer midplane to outer target in the three configurations, with colors corresponding to the left figure. Figure reprinted from [103].*

remapped to the LFS midplane. n_0 is the density value at the separatrix, and n_{bg} is a background density. The $\mathcal{S}_n$ parameter, called *spreading factor*, represents the width of the Gaussian function: physically, in the usual interpretation, it is a measure of the transport occurring along the divertor leg, towards the Private Flux Region. The λ_n factor instead, is the usual density decay length. This quantity must be remapped at the LFS midplane, and, in the common interpretation of experiments, it is a measure of the competition of the perpendicular and parallel transport processes occurring in the main SOL. Figure 4.13 shows the λ_N and the $\mathcal{S}_n$ factors resulting from the experiments.

It can be inferred from results shown in figure 4.13, that the density decay length increases almost linearly with the poloidal divertor leg length. Instead, no clear trend can be put in evidence on the spreading factor $\mathcal{S}_n$. These results are hardly explainable with the usual picture of the SOL transport. Indeed, from [26], the transport processes in the divertor are thought to be symmetric in the outwards and in the inward direction, leading to a bigger Gaussian spreading of the density profile if the divertor leg is increased, while the density decay length should be fixed by the upstream transport processes, and not affected by the divertor ones.
The numerical modelling of this experiment has been initially carried out with the 2D transport code SolEdge2D. Although the integrated values of density and heat flux profiles at the target have shown a good agreement with experiments, SolEdge2D simulations did not capture the modification in the profiles shape with the divertor leg length highlighted by experiments [103]. It has been decided, therefore, to utilise the TOKAM3X

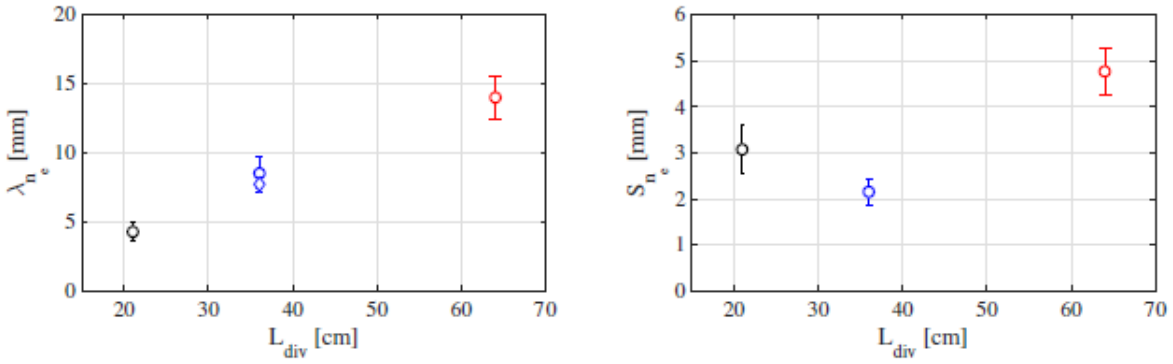

Figure 4.13: *Left: Density decay length at the target, measured by Langmuir Probes and remapped at LFS midplane, in the three geometries described before. On the abscissa, the poloidal length of the divertor leg in the three cases. The diamond in the intermediate case represents the reciprocating probe measurement at the LFS midplane. Right: Density spreading factor for the three cases. Figure reprinted from [103].*

code in order to have a deeper insight on transport processes occurring in the three different cases, which can have an impact on radial profiles.

4.4.2 Interpretation of experimental results by means of TOKAM3X simulations

The three magnetic equilibria involved in the experiment are used to create TOKAM3X mesh grids, which we will call in the following *short leg*, *medium leg* and *long leg*. Three simulations are run with the same parameters and the same particle source. The aspect ratio is fixed to 4.1, as in experiments, and the poloidal field amplitude is regulated so that the ratio $B^\theta/B^\varphi \simeq 0.16$ is the same as in experiments. A resistivity $\eta_\parallel = 2.5 \cdot 10^{-6}$ has been imposed, correspondent to a plasma at 39 eV and density $7.5 \cdot 10^{18} m^{-3}$. These data are relative to the LFS midplane, at the separatrix position, and are derived from experimental measurements with the reciprocating Langmuir probes. The diffusion coefficients and the particle source are fixed as in the reference simulations (see section 2.7.2). Figure 4.14 shows an example of density fluctuations in the three cases, with turbulent activity in the divertor.

Experimental and numerical results obtained with TOKAM3X are not quantitatively comparable for several reasons. First of all, the simulated plasma is characterised by a $\rho^\star = \rho_L/a = 3.9 \cdot 10^{-3}$. In the above-mentioned experiments, taking as reference the separatrix point at LFS midplane, $\rho_L \simeq 6.4 \cdot 10^{-4}$ m and $a \simeq 0.22$ m, giving $\rho^\star = \rho_L/a = 2.9 \cdot 10^{-3}$. The simulated machine is thus $\sim 25\%$ smaller than the real one. Moreover, TOKAM3X simulations are isothermal, so that the Larmor radius value does not change in space with temperature, contrarily to real experiments. This would result in a deformation of the observed profiles, proportional to $\sqrt{T/T_0}$, where T_0 is the reference temperature. Finally, since the presented TOKAM3X model cannot catch the

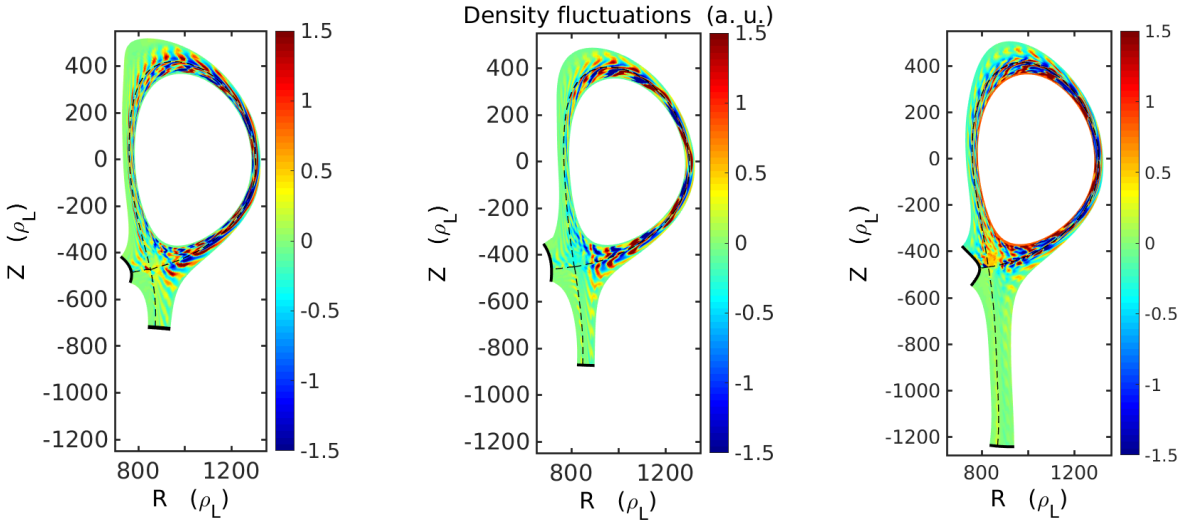

Figure 4.14: *Snapshot of density fluctuations in TOKAM3X simulations of TCV short leg (left), medium leg (centre), and long leg (right) configurations.*

temperature evolution and the plasma-neutral interaction, it cannot recover the different divertor regimes (see [12], Chapter 5, for an extensive discussion on divertor regimes). Experiments were characterised by a high-recycling regime ([103], [116]), where temperature varies in parallel direction and drops at the targets: this aspect cannot be described by TOKAM3X simulations. However, exploiting the flexibility in geometry definition, TOKAM3X can be useful to carry out a qualitative analysis of the modifications in transport processes with the modification in magnetic geometry.
First of all, we verify that the hypothesis underneath the experiments are indeed verified in simulations. The three simulations evolve to a similar overall equilibrium, and an exponential fit of the average density radial profiles at the LFS midplane (calculated at the separatrix) gives:

$$\lambda_N^{SHORT} \simeq 9\ \rho_L \qquad \lambda_N^{MEDIUM} \simeq 11\ \rho_L \qquad \lambda_N^{LONG} \simeq 11\ \rho_L \tag{4.14}$$

so comparable density decay lengths at the LFS midplane, with a difference of around 20% among the short leg case and the others. Figure 4.15 shows a poloidal profile of the density radial decay length along the main SOL.

One can notice that the density decay length is comparable over the majority of the poloidal extension of the main SOL, with a difference around the 20%. When getting close to the X-point, the density radial profile starts suddenly to flatten, and also the λ_N discrepancy grows among the different cases. At the target, as shown in figure 4.16, TOKAM3X profiles have a shape comparable to the experimental one, and suitable for a fit with the multi-parameters function (4.13).

We observe that the average density falls very rapidly in the PFR, both experimentally and in the code. This is due to the fact that the connection length $L_\parallel$ is much shorter in this region than in the SOL, by a factor around 10. As explained in Chapter 1, the

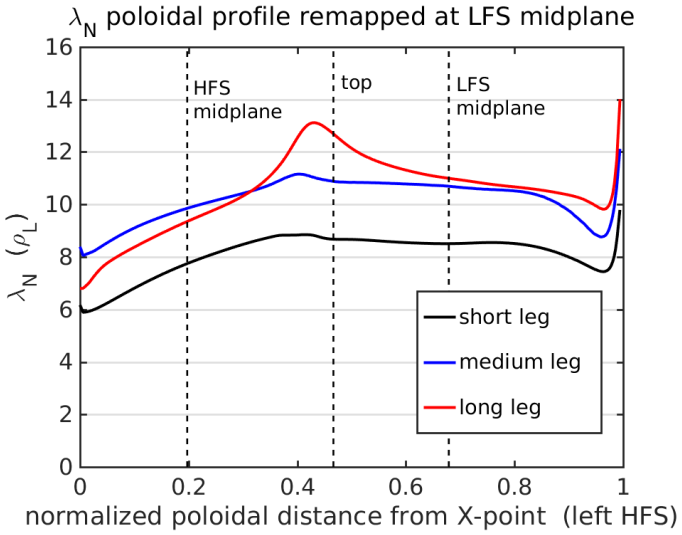

Figure 4.15: *Density decay length λ_N along the main SOL, for the three TOKAM3X simulations, obtained by an exponential fit at the separatrix.*

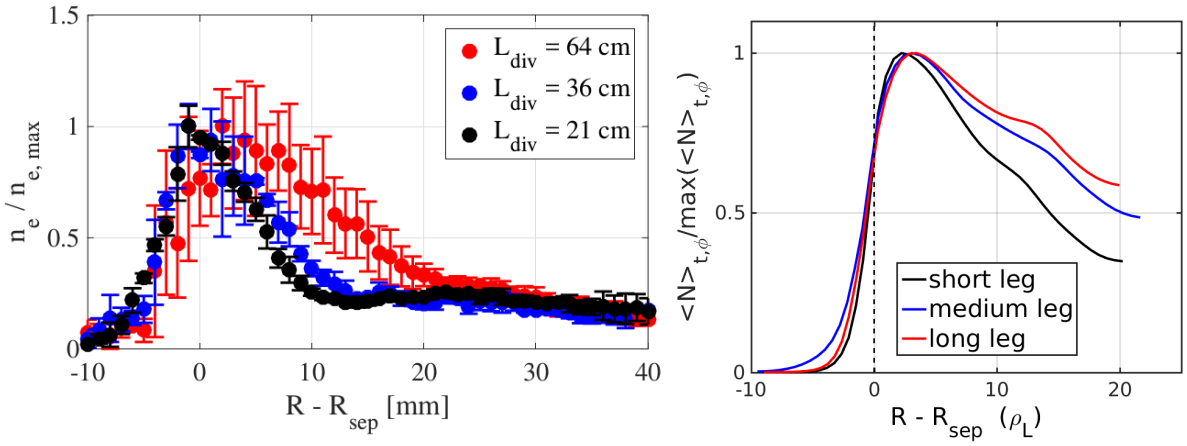

Figure 4.16: *Left: Density profile measured at the outer target of TCV by Langmuir probes and relative errorbars, normalised to its maximum value and remapped at the LFS midplane. Figure reprinted from [103]. Right: Normalised average density profiles calculated by TOKAM3X, remapped at LFS midplane.*

density decay length is proportional to $\sqrt{L_\parallel}$ in a diffusive case and to $L_\parallel$ in a convective case. In both cases, a much shorter decay length is expected in the PFR than in the divertor legs.
At the target we register a factor 2 of difference in λ_N between the shortest and the longest divertor leg case, the medium length case showing an intermediate behaviour. In particular, a fit with the function (4.13), gives:

$$\lambda_{N,t}^{SHORT} \simeq 16\ \rho_L \qquad \lambda_{N,t}^{MEDIUM} \simeq 25\ \rho_L \qquad \lambda_{N,t}^{LONG} \simeq 31\ \rho_L \tag{4.15}$$

where values are always referred to the profile remapped at the LFS midplane (even if

the magnetic flux values at the target are comparable in the three cases). Even if our aim is not a quantitative comparison between simulations and experiments, one can see that multiplying these values by the Larmor radius in the edge plasma of the analysed shots ($\sim 6.4 \cdot 10^{-4}\ m$), one obtains values of the same order of magnitude found in experiments. There is no clear trend, instead, describing the spreading factor variation in the three cases:

$$\mathcal{S}_{n,t}^{SHORT} \simeq 1.9\ \rho_L \qquad \mathcal{S}_{n,t}^{MEDIUM} \simeq 2.7\ \rho_L \qquad \mathcal{S}_{n,t}^{LONG} \simeq 2.3\ \rho_L \tag{4.16}$$

where the largest value is registered in the intermediate case. These values are nevertheless very small, since the density radial profile in the PFR is sharp, and extends over few points of the mesh grid.
Now we can analyse the behaviour of density average profiles along the divertor leg. Figure 4.17 shows the λ_N and $\mathcal{S}_n$ profiles along the outer divertor leg, derived from the fit of the radial average density profiles with equation (4.13).

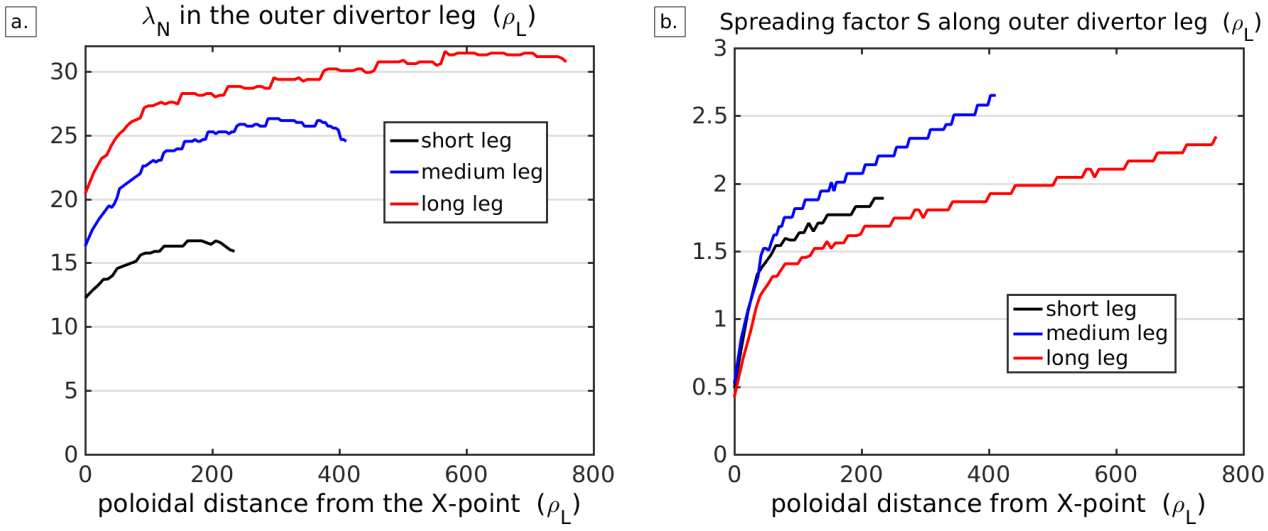

Figure 4.17: *a) Density decay length, remapped at LFS midplane, along the outer divertor leg in the three cases. The leftmost point of every curve represents the X-point position, the rightmost the target one. b) Density spreading factor along the outer divertor leg.*

Figure 4.17 shows a strong increase in $\mathcal{S}_n$ around the X-point, followed by a slower growth up to the target, with a similar slope in the three cases. The $\mathcal{S}_n$ factor translates the effect of a symmetric transport acting all along the outer divertor leg, which apparently has similar effects on the density profiles in the three cases. It is therefore logical to expect to reach higher spreading factors at positions close to the target.
The value of the density spreading factor is almost an order of magnitude lower than the density decay length. The spreading effect of diffusion is low in TOKAM3X simulations, where diffusive transport is kept as low as possible. In this region, instead, transport associated to turbulence and to the mean-field $E \times B$ drifts, dominates in TOKAM3X simulations. Turbulent fluxes contribute to the density spreading with fluxes directed

towards the outer radial direction, while non-negligible $E \times B$ mean-field fluxes can cross the separatrix in the divertor in inward radial direction. The effect of these two mechanisms is difficult to distinguish, and this operation would require dedicated simulations. However, the part of the profile shape in the PFR seems to be less sensible to the variation in the divertor geometry, and to the associated transport conditions. Interestingly, also TCV experiments show a low variation of the spreading factor with the divertor leg, suggesting an asymmetry in transport processes.

Figure 4.17a shows an increasing trend of the density decay length along the outer divertor leg. λ_N increases strongly in the first 100 ρ_L past the X-point (in this zone an increase is observed also in $\mathcal{S}_N$), and grows then more slowly up to the divertor target. This is an imprint of an active transport mechanism in the divertor region where, as we have seen in COMPASS-like simulations, both turbulence and mean-field drifts contribute to the transport.

TOKAM3X finds an approximately linear increase of λ_N with the total divertor leg length, in qualitative agreement with experiments. Considering the increase of the parallel connection length between the short leg and the long leg divertor case, one could expect, in the case of convective transport, an increase in the average λ_N proportional to $L_\parallel$, according to the simple relation (1.64). It is remarkable, however, that while at the LFS midplane the decay lengths are comparable, the main differences start to be visible in the region included between the X-point and the LFS midplane, getting amplified near the X-point and, finally, presenting a factor 2 difference at the target. These results show that the divertor region has an important weight in the determination of the transport across a flux surface.

Globally, TOKAM3X simulations show a divertor region with predominant asymmetric transport processes, among which turbulence, which transports particles preferentially in the outwards direction. Transverse transport processes contribute to the spreading of average density profiles, which are broader for longer divertor leg lengths. These simulations could provide important indications for the design of the divertor of new devices. Indeed, if we assume that heat transport behaves similarly to particle transport, a longer divertor leg could help in spreading the λ_q, thus limiting the power heat flux at the divertor targets. In this framework, it is worth to notice that measurements carried out in the above-mentioned experiment show the described trends also for the heat flux decay length in TCV L-mode plasmas [103]. These experimental investigations are being extended at present to H-mode plasmas in TCV, and could be tested soon in the super-X divertor of MAST-Upgrade, where the outer divertor leg will be significantly stretched.

Chapter 5

Impact of X-point geometry on radial turbulent transport

Contents

We inspect here the influence of a complex geometry on the turbulent transport, and, by consequence, on the radial equilibrium. In particular, the effects of flux expansion on confinement are described. We study TOKAM3X simulations in X-point geometry, which show an increased stability with respect to the ones in limiter configuration, with the presence of a spontaneous transport barrier in the vicinity of the separatrix. Finally, we describe the effects of transport barriers on turbulence, and we investigate the possible causes of their build-up.
Part of the topics treated in this chapter are included in the publication [117].

Since a complete theoretical understanding of the processes which determine the SOL width is not yet achieved, the design of the divertor of new devices, such as ITER, has been based up to now on empirical scaling laws. Focusing on L-mode plasmas, which are the ones treated in this thesis, existing scaling laws approximately show a dependence of λ_q on the inverse of the poloidal field at the LFS midplane. This is true both for limited ([28], [27]) and for diverted plasmas [29]. Nevertheless, once fixed the plasma current (and therefore the poloidal field), a higher multiplicative factor appears in the scaling laws referred to limited plasmas, determining a higher λ_q than in divertor. From a complementary point of view, the scaling laws show also that the divertor configuration is characterised in general by a better confinement than a limiter one. In this chapter, we examine the role of the geometrical features introduced by an X-point geometry in determining the confinement.

5.1 Flux expansion effect on turbulent transport

The poloidal field generated by the divertor coils, in X-point geometry, introduces a strong variability of the poloidal field across the poloidal section, and therefore a strong shaping of flux surfaces. We need now to understand how these geometrical features can affect the turbulent transport. We focus, first of all, on the effect of the local flux expansion on turbulent transport.
In chapter 3, we have presented an effect of the flux expansion on the poloidal extension of the structures, and, by consequence, on fluxes in the transverse direction. This effect is caused merely by the great effectiveness of the parallel transport with respect to the perpendicular one. We want now to put ourselves in a framework independent from this first-order geometrical effect. We are indeed interested in the effect of flux expansion on turbulent transport of particles across the flux surfaces, independently from the physical spacing among them.

5.1.1 Three limiter cases with different Shafranov shifts

The divertor geometry is characterised by an highly variable flux expansion in the poloidal plane, with a singularity at the X-point. Therefore, it is difficult to study, and quantify, the possible effect of the local flux expansion on turbulent transport. In order to tackle this problem, we build three analytical TOKAM3X mesh grids, including an infinitely thin limiter at the bottom of the plasma. These three geometries are characterised by a controlled flux expansion at every poloidal location, and are represented in figure 5.1.

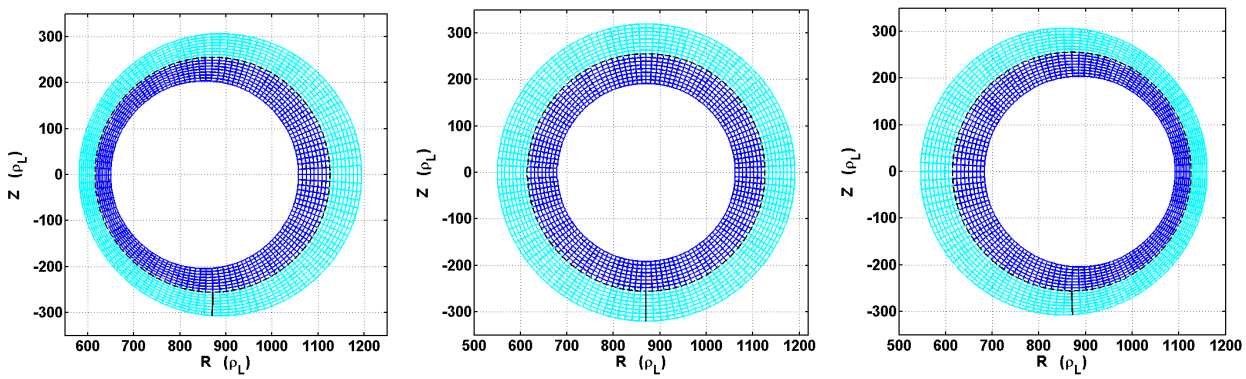

Figure 5.1: *On the left, poloidal section of the mesh for the inner shift case. On the centre, the case without shift. On the right, the mesh used for the outer shift case. The mesh grid is represented 4 times coarser than the actual one, in order to increase visibility.*

Flux surfaces are circular in all of the three geometries. The minor radius of each flux surface is the same for the three cases, while the only difference is the centre position of each flux surface, which is calculated as:

$$R_\psi(\psi) = R_0 + \Delta(\psi) = R_0 + S_\Delta\,(r(\psi) - a) \tag{5.1}$$

Where Δ is the Shafranov shift, defined as the displacement with respect to R_0 of the centre of the Last Closed Flux Surface, and the shift parameter S_Δ for the three mesh grids is respectively $1/3$, 0 and $-1/3$. These three cases will be referred to in the following as "inner shift", "no shift" and "outer shift" respectively. We impose, as additional constraint, the same safety factor profile $q(\psi)$ in the three geometries, and in particular the same parabolic profile of the reference limiter simulation is adopted (see section 2.7.2). The resulting poloidal field B^θ, which represents the main difference among the three cases, is represented in figure 5.2:

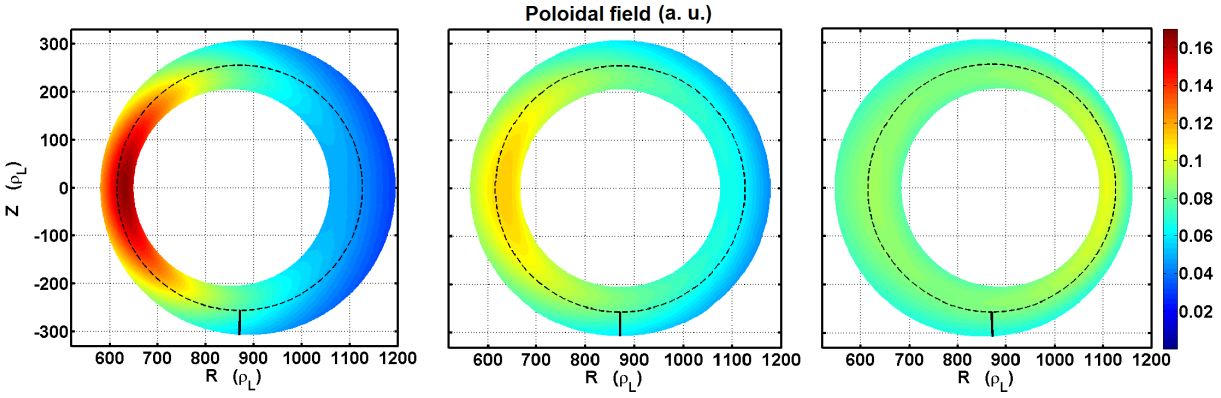

Figure 5.2: *Poloidal magnetic field for the three considered cases.*

As one can notice from figure 5.2, in the inner shift case flux surfaces are compressed on the HFS, so in order for the poloidal magnetic flux to be conserved, the poloidal magnetic field peaks at this position. In the outer shift case, on the contrary, the poloidal magnetic field is maximum at the LFS midplane. In the case without shift, there is no flux expansion, and the peaking of the poloidal field on the HFS is due to the smaller available surface ($\propto R$): this is a finite aspect ratio effect.

With this choice of the geometry, the flux expansion $f_x = \left\langle \|\vec{\nabla}\psi\| \right\rangle_\theta / \|\vec{\nabla}\psi\|$ on the HFS of the outer shift case ($f_x \simeq 1.4$) is twice the one on the LFS, and vice-versa for the inner shift case.

It is clear that the inner shift case does not represent a usual magnetic equilibrium for a tokamak. Indeed, poloidal field is radially stronger at the LFS, in order to balance the pressure force directed radially outwards, as can be inferred by the solution of the simplest MHD model for equilibrium (1.13). A plasma with a magnetic field like the inner shift case would probably lead to an MHD unstable situation. This cannot be modelled through TOKAM3X, which adopts the electrostatic assumption. The inner shift equilibrium (and more weakly also the other two, as they do not represent a perfect solution of the Grad-Shafranov equation [6]) must be seen, so, as an exercise intended to investigate the change of electrostatic turbulence with a magnetic geometry modification, even if mesh grids do not represent real magnetic equilibria.

The particle source in shifted cases is adjusted in the three cases by a multiplicative factor, in order to be equivalent to the source in the limiter reference simulation. The physical parameters are kept equal in the three cases, and so coincide with the ones of the reference limiter simulation.

5.1.2 Flux expansion at outer midplane enhancing turbulent transport

In order to inspect the change in turbulent transport with the flux expansion we must place in a reference system independent from this geometrical parameter. Excluding the local pitch angle, which varies on the poloidal direction, the physical system is the same for the three cases. The system indeed is forced by the same particle source. The fluxes at the limiter interface, which constitute the sink mechanism, are given by the global particle balance, which, at the steady-state and with unnormalised quantities, writes:

$$\begin{aligned}\int_V S_n \, dV &= \int_{t1} \langle n \rangle_{t,\varphi} \, c_s \left| \vec{b} \cdot \vec{n}_s \right| 2\pi R \frac{d\psi}{\|\vec{\nabla}\psi\|} + \int_{t2} \langle n \rangle_{t,\varphi} \left| \vec{b} \cdot \vec{n}_s \right| c_s 2\pi R \frac{d\psi}{\|\vec{\nabla}\psi\|} \\ &\simeq 2\pi \int_{t1} \langle n \rangle_{t,\varphi} \, c_s \frac{R \left| B^\theta \right|}{B} \frac{d\psi}{\|\vec{\nabla}\psi\|} + 2\pi \int_{t2} \langle n \rangle_{t,\varphi} \, c_s \frac{R \left| B^\theta \right|}{B} \frac{d\psi}{\|\vec{\nabla}\psi\|} \end{aligned} \tag{5.2}$$

where the integrals on the RHS must be calculated over the linear extension in the ψ direction of the interface between the plasma and the surface. In the limiter case t_1 and t_2 represent the two sides of the limiter. In divertor configuration, they represent the target plates. In both cases, $\vec{n}_s$ is the unitary vector perpendicular to the surface, and in the mesh grids used in this thesis coincides with the poloidal direction. In (5.2), the radial particle flux at the radial boundary is considered negligible. The Bohm condition in equality form $M = 1$ has been considered. Excluding the value of the mean density at the target, which is determined by the global equilibrium, the outgoing fluxes depend on the ratio B^θ/B. As one can notice from figure 5.2, the ratio B^θ/B is approximately the same in the three cases (at the limiter, the field line incidence angle is nearly the same since the only asymmetry in B^θ is left-right and not up-down).
Therefore, if the source and the sink mechanisms are the same in the three cases, we expect the same solution in a reference system independent from the flux expansion.
In a flux-driven system, as the one simulated by TOKAM3X, the radial flux, averaged over a flux surface, is constant in the radial direction and decays in the SOL because of the parallel losses. Radial gradients, instead, are not constrained. Therefore, a steep average density radial gradient reveals a good stability of the system, with respect to turbulent transport. Indeed, this means that in order to carry the same flux, a steeper gradient, which is the energy source for turbulence, is needed. We analyse, so, the density profile averaged on time and over a flux surface and we compare the three simulations, showing the result of the comparison in figure 5.3.

It is clear from figure 5.3 that the outer shift case is the most stable with respect to the interchange turbulence observed in simulations. The inner shift case shows instead the lower stability, while the reference limiter case shows an intermediate behaviour, even if it seems to be closer to the inner shift case. Since the average flux expansion on a flux surface is the same for the three cases, we can quantify the average density decay length in ρ_L remapping it on the LFS midplane of the limiter reference case. From an exponential fit at the separatrix, we obtain:

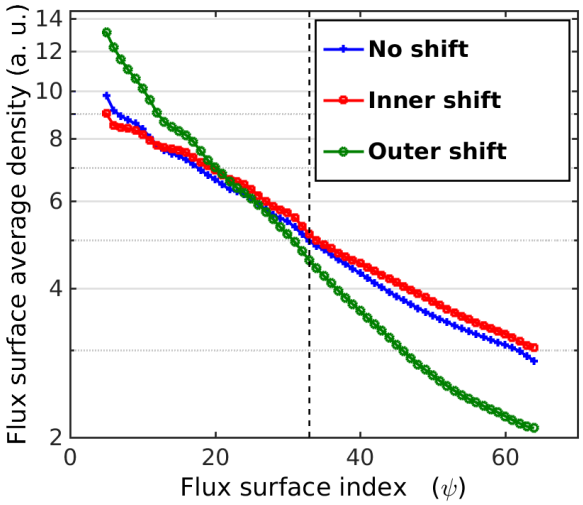

Figure 5.3: *Profile along the ψ coordinate of the density average over the flux surface, and in time, for the three considered cases. Points in the buffer region are artificially excluded for clarity.*

$$\lambda_N \simeq \begin{cases} 87\ \rho_L & \text{inner shift} \\ 80\ \rho_L & \text{no shift} \\ 50\ \rho_L & \text{outer shift} \end{cases}$$

One can see that the impact of the flux expansion on turbulent transport is pronounced, and in particular the outer shift case shows a much lower density decay length than the other two cases.

5.1.3 Driving and stabilisation mechanisms

We aim now at understanding what are the mechanisms that lead to different turbulent characteristics in the three cases. Firstly, we can look at the turbulence driving mechanisms.
Referring to the TOKAM2D model (2.48), we claimed that the curvature term driving the interchange instability can be modelled through a term named g, representing the average curvature on a flux surface. In TOKAM3X, the local curvature term is included in the term $2\vec{\nabla}\cdot(N\vec{u}^i_{\nabla B})$, appearing in the vorticity balance (2.38). In the framework of this analysis, we can name this term g_{loc}, in analogy with the TOKAM2D model. The local curvature term can be expressed as:

$$g_{loc} = 4\|\vec{\nabla}\psi\|\frac{\partial}{\partial\psi}\left(\frac{1}{B}\right) \tag{5.3}$$

This term reflects the spatial variation of the interchange growth rate, $\gamma^2 \propto \vec{\nabla}p\cdot\vec{\nabla}B$, considering a constant pressure over a flux surface. We can calculate, for a global 3D

simulation, the average curvature term on a specific flux surface. We choose, for the three simulations, a flux surface near the separatrix ($r/a \sim 0.99$), and we perform the integration

$$\langle g \rangle_{\parallel} = \left(\int_0^{2\pi} g_{loc} \frac{B}{B^\theta} \mathrm{d}\theta \right) / \left(\int_0^{2\pi} \frac{B}{B^\theta} \mathrm{d}\theta \right) = \left(\int_0^{2\pi} 4 \frac{B \| \vec{\nabla} \psi \|}{B^\theta} \frac{\partial}{\partial \psi} \left(\frac{1}{B} \right) \mathrm{d}\theta \right) / \left(\int_0^{2\pi} \frac{B}{B^\theta} \mathrm{d}\theta \right) \quad (5.4)$$

Results are summarised in table 5.1.

	Inner Shift	No Shift	Outer shift
$\langle g \rangle_{\parallel}$ $(a.u.)$	$8.5 \cdot 10^{-4}$	$9.6 \cdot 10^{-5}$	$-6.9 \cdot 10^{-4}$
s	1.6	2.1	3.3

Table 5.1: *Geometric parameters affecting turbulence driving and stabilisation in the three magnetic configurations.*

These results for $\langle g \rangle_{\parallel}$ show that the average curvature on a field line is the lowest in the outer shift case, where $\langle g \rangle_{\parallel} < 0$: this does not mean that the plasma is stable. Indeed turbulence develops in the region of bad curvature, but extends then immediately in parallel direction towards the HFS. The case without shift has an almost null integrated curvature. In fact the curvature term, which has a cosine shape in theta direction, is shifted towards average positive values if the shift parameter S_Δ is positive, so in the inner shift case. Moreover, the poloidal field is lower at the LFS in the inner shift case. This translates into the fact that a longer portion of parallel field line is poloidally localised at the LFS, so in the region where plasma is unstable.
Among the stabilisation mechanisms, we have to consider also the magnetic shear. Indeed, even if we imposed the same $q(\psi)$ parabolic profile in the magnetic space, the safety factor profile along the physical radial coordinate changes in the three cases. In particular, the global magnetic shear (3.16) is stronger in the outer shift case. The magnetic shear value s, calculated for each geometry at $r/a \sim 0.99$, is reported in table 5.1. One can notice that the magnetic shear varies of more than a factor 2 from the inner to the outer shift case.
Interchange turbulence has been proven to be strongly sensitive to magnetic shear. In the work by Antonsen et al. [118], a simple explanation is given for the effects of magnetic shear on turbulence stabilisation. Basically, since the charge separation due to the curvature drift happens mainly in vertical direction, an electric potential dipole builds-up locally in correspondence of a density excess (namely a filament), accelerating blobs in the radial outward direction. Globally, on a flux surface, $E \times B$ advection is more effective if turbulent structures stay more aligned on the horizontal direction. Typically analytical calculations considering a simple toroidal geometry, show that the most unstable case coincides with the situation in which $s = 0.5$ [60]. For higher and smaller

values, the inclination of density structures with respect to the horizontal direction grows up (especially on the LFS), leading to more stable plasma edge behaviours. Figure 5.4 shows the orientation of density structures in the three simulations.

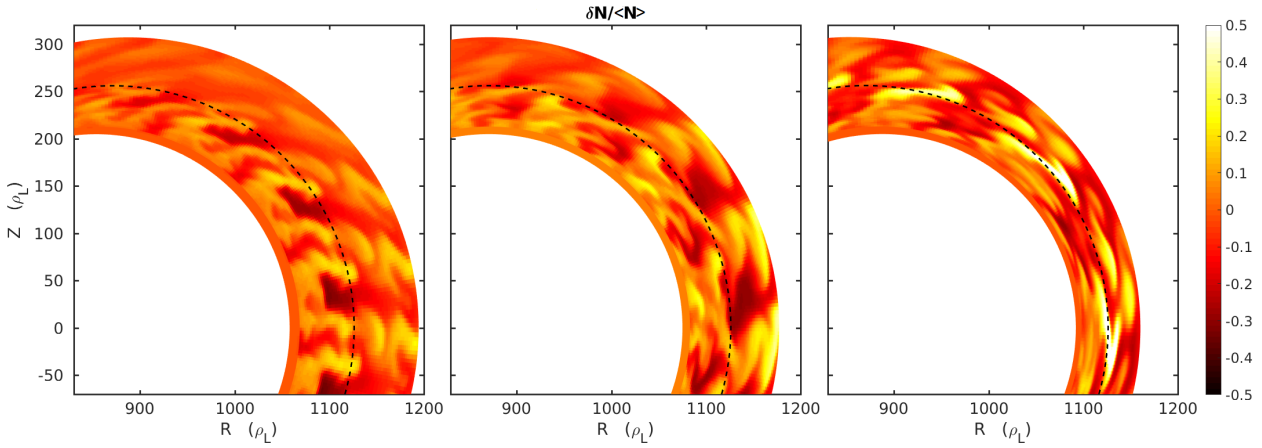

Figure 5.4: *Snapshot of the density fluctuation amplitude at a specific timestep normalised to the average value: focus on the region between LFS midplane and top.*

In the inner shift case turbulent structures stay aligned to the horizontal direction on a large poloidal angle span, approximately on the interval $-\pi/2 < \theta < \pi/2$. The orientation of turbulent structures is instead more and more tangential to the poloidal direction in higher shear cases, due to the increased poloidal field (or lower flux expansion).
In the three cases, the size of turbulent structures in poloidal direction are essentially unaltered. We underline also the fact that, as noticeable from figure 5.4, the modification in magnetic geometry leads to a density fluctuation amplitude progressively stronger for lower flux expansions at the LFS midplane.
We have scanned here the effect of flux expansion on turbulent transport in edge plasma, and we have seen that this parameter cannot be decoupled from the Shafranov shift, the safety factor and the magnetic shear. In [119] an accurate study is carried out on the effect of the triangularity ($\delta = (R_0 - R_{top})/a$) on turbulent transport, both with linear and non-linear simulations. Linear simulations show a stabilising effect of the Shafranov shift on RBMs, coherently with what is shown in the present analysis, and with theoretical predictions ([60], Chapter III). Non-linear GBS simulations show also a stabilising effect of negative triangularity, explaining this effect as driven by the small global curvature.
A statistical analysis [40] of TOKAM2D simulations gives the scaling law for the density decay length: $\lambda_N = g^{(0.3)}\sigma^{(-0.75)}\rho_L$, where σ is a parameter determining the parallel losses (so inversely proportional to the parallel connection length). This scaling has been tested also on a large set of experimental data from Tore-Supra L-mode discharges, showing a good quantitative agreement. TOKAM3X simulations results are in qualitative agreement with the 2D model, showing a weak proportionality to the curvature term, even if too few points are available to say if the scaling is respected. Moreover, in a 3D code as TOKAM3X poloidal asymmetries in turbulent transport are introduced, and the parallel flux is not constant on the field line (as shown in section 4.1), so evaluating correctly a parallel damping coefficient is not straightforward. This analysis of the flux expansion

effect would thus need a wider parametric scan, although it already gives important information about nature of turbulence, and inserts coherently in the panorama of turbulent simulations and experimental measurements.

5.2 Equilibrium in the divertor case

5.2.1 Comparison with limiter simulations

The most striking difference between limiter and divertor global turbulence simulations, run with the same sources and the same physical parameters, is given by the confinement. If we evaluate the particles confinement time τ_E as the ratio of the total number of particles in the closed field lines region and the particle source:

$$\tau_E = \frac{\int_V N \; dV}{\int_V S_N \; dV} \tag{5.5}$$

We obtain $\tau_E \sim 7.4 \cdot 10^8 / 2.0 \cdot 10^4 \; \omega_c^{-1} \sim 3.7 \cdot 10^4 \; \omega_c^{-1}$ for the reference limiter simulation and $\tau_E \sim 2.2 \cdot 10^9 / 1.9 \cdot 10^4 \; \omega_c^{-1} \sim 1.2 \cdot 10^5 \; \omega_c^{-1}$ for the divertor reference simulation. This is also the characteristic time of the evolution of our global physical system, needed to attain the convergence. By consequence, the computational cost for simulations run with the same mesh grid resolution, the same time step, and an initial condition of "empty box" (density and other fields null everywhere), is higher in divertor cases, proportionally to their confinement time.
Figure 5.5 shows a comparison of the flux-surface averaged densities in the reference COMPASS-like divertor and limiter TOKAM3X simulations.

One can notice from figure 5.5, that the radial density gradient in closed field line is much steeper in the divertor case, indicating an higher stability with respect to the interchange turbulence. In particular, the calculation of the characteristic decay length in the closed flux surfaces, which is an index of the efficiency of the transverse transport, gives:

$$L_N^{COMP} = \frac{\langle N \rangle}{\| \vec{\nabla} \langle N \rangle \|} \sim \; 19 \; \rho_L \qquad , \qquad L_N^{LIM} = \frac{\langle N \rangle}{\| \vec{\nabla} \langle N \rangle \|} \sim \; 62 \; \rho_L \tag{5.6}$$

where values are considered at the middle radial position of the closed flux surface region, and the average operation is performed on the flux surface and in time.
The observed modification in the stability of the system is reflected in a shorter density decay length in the SOL. Indeed, at the LFS midplane, $\lambda_N \simeq \; 12 \; \rho_L$ for the COMPASS-like configuration, and $\lambda_N \simeq \; 4 \; \rho_L$ for the JET-like configuration, values considerably lower than what is found in limiter geometry and shown in section 5.1.

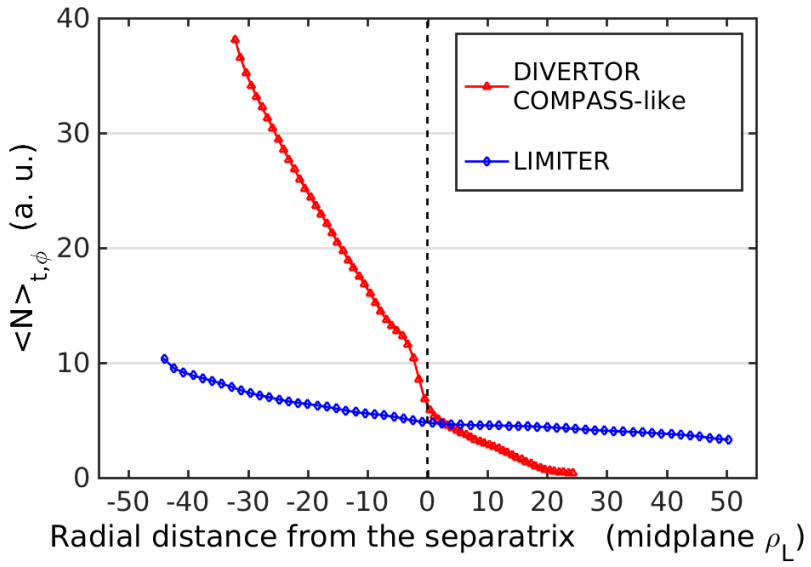

Figure 5.5: *Density averaged in time and on the flux surface, in COMPASS-like divertor and limiter reference simulations.*

5.2.2 Linear phase characteristics

A linear analysis of the TOKAM3X model is hardly comparable to our global simulations. We have seen indeed from the calculation of the parallel correlation length in chapter 3, that turbulent structures are strongly extended in the parallel direction. Since the linear analysis is based on local parameters, it cannot catch properly the global driving or stabilising effects on turbulent structures.
We decide therefore to measure a posteriori the linear growth rate in simulations, which can give us a useful indication on the stability of the system. Figure 5.6 shows the comparison of density fluctuations linear phases in divertor and limiter configuration. In order to analyse the evolution in time of fluctuations, we subtract to the instantaneous value the axysimmetric component $\langle N \rangle_\varphi$, being thus independent from the global evolution in time of the system.

In the divertor case, the time trace appears smoother because, in the early phase of turbulence, a single mode is dominant. Peaks and valleys are given by the fact that, as soon as the turbulent structure is created, it is advected poloidally by the average $E \times B$ drift. At the end of the linear phase, the levels of turbulence are comparable in the two configurations.
One can notice that the turbulence dynamics is much faster in the limiter case, with a linear growth rate, measured at the same position, which can be even a factor 6 higher than the divertor case. It must be specified that, the time trace represented in figure 5.6a, corresponds to the position of maximum linear growth rate for the COMPASS simulation. In figure 5.6b, the time trace is evaluated at the same position for comparison, but even higher growth rates can be found for smaller radii. Indeed, in both divertor and limiter cases, turbulence develops principally near the inner radial border, propagating then

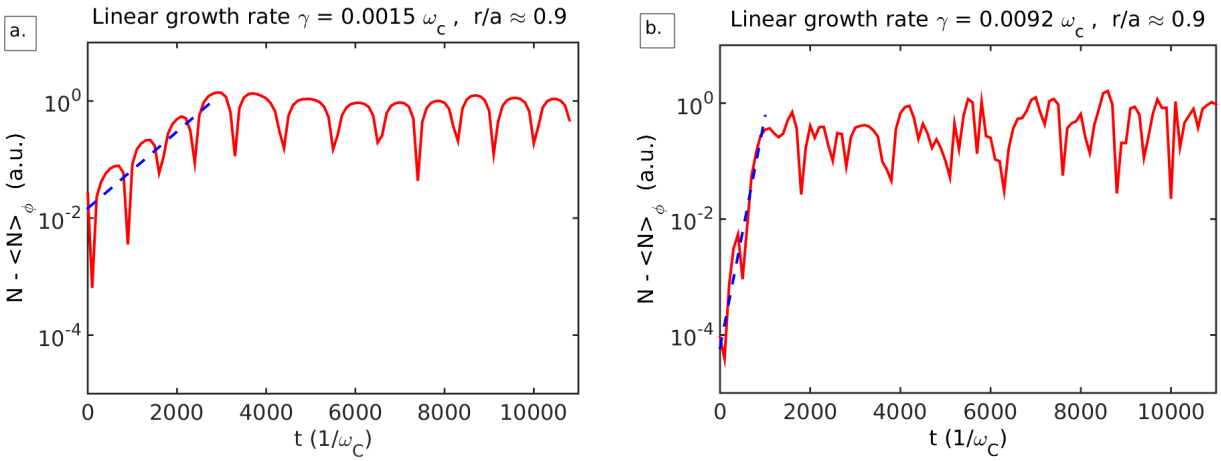

Figure 5.6: *a) Time trace of density fluctuations, calculated at the LFS midplane of the reference COMPASS simulation at $r/a = 0.9$, including the linear phase. In blue the exponential fit used to evaluate the linear growth rate. b) Same plot for a limiter configuration.*

radially outwards.
The calculated linear growth rate can be compared to the theoretical one, which, for a simple interchange system [120] where parallel and perpendicular advection are neglected, and only the curvature term is taken into account, can be expressed as:

$$\gamma^{THEO} = \frac{\sqrt{\langle \vec{u}^i_\star \rangle \cdot \vec{u}^i_{\nabla B}}}{\rho_L} \tag{5.7}$$

In COMPASS simulations,

$$\gamma^{THEO} \approx 9 \cdot 10^{-3} \omega_C \gg \gamma^{MEASURED} \approx 1.5 \cdot 10^{-3} \omega_C \tag{5.8}$$

In limiter simulations, instead, the actual linear growth rate is only a factor 2 lower then the theoretical one. This picture shows once again that, in TOKAM3X simulations, the divertor configuration is more stable towards the interchange turbulence. Therefore, a turbulence stabilising mechanism is likely at play with more efficiency in divertor than in limiter simulations.

5.2.3 Magnetic geometry parameters affecting equilibrium

The causes of the improvement in confinement can be multiple, as explained in section 5.1.3. We must analyse both the turbulence driving and the turbulence suppression mechanisms at play in our simulations.
Let's focus, for the moment, on the turbulence drive. In divertor geometry, the average curvature on a flux surface is performed as in section 5.1. The average value of the

curvature in parallel direction, over a poloidal turn, gives $\langle g \rangle_{\parallel} \approx -7 \cdot 10^{-4}$ for a flux surface close to the inner radial boundary. This value is comparable to what has been found in the limiter case with Shafranov shift (the "outer shift" case presented in section 5.1). Indeed, the curvature term depends mostly on the ratio ρ_L/R and on the Shafranov shift, which do not change significantly between the two configurations. Therefore, the global curvature in divertor configuration is stabilising, although it is not sufficient to explain the improved confinement with respect to limiter simulations.
As mentioned in chapter 3, the local magnetic shear in divertor configuration is not very different from the one in limited geometry at the LFS midplane, that is to say, where the turbulent transport is maximum. However, if we perform an average operation over a flux surface, we get significantly higher values for divertor configurations. In figure 5.7 we represent the average shear in parallel direction over a poloidal turn, for different magnetic geometries.

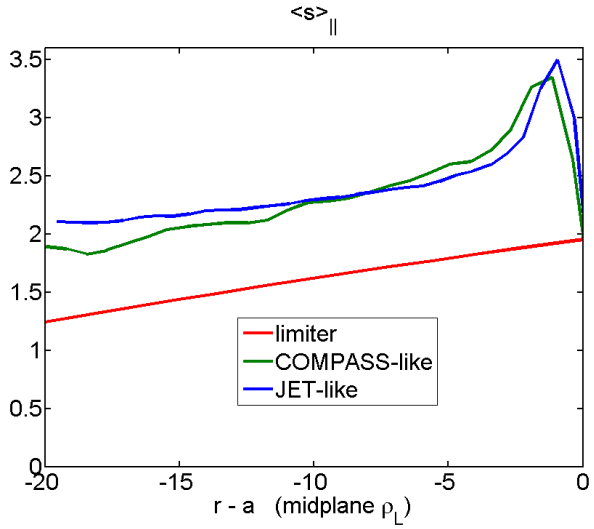

Figure 5.7: *Local magnetic shear averaged along the field line on a poloidal turn, remapped at LFS midplane, for the three reference simulations.*

One can notice that in the closed flux surface region, the average shear is considerably higher in divertor geometry than in limiter one. This happens because the poloidal field is perturbed by the X-point also at radial positions relatively far from it. In particular, in JET-like geometry the innermost region is characterised by the biggest magnetic shear, slightly higher than the COMPASS-like geometry. The two resulting equilibria are indeed comparable in the closed flux surfaces region (profiles shown in section 5.3).
Turbulence develops indeed, in TOKAM3X simulations, in the innermost flux surfaces of our domain, where the magnetic shear is minimum. Also, it develops much more easily in limiter configuration, with higher linear growth rates, as mentioned above. Even if this does not constitute a definitive explanation of the improved confinement in the divertor, we find a correlation between the average shear on a flux surface and the stability of our system, which is a theoretically known feature in simple magnetic geometries.
In divertor simulations a further element which contributes to the improvement of the confinement is the presence of a transport barrier, which is detailed in the next section.

5.3 Spontaneous transport barrier build-up in divertor geometry

A unique feature of the TOKAM3X simulations in divertor simulations is the presence of transport barriers, which are absent in TOKAM3X limiter isothermal simulations. We aim here at analysing their characteristics in TOKAM3X simulations in X-point geometry.
Fluid turbulence codes have addressed the transport barrier problem in various ways. On one hand, transport barriers were forced by reglating some physical parameters in 2D turbulence codes (see, for example, [121], [122]), then assessing the effect of barriers on turbulence properties. On the other hand, 2D turbulence codes have reproduced, without forcing artificial parameters, some transport barriers (see [35], [36], [37]) that in some case lead to a dynamics in the system behaviour coherent with an L-H transition. In 3D global edge turbulence simulations, macroscopic transport barriers have never been highlighted, in our knowledge. An enhancement of radial pressure gradient has been observed in GBS simulations in the first open flux surfaces [123], however not associated with a lowering of turbulence levels. In this chapter, we will describe the transport barriers occurring in TOKAM3X simulations with divertor configuration. First we identify them, then we characterise their effect on turbulence, and in the end we investigate the physical mechanism underneath their formation.

5.3.1 Characterisation of the transport barrier

The most important consequence of a transport barrier is the enhancement of the radial pressure gradient, which, in tokamaks, allows to achieve a higher pressure in the core plasma. TOKAM3X isothermal simulations in divertor configuration have shown an enhancement of the average density radial gradient in the proximity of the LCFS, as noticeable in figure 5.8.

We can notice from figure 5.8 that the local increase in the density gradient is more visible in the COMPASS-like case than in the JET-like one. Nevertheless, the presence of a transport barrier is a feature in common among all the divertor simulations that we run.
First of all, we decide to quantify the effectiveness of turbulent transport by the parameter R_b, defined as in [124]:

$$R_b = \frac{\left\langle \Gamma_E^{\psi} \right\rangle_{\theta,\varphi}}{\left\langle \Gamma_E^{\psi} \right\rangle_{\theta,\varphi} + \left\langle \Gamma_{Diff}^{\psi} \right\rangle_{\theta,\varphi}} \tag{5.9}$$

Equivalently, one could characterise the transport barrier through its efficiency, expressed by the criterion introduced in [39], $\varepsilon_{TB} = 1 - R_b$. We have seen in chapter 4, that the mean-field and the turbulent fluxes can actually have comparable orders of magnitude in the SOL. However, we must consider here the average fluxes on flux surfaces, which

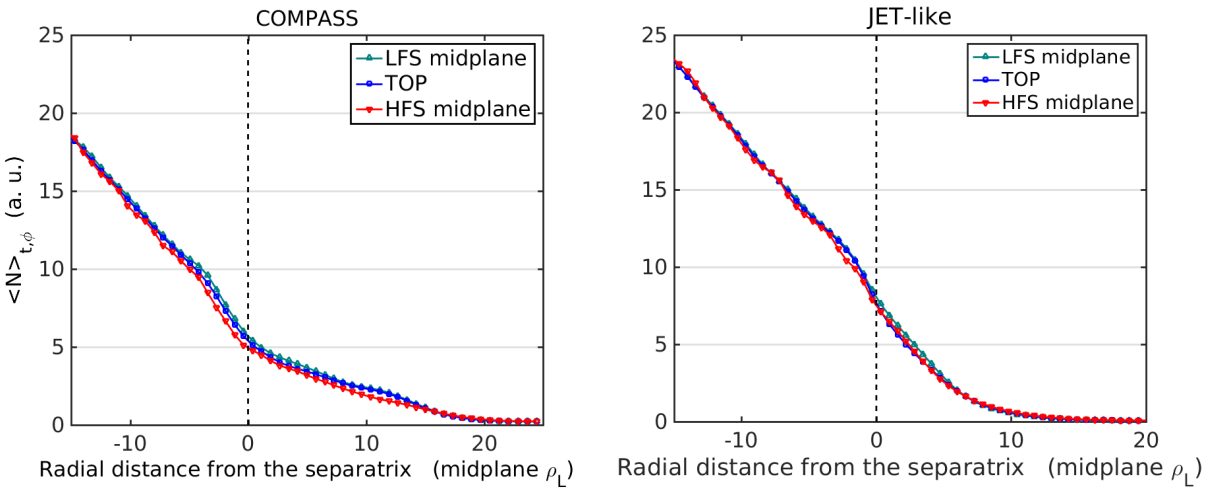

Figure 5.8: *Radial profiles of the average density at different poloidal position, for a COMPASS-like (left) and a JET-like (right) geometry. An enhanced radial gradient is visible near the LCFS.*

determine the net transport across flux surfaces. In our simulations, in the closed flux surfaces region, we have

$$\left\langle \langle N \rangle_\varphi \left\langle u_E^\psi \right\rangle_\varphi \right\rangle_\theta \ll \left\langle \tilde{N} \tilde{u}_E^\psi \right\rangle_{\theta,\varphi} \tag{5.10}$$

so the turbulent flux approximately coincides with the total flux. This hypothesis is not well fulfilled in the vicinity of the outer wall in radial direction, where fluctuations are considerably damped. However this region is not interesting from the point of view of the barrier build-up. It is useful to specify that the averaging operation on the flux surfaces is actually done weighting the fluxes by the surfaces that are affected:

$$\left\langle \Gamma^\psi \right\rangle_{\theta,\varphi} = \frac{\oint_\psi \vec{\Gamma} \cdot d\vec{S}}{\oint_\psi \|d\vec{S}\|} = \frac{\oint \vec{\Gamma} \cdot J \vec{e}^\psi d\theta d\varphi}{\oint J \|\vec{e}^\psi\| d\theta d\varphi} = \frac{\oint N u_E^\psi \, \|\vec{e}^\psi\| J d\theta d\varphi}{\oint J \, \|\vec{e}^\psi\| d\theta d\varphi} \tag{5.11}$$

In a flux-driven system, the transverse total flux averaged over a flux surface should be constant in the closed field lines, since the system is periodical both in the poloidal and in the toroidal directions, and no parallel losses intervene. Then, if the $E \times B$ turbulent transport is inhibited, and since the ∇B drift has a small divergence over the flux surface, the diffusive transverse flux will be locally enhanced, leading to a lower R_b index. Thus, an R_b coefficient close to 0 identifies a perfect transport barrier, while on the contrary $R_b \sim 1$ is characteristic of a weak or non existent barrier. Figure 5.9 shows the R_b coefficient, calculated for a given timespan, in a simulation in COMPASS diverted geometry, characterised by a diffusion coefficient of $1 \cdot 10^{-3} \rho_L^2 \omega_C$.

As one can notice, a mild transport barrier appears in the closed field lines, in the vicinity of the separatrix. The region affected by the transport barrier is very thin, of the

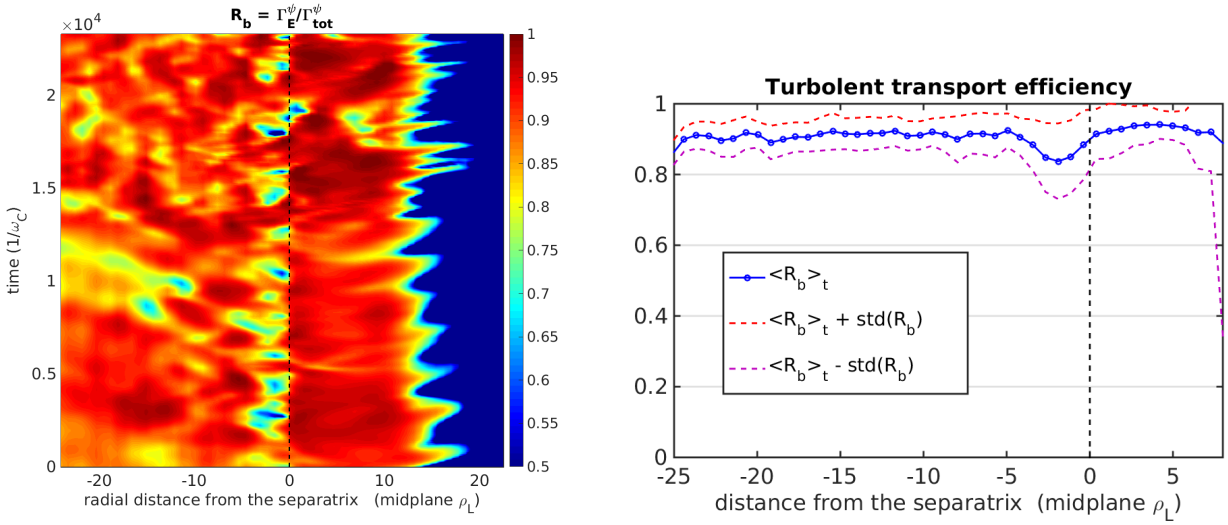

Figure 5.9: *Left: Turbulent transport efficiency coefficient R_b in a COMPASS-like simulation. On the abscissa, the radial distance from the separatrix is represented. On the ordinate, the time. The separatrix position is indicated by a black dashed line. Right: Turbulent transport efficiency averaged over a typical simulation time of $3 \cdot 10^4$ ω_C^{-1}. Dashed lines show the sum of the time-average and the standard deviation in time of the R_b fluctuations.*

order of 5 ρ_L: it must be admitted here that the drift-reduced model is at the limit of its applicability domain, since this structure develops on few Larmor radii. From the numerical point of view, the barrier affects mainly five-six points in our domain, highlighting the fact that a high resolution is necessary in this region to capture the phenomenon of transport barrier build-up.

In a COMPASS-like simulation with a diffusion coefficient $D_N = 10^{-3}\rho_L^2\omega_C$, turbulence carries on average the 80% of the flux in the barrier region. However, as visible in figure 5.9b, the standard deviation fluctuations of the turbulent transport efficiency value is around 0.1, and R_b can be reduced up to the 50%.

Outside the transport barrier, in the closed field lines region, turbulent $E \times B$ flux clearly prevails on the diffusive one. Averaging on time and on the flux surface, the diffusive flux sets around the 10 % of the total one. This is the residual value of the diffusive flux in the closed flux surfaces region, which is determined by local conditions and does not show a regular structure. Nevertheless, the drop in turbulent transport efficiency due to the transport barrier is clearly detectable, recognisable by its strong amplitude and its regular pattern in time. In other terms, at the barrier position, the diffusive flux is amplified by a factor $2 - 2.5$.

The values of the diffusion coefficients have been scanned in the range $[10^{-3}; 5 \cdot 10^{-3}]$ finding a finding a strong sensitivity of the R_b factor in the diffusion coefficient. In particular, decreasing the diffusion coefficients varies proportionally the diffusive flux, whereas the turbulent flux increases its relative weight. Globally, the gradients at the barrier position remain comparable.

In the SOL, the radial propagation of turbulent events is clearly visible from figure 5.9,

with a frequency around 10^3 ω_C. When getting closer to the outer wall, turbulence levels are progressively lowered by the action of parallel transport, with a sudden drop of R_b at around 14 ρ_L outside the separatrix. This value is comparable to the characteristic SOL radial decay length in COMPASS diverted simulations, which is around 12 ρ_L.
In our simulations, the increased density gradient is not enough energetic to trigger a relaxation event. The damping mechanisms here appear to be strong enough to lower fluctuations amplitude. However, isolated turbulent events can pass the barrier, without being significantly affected, as visible from figure 5.9 (left).
The transport barrier found in TOKAM3X divertor simulations seem to have some characteristics in common with the ones found in the 2D fluid turbulence code TOKAM2D in the work by Ph. Ghendrih et al. [125]. In those simulations, a transport barrier was triggered by an artificial suppression of the curvature driving term, in a specific region of the domain. The barrier was characterised by a bell shape in radial direction, and by a steady minimum value of the R_b factor (which was, however, close to 0.03, much lower than the one found in divertor simulations). In divertor geometry, the transport barrier builds up in a zone where the driving terms are normally at play. Instead, stabilising mechanisms are probably determining the decrease of density and potential fluctuation levels. These similarities suggest that a linear, steady mechanism of turbulence damping is at play.

5.3.2 Effects of transport barriers on turbulence properties

In order to understand which is the cause of the reduction of the turbulent flux it is useful to evaluate the nature of turbulence in the zone of the transport barrier. Figure 5.10 shows the standard deviation of density and potential fluctuations averaged on the poloidal coordinate.

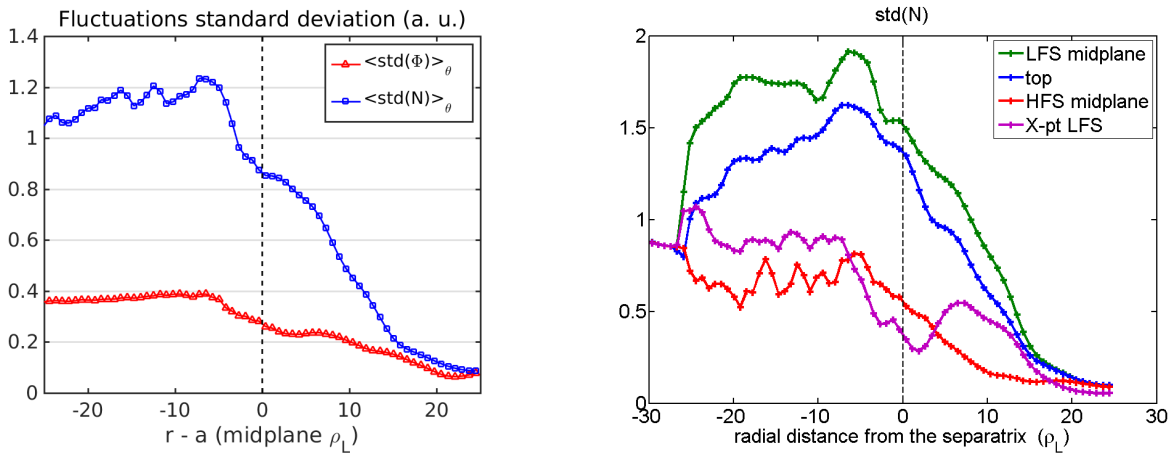

Figure 5.10: *Left: Standard deviation of density and electric potential fluctuations, sampled in time and toroidal direction and averaged on poloidal direction. In the SOL, only the main SOL is taken into account. Radial profiles are remapped at the LFS midplane. Right: standard deviation of the density fluctuations at different poloidal positions.*

One can notice that potential fluctuations are reduced in the barrier region by up to a 40%. However, density structures are more impacted at poloidal positions near the X-point. As visible in figure 5.10b, density fluctuations get strongly damped near the X-point, in the region of the barrier ($r/a \simeq 0.99$). In this region, the structure coherence is lost, as well as the typical shift of $\sim \pi/2$ which is normally found in the rest of the domain. In the barrier region, electric potential fluctuations are lowered in an homogeneous way on the whole field line. The k_θ spectrum is not strongly impacted in the barrier region, at positions away from the X-point.
Globally, over the whole flux surface, the average fluctuation amplitude is lowered at flux surfaces close to the separatrix: this can be due to the spreading of a local effect on the turbulent structure extension. Indeed, since turbulent structures are almost field-aligned, the action of the X-point could spread on a large portion of the connected field line. We could speculate that a low $\eta_\parallel$ parameter would help is the homogenisation of turbulent fluctuations over the field lines length. This hypothesis will be evaluated in a future work.
Transport barriers seem also to locally alter the statistical properties of turbulent fluctuations. Figure 5.11 represents the probability density function for different radial positions at the LFS midplane of the reference COMPASS-like simulation.

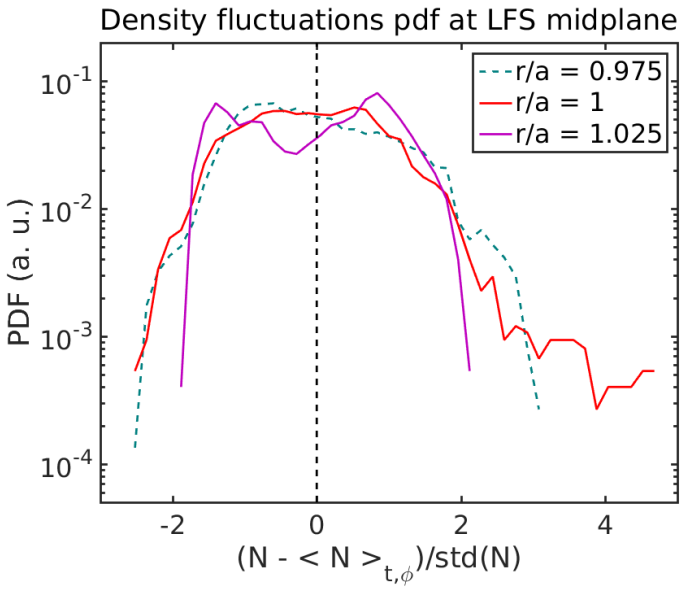

Figure 5.11: *Probability density function for density fluctuations at several radial positions, calculated at the LFS midplane, in the reference COMPASS-like divertor simulation.*

At the separatrix position, the probability density function starts to flatten, meaning that a decrease in small-amplitude fluctuations (both of positive and negative value) is at play. At the first flux surfaces outside the separatrix, this feature is even more evident, with a fall of the probability density function around 0. Further out in the SOL the influence of the transport barrier becomes negligible, and the usual positive skewness is recovered.
The analysis of turbulence properties in the barrier region provides the following global picture: after being generated in the closed flux surfaces, turbulent structures propagate radially outwards and encounter a thin, stable region before the separatrix. Some of the

structures, the ones characterised by bigger amplitudes, manage to pass the barrier, while the smallest can be damped. The low amplitude of the transport barrier can be partially due to its small width. Indeed in the COMPASS reference simulation, the radial portion affected by the barrier, measuring around 5 ρ_L at the LFS midplane, is lower than the average radial correlation length, which is around 10 ρ_L.

5.4 The complex interplay regulating turbulence

We need now to investigate more in detail which are the elements that can trigger the transport barrier. In doing this, we cannot overlook the complex interplay regulating this phenomenon. In this section, we will try to investigate the different mechanisms which contribute to the transport barrier formation, which are illustrated in figure 5.12, exploiting different features of the TOKAM3X code.

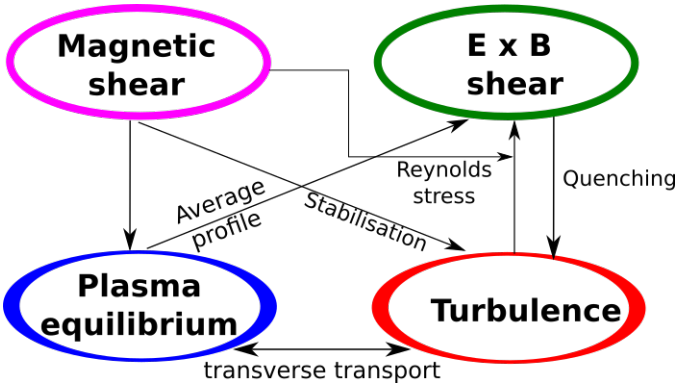

Figure 5.12: *Logical scheme of the interplay of physical mechanisms intervening the formation of transport barriers.*

We have discussed in previous sections the mechanisms which regulate the radial equilibrium. The magnetic geometry affects the equilibrium, and turbulence re-organizes according to it. We have also noticed in chapter 3 that the magnetic shear can have a direct stabilisation effect on turbulence.
The radial shear of the $E \times B$ poloidal velocity has been correlated by multiple studies with the onset of transport barriers and L-H transition ([126],[21]). The $E \times B$ shear can suppress turbulent transport both with non-linear mechanisms, as the de-correlation of density and velocity phases, or through linear effects. However, the onset of the $E \times B$ shear is the result of a complex mechanism. Indeed, the $E \times B$ shear derives from the radial profile of the electric field, and so, ultimately, from the electric charge conservation. Turbulence itself is a potential source of average $E \times B$ poloidal flows, as well-explained in [127], through the mechanism of the Reynolds stress. Small turbulence scales can, in fact, provide energy to large scale flows or Zonal Flows (ZF) in the so-called "inverse-cascade" process. Therefore the turbulent transport, which is affected by the $E \times B$ shear, contributes to the formation of the shear itself, as schematised in 5.12.
The average $E \times B$ shear could possibly have a quenching effect on turbulent structures, or a decorrelation of the poloidal phase of density and potential fluctuations. In a first

part of this section we will focus in this aspect. In a second part of this section, we will try to artificially separate the contributions of equilibrium and turbulence in determining the $E \times B$ shear, in order to give a complete view of the problem.

5.4.1 $E \times B$ shear in TOKAM3X simulations

The $E \times B$ shear is commonly defined as the radial variation of the poloidal $E \times B$ velocity:

$$u'^{\theta}_{E} = \frac{\partial}{\partial r} u^{\theta}_{E} \tag{5.12}$$

This is a quantity with the dimensions of a frequency. Since we are interested into the transport across flux surfaces, we can evaluate the average $E \times B$ shear in our simulations. Figure 5.13 shows the average $E \times B$ shear calculated for several different geometries, when the turbulence has reached a pseudo steady-state.

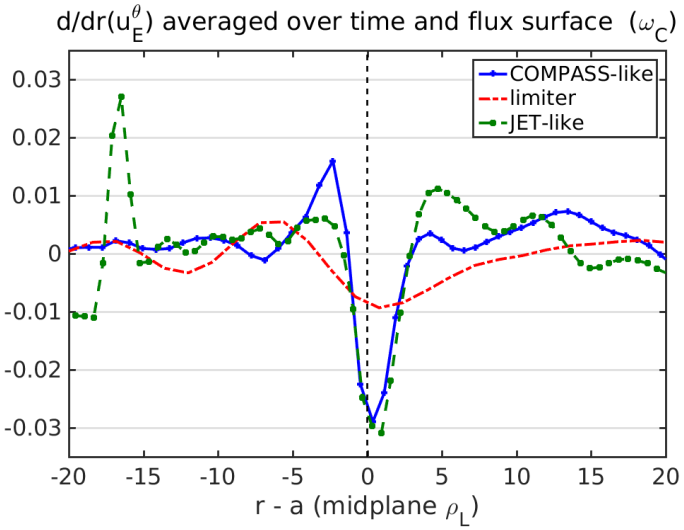

Figure 5.13: *Radial shear of the $E \times B$ poloidal velocity averaged in time and over the flux surface and remapped at LFS midplane in a COMPASS-like, a JET-like and a limiter simulation.*

We can notice from figure 5.13 that the $E \times B$ shear has a negative peak in correspondence of the separatrix, and it is stronger in the COMPASS-like and JET-like geometries. In order to understand this feature, we can study the electric potential and $E \times B$ poloidal velocity profiles.
In the closed flux surface region, the average potential gradient reacts to the density gradient. Indeed, from the momentum balance (2.4), one can understand that, in absence of momentum source, and in isothermal hypothesis, $\vec{\nabla}\phi \simeq -\vec{\nabla}n/n$. Figure 5.14a shows the electric potential radial profile at the LFS midplane.

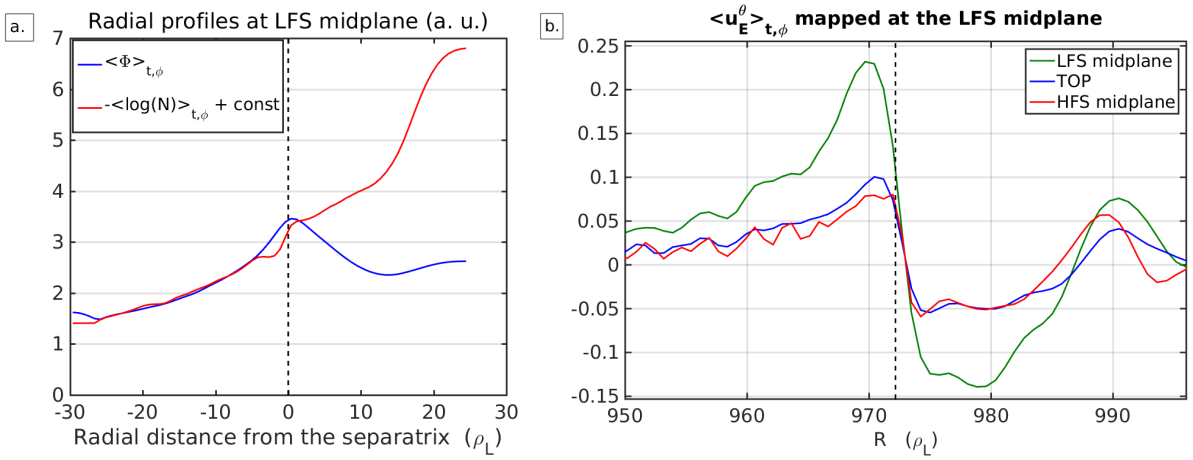

Figure 5.14: *a) Radial profile of the electric potential, averaged in time and toroidal direction, in a COMPASS-like simulation. For comparison, $-log(N)$ is plotted and adjusted by a constant to show the superposition in closed field lines. b) Poloidal $E \times B$ velocity averaged on time and toroidal direction, for a COMPASS-like simulation, at different poloidal positions.*

Interestingly, the only position where the average potential gradient does not compensate the density logarithm one, corresponds to the transport barrier. We also notice, in figure 5.14b that $E \times B$ poloidal velocity increases towards the separatrix, falling rapidly to negative values in the SOL. As understandable from the continuity equation (2.36), turbulent structures are advected in poloidal direction by the $E \times B$ velocity. In our simulations, this advection occurs with opposite directions in the closed flux surfaces region and in the SOL.
The shearing rate at the separatrix is of the order of $10^{-2}\ \omega_C$, which is comparable to the linear growth rate measured in limiter configuration, and much bigger than what is found in divertor. Usually, it is claimed that turbulence is suppressed if the shearing rate is bigger than the linear growth rate [126]:

$$\left|u_E'^{\theta}\right| > \gamma \tag{5.13}$$

In our simulations the $E \times B$ shear is around $0.8 \cdot 10^{-3}\ \omega_C$, in a region at around the 90% of the minor radius. This value is lower, therefore, than the linear growth rate, so that turbulence can easily develop, and spread then in radial direction.
We notice also that the maximum of the $E \times B$ shearing rate, occurring at the separatrix, does not correspond exactly with the position of the barrier, which is centred around $3\ \rho_L$ inside the separatrix. We need therefore further analyses to verify the importance of the $E \times B$ shear at the separatrix in the formation of transport barriers observed in our simulations.

5.4.2 The role of Reynolds stress in generating poloidal fluxes

The average profile of the electric potential is determined by the vorticity balance. In particular, turbulence can contribute in the determination of the average electric potential. The action of the Reynolds stress on the driving of poloidal mean flows is described in [127], where it is highlighted that

$$\partial_t \langle u_E^y \rangle_y = -\partial_x \langle \tilde{u}_E^y \tilde{u}_E^x \rangle_y \tag{5.14}$$

where a simplified cartesian geometry is considered, the coordinate x identifying the radial direction and the coordinate y to the poloidal one. The term $\tilde{u}_E^y \tilde{u}_E^x$ is the so-called Reynolds stress, in analogy with classic fluid mechanics.
In TOKAM3X model, the vorticity balance equation contains the information about the conservation of the poloidal momentum. Let's average the terms in the vorticity balance (2.38) on the surfaces inside the separatrix (θ and φ subscripts will be omitted for simplicity):

$$\partial_t \langle W \rangle + \left\langle \vec{\nabla} \cdot (W \vec{u}_E) \right\rangle = 2 \left\langle \vec{\nabla} \cdot \left(N \vec{u}^i_{\nabla B} \right) \right\rangle + D_W \left\langle \nabla_\perp^2 W \right\rangle \tag{5.15}$$

where the terms of loss in parallel direction have become null since we averaged on a closed flux surface. We can further expand equation (5.15), excluding temporarily the pressure term in the vorticity definition (2.40), which behaves as the potential perpendicular gradient, and neglecting the vorticity dependence on the magnetic field. We also put in a Cartesian reference as in [127], and we consider only the terms on the LHS of (5.15):

$$\begin{aligned}
&\partial_t \left\langle \nabla^2 \Phi \right\rangle_y + \left\langle \vec{\nabla} \cdot \left(\nabla^2 \Phi \vec{u}_E \right) \right\rangle_y \approx \\
&\approx \partial_t \left\langle \frac{\partial^2}{\partial^2 x} \Phi + \frac{\partial^2}{\partial^2 y} \Phi \right\rangle_y + \left\langle \frac{\partial}{\partial x} \left(\frac{\partial^2}{\partial^2 x} \Phi u_E^x + \frac{\partial^2}{\partial^2 y} \Phi u_E^x \right) \right\rangle_y + \cancel{\left\langle \frac{\partial}{\partial y} \left(\frac{\partial^2}{\partial^2 x} \Phi u_E^y + \frac{\partial^2}{\partial^2 y} \Phi u_E^y \right) \right\rangle_y} \\
&\approx \partial_t \left\langle \frac{\partial}{\partial x} u_E^y + \frac{\partial}{\partial y} u_E^x \right\rangle_y + \frac{\partial}{\partial x} \left\langle u_E^x \frac{\partial}{\partial x} u_E^y + u_E^x \frac{\partial}{\partial y} u_E^x \right\rangle_y \\
&= \frac{\partial}{\partial x} \left[\partial_t \langle u_E^y \rangle_y + \left\langle u_E^x \frac{\partial}{\partial x} u_E^y + \frac{1}{2} \frac{\partial}{\partial y} \left(u_E^x \right)^2 \right\rangle_y \right] \\
&\approx \frac{\partial}{\partial x} \left[\partial_t \langle u_E^y \rangle_y + \frac{\partial}{\partial x} \langle u_E^x \; u_E^y \rangle_y \right]
\end{aligned} \tag{5.16}$$

Where in the last passage we assume $\partial_x (\partial_y \Phi) \ll \partial_x (\partial_x \Phi)$, which is justified when the radial extension of turbulent structure is much smaller than the poloidal one, as it is the usually verified in our simulations. The non-linear term $u_E^x \; u_E^y$, moreover, can be approximated to the fluctuating part $\tilde{u}_E^x \; \tilde{u}_E^y$ since mean-field fluxes contribute weakly to the global term. The TOKAM3X model is therefore able to describe the driving of

average poloidal flows by the Reynolds stress, through the $E \times B$ advection term in vorticity equation. Other terms, as the divergence of the diamagnetic current or the diffusive term contribute to the equilibrium profile of the electric potential, and therefore of the $E \times B$ velocity and shear. In a diverted geometry, considering a finite extension in the poloidal direction of the ballooning envelop of turbulent structures, the bottom-up asymmetry introduced by the X-point can introduce a radial variation of the average orientation of turbulent structures. This implies also a radial modulation of the Reynolds stress, which, as observed, can lead to the driving of global $E \times B$ poloidal flows. This mechanism is well-described in the paper by Fedorczak et al. [83], and could potentially be at play in our simulations. We understand here that there is a further complication in our analysis: the magnetic shear introduced by the X-point can affect the $E \times B$ shear, making more difficult the identification of the relative effects.
In order to assess the impact of the Reynolds stress in determining the Φ equilibrium profile, we decided to run a COMPASS-like divertor simulation with the same parameters as the reference one, although artificially suppressing the Reynolds stress term in the vorticity equation. The resulting profile of $E \times B$ poloidal velocity is represented in figure 5.15.

One can see that the difference in the u_E^θ profile between the cases with and without Reynolds stress is low. Also in this case poloidal velocity peaks a few Larmor radii inside the separatrix, and a strong negative shear still holds at the LCFS. The mechanism of the generation of mean poloidal flows by the Reynolds stress does not seem to have a big impact in our simulations, which show a similar transport barrier in the cases with and without Reynolds stress, as visible in figure 5.15(bottom). Nevertheless, the $E \times B$ shear at the separatrix, could still affect the turbulence dynamics, as well as the magnetic shear introduced by the X-point.

5.5 Role of the magnetic shear in the transport barrier build-up

The divertor geometry introduces a strong magnetic shear in proximity of the X-point, whose effect could have implications for the whole flux surface. At the separatrix, also a strong $E \times B$ shear is at play, with a large amplitude over the whole LCFS. We want to inspect if the magnetic shear introduced by the X-point has a role itself in suppressing turbulence.

5.5.1 Simulations with a divertor-like safety factor profile

Exploiting the flexibility of TOKAM3X in defining geometry and magnetic fields, we impose on a limiter geometry a divertor-like safety factor profile. In order to do this, we superimpose to the usual parabolic safety factor profile, a Gaussian shape, centred on

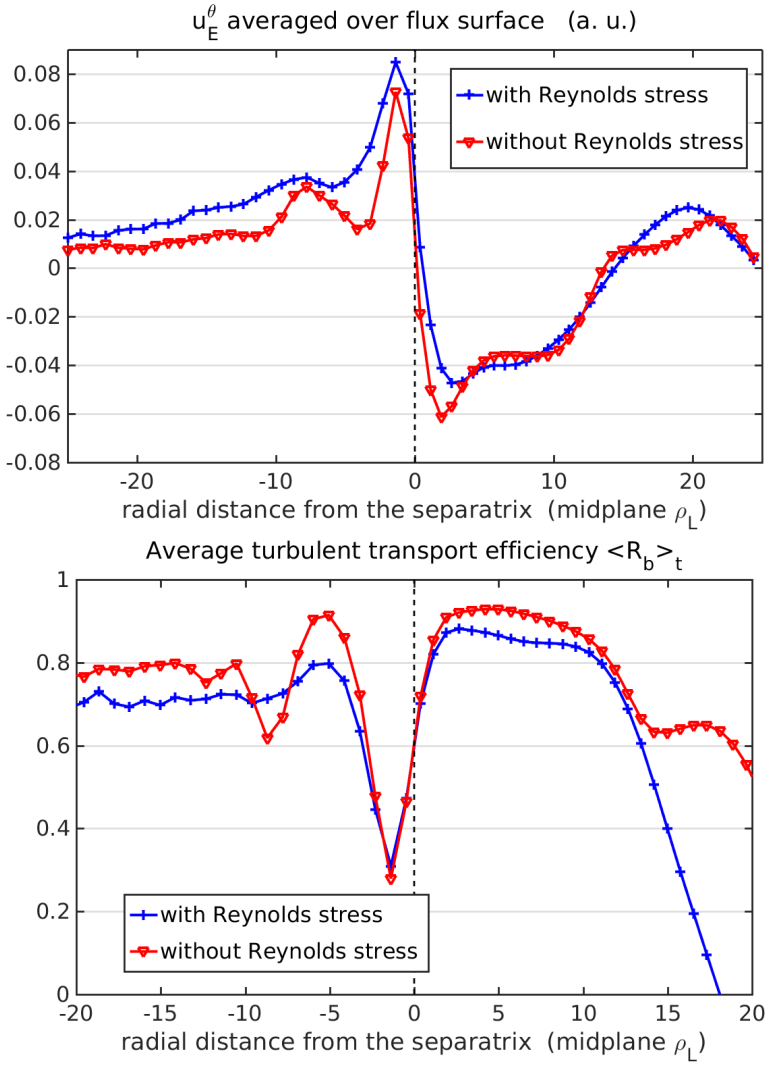

Figure 5.15: *Top: Radial profile of the $E \times B$ poloidal velocity averaged on time ad over the flux surface in a COMPASS-like geometry, in the cases with and without Reynolds stress. Bottom: comparison of the average turbulent transport efficiency in the two cases, simulations with $D_N = 5 \cdot 10^{-3}\ \rho_L^2 \omega_C$.*

the separatrix. Figure 5.16 shows the imposed safety factor profile and the associated poloidal field.

Contrarily to what is observed in TOKAM3X limiter simulations, two transport barriers appear, one on the inner side and one on the outer side of the separatrix, as shown in figure 5.17a.

In these simulations, turbulent transport is reduced to the $60\% - 70\%$ at the transport barrier location. These values are stronger than what is observed in divertor simulations, when the residual value of the diffusive flux is kept at the same level (about the 10% of the total transverse flux in the edge region). However, the transport barriers show similar characteristics. They have indeed a comparable behaviour in time, which translates in a similar standard deviation of the R_b coefficient. Moreover, transport barriers are char-

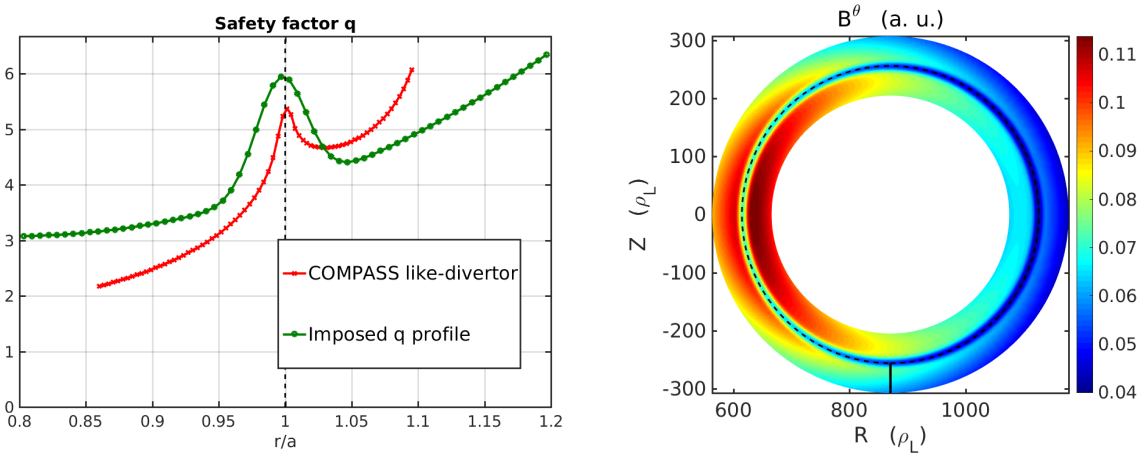

Figure 5.16: *Left: Divertor-like safety factor profile imposed in limiter geometry, compared with a divertor geometry. Right: Poloidal field in limiter simulation with divertor-like safety factor profile.*

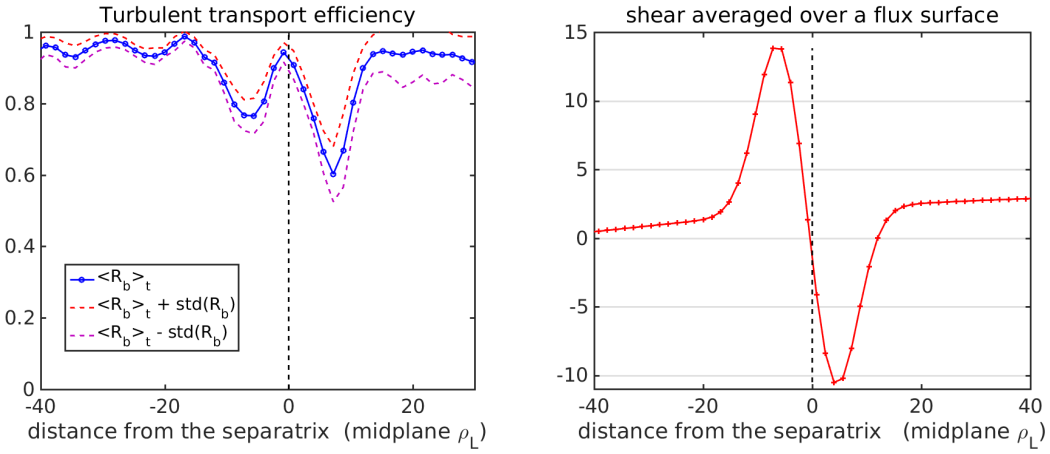

Figure 5.17: *Left: Radial profile of the average turbulent transport efficiency in limiter geometry with imposed divertor-like safety factor. Right: Radial profile of the average magnetic shear.*

acterised in the two cases by a bell-shape. This suggests that the physical mechanism underneath this type of barrier is similar.
Another element which can be readily noticed, is the correlation in the position of the transport barriers with the magnetic shear maximum absolute value, which can be observed in figure 5.17b. The stronger transport barrier efficiency than in divertor simulations can be explained quite easily, admitting that the magnetic shear has a turbulence suppression effect. Indeed, in the *sheared* limited case, a magnetic shear is active all around the flux surface. This means that turbulent structures can be affected over their whole parallel extension, implying a stronger damping than in the divertor case, where the magnetic shear is localised only in the vicinity of the X-point. It is more difficult to explain the presence of the transport barrier only on the closed field lines side in diverted geometry. This could be due to the fact that the parallel correlation length of the

structures increases in the first flux surfaces outside the separatrix, as shown in chapter 3, and the local effect of the X-point has a lower weight on the whole extension of the structure.
We notice from figure 5.17a that the most efficient transport barrier is localised on the side which is characterised by a negative magnetic shear. Even if the absolute value of the magnetic shear is higher in the closed flux surfaces region, the negative shear appears to be more efficient, coherently with the theoretical expectations, which predict a maximum linear growth rate for $s = 0.5$.
As understandable from the shape of the poloidal field represented in figure 5.16b, it would be practically impossible to achieve a magnetic configuration as the one described. Nevertheless, a magnetic shear localised at a radial position, like the one appearing in these simulations, could be introduced in tokamaks by a bootstrap current. This kind of currents, flowing in the parallel direction, are a neoclassical effect caused by trapped particles, and they are proportional to pressure radial gradients (see [6], Chapter 4). However, the bootstrap current would be limited to closed flux surfaces. Also, the value of the shear here imposed is too strong to simulate a realistic bootstrap current, as one can easily calculate by solving the Ampère-Maxwell equation $\vec{J} = \vec{\nabla} \times \vec{B}/\mu_0$ for the imposed magnetic field.

5.5.2 Decoupling $E \times B$ and magnetic shear

The $E \times B$ shear in this case peaks at the two sides of the separatrix, as visible in figure 5.18.

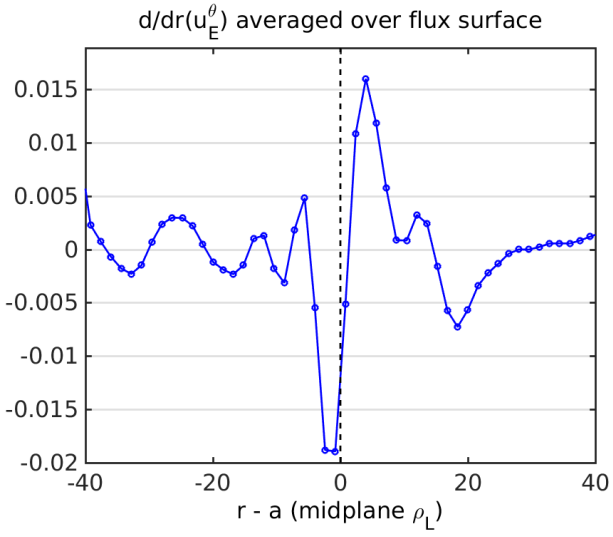

Figure 5.18: *$E \times B$ shear averaged in time and over the flux surface and remapped at LFS midplane in a limited geometry with divertor-like safety factor profile.*

There is no clear correlation between the locations where the $E \times B$ is maximum and the efficiency of the transport barriers. This element suggests that in our simulations the magnetic shear itself is a stabilising condition for turbulence, regardless of the $E \times B$

shear associated. However, the $E \times B$ shear could have a non-local effect, reducing turbulence at positions slightly shifted with respect to the actual shear maxima: further investigations are thus needed on this topic.
We have achieved with this numerical experiment, a further confirmation that the magnetic shear has a strong damping effect on turbulent transport, although it does not suppress turbulence completely. We are therefore able to trigger a transport barrier in global turbulence simulations by acting on the magnetic equilibrium. The magnetic shear introduced by the X-point in diverted simulations, peaked at few Larmor radii inside the separatrix, seems to be the responsible for the global reduction of turbulent transport over the flux surface, while the $E \times B$ shear itself does not seem to be the cause of the observed transport barrier.
The characterisation and the understanding of transport barriers in isothermal diverted simulations is important, in the perspective of including temperature and electro-magnetic effects in TOKAM3X model, which could potentially lead to a different dynamics and help in the understanding of the L-H transition.

Conclusions

The first TOKAM3X 3D fluid electrostatic turbulence simulations of the edge plasma of a tokamak in diverted geometry have been carried out. TOKAM3X solves a set of drift-reduced Braginskii equations and adopts a flux-driven approach. The flexibility of the magnetic geometry definition has been exploited to investigate the effects of the divertor geometry on turbulent transport.
Simulations in divertor configuration have shown statistical properties of turbulence similar to what was previously found in limiter simulations, except for spatial locations close to the X-point and to the separatrix. The dominant instability mechanism is due to Resistive Ballooning Modes, which present a characteristic phase shift between density and electric potential fluctuations around $\pi/2$.
A different pattern is found between the amplitude of the fluctuations, generally stronger at the LFS midplane, as expected from turbulence theory and experiments, and turbulent fluxes, which peak instead at the top of the machine and at the X-point. This duality is explained by the specific shape assumed by turbulent structures. The fast parallel transport, indeed, tends to homogenise turbulent structures on magnetic flux tubes: therefore, where the poloidal magnetic field is low, and thus the flux expansion is elevated, turbulent structures assume a radially elongated shape, while shrinking in the poloidal one.
Turbulent structures are generated around the LFS midplane, and they spread immediately over the magnetic field lines, reaching on one side the X-point, and on the other side the top of the machine, positions where they get strongly elongated. Since the $E \times B$ velocity depends on the poloidal gradient of the electric potential, the cross-field velocity is ultimately proportional to the flux expansion. The auto-organisation of turbulence found in 3D simulations, which leads to the enhancement of radial fluxes by the flux expansion, could give an important physical guideline to 2D transport codes. These kinds of codes, that are widely used in the modelling of edge plasma, make indeed use of an effective diffusive coefficient in order to describe the cross-field transport. Turbulence simulations show that a poloidal dependence of this coefficient on the flux expansion should be taken into account, in order to describe more realistically the turbulent transport in edge plasma.
Turbulence is found in the divertor region, although strongly connected to the LFS midplane. In the vicinity of the separatrix, at the outer leg, simulations in divertor configuration show the presence of a quiescent zone, where the amplitude of density fluctuations is significantly reduced, most likely because of the strong magnetic shear introduced by the X-point. Both the turbulent structures elongated shape and the turbulence damping close to the separatrix are confirmed by visible camera images of the MAST divertor.

In order to evaluate the effectiveness of turbulent radial transport in the divertor region, three different geometries characterised by different divertor leg lengths are numerically simulated, following the same strategy adopted in a recent experiment on TCV. The results show a broadening of the density decay length with the increase of the divertor leg length. Since the upstream turbulent transport is not strongly impacted, the main cause of this broadening seems to be the radial transport occurring at the divertor leg, which acquires a higher weight with respect to the total transport across the flux surface, when the extension of the leg is relatively longer. Moreover, we notice that the transport in the divertor leg presents a strong asymmetry, with the outward direction clearly preferential with respect to the inward one (towards the Private Flux Region). These elements reproduce qualitatively well the findings of TCV experiments. This interpretation of the transport in the divertor region is different from its present prevalent understanding, and could provide interesting guidelines for the design of the divertor in new devices.
Large-scale features linked to turbulence have then been analysed. In particular, we have compared the amplitude of mean-field fluxes across flux surfaces, associated to the average $E \times B$ and ∇B drifts, to turbulent fluxes. The mean-field and the fluctuating fluxes have comparable magnitudes in the SOL, in the proximity of the X-point. This can be explained by the topological discontinuity introduced by the X-point, which causes losses of particles and momentum towards the PFR, and leads to the build-up of density and potential gradients. These cross-field fluxes constitute sources for the particle flows in parallel direction in the SOL. These parallel flows, as in experiments, appear to be strongly asymmetric in poloidal direction: this asymmetry is the result of a contribution of the same extent of turbulent and mean-field fluxes.
The geometry of magnetic flux surfaces is found to modify the overall radial equilibrium achieved in a simulation. Three test cases have been set-up where the Shafranov shift is varied in a limiter geometry. The resulting density gradients are steeper for a stronger Shafranov shift, denoting a higher stability of the system. Two factors are identified for this increase in turbulence stability. On one hand, turbulent structures extend on average on a region characterised by low curvature, such that the global instability drive is lower. On the other hand, a big Shafranov shift implies, in our simulations, stronger magnetic shears, which again are stabilising for interchange turbulence. We show in particular that at certain shear values, the orientation of turbulent structures is favourable for the radial $E \times B$ outer advection of filaments. These geometrical features are usually enhanced in diverted geometry, which shows indeed better confinement times with respect to the limiter configuration. In both configurations, turbulence generates where these conditions are more favourable. In general this occurs at the position where the global shear is minimum, so usually near the radial inner boundary in the closed flux surfaces region. The linear growth rates in divertor configuration are sensibly lower than in limiter geometry, reflecting the increased stability of the system.
Another element characteristic of the divertor simulations is the presence of transport barriers, that is to say, zones where the turbulent transport is partially inhibited. In particular, fluctuations are partially damped on the first flux surfaces inside the separatrix, leading to a lower turbulent $E \times B$ radial transport and to a higher diffusive flux: this process causes an enhancement of the pressure radial gradient, which is ultimately beneficial for the confinement. Different mechanisms which are possibly involved in the

build-up of the transport barriers are investigated and disentangled. In our simulations, the magnetic shear introduced by the X-point seems to be the main actor in the turbulence damping, with its effect spreading around the last closed flux surfaces. Turbulent structures, generated at inner radial positions, are partially damped when arriving in this stable region, and only the events of higher amplitude can manage to pass through it.
More in general, we find a non-trivial effect on turbulent transport of the complex geometry introduced by the X-point geometry, which increases the stability of the system. The non-local character of turbulence is also underlined. Turbulent structures indeed are generated, and then propagate, in zones with different local conditions, and in particular with different driving and damping mechanisms. Therefore, the overall equilibrium is given by the integrated effects of these mechanisms on the global extension of the structures, throughout their generation and propagation.
The results presented in this thesis are part of a step-by-step process towards the understanding of the complex mechanisms regulating the edge plasma dynamics, started with 2D turbulence codes and perpetrated with 3D numerical tools. Two key elements of the edge plasma are not considered in this thesis, but will be included in the next future analysis with TOKAM3X: the temperature evolution and the coupling with a neutral model.
The solution of the energy conservation equations is implemented in TOKAM3X, and the first anisothermal simulations have already been run [58]. The inclusion of temperature dynamics is not expected to significantly change the local turbulence properties here described. However, quantitative changes in particle transport could occur, since the pressure gradient represents the energy source for turbulence, and it is directly affected by the energy transport equilibrium. The inclusion of the electron temperature could lead also to the sheath-driven conducting-wall instability [38], especially in zones with low resistivity and electronic temperature as the PFR, potentially changing the heat flux spreading at the divertor target. The transport barriers, which in the presented simulations have a limited impact on the equilibrium gradient, could be strongly affected by the inclusion of temperature dynamics. Indeed, the electric potential will react also to the temperature gradients, increasing the $E \times B$ rotation and probably also the $E \times B$ shear at the separatrix. As the experiments in divertor configuration suggest, anisothermal simulations may give access to a plasma dynamics more similar to the L-H transition.

Appendices

Appendix A

Details on the derivation of TOKAM3X equations

A.1 Passing from diamagnetic to curvature drift

We want to demonstrate that we can replace the diamagnetic drift by a curvature drift, when we are considering the divergence of the respective fluxes. Firstly we calculate the divergence of the diamagnetic flux for the ion specie.

$$\begin{aligned}
\vec{\nabla}\cdot(n\vec{u}_\star) &= \vec{\nabla}\cdot\left(\cancel{n}\frac{\vec{B}\times\vec{\nabla}p}{\cancel{n}eB^2}\right) = \vec{\nabla}(\frac{1}{B^2})\cdot\left(\vec{B}\times\vec{\nabla}p\right) + \frac{1}{B^2}\vec{\nabla}\cdot\left(\vec{B}\times\vec{\nabla}p\right) \\
&= \vec{\nabla}(\frac{1}{B^2})\cdot\left(\vec{B}\times\vec{\nabla}p\right) + \frac{1}{B^2}\left[\underbrace{\left(\vec{\nabla}\times\vec{B}\right)}_{\approx 0}\cdot\vec{\nabla}p - \vec{B}\cdot\cancel{\left(\vec{\nabla}\times\vec{\nabla}p\right)}\right] \qquad \text{(A.1)}
\end{aligned}$$

We calculate now the divergence of the flux associated to the $\vec{\nabla}B$ drift:

$$\begin{aligned}
\vec{\nabla}\cdot(n\vec{u}_{\nabla B}) &= \vec{\nabla}\cdot\left(2p\frac{\vec{B}\times\vec{\nabla}B}{B^3}\right) = \vec{\nabla}\left(\frac{2p}{B^3}\right)\cdot\left(\vec{B}\times\vec{\nabla}B\right) + \frac{2p}{B^3}\vec{\nabla}\cdot\left(\vec{B}\times\vec{\nabla}B\right) \\
&= \vec{\nabla}\left(\frac{2p}{B^3}\right)\cdot\left(\vec{B}\times\vec{\nabla}B\right) + \frac{2p}{B^3}\left[\underbrace{\left(\vec{\nabla}\times\vec{B}\right)}_{\approx 0}\cdot\vec{\nabla}B - \vec{B}\cdot\cancel{\left(\vec{\nabla}\times\vec{\nabla}B\right)}\right]
\end{aligned}$$

$$\begin{aligned} &= 2\frac{1}{B^3}\vec{\nabla}p\cdot\left(\vec{B}\times\vec{\nabla}B\right)+2p\vec{\nabla}(\frac{1}{B^3})\cdot\left(\vec{B}\times\vec{\nabla}B\right)\\ &= 2\frac{1}{B^3}\vec{\nabla}B\cdot\left(\vec{\nabla}p\times\vec{B}\right)-\frac{6p}{B^4}\vec{\nabla}B\cdot\cancel{\left(\vec{B}\times\vec{\nabla}B\right)}\\ &= -\vec{\nabla}(\frac{1}{B^2})\cdot\left(\vec{\nabla}p\times\vec{B}\right)=\vec{\nabla}(\frac{1}{B^2})\cdot\left(\vec{B}\times\vec{\nabla}p\right) \end{aligned} \tag{A.2}$$

We find thus the same divergence of the flux in the two cases. This result is valid both for ions and electrons since the diamagnetic and the ∇B drift both depend on the electric charge sign. It must be noticed that we have used $\vec{\nabla}\times\vec{B}\sim 0$, which is reasonable in an electrostatic framework: this approach must be questioned if magnetic field variations are taken into account.

A.2 Projection of momentum equation on parallel direction

We must project the momentum equation (1.25) on the parallel direction. The only non-trivial term in the calculation of this projection is:

$$\vec{b}\cdot\vec{\nabla}\cdot(n\vec{u}\otimes\vec{u})=\vec{\nabla}\cdot\left(n\vec{b}\cdot\vec{u}\otimes\vec{u}\right)-\left(n\vec{u}\otimes\vec{u}\cdot\vec{\nabla}\right)\cdot\vec{b} \tag{A.3}$$

where we have dropped the subscript s indicating the specie, and the mass of the specie has not been considered as it is a constant. The first term on the RHS of (A.3) can be further developed into $\vec{\nabla}\cdot\left(nu_{\parallel}\vec{u}\right)$, which is the actual term which is retained in TOKAM3X. The second term on the RHS of (A.3) is a "curvature" term, linked so to the variation of the orientation of the magnetic field. This term is neglected in the derivation of TOKAM3X equations, since it is a second-order term ($1/(k_{\perp}R_0)\approx\varepsilon_w$).

A.3 Vorticity equation

We aim at writing an equation describing the electric potential evolution in a suitable form for the numerical resolution. We need, for this purpose, to calculate the divergence of the polarisation current j_p, which has a rather complex expression. From (2.9), straightforwardly:

$$\vec{j_p}=\frac{m_i\vec{b}}{B}\times\left[\partial_t\left(n_i\vec{u}_{\perp}^{(1)}\right)+\vec{\nabla}\cdot\left(n_i\vec{u}_{\perp}^{(1)}\otimes\vec{u}_i\right)\right]+\frac{\vec{B}\times\left(\vec{\nabla}\cdot\boldsymbol{\Xi}_{\perp}^{(1)}+\mathcal{R}_i\right)}{q_iB^2} \tag{A.4}$$

It can be shown that these two last terms have the effect to cancel the advection by the diamagnetic velocity, in analogy with the diamagnetic cancellation (see Patrick Tamain

Ph.D. Thesis p. 77). The resulting polarisation current, obtained by substituting the electric and diamagnetic drift expressions in $u_\perp^{(1)}$, is:

$$\vec{j}_p = \frac{m_i \vec{b}}{B} \times \left[\partial_t \left(n_i \frac{\vec{B} \times \vec{\nabla}_\perp \phi}{eB^2} + \frac{\vec{B} \times \vec{\nabla}_\perp p_i}{B^2} \right) + \vec{\nabla} \cdot \left(n_i \left(\frac{\vec{B} \times \vec{\nabla}_\perp \phi}{B^2} + \frac{\vec{B} \times \vec{\nabla}_\perp p_i}{eB^2} \right) \otimes \vec{u}_i \right) \right] \tag{A.5}$$

We see that in the polarisation current, the terms $\nabla_\perp \phi$ and $\vec{\nabla}_\perp p_i/(e\, n_i)$ can be treated in the same way, so we omit the diamagnetic part in the following calculations. Assuming the electrostatic approximation, the polarisation current reads:

$$\vec{j}_p = \frac{m_i \vec{b}}{B} \times \left[\frac{\vec{B}}{B^2} \times \partial_t \left(n_i \vec{\nabla}_\perp \phi \right) + \vec{\nabla} \cdot \left(n_i \frac{\vec{B} \times \vec{\nabla}_\perp \phi}{B^2} \otimes \vec{u}_i \right) \right] \tag{A.6}$$

The first term on the RHS of equation (A.6) can be expanded as:

$$\frac{m_i \vec{B}}{B^4} \times \vec{B} \times \partial_t \left(n_i \vec{\nabla}_\perp \phi \right) = \frac{m_i}{B^3} \partial_t \cancel{\left(n_i \vec{B} \times \vec{\nabla}_\perp \phi \right)} \vec{B} - \frac{m_i}{B^2} \partial_t \left(n_i \vec{\nabla}_\perp \phi \right) = -\frac{m_i}{B^2} \partial_t \left(n_i \vec{\nabla}_\perp \phi \right)$$

Neglecting the curvature term, we can approximate the second term in the RHS of (A.6) as:

$$\begin{aligned} \frac{m_i \vec{b}}{B} \times \vec{\nabla} \cdot \left(n_i \frac{\vec{B} \times \vec{\nabla}_\perp \phi}{B^2} \otimes \vec{u}_i \right) &\simeq m_i \vec{\nabla} \cdot \left[\frac{\vec{B}}{B^4} \times \left(n_i \vec{B} \times \vec{\nabla}_\perp \phi \otimes \vec{u}_i \right) \right] = \\ m_i \vec{\nabla} \cdot \left[\frac{n_i}{B^4} \left(\vec{B} \cancel{\vec{B} \cdot \vec{\nabla}_\perp \phi} - B^2 \vec{\nabla}_\perp \phi \right) \otimes \vec{u}_i \right] &= -m_i \vec{\nabla} \cdot \left[\frac{n_i}{B^2} \vec{\nabla}_\perp \phi \otimes \vec{u}_i \right] \end{aligned}$$

So, considering again also the diamagnetic contribution, a compact expression for the polarisation current is:

$$\vec{j}_p = -\frac{m_i}{B^2} \partial_t \left[n_i \left(\vec{\nabla}_\perp \phi + \frac{\vec{\nabla}_\perp p_i}{e n_i} \right) \right] - m_i \vec{\nabla} \cdot \left[\frac{n_i}{B^2} \left(\vec{\nabla}_\perp \phi + \frac{\vec{\nabla}_\perp p_i}{e n_i} \right) \otimes \vec{u}_i \right] \tag{A.7}$$

Let's calculate the divergence of this expression:

$$\vec{\nabla}\cdot\vec{j_p} = -m_i\partial_t\vec{\nabla}\cdot\left[\frac{n_i}{B^2}\left(\vec{\nabla}_\perp\phi + \frac{\vec{\nabla}_\perp p_i}{en_i}\right)\right] - m_i\vec{\nabla}\cdot\left\{\vec{\nabla}\cdot\left[\frac{n_i}{B^2}\left(\vec{\nabla}_\perp\phi + \frac{\vec{\nabla}_\perp p_i}{en_i}\right)\otimes\vec{u}_i\right]\right\} =$$
$$- m_i\partial_t\vec{\nabla}\cdot\left[\frac{n_i}{B^2}\left(\vec{\nabla}_\perp\phi + \frac{\vec{\nabla}_\perp p_i}{en_i}\right)\right] - m_i\vec{\nabla}\cdot\left\{\vec{u}_i\vec{\nabla}\cdot\left[\frac{n_i}{B^2}\left(\vec{\nabla}_\perp\phi + \frac{\vec{\nabla}_\perp p_i}{en_i}\right)\right]\right\}$$
$$- m_i\vec{\nabla}\cdot\left[\frac{n_i}{B^2}\left(\vec{\nabla}_\perp\phi + \frac{\vec{\nabla}_\perp p_i}{en_i}\right)\underbrace{\vec{\nabla}\cdot\vec{u}_i}_{\approx 0}\right]$$

At the moment the last term of this equation is neglected in TOKAM3X, relying on the low compressibility of the velocity.

Appendix B

Metrics in TOKAM3X

Once the mesh grid is built, choosing the desired number of point in each direction, the Jacobian matrix is calculated as:

$$\mathbf{J} = \begin{pmatrix} {}^{\partial R}/_{\partial i_\psi} & {}^{\partial R}/_{\partial i_\theta} & 0 \\ {}^{\partial Z}/_{\partial i_\psi} & {}^{\partial Z}/_{\partial i_\theta} & 0 \\ 0 & 0 & {}^{d\varphi'}/_{di_\varphi} \end{pmatrix} = \begin{pmatrix} \vec{e}_{i_\psi} & \vec{e}_{i_\theta} & \vec{e}_{i_\varphi} \end{pmatrix} \tag{B.1}$$

where the derivatives are calculated with second-order finite differences applied to the (R, Z) coordinates of the cells centres. Since the equilibrium is axisymmetric, in order to save storage memory, we divide this matrix in two blocks:

$$\mathbf{J}_{2D} = \begin{pmatrix} {}^{\partial R}/_{\partial i_\psi} & {}^{\partial R}/_{\partial i_\theta} \\ {}^{\partial Z}/_{\partial i_\psi} & {}^{\partial Z}/_{\partial i_\theta} \end{pmatrix} \quad , \quad \frac{d\varphi'}{di_\varphi} = \|\vec{e}_{i_\varphi}\| = \|\vec{e}_\varphi\| \frac{d\varphi}{di_\varphi} = R\frac{d\varphi}{di_\varphi}$$

So that:

$$J = det(\mathbf{J}) = det(\mathbf{J}_{2D}) R \frac{d\varphi}{di_\varphi} = J_{2D} R \frac{d\varphi}{di_\varphi}$$

The quantity $d\varphi/di_\varphi$ simply expresses the angular extension in toroidal direction of a cell, and it is calculated as:

$$\frac{d\varphi}{di_\varphi} = \frac{L_\varphi}{N_\varphi}$$

where L_φ is the angular measure of the simulated toroidal section, expressed in radians. The mesh grid is here assumed regular in the φ direction, as in the case of the simulations presented in this thesis, but $\frac{d\varphi}{di_\varphi}$ can actually vary in the toroidal direction. J_{2D} instead represents geometrically the surface covered by a cell in the poloidal plane. We also define

the inverse of the Jacobian:

$$\mathbf{J}^{-1} = \begin{pmatrix} \partial i_\psi/\partial R & \partial i_\psi/\partial Z & 0 \\ \partial i_\theta/\partial R & \partial i_\theta/\partial Z & 0 \\ 0 & 0 & di_\varphi/d\varphi' \end{pmatrix} = \begin{pmatrix} \vec{e}^{i_\psi} \\ \vec{e}^{i_\theta} \\ \vec{e}^{i_\varphi} \end{pmatrix} \tag{B.2}$$

and two 2D arrays storing the metric coefficients:

$$\mathbf{G} = (g_{ij}) = (\vec{e}_i \cdot \vec{e}_j) \qquad , \qquad \mathbf{H} = \left(h^{ij}\right) = \left(\vec{e}^i \cdot \vec{e}^j\right) \tag{B.3}$$

Using these definitions, we can express the magnetic field associated to each cell:

$$\vec{B} = B^\theta \frac{\vec{e}_{i_\theta}}{\|\vec{e}_{i\theta}\|} + B^\varphi \frac{\vec{e}_{i_\varphi}}{\|\vec{e}_{i_\varphi}\|} \tag{B.4}$$

where the toroidal field has the form:

$$B^\varphi = \frac{F}{R} = \frac{B_0 R_0}{R} \tag{B.5}$$

and the poloidal one, taking into account that the total poloidal flux in a cell is $\psi'_p(i_\varphi) = \psi_p \frac{d\varphi}{di_\varphi}$:

$$B^\theta = -\frac{1}{J}\frac{d\psi'_p}{di_\psi}\frac{d\varphi}{di_\varphi}\|\vec{e}_{i_\theta}\| = -\frac{1}{J_{2D}R}\frac{d\psi_p}{di_\psi}\|\vec{e}_{i_\theta}\| \tag{B.6}$$

Since the effective size of the machine is determined by the parameter $\rho^\star$, which is a free parameter for the simulation, the toroidal flux ψ_t scales as $\rho^{\star -2}$. If one wants to maintain a reasonable pitch angle of the field line, it has therefore to multiply expression B.6 by a factor $\rho^{\star -2}$. Moreover, in TOKAM3X one can regulate the intensity of the poloidal field with an additional multiplicative factor, called *psiscale*.
The calculation of the global safety factor then leads to:

$$q(\psi) = \frac{1}{\sum_{i\theta}\|\vec{e}_{i_\theta}\|}\oint q_{loc}\mathrm{d}\theta = \frac{1}{\sum_{i\theta}\|\vec{e}_{i_\theta}\|}\sum_{i\theta}\frac{B^\varphi \sum_{i\theta}\|\vec{e}_{i_\theta}\|}{RB^\theta 2\pi}\|\vec{e}_{i_\theta}\| = -\frac{F_0 R_0}{2\pi\frac{d\psi_p}{d\psi}}\sum_{i\theta}\frac{J_{2D}}{R} \tag{B.7}$$

Now we can express the main operators appearing in TOKAM3X equations. For a scalar field f, using the Einstein notation, the gradient has the form [64]:

$$\vec{\nabla} f = \frac{\partial f}{\partial i}\vec{e}^i \tag{B.8}$$

and the parallel gradient:

$$\nabla_{\|} f = \vec{b} \cdot \vec{\nabla} f = \left(\frac{B^{\theta}}{B} \frac{\vec{e}_{i_\theta}}{\|\vec{e}_{i\theta}\|} + \frac{B^{\varphi}}{B} \frac{\vec{e}_{i_\varphi}}{\|\vec{e}_{i_\varphi}\|} \right) \cdot \left(\frac{\partial f}{\partial i_\psi} \vec{e}^{i_\psi} + \frac{\partial f}{\partial i_\theta} \vec{e}^{i_\theta} + \frac{\partial f}{\partial i_\varphi} \vec{e}^{i_\varphi} \right) = \frac{B^{\theta}}{B\vec{e}_{i_\theta}} \frac{\partial f}{\partial i_\theta} + \frac{B^{\varphi}}{B\|\vec{e}_{i_\varphi}\|} \frac{\partial f}{\partial i_\varphi} \quad \text{(B.9)}$$

The divergence of a vectorial field $\vec{A}$ is:

$$\vec{\nabla} \cdot \vec{A} = \frac{1}{J} \frac{\partial}{\partial i} \left(J \vec{A} \cdot \vec{e}^{i} \right) \quad \text{(B.10)}$$

Drift velocities have the form $\frac{\vec{B} \times \vec{\nabla} f}{B^2}$. In order to calculate their expression, it is useful to express the magnetic field in the contravariant basis:

$$\vec{B} = \left(B^i \frac{\vec{e}_i}{\|\vec{e}_i\|} \cdot \vec{e}_j \right) \vec{e}^{j} = B^{\theta} \frac{g_{i_\theta, i_\psi}}{\sqrt{g_{i_\theta, i_\theta}}} \vec{e}^{i_\psi} + B^{\theta} \sqrt{g_{i_\theta, i_\theta}} \vec{e}^{i_\theta} + B^{\varphi} \|\vec{e}_{i_\varphi}\| \vec{e}^{i_\varphi} \quad \text{(B.11)}$$

So that the generic drift velocity has the expression:

$$\frac{\vec{B}}{B^2} \times \vec{\nabla} f = \left(\frac{B^{\theta}}{B^2} \frac{g_{i_\theta, i_\psi}}{\sqrt{g_{i_\theta, i_\theta}}} \vec{e}^{i_\psi} + \frac{B^{\theta}}{B^2} \sqrt{g_{i_\theta, i_\theta}} \vec{e}^{i_\theta} + \frac{B^{\varphi}}{B^2} \|\vec{e}_{i_\varphi}\| \vec{e}^{i_\varphi} \right) \times \left(\frac{\partial f}{\partial i_\psi} \vec{e}^{i_\psi} + \frac{\partial f}{\partial i_\theta} \vec{e}^{i_\theta} + \frac{\partial f}{\partial i_\varphi} \vec{e}^{i_\varphi} \right) \quad \text{(B.12)}$$

And finally the expression for three components of the drift velocities, referred to a unitary vectors basis, is:

$$u^{\psi} = \left(\frac{\vec{B}}{B^2} \times \vec{\nabla} f \right) \cdot \frac{\vec{e}^{i_\psi}}{\|\vec{e}^{i_\psi}\|} = \frac{1}{JB^2 \sqrt{h^{i_\psi, i_\psi}}} \left(B^{\theta} \sqrt{g_{i_\theta, i_\theta}} \frac{\partial f}{\partial i_\varphi} - B^{\varphi} \|\vec{e}_{i_\varphi}\| \frac{\partial f}{\partial i_\theta} \right) \quad \text{(B.13)}$$

$$u^{\theta} = \left(\frac{\vec{B}}{B^2} \times \vec{\nabla} f \right) \cdot \frac{\vec{e}^{i_\theta}}{\|\vec{e}^{i_\theta}\|} = \frac{1}{JB^2 \sqrt{h^{i_\theta, i_\theta}}} \left(B^{\varphi} \|\vec{e}_{i_\varphi}\| \frac{\partial f}{\partial i_\psi} - B^{\theta} \frac{g_{i_\theta, i_\psi}}{\sqrt{g_{i_\theta, i_\theta}}} \frac{\partial f}{\partial i_\varphi} \right) \quad \text{(B.14)}$$

$$u^{\varphi} = \left(\frac{\vec{B}}{B^2} \times \vec{\nabla} f \right) \cdot \frac{\vec{e}^{i_\varphi}}{\|\vec{e}^{i_\varphi}\|} = \frac{B^{\theta}}{JB^2 \sqrt{g_{i_\theta, i_\theta}}} \left(g_{i_\theta, i_\psi} \frac{\partial f}{\partial i_\theta} - g_{i_\theta, i_\theta} \frac{\partial f}{\partial i_\psi} \right) \quad \text{(B.15)}$$

Appendix C

Poloidal asymmetries in closed flux surfaces region

We aim here at studying the poloidal asymmetries in the closed flux surfaces region. Indeed, in global turbulent simulations, we find in some cases poloidal asymmetries in the average total pressure Π between the inner and the outer midplane. In order to do this, we reduce the TOKAM3X model to a simpler one. We study a steady-state system, where every quantity is meant to be averaged in time and toroidal direction. We exclude the temperature and the electric charge conservation equations, since we do not need the evolution of the electric potential. We also focus on closed flux surfaces, sufficiently far from the particle source and where the diffusion plays a minor role. Under these assumptions our reduced model can be written as:

$$\begin{cases} \vec{\nabla} \cdot \left(\Gamma \vec{b}\right) + \vec{\nabla}_\perp \cdot (N \vec{u}_\perp) = 0 \\ \vec{\nabla} \cdot \left[\left(\frac{\Gamma^2}{N} + 2N\right) \vec{b}\right] + \vec{\nabla}_\perp \cdot (\Gamma \vec{u}_\perp) - 2N \vec{\nabla} \cdot \vec{b} = 0 \end{cases} \tag{C.1}$$

We are only interested here in the dynamics along the parallel direction. As further hypothesis we admit that:

$$\vec{\nabla}_\perp \cdot (X \vec{u}_\perp) = \frac{1}{J} \left[\underbrace{\frac{\partial}{\partial \psi} \left(J X u^\psi\right)}_{\simeq 0} + \frac{\partial}{\partial \theta} \left(J X u^\theta\right) \right] \tag{C.2}$$

where X can be either the density or the parallel momentum field. This is the strongest hypothesis of the model, and it is usually verified in our simulations, in the zone of closed flux surfaces.
We place in a toroidal coordinate system (r, θ, φ). We can write then:

$$\begin{cases} \frac{1}{Rr}\frac{d}{d\theta}\left(R\left(\Gamma\frac{B^\theta}{B}+Nu^\theta\right)\right)=0 \\ \frac{1}{R}\frac{d}{d\theta}\left(R\frac{B^\theta}{B}\left(\frac{\Gamma^2}{N}+2N\right)+R\Gamma u^\theta\right)+2N\frac{B^\theta}{B^2}\frac{d}{d\theta}B=0 \end{cases} \tag{C.3}$$

Where u^θ is the drift velocity projected on the poloidal plane:

$$u^\theta(\theta)=\frac{B^\varphi}{B^2}\left(\partial_r\Phi+\frac{\partial_r P_i}{N}\right) \tag{C.4}$$

Since we do not consider the radial direction, we assume this quantity dependent only on the poloidal angle. Basically, we admit a source of poloidal momentum without specifying its origin.
From the first equation of the system (C.3), the quantity $\mathcal{G}=R(\Gamma\frac{B^\theta}{B}+Nu^\theta)$ is constant on a flux surface and it is considered here as a parameter related to the parallel and poloidal momentum. In fact, this is just the sum of parallel and drift fluxes projected on the poloidal direction. Reducing the system to one equation, we find:

$$\frac{dN}{d\theta}=\frac{1}{2\frac{B^\theta}{B}RN^2-\mathcal{G}^2\frac{B}{B^\theta R}}\left[\mathcal{G}^2N\frac{B}{B^\theta R^2}\frac{dR}{d\theta}+\mathcal{G}N^2\frac{B}{B^\theta}\frac{du^\theta}{d\theta}-2N^3\frac{B^\theta}{B}\left(\frac{dR}{d\theta}+\frac{R}{B}\frac{dB}{d\theta}\right)\right] \tag{C.5}$$

We solve this equation numerically. We choose a u^θ with a sinusoidal shape and different values at the midplane. The results are presented in figure C.1.

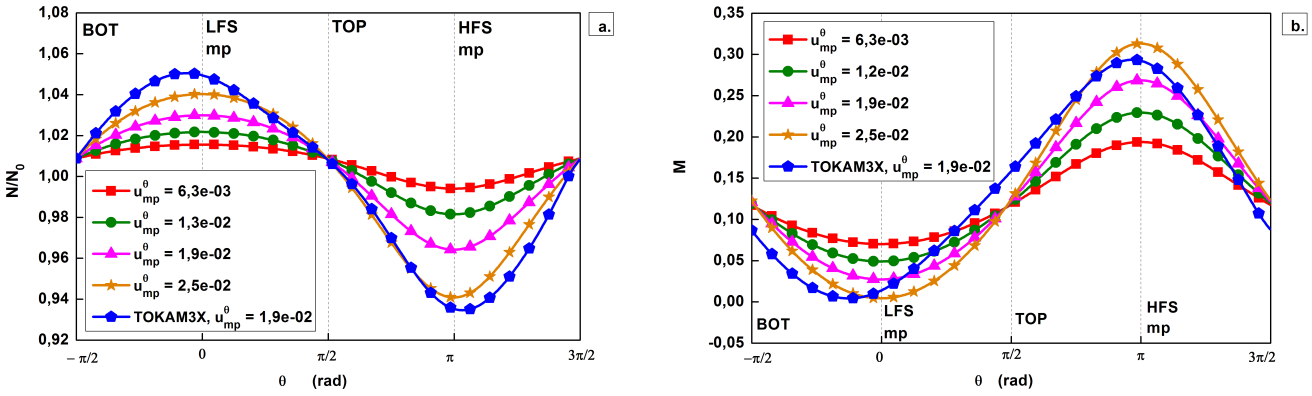

Figure C.1: *a) Poloidal plot of the density in a closed flux surface for different values of the poloidal velocity. b) Parallel Mach number profiles.*

One can notice that, the stronger the poloidal velocity is, the stronger will be the poloidal parallel asymmetry both in parallel Mach number and plasma density. Moreover, one can

notice that the parallel Mach number is a sensitive quantity to the poloidal asymmetry generated by an asymmetric poloidal velocity. The stronger amplitudes on the HFS are due to the finite aspect ratio.
The blue curves in figure C.1 refer to a TOKAM3X axisymmetric simulation, where the turbulent transport is not active, but the electric potential is determined coherently by the charge conservation equation. One can see that global simulations follow well the trend described by the reduced model.
We have shown by a reduced model that, when trying to explain the parallel flows as a reaction of fluid drifts, one always has to take into account at least the conservation of mass and of poloidal momentum. In turbulent simulations, for example, one can find strong variations of the poloidal velocity in the poloidal direction. In particular, as mentioned in chapter 5, the lower magnetic field and the stronger compression of the flux surfaces at the LFS midplane maximise the $E \times B$ poloidal velocity at this position. This reduced model helps in understanding how the different fields can react to an asymmetry in the poloidal velocity.

Appendix D

Verification of TOKAM3X using the PoPe method

D.1 PoPe method in a nutshell: decomposition onto a relevant basis plus an error

The Projection on Proper elements (PoPe) method [72] is a code verification tool allowing to recover the equations that have generated a set of data. In terms of verification, this method is fundamentally different from classical ones, since it is based on simulations outputs, and it can be performed using simulations in any regime. Classic verification methods, instead, are based on specific code runs. This is the case of the code verification with the Method of Manufactured Solutions (MMS), which is carried out using a target analytical solution (see e.g. [128], [129]). This solution is usually not fully representative of typical outputs of numerical simulations.
The verification of 3D turbulence codes for the edge plasma simulation is usually performed with the MMS method. In order to verify TOKAM3X, this method has been applied to the isothermal version of the code, as discussed in the work [33]. Several conditions differ significantly between the analytical solution and the usual global simulations. First of all, the target analytical solution is smooth in space and time with respect to the discretisation (e.g. $\propto cos(2\pi t)\sin(2\pi r/a)\sin(\theta)\sin(\varphi)$ in [33]), while a broad spectra of fluctuations appear in simulations with turbulence. Moreover, the verification method is applied exclusively in a simple geometry (slab or limiter with circular cross section), and prescribing simplified boundary conditions (usually Dirichlet's).
Under these conditions, some operators might not be involved in the solution, leading to an incomplete verification of the equations. The PoPe method allows a more generalised process of verification. In particular, PoPe can be used purely for the code verification, if the full set of equations implemented in the code is considered, or alternatively as a tool for model reduction, if the aim is to find the dominant operators in the model. Moreover, PoPe can also be understood as an "a posteriori" procedure of error checking.
In this section, we describe the application of PoPe to several sets of data obtained with the TOKAM3X code. In the framework of this thesis, PoPe has been used as a

post-treatment tool, developed independently of the code as a Matlab/Octave toolbox.

D.2 Application of the PoPe method to TOKAM3X

D.2.1 The PoPe method step-by-step

In order to explain the method, we describe the application of PoPe to the following density equation, eq. (D.1), as an example:

$$\partial_t N = \vec{\nabla} \cdot (D_N \vec{\nabla}_\perp N) - \vec{\nabla} \cdot (\Gamma \vec{b}) - \vec{\nabla} \cdot (N \vec{u}_E) - \vec{\nabla} \cdot (N \vec{u}^{ion}_{\nabla B}) + S_N \tag{D.1}$$

This equation expresses the ion density conservation equation, where the advection of the polarisation velocity is neglected. The set of simulations shown in this section are referred to a TOKAM3X model where this continuity equation is solved. We can immediately rewrite (D.1) in a more compact form, using the "th" subscript for "theoretical", and naming $\{O^i\}_{th}$ the five operators at the RHS of (D.1):

$$\{\partial_t N\}_{th} = w^i_{th} \{O^i\}_{th} \tag{D.2}$$

where Einstein's convention on indexes has been used. Operators are listed in (D.3) for $i \in [1, 5]$, and they are associated to five theoretical weights w^i_{th} listed in eq.(D.4):

$$\{O^i\}_{th} = \{\vec{\nabla} \cdot (D_N \vec{\nabla}_\perp N),\ \vec{\nabla} \cdot (\Gamma \vec{b}),\ \vec{\nabla} \cdot (N \vec{u}_E)\ \vec{\nabla} \cdot (N \vec{u}^{ion}_{\nabla B}),\ S_N\} \tag{D.3}$$

$$w_{th} = [+1, -1, -1, -1, +1] \tag{D.4}$$

The first, necessary steps of the code verification with the PoPe method, are:

1. Measurement of $\{\partial_t N\}_{eff}$, the effective ("eff" subscript) time derivative computed with finite differences from the outputs of a given code. In the present case, finite differences of order four are compared to the order one time integration scheme used in TOKAM3X in the framework of this thesis.

$$\{\partial_t N\}_{eff}(t) = \sum_{j=-2}^{2} c(j) N(t + j\Delta t) + \mathcal{O}(\Delta t^4) \tag{D.5}$$

$$c(-2:2) = [+1, -8, 0, +8, -1]/(12\Delta t) \tag{D.6}$$

2. Computation of each operator in eq.(D.1), labeled $\{O\}^i_{ol}$ for $i \in [1, 5]$, using higly accurate off-line ("ol" subscript) post-treatments. While TOKAM3X, in the simulations shown in this thesis, makes use of a second order method in space, the offline estimation uses method of order two to six, giving therefore a better approximation of the theoretical operators. We can actually write:

$$\|\{O^i\}_{th} - \{O^i\}_{ol}\| \ll \|\{O^i\}_{th} - \{O^i\}_{eff}\| \tag{D.7}$$

so that

$$\{O^i\}_{ol} \simeq \{O^i\}_{th} \tag{D.8}$$

3. Linear projection of $\{\partial_t N\}_{eff}$ onto $\{O\}^i_{ol}$, thus recovering the effective weights w^i_{eff} and an effective residual ε_{eff} linearly independent of $\{O\}^i_{ol}$.

$$\{\partial_t N\}_{eff} = w^i_{eff}\{O\}^i_{ol} + \varepsilon_{eff} \tag{D.9}$$

This latter projection is simply performed by solving the following linear system based on the least mean square algorithm:

$$A^t A\ w_{eff} = A^t\{\partial_t N\}_{eff} \tag{D.10}$$

where the matrix A is defined as

$$A(p,i) \equiv \{O(p)^i\}_{ol} \tag{D.11}$$

and it is of size $P \times I$. Each column of the matrix A is the evaluation of the i^{th} operator from the set of I operators in the tested equation. These evaluations are performed for P points labelled by the index p. P is defined by the discretisation used to solve the equation with the code that we want to verify in the first place. Usually $P \gg I$, so that a large number of points can be considered in order to reduce the statistical error in the estimation of w_{eff}. For TOKAM3X, typically, we have $P = N_r \times N_\theta \times N_\varphi \times N_t \gg 10^6$ for a unique simulation. Nevertheless, in order to introduce a time dependence in w_{eff}, we usually use N_t sets of $N_r \times N_\theta \times N_\varphi \geq 10^4$ points.
The residual is then recovered by explicitly computing:

$$\{\partial_t N\}_{eff} - A\ w_{eff} = \varepsilon_{eff} \tag{D.12}$$

This procedure leads to the interpretation of the effective time derivative of a given code ($\{\partial_t N\}_{eff}$) as the sum of weighted (by w^i_{eff}) operators ($\{O\}^i_{ol}$) plus a residual (ε_{eff}) which has no linear dependency on the operators of the equations. Ideally, $w_{eff} = w_{th}$ and $\varepsilon_{eff} = 0$. This decomposition is relevant since effective weights define the nature of the equation, so they control the behaviour of the system (theoretically and numerically). A simple error, such as the use of a diffusion coefficient two times higher than the one theoretically wanted, would immediately be identified by PoPe with $w^1_{eff} = 2w^i_{th}$, without necessarily impacting ε_{eff}. The control of weights would be absolute if $\{O^i\}_{eff}$, operators effectively calculated by the code, were "exact". As we discretise solutions over a finite number of degrees of freedom, each of them having a finite accuracy, operators $\{O^i\}_{eff}$ usually differ from theoretical expression of operators $\{O^i\}_{th}$. The theoretical expression of operators being not usually accessible, we do not compare $\{O^i\}_{eff}$ to $\{O^i\}_{th}$ but rather to $\{O^i\}_{ol}$, a set of operators computed off-line using a greater accuracy than for $\{O^i\}_{eff}$, as expressed in (D.7). This point is important to be able to associate the residual ε_{eff} to an error in the code and not to an error in the verification process. This

off-line greater accuracy is easily obtained, as for off-line computations we do not have to take care of any stability with respect to time integration. Also, the verification is usually performed on about 1% of the data generated by a code, so it is not a bottleneck in the overall computational cost. For example 1 time step out of 100 is sufficient, since generally the time step is defined to insure small variations of the solution between consecutive iterations. Verifying each time step is still possible but it would lead to a situation in which one verifies many systems very close to each other.
A common mistake concerns the localisation in space and time of the data used for the verification process. Each equation can be seen as a law that has to be verified anywhere and at any time, with respect to the state of the system at the considered exact location and time. Thus, we have to carefully handle variables used to recompute the equation in order to be sure not to mix a variable a evaluated at (x,t) with a variable b evaluated at $(x+\Delta x, t+\Delta t)$, where in general a and b are not explicitly related.
Finally, using $\{O^i\}_{ol} = \{O^i\}_{th}$ for simplification, we can introduce a more general definition of the effective residual ε_{eff}, the total residual ε_{tot} ("*tot*" subscript for "total") defined as :

$$\begin{aligned} \varepsilon_{tot} &\equiv \{\partial_t N\}_{eff} - \{\partial_t N\}_{th} && \text{(D.13)} \\ &= \left(w^i_{eff} - w^i_{th}\right) \{O\}^i_{ol} + \varepsilon_{eff} && \text{(D.14)} \end{aligned}$$

This total residual contains a part linearly dependent on the operators as seen in equation (D.14). Also, here we clearly identify $\delta^i = w^i_{eff} - w^i_{th}$ as the error on weights of the equations. Nevertheless, using only (D.13) we do not need to solve any linear system to obtain ε_{tot}.

D.2.2 Verification protocol

Two representative simulations are used in this study, the first one in a limiter configuration and the second one in divertor configuration, with a COMPASS-like geometry. These are two reference simulations, and the imposed numerical and physical parameters are listed in table 2.1.
The PoPe analysis is usually carried out in 3 steps :

- Study of $\varepsilon_{tot}(\psi, \theta, \varphi, t)$, which contains the entire information on the discrepancy between the theoretical evolution of the system and the effective evolution;
- Study of A (see (D.11)) and A^tA, to insure that the linear system solved in PoPe is not too close to singularity;
- Study of ε_{eff} and w_{eff} to achieve a physical understanding of the errors.

In this Appendix, for clarity and willing to keep this note short, we skip the presentation of the second step and only give details of the first and third steps. Nevertheless, the matrix A has been verified in every case to be invertible. Also, as first attempt to use of PoPe for the TOKAM3X verification, and in order to ease the verification process, we do not take into account the entire mesh but we avoid points close to the boundary of the domain and of each of the subdomains. In particular, we exclude the first six point

in every direction starting from each subdomain boundary.
We remind, in the following table, the equations solved by TOKAM3X in the simulations presented in this thesis, with the associated operators and theoretical weights.

Equation	Operator	Designation	Theoretical weight
$\partial_t N =$	$\vec{\nabla}\cdot\left(D_N\vec{\nabla}_\perp N\right)$	$\{O^1\}$	$+1$
	$\vec{\nabla}\cdot\left(\Gamma\ \vec{b}\right)$	$\{O^2\}$	-1
	$\vec{\nabla}\cdot(N\vec{u}_E)$	$\{O^3\}$	-1
	$\vec{\nabla}\cdot(N\vec{u}^{ion}_{\nabla B})$	$\{O^4\}$	-1
$\partial_t \Gamma =$	$\vec{\nabla}\cdot\left(D_\Gamma\vec{\nabla}_\perp \Gamma\right)$	$\{O^1\}$	$+1$
	$\vec{\nabla}\cdot\left(\Gamma^2/N\vec{b}\right)$	$\{O^2\}$	-1
	$\vec{\nabla}\cdot(\Gamma\vec{u}_E)$	$\{O^3\}$	-1
	$\vec{\nabla}\cdot(\Gamma\vec{u}^{ion}_{\nabla B})$	$\{O^4\}$	-1
	$\nabla_\parallel(2N)$	$\{O^5\}$	-1
$\partial_t W =$	$\vec{\nabla}\cdot\left(D_W\vec{\nabla}_\perp W\right)$	$\{O^1\}$	$+1$
	$\vec{\nabla}\cdot\left(\Gamma W/N\vec{b}\right)$	$\{O^2\}$	-1
	$\vec{\nabla}\cdot(W\vec{u}_E)$	$\{O^3\}$	-1
	$2\vec{\nabla}\cdot(N\vec{u}^{ion}_{\nabla B})$	$\{O^4\}$	$+1$
	$1/\eta_\parallel\vec{\nabla}\cdot\left[\left(\nabla_\parallel log\,(N)-\nabla_\parallel\Phi\right)\vec{b}\right]$	$\{O^5\}$	$+1$

Table D.1: *Table of the considered equations and the associated operators and theoretical weights.*

In the continuity equation, excluding the points close to the boundary, we also exclude the source term S_N, which does not appear, for this reason, in table D.1.

D.3 Study of $\partial_t N$ equation

We start our analysis by the study of the continuity equation. Figure D.1 shows an example of the time-derivative of density calculated in post-treatment with a high-order accuracy at a specific time-step and toroidal position, compared to the effective one calculated by the code, for the reference limiter simulation.

The residual, represented in figure D.1(right), has relative values spanning from 10% to 25%. We notice that the pattern of the residual is similar to the one of the time derivative,

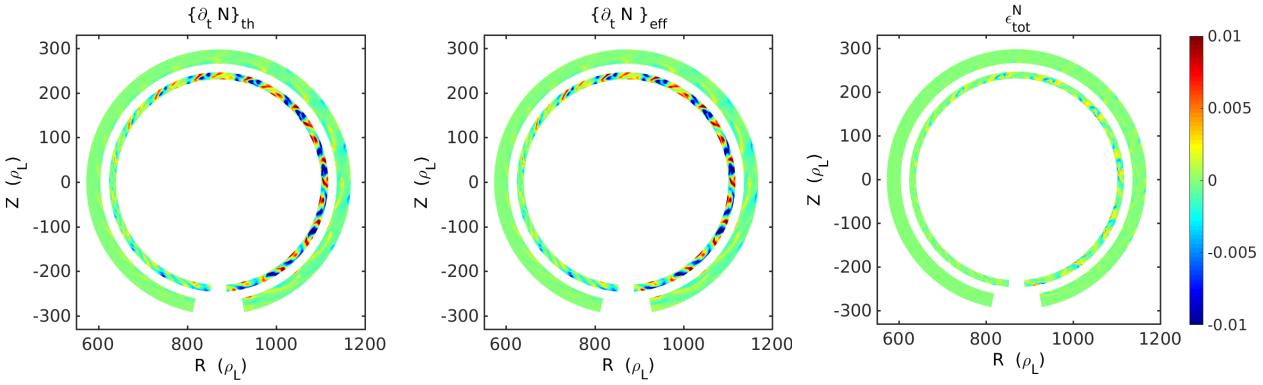

Figure D.1: *Snapshot at a specific time step and toroidal position of the theoretical time derivative of density (left), of the effective derivative calculated by TOKAM3X (centre) and of the total residual (right) in the reference limiter simulation.*

so that the numerical error is stronger where the time derivative is higher: this condition holds especially in the closed field lines region, where the density fluctuation amplitude is stronger.
We perform now the same kind of analysis on COMPASS-like divertor simulations, and we report an example of the results in figure D.2.

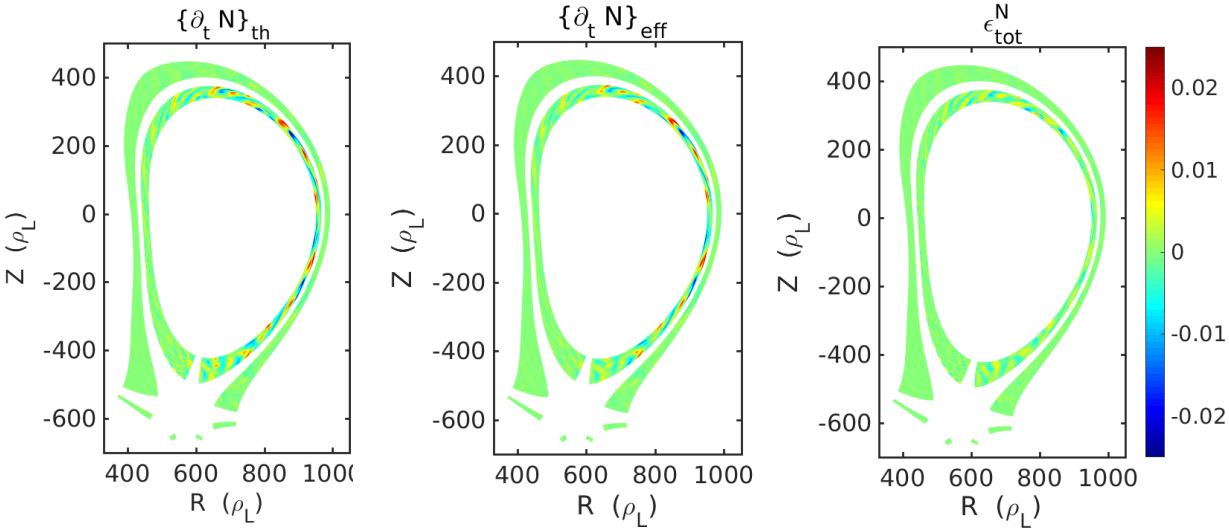

Figure D.2: *Snapshot of the theoretical time derivative of density (left), of the effective derivative calculated by TOKAM3X (centre) and of the total residual (right) in the reference COMPASS-like divertor simulation.*

In the case of the divertor, in correspondence of the high-amplitude turbulence structures, the residual can increase up to the 50%. Once again, this error is more evident in closed field lines. In particular, the amplitude of the turbulent fluctuations seems to be in general underestimated by the code. Moreover, a small shift in the poloidal direction is sometimes noticeable between the theoretical and the effective wave form of the structures. The Roe-Marquina numerical scheme, and the associated WENO interpolation

method, are probably responsible for the discrepancy between the calculated and the theoretical values: indeed this scheme can modify fluxes [67], in order to maintain the code stable and conservative.
We proceed then to the calculation of the effective weights of the operators of the continuity equation solved by TOKAM3X, and we list them in table D.2. PoPe is applied in each case to a set of points in the 3D space (ψ, θ, φ) for the determination of the weights w^i_{th}. Their variation in time is then statistically analysed giving $\left\langle w^i_{eff} \right\rangle_t$ and $std\left(w^i_{eff}\right)$. We also calculate, as a 0D criterion, the L-2 norm of the time derivative $\{\partial_t N\}_{eff}$, sampled over all the considered points in time and space. The norm of the residual $\{\varepsilon\}_{eff}$ must be compared to this number. In an ideal situation, $\|\{\varepsilon\}_{eff}\|_2 \ll \|\{\partial_t N\}_{eff}\|_2$, so that PoPe can identify perfectly the operators intervening in the time derivative. Instead, $\|\{\varepsilon\}_{eff}\|_2 \simeq \|\{\partial_t N\}_{eff}\|_2$, meaning that the linear projection is not able to describe an important part of the effective derivative, included in the residual.

Geometry	$\{O^i\}_{th}$	w^i_{th}	$\left\langle w^i_{eff} \right\rangle_t$	$std\left(w^i_{eff}\right)$	$\|\{\partial_t N\}_{eff}\|_2$	$\|\varepsilon_{eff}\|_2$
Limiter	$\vec{\nabla}\cdot\left(D_N\vec{\nabla}_\perp N\right)$	$+1$	$+2.9761$	0.5638	0.0021	0.0008
	$\vec{\nabla}\cdot\left(\Gamma\,\vec{b}\right)$	-1	-0.937	0.0951		
	$\vec{\nabla}\cdot(N\vec{u}_E)$	-1	-0.8495	0.0788		
	$\vec{\nabla}\cdot(N\vec{u}^{ion}_{\nabla B})$	-1	-0.6176	0.3422		
Divertor	$\vec{\nabla}\cdot\left(D_N\vec{\nabla}_\perp N\right)$	$+1$	$+1.3430$	0.1303	0.0028	0.0013
	$\vec{\nabla}\cdot\left(\Gamma\,\vec{b}\right)$	-1	-0.9455	0.0944		
	$\vec{\nabla}\cdot(N\vec{u}_E)$	-1	-0.7792	0.0471		
	$\vec{\nabla}\cdot(N\vec{u}^{ion}_{\nabla B})$	-1	-0.6461	0.0606		

Table D.2: *Table of the theoretical and effective average weights in density equation, with the associated standard deviation, in the limiter and in the divertor cases. The vectorial norm of the RHS of the equation, as well as the residuals, are also reported.*

In our case, both in limiter and divertor geometry, the linear projection can catch the fundamental part of the system dynamics, since $\|\{\varepsilon\}_{eff}\|_2 < 0.5\|\{\partial_t N\}_{eff}\|_2$. The standard deviation of weights is around 10% of the effective weights (except for w^4 in the limiter case), implying that the mean value is representative of the values spanned in the time series.
One can notice in table D.2 that the diffusion operator, in limiter cases, attains values around three times larger than the theoretical one. On the other hand, the remaining operators are characterised by weights with smaller absolute values than the theoretical one. This is probably a consequence of the adopted numerical scheme (Roe-Marquina with WENO interpolation), which tends to smooth gradients, as it would be done by a strong physical diffusion. Also the Runge-Kutta scheme, applied in these simulations at order one, can intervene in determining the numerical diffusion. Nevertheless, the evolu-

tion of the physical system, at least for the diffusion equation, is fairly slow with respect to the time-step, at least for the density and the parallel momentum equations, so we do not expect a significant effect of a refinement in the time discretisation. We also notice that the divertor case is characterised by generally lower weights of the diffusive operator. This could be due to the fact that, on average, in the bulk region considered by the PoPe analysis, turbulent structures extension in the perpendicular plane is generally higher than in limiter cases. Since the size of the mesh cells is comparable in the two cases, a bigger numerical diffusion is probably intervening in the limiter case. Notice that in the vicinity of the X-point, the situation would be the opposite, with smaller structures (at least in the poloidal direction) for the divertor geometry, possibly resulting in a higher numerical diffusion. This hypothesis will have to be verified in future analyses. The rest of the operators behave similarly in the two geometries.
Figure D.3 shows the effective diffusion coefficient derived with the PoPe method, compared to the theoretical D_N imposed as parameter in TOKAM3X simulations, in a scan of the latter parameter with limiter geometry.

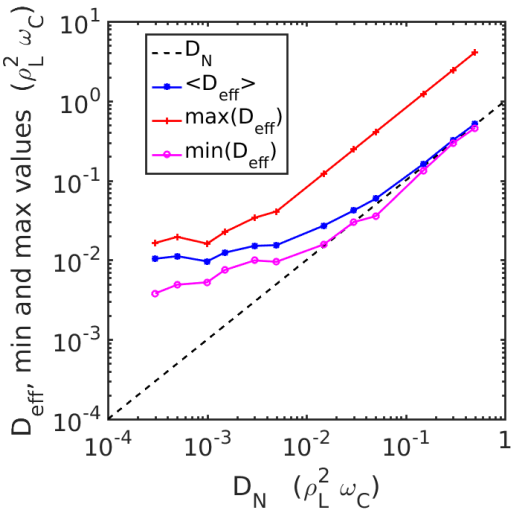

Figure D.3: *Comparison between effective and theoretical density diffusion coefficient in TOKAM3X limiter simulations. Lines with crosses and circles indicate respectively the maximum and the minimum registered value for the effective diffusion coefficient in each simulation.*

One can notice that the average effective diffusion coefficient does not decrease below approximately $10^{-2}\rho_L^2\omega_C$, so that changing the imposed D_N under this value does not change much, globally, the effects on our system. This minimal diffusion coefficient is understood as the numerical diffusion intrinsic to the numerical methods. In the framework of this thesis, imposing usually $D_N = 0.5 \cdot 10^{-2}\rho_L^2\omega_C$, we placed in this saturation range of the effective diffusion coefficient.

D.4 Study of $\partial_t \Gamma$ equation

We first calculate the total residual in the parallel momentum conservation equation, for simulations in limiter geometry. An example of the effective time derivative compared to the theoretical one, with the associated residual, is shown in figure D.4.

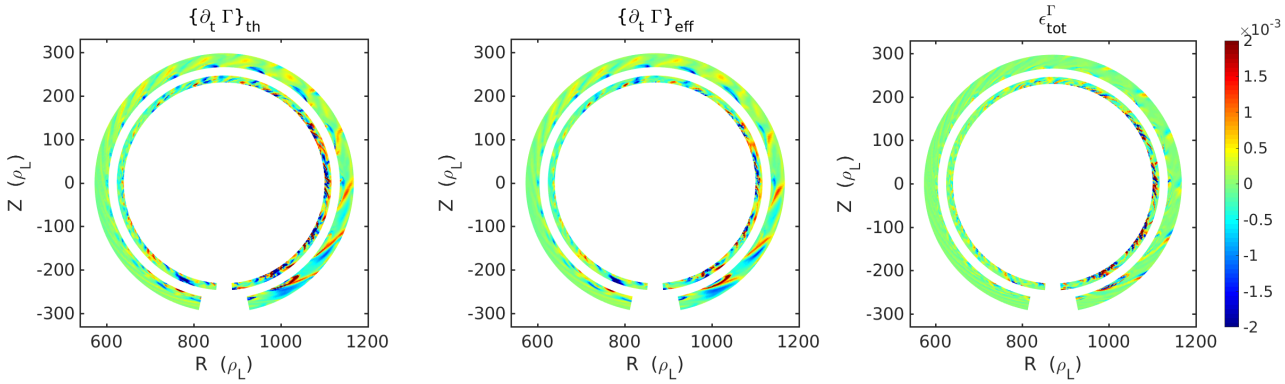

Figure D.4: *Snapshot at a specific time step and toroidal position of the theoretical time derivative of* Γ *(left), of the effective derivative calculated by TOKAM3X (centre) and of the total residual (right) in the reference limiter simulation.*

One can see that also in the case of the $\partial_t \Gamma$ equation, the numerical error is mainly localised in the closed field lines region, in correspondence of high-amplitude fluctuations. Nevertheless, the residual can be strong also in the SOL, in correspondence of large amplitude events. These characteristics are observable also in divertor simulations, represented in figure D.5.

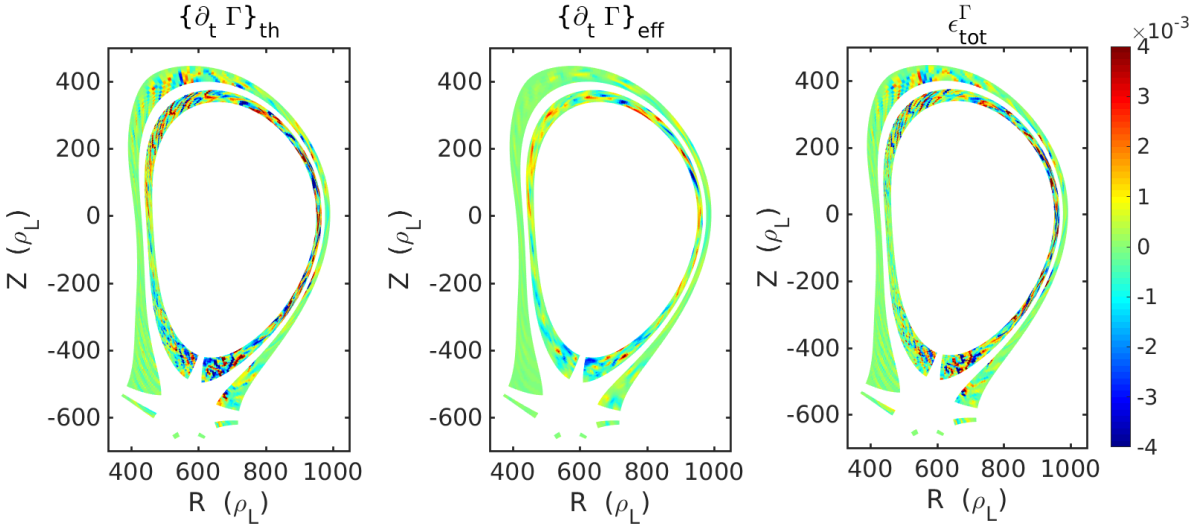

Figure D.5: *Snapshot at a specific time step and toroidal position of the theoretical time derivative of* Γ *(left), of the effective derivative calculated by TOKAM3X (centre) and of the total residual (right) in the reference COMPASS-like simulation.*

One can observe in figure D.5 that, although the global shape of the theoretical time-derivative is well reproduced by the code, locally the calculated solution seems to be more smooth than the one predicted by PoPe. In both limiter and divertor simulations the total residual can exceed the 50% of the theoretical time derivative.
We apply then the linear projection, in order to understand which operators are the principal cause of the discrepancy between the effective and the theoretical time derivatives. The effective weights of the operators of the parallel momentum conservation, resulting from TOKAM3X simulations, are represented in table D.3.

Geometry	$\{O^i\}_{th}$	w^i_{th}	$\langle w^i_{eff}\rangle_t$	$std\left(w^i_{eff}\right)$	$\|\{\partial_t\Gamma\}_{eff}\|_2$	$\|\varepsilon_{eff}\|_2$
Limiter	$\vec{\nabla}\cdot\left(D_\Gamma\vec{\nabla}_\perp\Gamma\right)$	$+1$	$+2.3574$	0.4128	0.0006	0.0003
	$\vec{\nabla}\cdot\left(\Gamma^2/N\ \vec{b}\right)$	-1	-0.2941	0.1462		
	$\vec{\nabla}\cdot(\Gamma\vec{u}_E)$	-1	-0.6668	0.1090		
	$\vec{\nabla}\cdot(\Gamma\vec{u}^{ion}_{\nabla B})$	-1	-0.8106	0.3838		
	$\nabla_\parallel(2N)$	-1	-0.3838	0.1232		
Divertor	$\vec{\nabla}\cdot\left(D_\Gamma\vec{\nabla}_\perp\Gamma\right)$	$+1$	$+0.7616$	0.1653	0.0006	0.0004
	$\vec{\nabla}\cdot\left(\Gamma^2/N\ \vec{b}\right)$	-1	-0.4174	0.1302		
	$\vec{\nabla}\cdot(\Gamma\vec{u}_E)$	-1	-0.6041	0.0741		
	$\vec{\nabla}\cdot(\Gamma\vec{u}^{ion}_{\nabla B})$	-1	-0.1668	0.2498		
	$\nabla_\parallel(2N)$	-1	-0.1326	0.0269		

Table D.3: *Table of the effective weights of operators in the parallel momentum conservation equation, in limiter and COMPASS-like reference simulations.*

One can notice that in the case of the parallel momentum equations, the $\nabla_\parallel(2N)$ term is on average the most distant from the the theoretical value. In the divertor case, also the advection by the ∇B drift is problematic.
More in general, the effective weights of the operators in parallel momentum conservation equations present a higher discrepancy than the one observed in the continuity equation. However, we also notice that the residual value can exceed the 50% of the norm of the RHS of the equation, revealing that some of the dynamics is not caught by the linear projection. Further analyses must be carried out in order to better characterise the behaviour of the $\partial_t\Gamma$ equation. First hints suggest that the impact on this equation of the Roe-Marquina scheme, and of the related WENO interpolation, is higher than on the continuity one.

D.5 Study of $\partial_t W$ equation

Table D.4 represents the results of the PoPe analysis on the TOKAM3X outputs for the vorticity conservation, in limiter and divertor cases.

Geometry	$\{O^i\}_{th}$	w^i_{th}	$\langle w^i_{eff} \rangle_t$	$std\left(w^i_{eff}\right)$	$\|\{\partial_t W\}_{eff}\|_2$	$\|\varepsilon_{eff}\|_2$
Limiter	$\vec{\nabla} \cdot \left(D_W \vec{\nabla}_\perp W\right)$	$+1$	$+1.2291$	0.3575	0.0002	0.0002
	$\vec{\nabla} \cdot \left(\Gamma W/N\ \vec{b}\right)$	-1	-0.5692	0.6481		
	$\vec{\nabla} \cdot (W \vec{u}_E)$	-1	-0.5816	0.1450		
	$2\vec{\nabla} \cdot (N \vec{u}^{ion}_{\nabla B})$	$+1$	$+0.3745$	0.0890		
	$\frac{1}{\eta_\parallel} \vec{\nabla} \cdot \left[\left(\nabla_\parallel log(N) - \nabla_\parallel \Phi\right) \vec{b}\right]$	$+1$	$+0.3424$	0.0876		
Divertor	$\vec{\nabla} \cdot \left(D_W \vec{\nabla}_\perp W\right)$	$+1$	$+0.1019$	0.0639	0.0002	0.0002
	$\vec{\nabla} \cdot \left(\Gamma W/N\ \vec{b}\right)$	-1	$+0.0335$	0.3116		
	$\vec{\nabla} \cdot (W \vec{u}_E)$	-1	-0.3943	0.0981		
	$2\vec{\nabla} \cdot (N \vec{u}^{ion}_{\nabla B})$	$+1$	$+0.0482$	0.0114		
	$\frac{1}{\eta_\parallel} \vec{\nabla} \cdot \left[\left(\nabla_\parallel log(N) - \nabla_\parallel \Phi\right) \vec{b}\right]$	$+1$	$+0.0471$	0.0105		

Table D.4: *Table of the effective weights of operators in the vorticity conservation equation, in limiter and COMPASS-like reference simulations.*

One can readily notice that, especially in the divertor case, there is a large discrepancy between the theoretical and the effective values of the weight of some operators, and in particular w^4 and w^5. Moreover, in both cases the value of the residual is comparable to the norm of the RHS.
Nevertheless, even if weights are far from being equal to the theoretical ones, it seems that they are correlated in such a way that main contributions compensate each other. Particularly important is the fact that diamagnetic currents, created through the term $2\vec{\nabla} \cdot (N \vec{u}^{ion}_{\nabla B})$, are compensated by the divergence of the parallel current $\vec{\nabla} \cdot (J_\parallel \vec{b})$, with approximately the same weight. Considering the average weight varying in time, the correlation number of these two terms, $w^4(t)$ and $w^5(t)$, is close to 1, as can be noticed in figure D.6. The same can be stated for $\partial_t w^4(t)$ and $\partial_t w^5(t)$ as well as $\partial_t^2 w^4(t)$ and $\partial_t^2 w^5(t)$.

Also interestingly, $w^1(t)$ and $w^3(t)$ are only correlated between each other up to 0.2, also when considering first and second derivative in time, but are both correlated to w_4 and w_5 with a value of 0.5. These correlations remind the role of the adopted numerical scheme, which modifies fluxes but insures the conservation. Here the implicit part of

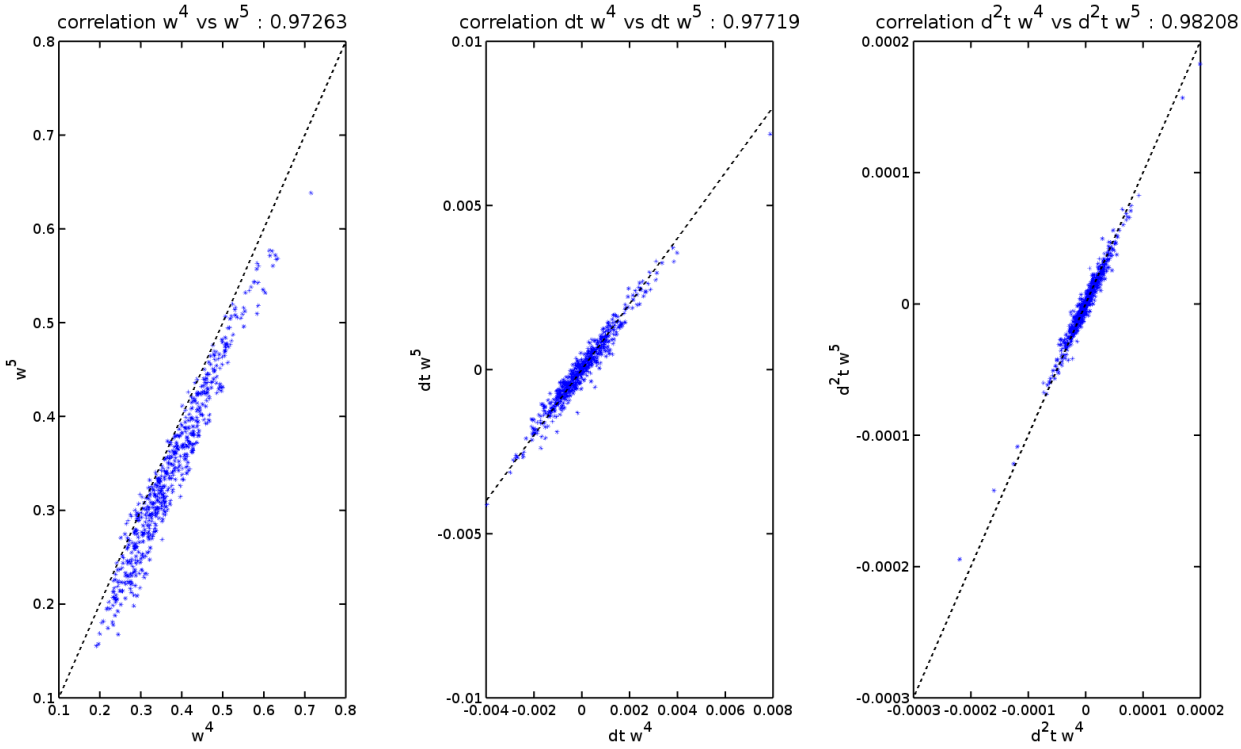

Figure D.6: *Correlation of the weights of operators* $2\vec{\nabla}\cdot(N\vec{u}^{ion}_{\nabla B})(w^4)$ *and* $\vec{\nabla}\cdot(J_{\parallel}\vec{b})(w^5)$. *The correlation in the first and second order time derivative is also represented. Limiter simulations are considered in this plot.*

the vorticity equation does not seem to meet the theoretical expectation, nevertheless it respects the correlation between dominant operators, while insuring the stability of the numerical method.
Some difficulties in the vorticity equation resolution had already been underlined in [33], by means of the MMS method. Indeed, the order of convergence found in that case ($\simeq 1$) was lower than the used spatial discretisation scheme (order 2).
We propose two possible explanations for the lower accuracy of the effective weights in the vorticity equation, and we explore them in the next sections.

D.5.1 Effective weights in axysimmetric simulations

The first explanation for the discrepancy in theoretical and effective weights is that the vorticity, being by definition the sum of electric potential and density logarithms perpendicular laplacians, is characterised by small-size structures in the perpendicular plane. This characteristic implies strong gradients, and so an enhanced numerical diffusion. This first hypothesis has been tested by performing TOKAM3X axysimmetric simulations. In these simulations, the fields are averaged over the toroidal direction at every time-step, thus artificially suppressing turbulence. Axisymmetric simulations thus have smooth solutions. Every weight of every operators in each equations are very well recovered, except for the vorticity equation. As an example, we report in table D.5 the effective weights of

operators in density and vorticity equations in an axysimmetric divertor geometry.

Equation	$\{O^i\}_{th}$	w^i_{th}	$\langle w^i_{eff} \rangle_t$	$std\left(w^i_{eff}\right)$
Density	$\vec{\nabla} \cdot \left(D_N \vec{\nabla}_\perp N \right)$	$+1$	$+0.998$	0.002
	$\vec{\nabla} \cdot \left(\Gamma\ \vec{b} \right)$	-1	-0.999	0.001
	$\vec{\nabla} \cdot (N \vec{u}_E)$	-1	-1.001	0.001
	$\vec{\nabla} \cdot (N \vec{u}^{ion}_{\nabla B})$	-1	-1.000	0.001
Vorticity	$\vec{\nabla} \cdot \left(D_W \vec{\nabla}_\perp W \right)$	$+1$	$+0.026$	0.080
	$\vec{\nabla} \cdot \left(\Gamma W/N\ \vec{b} \right)$	-1	$+0.080$	0.080
	$\vec{\nabla} \cdot (W \vec{u}_E)$	-1	$+0.020$	0.046
	$2\vec{\nabla} \cdot (N \vec{u}^{ion}_{\nabla B})$	$+1$	$+0.002$	0.002
	$1/\eta_\parallel \vec{\nabla} \cdot \left[\left(\nabla_\parallel log\,(N) - \nabla_\parallel \Phi \right) \vec{b} \right]$	$+1$	$+0.002$	0.002

Table D.5: *Table of the effective weights of density and vorticity equations, for axysimmetric simulations in COMPASS-like geometry.*

One can see that the theoretical weight of operators in the density equation is perfectly recovered in an axysimmetric solution. In the case of vorticity, instead, no significant change in the operators behaviour is detected by PoPe. The small characteristic size of the vorticity structures in turbulent simulations, so, does not seem to be the principal reason for the low accuracy in the solution of the vorticity equation. At least, turbulence suppression does not increase the quality of the resolution of the equation.

D.5.2 Separation of explicit and implicit advancement contributions

The second possible explanation for the difficulties in the solution of the vorticity equation is to be found in the semi-implicit method used for its solution. As explained in section 2.5, indeed, the solution is performed in two steps. The first one is the explicit advancement of some operators (in particular w^2, w^3 and w^4, see table D.1) basing on fields at the precedent time-step, while the remaining part of the equation is advanced implicitly, basing on the intermediate operators just calculated. While the explicit part only adds small increments to a current state, computing $W(t+\delta t) = W(t) + \delta t(\partial_t W)$, the implicit part acts as $W(t+\delta t) = f(W(t))$, mixing contributions on long range. In particular, the boundary conditions at the targets, which are unfortunately ill defined, can affect the global solution, even at points far from the geometrical borders. In particular, the Bohm's boundary condition on the electric potential (2.80), in the isothermal

case with $T_e = T_i = 1$ can be rewritten as:

$$\nabla_\parallel \Phi \pm \eta_\parallel N\Phi = \nabla_\parallel log(N) \tag{D.15}$$

so it has a Robin form. Since $\eta_\parallel$ is very small, this condition tends to be similar to a Neumann condition, which, combined with the Neumann conditions acting on the other boundaries, can lead to an ill-conditioning of the matrix to be inverted.
In order to test this second hypothesis, two runs have been performed, excluding artificially the explicit terms in the first case, and the implicit terms in the second case.

In the study of both runs, as the system of equations has been deeply modified and it is not "physical" any more, only the first time step is analysed, before non-physical behaviours appear. Thus, no standard deviation is computed, and the value of the weights is to be understood as unique value of time step considered.

Case	$\{O^i\}_{th}$	w^i_{th}	w^i_{eff}
No explicit terms	$\vec{\nabla}\cdot\left(D_W\vec{\nabla}_\perp W\right)$	$+1$	$+1.117$
	$\vec{\nabla}\cdot\left(\Gamma W/N\ \vec{b}\right)$	-1	-0.031
	$\vec{\nabla}\cdot(W\vec{u}_E)$	-1	-0.095
	$2\vec{\nabla}\cdot(N\vec{u}^{ion}_{\nabla B})$	$+1$	-0.032
	$1/\eta_\parallel\vec{\nabla}\cdot\left[\left(\nabla_\parallel log\,(N)-\nabla_\parallel\Phi\right)\vec{b}\right]$	$+1$	$+0.135$
No implicit terms	$\vec{\nabla}\cdot\left(D_W\vec{\nabla}_\perp W\right)$	$+1$	$+1.562$
	$\vec{\nabla}\cdot\left(\Gamma W/N\ \vec{b}\right)$	-1	-0.864
	$\vec{\nabla}\cdot(W\vec{u}_E)$	-1	-0.991
	$2\vec{\nabla}\cdot(N\vec{u}^{ion}_{\nabla B})$	$+1$	$+1.001$
	$1/\eta_\parallel\vec{\nabla}\cdot\left[\left(\nabla_\parallel log\,(N)-\nabla_\parallel\Phi\right)\vec{b}\right]$	$+1$	$+2\cdot10^{-5}$

Table D.6: *Table of the effective weights of the operators in the vorticity equation, when explicit or implicit terms are switched off.*

When explicit terms are switched off in the code, we indeed recover weights close to 0 in the density equation for the operators explicitly solved. Also the diffusion operator seems slightly better solved. In the vorticity equation, as visible in table D.6, the weights of 2 explicit terms out of 3 are comparable to the regular case. Moreover the last term w^5, the divergence of the parallel current, which is basically solved with the implicit method, increases in weight of a factor 2, but it is still far from the theoretical value of 1.
When implicit terms are switched off, in the vorticity equation, the weight of $\vec{\nabla}\cdot(J_\parallel\vec{b})$ falls down to $2\cdot10^{-5}$, which we regard as 0, while explicit terms are finally recovered with an accuracy comparable to others equations. This last point means that the implicit part of

the vorticity equations is responsible for the discrepancy between the theoretical and the effective weights of the operators. Since this simulation is carried out in regular turbulent regime, we can also state that the small size of W fluctuations is not responsible for the lack of accuracy on explicit terms, as long as the implicit terms are switched off.
As mentioned before, the implicit advancement of some terms, correlates points potentially far in space and time, with respect to the characteristic variation of the system. It is thus useful to understand how the equations behaviour changes when varying the time-step value, which, for all the simulations reported until now, has been fixed to $dt = 1\ \omega_C^{-1}$ ($dt = 1$ in dimensionless units).

D.5.3 Scan in time-step value

The time-step dt and the parallel resistivity $\eta_\parallel$ determine the condition number of the matrix solved by TOKAM3X in the vorticity equation. Together, they determine the anisotropy in the dynamics of the system between the parallel direction, described by the $\mathcal{L}_\parallel$ operator presented in section 2.5, and the perpendicular direction, described by $\mathcal{L}_\perp$. To go deeper into the understanding of the vorticity equation, a scan in dt, the time step used for simulations, has been performed, using the set of values

$$dt = [10^{-5}, 10^{-4}, 10^{-3}, 10^{-2}, 10^{-1}, 1]$$

and carrying out the simulations in divertor geometry.

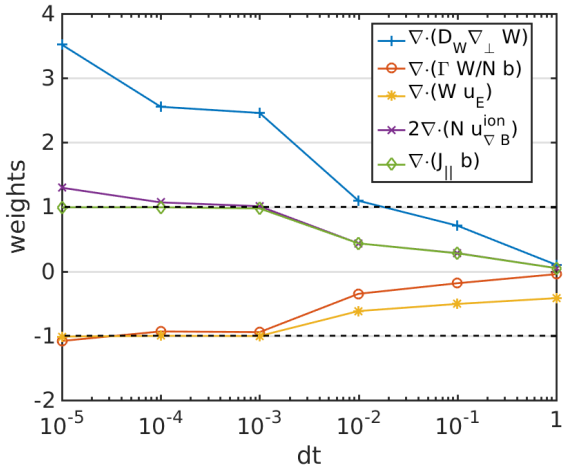

Figure D.7: *Effective weigths of the different operators intervening in the vorticity equations, in simulations performed using different time-steps, and compared to the theoretical ones (represented by black dashed lines).*

In figure D.7 one can see that a decrease from $dt = 1$ to $dt = 10^{-3}$ significantly changes the value of weights for the vorticity equation. Also the ratio between norms of the effective residual and of the RHS of the vorticity equation clearly increases as dt decreases.

With respect to this two criteria, we notice that a time step of 10^{-3} would be the optimum for the accuracy in resolution. A higher effective diffusion coefficient appears at low dt. This could be a sign of a slightly different dynamics when fast timescales are taken into account. However values around 2 times larger than the theoretical ones are tolerable, since they have been found also in the other equations of the system.

D.6 Conclusions on the TOKAM3X verification with PoPe method

A first attempt of verification of TOKAM3X by means of the PoPe method has been carried out. PoPe allows to verify the solution of each equation basing on the code output in turbulent regime, rather than on an analytical function, constituting therefore a more stringent verification process with respect to the MMS one.
No significant difference is found in the solution accuracy between the limiter and the divertor configurations, which are solved with the same numerical methods and using grids of comparable refinement. This is coherent with the fact that the turbulence nature is the same in the two geometries, as pointed out in chapter 3. Nevertheless, the region in the vicinity of the X-point has been excluded from this analysis, and it will have to be further investigated.
In the continuity equation, the numerical error is concentrated in the region where the amplitude of the fluctuations is higher, that is to say, in the closed field-lines region. This equation presents acceptable effective weights of the operators. The diffusion operator is generally higher than the theoretical one, probably accounting for the smoothing effect of the shock-capturing Roe-Marquina scheme and of the associated WENO interpolation method. In particular, decreasing the imposed diffusion coefficient, the effective value of this operator saturates at a certain value ($D_N \simeq 10^{-2}$), where the numerical diffusion becomes comparable to the "physical" one. The parallel momentum conservation equation presents a similar behaviour as the continuity one, although some operators, especially the ones involving the parallel dynamics, present a higher discrepancy with respect to the theoretical values.
The density and parallel momentum conservation equation had already been verified by the MMS method showing the expected convergence order and excluding errors in the equations implementation. The present analysis with PoPe has allowed to evaluate the numerical error introduced by the adopted numerical schemes, and to find its origin. Nevertheless, the values of effective operators are reasonable, and the difference with theoretical weights is comparable with the one already found in former analysis of other codes, such as TERESA [72].
The most critical equation is the vorticity conservation, where the effective weights depart significantly from the theoretical ones, in TOKAM3X simulations with the usual set of parameters. This discrepancy is most probably to be attributed to the semi-implicit advancement in time of the equation: indeed, when implicit operators are artificially excluded in simulations, a good accuracy is recovered, also in the other two examined

equations (which are coupled to the vorticity one). A scan in the time-step parameter, using the full TOKAM3X model, indicates that for low time-step values, of the order of 10^{-3}, the theoretical weights are almost perfectly recovered. This demonstrates that the numerical implementation of the operators is correct, but at the same time a smaller time-step would be needed to solve the equations with an elevated accuracy.
The time-step affects the solution of the vorticity equation in two ways. Firstly, a high value of the time-step leads to a higher condition number of the 3D operator appearing in the vorticity equation, causing in the end a proportional numerical error in the solution. The order of magnitude of the final numerical error introduced with the inversion operation has still to be evaluated rigorously.
On the other hand, the physical system may show, regarding uniquely the vorticity equation, a fast dynamics (linked especially to the divergence of the parallel current) that cannot be caught when the time-step is set equal to the inverse of the cyclotron frequency ($dt = 1$). Figure D.8 shows a sketch of the advancement in time determined by the implicit method adopted with TOKAM3X, compared with the theoretical advancement calculated by PoPe.

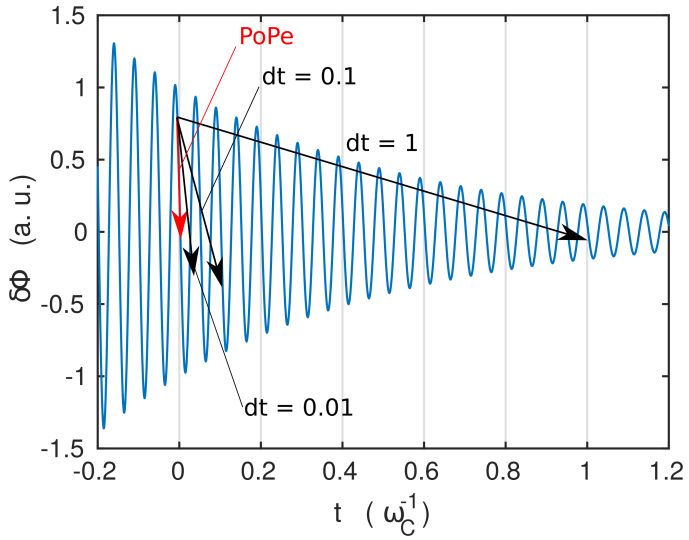

Figure D.8: *Sketch of the advancement of an arbitrary field in time, with an implicit method, as the one adopted in TOKAM3X, when the time-step is varied. In blue we represent the exact solution. The theoretical advancement in time, objective of the PoPe analysis, is represented in red, for comparison.*

One can notice that if the effective dynamics of the system developed on smaller time scales than the time-step adopted by TOKAM3X, this dynamics would be filtered by the code. However, in this case, the PoPe method would find that the time-derivative calculated by the code is different from the theoretical one, and, by consequence, also the weights associated to the different operators. Only when the time-step is decreased towards the small physical time-scale, the advancement in time would be close to the theoretical one, and thus also to the one calculated by PoPe. In this way the theoretical weights would be recovered, as it has been shown in figure D.7.
Nevertheless, at time-steps smaller than $dt = 1$, the physical model of TOKAM3X would

lose its validity, since it is based on drift-reduced equations. For this reason we adopt an implicit method, in order to catch the evolution on time scales of the order of 1 ω_C^{-1}. In this case, the average dynamics cannot be properly tested by means of the PoPe method. Even with $dt = 1$, however, the operators in the vorticity equation, as well as in the other equations, although differing from the theoretical ones, are well correlated among each other, so that the physics of the system at the time-scales of interest is qualitatively correct. This is confirmed by the fact that TOKAM3X is in qualitative (and in some case quantitative) agreement both with the other turbulence codes (see [51], [52]), and, as described in this thesis, also with experimental results (see chapter 4 for large-scale aspects, and 3 for small-scale turbulence properties).
Further investigations are ongoing on the most recent version of TOKAM3X (release 2017), which has introduced small modifications to the adopted numerical schemes. This analysis has allowed, however, to find some criticality in the solution of the TOKAM3X system, in particular in the implicit advancement, which will have to be taken into account also in the further developments on the new TOKAM3X version.

Bibliography

[1] Jeffrey P. Freidberg. *Plasma Physics and Fusion Energy*. Cambridge University Press, 2007. (Cited in sections 1.1 and 1.2.)

[2] J D Lawson. Some criteria for a power producing thermonuclear reactor. *Proceedings of the Physical Society. Section B*, 70(1):6, 1957. (Cited in section 1.1.)

[3] P. R. Thomas, P. Andrew, B. Balet, D. Bartlett, J. Bull, B. de Esch, A. Gibson, C. Gowers, H. Guo, G. Huysmans, T. Jones, M. Keilhacker, R. Koenig, M. Lennholm, P. Lomas, A. Maas, F. Marcus, F. Nave, V. Parail, F. Rimini, J. Strachan, K-D. Zastrow, and N. Zornig. Observation of alpha heating in jet dt plasmas. *Phys. Rev. Lett.*, 80:5548–5551, Jun 1998. (Cited in section 1.1.)

[4] Iter website. `https://www.iter.org/`. (Cited in section 1.1.)

[5] Francis F. Chen. *Introduction to plasma physics and controlled fusion. Volume 1*. Springer, second edition, 1984. (Cited in sections 1.2, 1.4.1, 1.5.1, 1.5.1, 1.6.1, and 2.3.3.)

[6] J. Wesson. *Tokamaks*. Oxford University Press, 2004. (Cited in sections 1.2, 1.2.3, 1.5.1, 2.4.3, 4.1.4, 5.1.1, and 5.5.1.)

[7] Eurofusion website. `https://www.euro-fusion.org/`. (Cited in section 1.2.)

[8] D. van Houtte, G. Martin, and A. Bécoulet et al. Recent fully non-inductive operation results in tore supra with 6 min, 1 gj plasma discharges. *Nuclear Fusion*, 44(5), 2004. (Cited in section 1.3.)

[9] G. Pucella, E. Alessi, and L. Amicucci et al. Overview of the ftu results. *Nuclear Fusion*, 57(10):102004, 2017. (Cited in section 1.3.)

[10] H. Fernandes, C. Silva, R. B. Gomes, A. Neto, P. Duarte, G. Van Oost, M. Gryaznevich, and A. Malaquias. The international joint experiment isttok. *Plasma Physics Reports*, 35(10):841, Nov 2009. (Cited in section 1.3.)

[11] M. Kocan, R.A. Pitts, G. Arnoux, I. Balboa, P.C. de Vries, R. Dejarnac, I. Furno, R.J. Goldston, Y. Gribov, J. Horacek, M. Komm, B. Labit, B. LaBombard, C.J. Lasnier, R. Mitteau, F. Nespoli, D. Pace, R. Panek, P.C. Stangeby, J.L. Terry, C. Tsui, and P. Vondracek. Impact of a narrow limiter sol heat flux channel on the iter first wall panel shaping. *Nuclear Fusion*, 55(3):033019, 2015. (Cited in section 1.3.)

[12] P. C. Stangeby. *The Plasma Boundary of Magnetic Fusion Devices*. 2000. (Cited in sections 1.3, 1.6.1, 1.6.2, and 4.4.2.)

[13] F. L. Hinton and R. D. Hazeltine. Theory of Plasma Transport in Toroidal Confinements Systems, 1976. (Cited in sections 1.4.1 and 2.4.2.)

[14] T. Gerbaud. *Étude de la microturbulence par réflectométrie dans un plasma de fusion sur le tokamak Tore-Supra.* PhD thesis, 2006. (Cited in section 1.4.1.)

[15] F. Wagner, G. Becker, K. Behringer, D. Campbell, A. Eberhagen, W. Engelhardt, G. Fussmann, O. Gehre, J. Gernhardt, G. v. Gierke, G. Haas, M. Huang, F. Karger, M. Keilhacker, O. Klüber, M. Kornherr, K. Lackner, G. Lisitano, G. G. Lister, H. M. Mayer, D. Meisel, E. R. Müller, H. Murmann, H. Niedermeyer, W. Poschenrieder, H. Rapp, H. Röhr, F. Schneider, G. Siller, E. Speth, A. Stäbler, K. H. Steuer, G. Venus, O. Vollmer, and Z. Yü. Regime of improved confinement and high beta in neutral-beam-heated divertor discharges of the asdex tokamak. *Phys. Rev. Lett.*, 49:1408–1412, Nov 1982. (Cited in section 1.4.2.)

[16] Y. Ma, J.W. Hughes, A.E. Hubbard, B. LaBombard, R.M. Churchill, T. Golfinopolous, N. Tsujii, and E.S. Marmar. Scaling of h-mode threshold power and l–h edge conditions with favourable ion grad- b drift in alcator c-mod tokamak. *Nuclear Fusion*, 52(2):023010, 2012. (Cited in section 1.6.)

[17] D. Frigione, L. Garzotti, C. D. Challis, M. De Baar, P. De Vries, M. Brix, X. Garbet, N. Hawkes, A. Thyagaraja, L. Zabeo, and JET EFDA contributors. Pellet injection and high density itb formation in jet advanced tokamak plasmas. *Nuclear Fusion*, 47(2):74, 2007. (Cited in section 1.6.)

[18] Y R Martin, T Takizuka, and the ITPA CDBM H-mode Threshold Database Working Group. Power requirement for accessing the h-mode in iter. *Journal of Physics: Conference Series*, 123(1):012033, 2008. (Cited in sections 1.4.2 and 1.7.)

[19] S. I. Braginskii. *Transport Processes in a Plasma*, volume 1. Provided by the SAO/-NASA Astrophysics Data System, 1965. (Cited in sections 1.5.5, 2.2.4, and 2.7.1.)

[20] Ph. Ghendrih, K. Bodi, H. Bufferand, G. Chiavassa, G. Ciraolo, N. Fedorczak, L. Isoardi, A. Paredes, Y. Sarazin, E. Serre, F. Schwander, and P. Tamain. Transition to supersonic flows in the edge plasma. *Plasma Physics and Controlled Fusion*, 53(5):054019, 2011. (Cited in sections 1.6.1 and 4.1.1.)

[21] G R Tynan, I Cziegler, P H Diamond, M Malkov, A Hubbard, J W Hughes, J L Terry, and J H Irby. Recent progress towards a physics-based understanding of the h-mode transition. *Plasma Physics and Controlled Fusion*, 58(4):044003, 2016. (Cited in sections 1.7 and 5.4.)

[22] A. Loarte, B. Lipschultz, A.S. Kukushkin, G.F. Matthews, P.C. Stangeby, N. Asakura, G.F. Counsell, G. Federici, A. Kallenbach, K. Krieger, A. Mahdavi, V. Philipps, D. Reiter, J. Roth, J. Strachan, D. Whyte, R. Doerner, T. Eich, W. Fundamenski, A. Herrmann, M. Fenstermacher, P. Ghendrih, M. Groth, A. Kirschner, S. Konoshima, B. LaBombard, P. Lang, A.W. Leonard, P. Monier-

Garbet, R. Neu, H. Pacher, B. Pegourie, R.A. Pitts, S. Takamura, J. Terry, E. Tsitrone, the ITPA Scrape-off Layer, and Divertor Physics Topical Group. Chapter 4: Power and particle control. *Nuclear Fusion*, 47(6):S203, 2007. (Cited in section 1.7.)

[23] R.A. Pitts, S. Bardin, B. Bazylev, M.A. van den Berg, P. Bunting, S. Carpentier-Chouchana, J.W. Coenen, Y. Corre, R. Dejarnac, F. Escourbiac, J. Gaspar, J.P. Gunn, T. Hirai, S-H. Hong, J. Horacek, D. Iglesias, M. Komm, K. Krieger, C. Lasnier, G.F. Matthews, T.W. Morgan, S. Panayotis, S. Pestchanyi, A. Podolnik, R.E. Nygren, D.L. Rudakov, G. De Temmerman, P. Vondracek, and J.G. Watkins. Physics conclusions in support of iter w divertor monoblock shaping. *Nuclear Materials and Energy*, 2017. (Cited in section 1.7.)

[24] S. Tsuji, K. Ushigusa, Y. Ikeda, T. Imai, T. Itami, M. Nemoto, K. Nagashima, Y. Koide, Y. Kawano, T. Fukuda, T. Kondoh, M. Shimada, H. Nakamura, O. Naito, H. Yoshida, T. Nishitani, H. Kubo, K. Tobita, Y. Kusama, S. Ishida, M. Sato, N. Isei, T. Sugie, N. Miya, R. Yoshino, and K. Uehara. Observation of the limiter h mode in the jt-60 tokamak with lower-hybrid current drive. *Phys. Rev. Lett.*, 64:1023–1026, Feb 1990. (Cited in section 1.7.)

[25] F. Wagner. A study of the perpendicular particle transport properties in the scrape-off layer of asdex. *Nuclear Fusion*, 25(5):525, 1985. (Cited in section 1.7.)

[26] T. Eich, B. Sieglin, A. Scarabosio, W. Fundamenski, R. J. Goldston, and A. Herrmann. Inter-elm power decay length for jet and asdex upgrade: Measurement and comparison with heuristic drift-based model. *Phys. Rev. Lett.*, 107:215001, Nov 2011. (Cited in sections 1.7, 4.4.1, and 4.4.1.)

[27] J Horacek, R A Pitts, J Adamek, G Arnoux, J-G Bak, S Brezinsek, M Dimitrova, R J Goldston, J P Gunn, J Havlicek, S-H Hong, F Janky, B LaBombard, S Marsen, G Maddaluno, L Nie, V Pericoli, Tsv Popov, R Panek, D Rudakov, J Seidl, D S Seo, M Shimada, C Silva, P C Stangeby, B Viola, P Vondracek, H Wang, G S Xu, Y Xu, and JET Contributors. Multi-machine scaling of the main sol parallel heat flux width in tokamak limiter plasmas. *Plasma Physics and Controlled Fusion*, 58(7):074005, 2016. (Cited in sections 1.7 and 5.)

[28] J.P. Gunn, R. Dejarnac, P. Devynck, N. Fedorczak, V. Fuchs, C. Gil, M. Kočan, M. Komm, M. Kubič, T. Lunt, P. Monier-Garbet, J.-Y. Pascal, and F. Saint-Laurent. Scrape-off layer power flux measurements in the tore supra tokamak. *Journal of Nuclear Materials*, 438(Supplement):S184 – S188, 2013. Proceedings of the 20th International Conference on Plasma-Surface Interactions in Controlled Fusion Devices. (Cited in sections 1.7 and 5.)

[29] A. Scarabosio, T. Eich, A. Herrmann, and B. Sieglin. Outer target heat fluxes and power decay length scaling in l-mode plasmas at jet and aug. *Journal of Nuclear Materials*, 438(Supplement):S426 – S430, 2013. Proceedings of the 20th International Conference on Plasma-Surface Interactions in Controlled Fusion Devices. (Cited in sections 1.7 and 5.)

[30] T. Eich, A.W. Leonard, R.A. Pitts, W. Fundamenski, R.J. Goldston, T.K. Gray, A. Herrmann, A. Kirk, A. Kallenbach, O. Kardaun, A.S. Kukushkin, B. LaBombard, R. Maingi, M.A. Makowski, A. Scarabosio, B. Sieglin, J. Terry, A. Thornton, ASDEX Upgrade Team, and JET EFDA Contributors. Scaling of the tokamak near the scrape-off layer h-mode power width and implications for iter. *Nuclear Fusion*, 53(9):093031, 2013. (Cited in sections 1.7, 3.3.2, and 4.4.1.)

[31] J.R. Harrison, G.M. Fishpool, and B.D. Dudson. Filamentary transport in the private flux region in MAST. *Journal of Nuclear Materials*, 463:757 – 760, 2015. PLASMA-SURFACE INTERACTIONS 21Proceedings of the 21st International Conference on Plasma-Surface Interactions in Controlled Fusion Devices Kanazawa, Japan May 26-30, 2014. (Cited in sections 1.7 and 3.3.1.)

[32] J.L. Terry, S. Ballinger, D. Brunner, B. LaBombard, A.E. White, and S.J. Zweben. Fast imaging of filaments in the x-point region of alcator c-mod. *Nuclear Materials and Energy*, 2017. (Cited in sections 1.7 and 4.4.)

[33] P. Tamain, H. Bufferand, G. Ciraolo, C. Colin, E. Serre, and F. Schwander. The tokam3x code for edge turbulence fluid simulations of tokamak plasmas in versatile magnetic geometries. *Journal of Computational Physics*, Accepted for publication, 2016. (Cited in sections 1.7, 2, 2.1.2, 2.5.1, 2.6.2, 3, D.1, and D.5.)

[34] Y. Sarazin and Ph. Ghendrih. Intermittent particle transport in two-dimensional edge turbulence. *Physics of Plasmas*, 5(12):4214–4228, 1998. (Cited in sections 2.1.1, 2.3.2, 3, 3.1.2, and 3.3.1.)

[35] J Juul Rasmussen, A H Nielsen, J Madsen, V Naulin, and G S Xu. Numerical modeling of the transition from low to high confinement in magnetically confined plasma. *Plasma Physics and Controlled Fusion*, 58(1):014031, 2016. (Cited in sections 2.1.1, 3, and 5.3.)

[36] Paolo Ricci, B. N. Rogers, and S. Brunner. High and low-confinement modes in simple magnetized toroidal plasmas. *Phys. Rev. Lett.*, 100:225002, Jun 2008. (Cited in sections 2.1.1 and 5.3.)

[37] C. Norscini. *Self-organized turbulent transport in fusion plasmas*. PhD thesis. (Cited in sections 2.1.1, 2.3.2, and 5.3.)

[38] C. Baudoin, P. Tamain, G. Ciraolo, R. Futtersack, A. Gallo, P. Ghendrih, Y. Marandet, N. Nace, and C. Norscini. On the effect of electron temperature fluctuations on turbulent heat transport in the edge plasma of tokamaks. *Contributions to Plasma Physics*, 56(6-8):563–568, 2016. (Cited in sections 2.1.1 and 5.5.2.)

[39] N. Nace, M. Perin, P. Tamain, G. Ciraolo, C. Baudoin, R. Futtersack, Ph. Ghendrih, and C. Norscini. Turbulence interaction with driven transport barriers in the scrape-off layer of tokamaks. *Contributions to Plasma Physics*, 56(6-8):581–586, 2016. (Cited in sections 2.1.1 and 5.3.1.)

[40] N. Fedorczak, J.P. Gunn, N. Nace, A. Gallo, C. Baudoin, H. Bufferand, G. Ciraolo, Th. Eich, Ph. Ghendrih, and P. Tamain. Width of turbulent sol in circular plasmas:

A theoretical model validated on experiments in tore supra tokamak. *Nuclear Materials and Energy*, 2017. (Cited in sections 2.1.1 and 5.1.3.)

[41] B. LaBombard, J.E. Rice, A.E. Hubbard, J.W. Hughes, M. Greenwald, J. Irby, Y. Lin, B. Lipschultz, E.S. Marmar, C.S. Pitcher, N. Smick, S.M. Wolfe, S.J. Wukitch, and the Alcator Group. Transport-driven scrape-off-layer flows and the boundary conditions imposed at the magnetic separatrix in a tokamak plasma. *Nuclear Fusion*, 44(10):1047, 2004. (Cited in sections 2.1.1, 2.6.1, 4.1, 4.1.1, 4.2, 4.2.1, and 4.3.)

[42] J. P. Gunn, C. Boucher, M. Dionne, V. Fuchs, T. Loarer, J. Sto, I. Nanobashvili, R. Pa, J. Ada, J. Bucalossi, R. Dejarnac, T. Van. Rompuy, R. Zago, P. Devynck, P. Hertout, M. Hron, G. Lebrun, P. Moreau, F. Rimini, A. Sarkissian, and G. Van. Oost. Evidence for a poloidally localized enhancement of radial transport in the scrape-off layer of the Tore Supra tokamak. *Journal of Nuclear Materials*, 365:484–490, 2007. (Cited in sections 2.1.1, 4.1.1, and 4.1.4.)

[43] N. Smick, B. LaBombard, and I. H. Hutchinson. Transport and drift-driven plasma flow components in the Alcator C-Mod boundary plasma. *Nuclear Fusion*, 53(2):023001, feb 2013. (Cited in sections 2.1.2 and 4.3.)

[44] N. Fedorczak. *Experimental investigation of turbulent transport at the edge of a tokamak plasma*. PhD thesis. (Cited in section 2.1.2.)

[45] P Ricci, F D Halpern, S Jolliet, J Loizu, A Mosetto, A Fasoli, I Furno, and C Theiler. Simulation of plasma turbulence in scrape-off layer conditions: the gbs code, simulation results and code validation. *Plasma Physics and Controlled Fusion*, 54(12):124047, 2012. (Cited in sections 2.1.2 and 2.6.1.)

[46] B.D. Dudson, M.V. Umansky, X.Q. Xu, P.B. Snyder, and H.R. Wilson. BOUT++: A framework for parallel plasma fluid simulations. *Computer Physics Communications*, 180(9):1467–1480, sep 2009. (Cited in section 2.1.2.)

[47] A. Stegmeir. *GRILLIX: A 3D turbulence code for magnetic fusion devices based on a field line map*. PhD thesis, 2015. (Cited in section 2.1.2.)

[48] P. Tamain, Ph. Ghendrih, E. Tsitrone, Y. Sarazin, X. Garbet, V. Grandgirard, J. Gunn, E. Serre, G. Ciraolo, and G. Chiavassa. 3D modelling of edge parallel flow asymmetries. *Journal of Nuclear Materials*, 390-391:347–350, jun 2009. (Cited in sections 2.1.2, 4.1.1, and 4.1.4.)

[49] J. Loizu, P. Ricci, F. D. Halpern, S. Jolliet, and A. Mosetto. Intrinsic toroidal rotation in the scrape-off layer of tokamaks. *Physics of Plasmas*, 062309, 2014. (Cited in sections 2.1.2, 4.1.1, 4.1.2, and 4.1.4.)

[50] C. Colin, P. Tamain, F. Schwander, E. Serre, H. Bufferand, G. Ciraolo, N. Fedorczak, and Ph. Ghendrih. Impact of the plasma-wall contact position on edge turbulent transport and poloidal asymmetries in 3D global turbulence simulations. *Journal of Nuclear Materials*, 463:654–658, 2015. (Cited in sections 2.1.2, 4.1.1, and 4.1.4.)

[51] F Riva, C Colin, J Denis, L Easy, I Furno, J Madsen, F Militello, V Naulin, A H Nielsen, J M B Olsen, J T Omotani, J J Rasmussen, P Ricci, E Serre, P Tamain, and C Theiler. Blob dynamics in the torpex experiment: a multi-code validation. *Plasma Physics and Controlled Fusion*, 58(4):044005, 2016. (Cited in sections 2.1.2, 2.6.2, and D.6.)

[52] F Militello, N R Walkden, T Farley, W A Gracias, J Olsen, F Riva, L Easy, N Fedorczak, I Lupelli, J Madsen, A H Nielsen, P Ricci, P Tamain, and J Young. Multi-code analysis of scrape-off layer filament dynamics in mast. *Plasma Physics and Controlled Fusion*, 58(10):105002, 2016. (Cited in sections 2.1.2, 2.6.2, and D.6.)

[53] P. Paruta, P. Ricci, F. Riva, C. Wersal, and J. Morales. A flexible numerical scheme for simulating plasma turbulence in the tokamak scrape off layer. In *Joint Varenna-Lausanne International workshop, Varenna, Italy*, 2016. (Cited in section 2.1.2.)

[54] B D Dudson and J Leddy. Hermes: global plasma edge fluid turbulence simulations. *Plasma Physics and Controlled Fusion*, 59(5):054010, 2017. (Cited in section 2.1.2.)

[55] C. S. Chang and S. Ku. Spontaneous rotation sources in a quiescent tokamak edge plasma. *Physics of Plasmas*, 15(6), 2008. (Cited in section 2.1.2.)

[56] F. L. Hinton and C. W. Horton. Amplitude Limitation of a Collisional Drift Wave Instability. *Physics of Fluids*, 14:116, 1971. (Cited in section 2.2.4.)

[57] K. Bodi, G Ciraolo, Ph. Ghendrih, Schwander F., Serre E., and P. Tamain. Impact of the boussinesq approximation in tokamak scrape-off layer turbulence. In *Proceedings of 38th EPS conference on Plasma Physics*, 2011. (Cited in section 2.2.4.)

[58] C. Baudoin, P. Tamain, H. Bufferand, G. Ciraolo, N. Fedorczak, D. Galassi, A. Gallo, Ph. Ghendrih, and N. Nace. Drift driven vs turbulent heat transport in 3d edge plasma simulations. In *Proceedings of the 16th PET conference, Marseille*, 2017. (Cited in sections 2.2.4 and 5.5.2.)

[59] Akira Hasegawa and Masahiro Wakatani. Plasma edge turbulence. *Phys. Rev. Lett.*, 50:682–686, Feb 1983. (Cited in section 2.3.2.)

[60] X. Garbet. Instabilités, turbulence et transport dans un plasma magnetisé. 2001. (Cited in sections 2.3.2, 3.2.2, 3.3.2, 5.1.3, and 5.1.3.)

[61] X. Garbet, C. Fenzi, H. Capes, P. Devynck, and G. Antar. Kelvin–helmholtz instabilities in tokamak edge plasmas. *Physics of Plasmas*, 6(10):3955–3965, 1999. (Cited in section 2.3.4.)

[62] F. Schwander, G. Chiavassa, G. Ciraolo, Ph. Ghendrih, L. Isoardi, A. Paredes, Y. Sarazin, E. Serre, and P. Tamain. Parallel shear flow instability in the tokamak edge. *J. of Nucl. Mat.*, 415(1, Supplement):S601 – S604, 2011. Proceedings of the 19th International Conference on Plasma-Surface Interactions in Controlled Fusion. (Cited in section 2.3.4.)

[63] L.L. Lao, H. St. John, R.D. Stambaugh, and W. Pfeiffer. Separation of beta p and l i in tokamaks of non-circular cross-section. *Nuclear Fusion*, 25(10):1421, 1985. (Cited in sections 2.4.1 and 2.4.4.)

[64] W. D. D'haeseleer, W. N. G. Hitchon, J. D. Callen, and J. L. Shohet. *Flux Coordinates and Magnetic field Structure: A Guide to a Fundamental Tool of Plasma Theory*. Springer-Verlag, 1991. (Cited in sections 2.4.1, 2.4.1, and B.)

[65] P.L Roe. Approximate riemann solvers, parameter vectors, and difference schemes. *Journal of Computational Physics*, 43(2):357 – 372, 1981. (Cited in section 2.5.1.)

[66] Rosa Donat and Antonio Marquina. Capturing shock reflections: An improved flux formula. *Journal of Computational Physics*, 125(1):42 – 58, 1996. (Cited in section 2.5.1.)

[67] Xu-Dong Liu, Stanley Osher, and Tony Chan. Weighted essentially non-oscillatory schemes. *Journal of Computational Physics*, 115(1):200 – 212, 1994. (Cited in sections 2.5.1 and D.3.)

[68] Pastix (parallel sparse matrix package). `http://pastix.gforge.inria.fr`. (Cited in section 2.5.1.)

[69] H. Bufferand, G. Ciraolo, Y. Marandet, J. Bucalossi, Ph. Ghendrih, J. Gunn, N. Mellet, P. Tamain, R. Leybros, N. Fedorczak, F. Schwander, and E. Serre. Numerical modelling for divertor design of the west device with a focus on plasma-wall interactions. *Nuclear Fusion*, 55(5):053025, 2015. (Cited in section 2.5.2.)

[70] S. Wiesen, D. Reiter, V. Kotov, M. Baelmans, W. Dekeyser, A.S. Kukushkin, S.W. Lisgo, R.A. Pitts, V. Rozhansky, G. Saibene, I. Veselova, and S. Voskoboynikov. The new solps-iter code package. *Journal of Nuclear Materials*, 463(Supplement C):480 – 484, 2015. PLASMA-SURFACE INTERACTIONS 21. (Cited in section 2.5.2.)

[71] V. Grandgirard, J. Abiteboul, J. Bigot, T. Cartier-Michaud, N. Crouseilles, G. Dif-Pradalier, Ch. Ehrlacher, D. Esteve, X. Garbet, Ph. Ghendrih, G. Latu, M. Mehrenberger, C. Norscini, Ch. Passeron, F. Rozar, Y. Sarazin, E. Sonnendrücker, A. Strugarek, and D. Zarzoso. A 5d gyrokinetic full-f global semi-lagrangian code for flux-driven ion turbulence simulations. *Computer Physics Communications*, 207(Supplement C):35 – 68, 2016. (Cited in section 2.6.1.)

[72] T. Cartier-Michaud, P. Ghendrih, Y. Sarazin, J. Abiteboul, H. Bufferand, G. Dif-Pradalier, X. Garbet, V. Grandgirard, G. Latu, C. Norscini, C. Passeron, and P. Tamain. Projection on proper elements for code control: Verification, numerical convergence, and reduced models. application to plasma turbulence simulations. *Physics of Plasmas*, 23(2):020702, 2016. (Cited in sections 2.6.2, D.1, and D.6.)

[73] D. Galassi, P. Tamain, H. Bufferand, G. Ciraolo, Ph. Ghendrih, C. Baudoin, C. Colin, N. Fedorczak, N. Nace, and E. Serre. Drive of parallel flows by turbulence and large-scale e x b transverse transport in divertor geometry. *Nuclear Fusion*, 57(3):036029, 2017. (Cited in sections 3 and 4.)

[74] Annamaria Mosetto, Federico D. Halpern, Sébastien Jolliet, and Paolo Ricci. Low-frequency linear-mode regimes in the tokamak scrape-off layer. *Physics of Plasmas*, 19(11):112103, 2012. (Cited in sections 3.1.1 and 3.3.2.)

[75] Justin R. Angus, Maxim V. Umansky, and Sergei I. Krasheninnikov. Effect of drift waves on plasma blob dynamics. *Phys. Rev. Lett.*, 108:215002, May 2012. (Cited in section 3.1.1.)

[76] Bruce D. Scott. Drift wave versus interchange turbulence in tokamak geometry: Linear versus nonlinear mode structure. *Physics of Plasmas*, 12(6):062314, 2005. (Cited in sections 3.1.1 and 3.1.1.)

[77] B Nold, G D Conway, T Happel, H W Müller, M Ramisch, V Rohde, U Stroth, and the ASDEX Upgrade Team. Generation of blobs and holes in the edge of the asdex upgrade tokamak. *Plasma Physics and Controlled Fusion*, 52(6):065005, 2010. (Cited in sections 3.1.2 and 3.1.2.)

[78] P. Tamain, H. Bufferand, G. Ciraolo, C. Colin, E. Serre, and F. Schwander. 3D Properties of Edge Turbulent Transport in Full-Torus Simulations and their Impact on Poloidal Asymmetries. *Contributions to Plasma Physics*, 559(4):555–559, 2014. (Cited in sections 3.1.2, 3.1.2, 3.1.3, and 3.2.3.)

[79] P Tamain, Ph Ghendrih, H Bufferand, G Ciraolo, C Colin, N Fedorczak, N Nace, F Schwander, and E Serre. Multi-scale self-organisation of edge plasma turbulent transport in 3d global simulations. *Plasma Physics and Controlled Fusion*, 57(5):054014, 2015. (Cited in section 3.2.1.)

[80] S. Brunner, M. Fivaz, T. M. Tran, and J. Vaclavik. Global approach to the spectral problem of microinstabilities in tokamak plasmas using a gyrokinetic model. *Physics of Plasmas*, 5(11):3929–3949, 1998. (Cited in sections 3.2.2 and 3.2.2.)

[81] D. Farina, R. Pozzoli, and D.D. Ryutov. Effect of the magnetic field geometry on the flute-like perturbations near the divertor x point. *Nuclear Fusion*, 33(9):1315, 1993. (Cited in section 3.2.2.)

[82] N. R. Walkden, B. D. Dudson, and G. Fishpool. Characterization of 3D filament dynamics in a MAST SOL flux tube geometry. *Plasma Phys. Control. Fusion*, 55:105005, 2013. (Cited in section 3.2.2.)

[83] N. Fedorczak, P.H. Diamond, G. Tynan, and P. Manz. Shear-induced reynolds stress at the edge of l-mode tokamak plasmas. *Nuclear Fusion*, 52(10):103013, 2012. (Cited in sections 3.2.2 and 5.4.2.)

[84] N Fedorczak, P Manz, S Chakraborty Thakur, M Xu, and G R Tynan. Zonal flow shear amplification by depletion of anisotropic potential eddies in a magnetized plasma: idealized models and laboratory experiment. *Plasma Physics and Controlled Fusion*, 55(2):025011, 2013. (Cited in section 3.2.2.)

[85] A.V. Chankin. Classical drifts in the tokamak sol and divertor: models and experiment. *Journal of Nuclear Materials*, 241:199 – 213, 1997. (Cited in sections 3.2.4 and 4.1.2.)

[86] T.D. Rognlien, G.D. Porter, and D.D. Ryutov. Influence of exb and grad-b drift terms in 2-d edge/sol transport simulations. *Journal of Nuclear Materials*, 266–269:654 – 659, 1999. (Cited in sections 3.2.4, 4.1.2, and 4.1.3.)

[87] V.A. Rozhansky, S.P. Voskoboynikov, E.G. Kaveeva, D.P. Coster, and R. Schneider. Simulation of tokamak edge plasma including self-consistent electric fields. *Nuclear Fusion*, 41(4):387, 2001. (Cited in sections 3.2.4 and 4.1.2.)

[88] H. Bufferand, C. Baudoin, J. Bucalossi, G. Ciraolo, J. Denis, N. Fedorczak, D. Galassi, Ph. Ghendrih, R. Leybros, Y. Marandet, N. Mellet, J. Morales, N. Nace, E. Serre, P. Tamain, and M. Valentinuzzi. Implementation of drift velocities and currents in soledge2d–eirene. *Nuclear Materials and Energy*, pages –, 2017. (Cited in sections 3.2.4 and 4.1.2.)

[89] G.S. Kirnev, G. Corrigan, D. Coster, S.K. Erents, W. Fundamenski, G.F. Matthews, and R.A. Pitts. EDGE2D code simulations of SOL flows and in–out divertor asymmetries in JET. *Journal of Nuclear Materials*, 337-339:271–275, mar 2005. (Cited in sections 3.2.4 and 4.1.1.)

[90] H. Bufferand, G. Ciraolo, Ph. Ghendrih, Y. Marandet, J. Bucalossi, C. Colin, N. Fedorczak, D. Galassi, J. Gunn, R. Leybros, E. Serre, and P. Tamain. Interchange turbulence model for the edge plasma in soledge2d-eirene. *Contributions to Plasma Physics*, 56(6-8):555–562, 2016. (Cited in section 3.2.4.)

[91] S J Zweben, J A Boedo, O Grulke, C Hidalgo, B LaBombard, R J Maqueda, P Scarin, and J L Terry. Edge turbulence measurements in toroidal fusion devices. *Plasma Physics and Controlled Fusion*, 49(7):S1, 2007. (Cited in section 3.3.)

[92] B. I. Cohen, M. V. Umansky, W. M. Nevins, M. A. Makowski, J. A. Boedo, D. L. Rudakov, G. R. McKee, Z. Yan, and R. J. Groebner. Simulations of drift resistive ballooning l-mode turbulence in the edge plasma of the diii-d tokamak. *Physics of Plasmas*, 20(5):055906, 2013. (Cited in section 3.3.1.)

[93] N.R. Walkden, F. Militello, J. Harrison, T. Farley, S. Silburn, and J. Young. Identification of intermittent transport in the scrape-off layer of {MAST} through high speed imaging. *Nuclear Materials and Energy*, pages –, 2016. (Cited in sections 3.3.1, 3.14, 3.3.2, and 3.3.2.)

[94] R. E. Waltz, G. M. Staebler, W. Dorland, G. W. Hammett, M. Kotschenreuther, and J. A. Konings. A gyro-Landau-fluid transport model. *Phys. Plasmas*, 4(7):2482, 1997. (Cited in section 3.3.2.)

[95] P. Xanthopoulos, D. Mikkelsen, F. Jenko, W. Dorland, and O. Kalentev. Verification and application of numerically generated magnetic coordinate systems in gyrokinetics. *Physics of Plasmas*, 15(12):122108, 2008. (Cited in section 3.3.2.)

[96] J L V Lewandowski and M Persson. Local magnetic shear in tokamak plasmas. *Plasma Physics and Controlled Fusion*, 37(11):1199, 1995. (Cited in section 3.3.2.)

[97] M. Nadeem, T. Rafiq, and M. Persson. Local magnetic shear and drift waves in stellarators. *Physics of Plasmas*, 8(10):4375–4385, 2001. (Cited in section 3.3.2.)

[98] T. S. Hahm and K. H. Burrell. Flow shear induced fluctuation suppression in finite aspect ratio shaped tokamak plasma. *Physics of Plasmas*, 2(5):1648–1651, 1995. (Cited in section 3.3.2.)

[99] T.S. Hahm, D.H. Na, J.W. Lee, J.W. Park, Y.S. Na, S.S. Kim, W.H. Ko, P.H. Diamond, Hogun Jhang, and Y.M. Jeon. E x b shear suppression of turbulence in diverted h-mode plasmas: role of edge magnetic shear. *Nuclear Fusion*, 53(9):093005, 2013. (Cited in section 3.3.2.)

[100] X. Garbet, C. Bourdelle, G. T. Hoang, P. Maget, S. Benkadda, P. Beyer, C. Figarella, I. Voitsekovitch, O. Agullo, and N. Bian. Global simulations of ion turbulence with magnetic shear reversal. *Physics of Plasmas*, 8(6):2793–2803, 2001. (Cited in section 3.3.2.)

[101] X Litaudon, R Arslanbekov, G T Hoang, E Joffrin, F Kazarian-Vibert, D Moreau, Y Peysson, P Bibet, P Froissard, M Goniche, G Rey, J Ferron, and K Kupfer. Stationary magnetic shear reversal experiments in tore supra. *Plasma Physics and Controlled Fusion*, 38(9):1603, 1996. (Cited in section 3.3.2.)

[102] W.A. Gracias, P. Tamain, E. Serre, R.A. Pitts, and L. García. The impact of magnetic shear on the dynamics of a seeded 3d filament in slab geometry. *Nuclear Materials and Energy*, 2017. (Cited in section 3.3.2.)

[103] A Gallo, N Fedorczak, S Elmore, R Maurizio, H Reimerdes, C Theiler, C K Tsui, J A Boedo, M Faitsch, H Bufferand, G Ciraolo, D Galassi, P Ghendrih, M Valentinuzzi, P Tamain, the EUROfusion MST1 team, and the TCV team. Impact of the plasma geometry on divertor power exhaust: experimental evidence from tcv and simulations with soledge2d and tokam3x. *Plasma Physics and Controlled Fusion*, 60(1):014007, 2018. (Cited in sections 4, 4.12, 4.4.1, 4.13, 4.4.2, 4.16, and 4.4.2.)

[104] Divertor imbalance and divertor density regimes for ballooned cross-field turbulence. *Journal of Nuclear Materials*, 438:S368 – S371, 2013. Proceedings of the 20th International Conference on Plasma-Surface Interactions in Controlled Fusion Devices. (Cited in section 4.1.)

[105] G F Matthews. Tokamak plasma diagnosis by electrical probes. *Plasma Physics and Controlled Fusion*, 36(10):1595, 1994. (Cited in section 4.1.1.)

[106] N. Asakura. Understanding the SOL flow in L-mode plasma on divertor tokamaks, and its influence on the plasma transport. *Journal of Nuclear Materials*, 365:41–51, 2007. (Cited in sections 4.1.1, 4.7, 4.1.4, and 4.3.)

[107] R. A. Pitts, P. Andrew, X. Bonnin, A. V. Chankin, Y. Corre, G. Corrigan, D. Coster, I. Duran, T Eich, S. K. Erents, W. Fundamenski, A. Huber, S. Jachmich, G. Kirnev, M. Lehnen, P. J. Lomas, A. Loarte, G. F. Matthews, J. Rapp, C. Silva, M. F. Stamp, J. D. Strachan, and E. Tsitrone. Edge and divertor physics with reversed toroidal field in JET. *Journal of Nuclear Materials*, 339:146–153, 2005. (Cited in sections 4.1.1 and 4.2.)

[108] A. Gallo, N. Fedorczak, R. Maurizio, C. Theiler, S. Elmore, B. Labit, H. Reimerdes, F. Nespoli, P. Ghendrih, and T. Eich. Effect of plasma geometry on divertor heat flux spreading: Monalisa simulations and experimental results from tcv. *Nuclear Materials and Energy*, 2016. (Cited in sections 4.1.3 and 4.4.1.)

[109] P. Hennequin, C. Honoré, A. Truc, A. Quéméneur, C. Fenzi-Bonizec, C. Bourdelle, X. Garbet, G.T. Hoang, and the Tore Supra team. Fluctuation spectra and velocity profile from doppler backscattering on tore supra. *Nuclear Fusion*, 46(9):S771, 2006. (Cited in section 4.1.3.)

[110] M.J. Schaffer, J.A. Boedo, R.A. Moyer, T.N. Carlstrom, and J.G. Watkins. Large exb convection near the divertor x-point. *Journal of Nuclear Materials*, 290:530 – 536, 2001. 14th Int. Conf. on Plasma-Surface Interactions in Controlled Fusion Devices. (Cited in section 4.1.3.)

[111] Ronald H. Cohen and Dmitri Ryutov. Drifts, boundary conditions and convection on open field lines. *Physics of Plasmas*, 6(5):1995–2001, 1999. (Cited in section 4.1.4.)

[112] N Asakura, H Takenaga, S Sakurai, H Tamai, A Sakasai, K Shimizu, and G D Porter. Particle control and sol plasma flow in the w -shaped divertor of jt-60u tokamak. *Plasma Physics and Controlled Fusion*, 44(10):2101, 2002. (Cited in section 4.2.)

[113] P. Tamain. Progress towards self-consistent modelling of the interaction between turbulence and pwi physics in edge transport and turbulence codes. In *Proceedings of ITPA Div-SOL meeting, Princeton*, 2015. (Cited in section 4.3.)

[114] C. Wersal and P. Ricci. A first-principles self-consistent model of plasma turbulence and kinetic neutral dynamics in the tokamak scrape-off layer. *Nuclear Fusion*, 55(12):123014, 2015. (Cited in section 4.3.)

[115] J. R. Harrison, G. M. Fishpool, and B. D. Dudson. Filamentary transport in the private flux region in MAST. *Journal of Nuclear Materials*, 2:2–5, 2014. (Cited in section 4.4.)

[116] R. Maurizio et al. Divertor power load studies for attached l-mode single-null plasmas in tcv. *submitted to Nuclear Fusion.* (Cited in section 4.4.2.)

[117] D. Galassi, P. Tamain, C. Baudoin, H. Bufferand, G. Ciraolo, N. Fedorczak, Ph. Ghendrih, N. Nace, and E. Serre. Flux expansion effect on turbulent transport in 3d global simulations. *Nuclear Materials and Energy*, 2017. (Cited in section 5.)

[118] T. M. Antonsen, J. F. Drake, P. N. Guzdar, A. B. Hassam, Y. T. Lau, C. S. Liu, and S. V. Novakovskii. Physical mechanism of enhanced stability from negative shear in tokamaks: Implications for edge transport and the L-H transition. *Phys. Plasmas*, 3(6):2221, 1996. (Cited in section 5.1.3.)

[119] Fabio Riva, Emmanuel Lanti, Sébastien Jolliet, and Paolo Ricci. Plasma shaping effects on tokamak scrape-off layer turbulence. *Plasma Physics and Controlled Fusion*, 59(3):035001, 2017. (Cited in section 5.1.3.)

[120] X. Garbet, L. Laurent, J.-P. Roubin, and A. Samain. A model for the turbulence in the scrape-off layer of tokamaks. *Nuclear Fusion*, 31(5):967, 1991. (Cited in section 5.2.2.)

[121] Ph. Ghendrih, G. Ciraolo, Y. Larmande, Y. Sarazin, P. Tamain, P. Beyer, G. Chiavassa, G. Darmet, X. Garbet, and V. Grandgirard. Shearing effects on density burst propagation in sol plasmas. *Journal of Nuclear Materials*, 390:425 – 427, 2009. Proceedings of the 18th International Conference on Plasma-Surface Interactions in Controlled Fusion Device. (Cited in section 5.3.)

[122] G. Ciraolo, Ph. Ghendrih, Y. Sarazin, C. Chandre, R. Lima, M. Vittot, and M. Pettini. Control of test particle transport in a turbulent electrostatic model of the scrape-off-layer. *Journal of Nuclear Materials*, 363(Supplement C):550 – 554, 2007. Plasma-Surface Interactions-17. (Cited in section 5.3.)

[123] F.D. Halpern and P. Ricci. Velocity shear, turbulent saturation, and steep plasma gradients in the scrape-off layer of inner-wall limited tokamaks. *Nuclear Fusion*, 57(3):034001, 2017. (Cited in section 5.3.)

[124] E Floriani, G Ciraolo, Ph Ghendrih, R Lima, and Y Sarazin. Self-regulation of turbulence bursts and transport barriers. *Plasma Physics and Controlled Fusion*, 55(9):095012, 2013. (Cited in section 5.3.1.)

[125] Ph. Ghendrih, Y. Sarazin, G. Ciraolo, G. Darmet, X. Garbet, V. Grangirard, P. Tamain, S. Benkadda, and P. Beyer. Transport barrier fluctuations governed by sol turbulence spreading. *Journal of Nuclear Materials*, 363:581 – 585, 2007. Plasma-Surface Interactions-17. (Cited in section 5.3.1.)

[126] K. H. Burrell. Effects of exb velocity shear and magnetic shear on turbulence and transport in magnetic confinement devices. *Physics of Plasmas*, 4(5):1499–1518, 1997. (Cited in sections 5.4 and 5.4.1.)

[127] P. H. Diamond and Y. B. Kim. Theory of mean poloidal flow generation by turbulence. *Physics of Fluids B*, 3:1626, 1991. (Cited in sections 5.4, 5.4.2, and 5.4.2.)

[128] P.J. Roache. *Verification and Validation in Computational Science and Engineering*. Hermosa, 1998. (Cited in section D.1.)

[129] P. Knupp and K. Salari. *Verification of Computer Codes in Computational Science and Engineering*. CRC Press, 2002. (Cited in section D.1.)